Title
Snacktime for Hungry Black Holes: Theoretical Studies of the Tidal Disruption of Stars

Author
Strubbe, Linda Elisabeth

Publication Date
2011

Peer reviewed|Thesis/dissertation

Snacktime for Hungry Black Holes:
Theoretical Studies of the Tidal Disruption of Stars

by

Linda Elisabeth Strubbe

A dissertation submitted in partial satisfaction of the
requirements for the degree of
Doctor of Philosophy

in

Astrophysics

in the

Graduate Division
of the
University of California, Berkeley

Committee in charge:
Professor Eliot Quataert, Chair
Professor Joshua Bloom
Professor Steven Boggs

Fall 2011

Snacktime for Hungry Black Holes:
Theoretical Studies of the Tidal Disruption of Stars

Abstract

Snacktime for Hungry Black Holes:
Theoretical Studies of the Tidal Disruption of Stars

by

Linda Elisabeth Strubbe
Doctor of Philosophy in Astrophysics

University of California, Berkeley

Professor Eliot Quataert, Chair

A star that wanders too close to the massive black hole (BH) in the center of a galaxy is headed for trouble: within a distance $r_{\rm T} \sim r_\star (M_{\rm BH}/M_\star)^{1/3}$ (where $r_\star$ and $M_\star$ are the star's radius and mass, and $M_{\rm BH}$ is the BH's mass), the BH's tidal gravity overcomes the binding gravity of the star, and the star is shredded into a stream of stellar debris. Studying this process of tidal disruption has the potential to give us insights into how central BHs and their surrounding stellar population grow and evolve. Motivated by new and upcoming rapid-cadence optical transient surveys, which should detect and allow study of tidal disruption events (TDEs) in unprecedented detail, I make theoretical predictions of the observable properties of these events to aid in their detection, identification, and interpretation. I find that stellar debris falling towards the BH is likely driven off again by radiation pressure at early times when the feeding rate is super-Eddington: this outflow has a large photosphere and relatively cool temperature, producing a luminous ($\sim 10^{43} - {\rm few} \times 10^{44}\,{\rm erg\,s^{-1}}$) transient event at *optical* wavelengths. I predict that new transient surveys such as the Palomar Transient Factory are likely to find tens to hundreds of these events. I further predict the spectroscopic signature of super-Eddington outflows—broad, blueshifted absorption lines in the ultraviolet—which should help confirm and teach us more about TDE candidates. Finding that the observable appearance of TDEs depends not only on BH mass but on pericenter radius of the star's last fateful orbit, I derive a theoretical expression for the disruption rate as a function of pericenter and apply it to the galaxy NGC 4467 using real observational data, laying the groundwork for more extensive studies in the future. Finally, I also present my work on the debris disk surrounding the star AU Mic, in which I propose an explanation for the physical processes of dust dynamics that give rise to the observed disk profile.

For Mummy and Papa, who taught me to wonder about Nature,
and who encourage me at every step.
And for David, the best brother in the Universe.

Contents

List of Figures

List of Tables

Acknowledgments

I would like to thank my advisor Eliot Quataert for teaching me so much, for being encouraging always and for sharing your excitement and curiosity about the Universe.

I would like to thank all the wonderful people around me for your love and for helping me to see so many butterflies along my path.

And I thank God for the amazing beauty of the Universe, and for the opportunity to study it and share it with others.

Chapter 1

Introduction

1.1 Overview: for non-scientists and scientists

Little did the star know, this was going to be its final orbit, ever. The star was just an ordinary star, several billion years old, very similar to our sun, in the central region of an ordinary galaxy similar to our own Milky Way. Only recently, small gravitational jostlings from other stars in the neighborhood had succeeded in nudging this star's orbit into the danger zone surrounding the mighty black hole at the galaxy's center. For its final year, the star hurtled towards the black hole at close to the speed of light—feeling the black hole's gravity ever more intensely as the distance from the black hole diminished—until it arrived at a spot no further from the black hole than our sun is from us here on earth: the edge of the danger zone. As the star reached that spot, the difference in the black hole's gravity between the opposite sides of the star (nearest and furthest from the black hole) overwhelmed even the star's own gravity that had been holding the star together. The outer layers of the star began to be ripped off, then stellar layers deeper and deeper inside, until there was no longer any star at all—only a long stream of stellar gas stretching around the black hole.

Stellar gas now flowed swiftly towards the black hole. As the high-speed flow funneled in, gas particles collided with each other, heating the gas to enormous temperatures and releasing immense amounts of energy. Some stellar gas was pushed back out and away from the black hole by that extreme release of energy. The remaining gas closely circled the black hole, the circular path shrinking and shrinking like water spiraling down a drain, until gas started spilling over the black hole's edge. This gas released yet more energy as neighboring parcels of gas rubbed past each other, like rubbing your hands together to warm them on a chilly day. All in all, so much energy was released so quickly that for several weeks, the region around the black hole lit up almost as bright as the entire galaxy, 100 billion times as bright as the star had ever shone during its lifetime.

This is the story of the *tidal disruption of a star*—a dramatic astronomical firework that has the potential to reveal secrets about giant black holes and the inner workings of galaxies.[1] Just about every galaxy in the Universe—ours included—is thought to house a giant black hole in its center. A black hole is a creature so incredibly dense that even light can't escape from it, so it looks black. We understand reasonably well how fairly small black holes form—stars at the end of their lives run out of fuel and can collapse under their own gravity—but there are major questions about how the giant black holes in the centers of galaxies came about. The overall idea is that black holes form small but then grow over time by eating nearby stuff in the galaxy: stuff like stars or gas, but mostly gas. An important point is that when black holes eat, their meal heats up and shines very brightly, just before they swallow it. Seeing the light from feasting black holes gives us a way of learning about how black holes eat and grow. Black holes probably feast the most when two galaxies crash into each other and merge into one: gas trajectories in the merging galaxy are thrown into disarray, and so some of the gas ends up flying right into the black hole. The details of how all of this works, though, are not yet understood very well.

One path to understanding this better is to watch closely while a black hole eats a star—a mini-version of a black hole gorging on a galaxy's worth of gas. If a star's orbit carries it too close to the black hole, the black hole's gravity rips it apart, sending some of the star's gas down into the black hole. Just like bigger meals, the star's gas should shine brightly as the black hole eats it, and so we should be able to see it. Unfortunately, telescope surveys of the sky haven't been able to find many of these events so far, because the telescopes and cameras haven't been powerful enough. But now, with new technology, several new powerful, fast-paced surveys are starting up. There's a twist though: while everyone thought stellar meals would be so hot that they'd shine at X-ray wavelengths, these new surveys are at *optical* wavelengths (the kind of light we see with our eyes). Will the new surveys be able to find black holes eating stars?

My thesis work says that they *will*. I have made theoretical calculations to predict what it should look like when a black hole eats a star: how bright it should be, how long the brightness should last, what color it should be, and what the spectrum should look like (when the light is passed through an instrument like a prism, to separate the light into different wavelengths). I made these calculations by building on previous work. Earlier studies used simple physics to theorize how quickly stellar gas is fed to the black hole. Many other studies have investigated black holes eating gas in other situations—small, medium and large black holes eating gas quickly or slowly. The process is actually extremely complicated: magnetic fields are created that help the gas drain into the black hole, while all that light created when the gas heats up can push the gas around. Astronomers observe black holes eating, create models to explain what they see, use the models to make predictions, test the predictions by observing more black holes, refine the models, etc., improving our understanding all the time. I adapted some of these results to the situation of a black hole eating a star, and

[1] To keep this section uncluttered, I'm refraining from giving references here; the technical introductory sections §§1.2 and 1.3 contain references for the ideas and work mentioned here.

used them to predict what we'll see. Many of my calculations are simple—I can just write down a few equations on a piece of paper—which makes them easier to understand than complicated work on a computer. The art, though, lies in choosing the correct equations: they're simple because they capture only the most important physics—which means I have to make sure I have a good idea of what's important and what's not, so I don't end up leaving out something important.

One of the most significant conclusions of my thesis is that, as I mentioned, these new optical surveys have the potential to find lots of black holes eating stars. They could find *hundreds*, compared with the handful we know about today. The reason is that after a star is disrupted, its gas flows very quickly towards the black hole, heating up a lot and creating lots of photons (particles of light). Photons can actually push back on gas particles, like hurling tennis balls up at falling balloons, so that much of the star's gas is blown back out from the black hole. (It's not an explosion, but you can picture the gas expanding out from the black hole in all directions kind of like that.) Because the gas is now fairly far from the black hole, it's cooler in temperature than was previously thought, which means it shines in *optical* light, not (just) X-rays. They shine very brightly, too—almost as bright as a whole galaxy! And they appear and disappear on very human timescales (unusual for astronomy), lasting a few days up to a few weeks.

Along the way, I also made calculations about how often we should expect black holes to eat stars. Many people have studied this question before, but my work takes a different slant: I wondered how often stars approach very close to the black hole on their last fateful orbits, versus how often stars are only *just* torn apart as they graze the edge of the black hole's disruption zone. My earlier work showed that we should be able to tell the difference between these two scenarios when we watch a star get eaten, because the former is more violent. I concluded that the violent events are significantly less frequent than the gentler ones. Another part of my research—unrelated to black holes eating stars—was studying a disk of dust around a young star. The dust is probably created when rocks—baby planets—collide as they orbit the star. I explained why we see the dust arranged the way it is, helping give us a foundation for using disks like this to improve our understanding of how planets form.

Back to black holes eating stars. Excitingly, after I published my first results a couple of years ago, candidate black-holes-eating-stars have been identified using *optical* data for the very first time! And the way these events look is quite consistent with my predictions. These surveys are just getting underway, and are likely to find many more events soon, giving us the chance to study black holes eating stars in far greater detail than ever before. Stars may be just a little snack for a huge black hole, but learning about how black holes eat these morsels will teach us about how black holes eat when a flood of gas comes their way—say, when two galaxies merge together. Ultimately, my work will help us understand better how black holes in the centers of galaxies—including the center of our own Milky Way—grew up from baby black holes all the way into *giants*.

1.2 Astrophysical context for studying the tidal disruption of stars (technical)

Observational studies over the past decade have shown that the nuclei of all (or nearly all) moderately massive galaxies host a massive black hole (BH) (e.g., Richstone et al. 1998), and that the mass of the BH correlates with properties of the surrounding stellar bulge (e.g., Ferrarese & Merritt 2000; Gebhardt et al. 2000a; Häring & Rix 2004). The observed BH-bulge correlations are quite surprising since the bulge extends far outside the region where the BH's gravity can be felt, and suggest that BHs and bulges evolve together, somehow checking each other's growth (e.g., Silk & Rees 1998; Di Matteo et al. 2005). However, this "feedback" is poorly understood—and so "How do black holes work and influence their surroundings?" is one of the 2010 Decadal Survey's science frontier questions (National Research Council; Committee for a Decadal Survey of Astronomy and Astrophysics 2011). The connection between BH growth and bulge growth stands as one of the most important questions in galaxy formation.

Studying the tidal disruption of stars offers promising avenues for investigating the BH-bulge connection. An unlucky star that passes within $r_{\rm T} \sim r_\star (M_{\rm BH}/M_\star)^{1/3}$ of a galaxy's central black hole (BH) will disrupt as the BH's tidal gravity exceeds the star's self-gravity. (Here, $r_\star$ and $M_\star$ are the mass and radius of the star, and $M_{\rm BH}$ is the mass of the BH.) For BHs of mass $M_{\rm BH} \leq 10^8 M_\odot$, the disruption of a solar-type star occurs outside the horizon and is likely accompanied by a week- to year-long electromagnetic flare (e.g., Rees 1988). Detecting and studying these flares ("tidal disruption events," or TDEs) has the potential to teach us about BHs in galactic nuclei in several ways, which we summarize quickly and then elaborate on further through this section.

1. A TDE indicates the presence of a BH in a particular galaxy, and can offer an estimate of the BH's mass. Direct detections and mass measurements of BHs in galactic nuclei are otherwise only possible in a very restricted set of galaxies.

2. The accretion of stellar gas onto the BH in the aftermath of a star's disruption provides a "clean lab" for observationally studying accretion physics, wherein we have an idea of the mass and dynamics of the gas being fed to the BH. Understanding this accretion process will help us better understand the physics of gas accretion onto BHs during galaxy mergers as well.

3. Galaxy and BH mergers likely leave their mark on the structure of galactic nuclei, but particularly on scales well below the resolution accessible to imaging studies. The observed rate of TDEs may in future be able to indicate the structure of galactic nuclei close to the BH as a function of larger galaxy properties.

4. The observed rate of TDEs will also indicate how important consumption of stars is in the process of BH growth for different BH masses and galaxy types.

Much of my thesis work has been to make detailed predictions for the observational appearance of TDEs. Although attempts over the last $\sim$ 15 years to observationally find and study TDEs have been challenged by sparse amounts of data, we are now entering a new era of wide-field rapid-cadence transient surveys with the potential to detect and study TDEs in unprecedented detail. I have made predictions to help these new surveys find and interpret tidal disruptions—with the aim of using TDEs to improve our understanding of BH and bulge co-evolution. In this section, I will describe in detail each of these four aspects of how TDEs can teach us about BHs and their surrounding galactic nuclei, at the same time highlighting physical concepts and phenomenology that inform our predictions about TDEs.

1.2.1 The presence and masses of central black holes

Quasars (or quasi-stellar objects: QSOs), first uncovered by radio surveys in the 1950s (see Krolik 1999, for review), were the first signposts to the presence of giant BHs residing in very distant galaxies. The extreme luminosity of these objects could only plausibly be explained by high rates of gas accretion onto very massive ($\gtrsim 10^8 M_\odot$) BHs (e.g., Rees 1977). In the decades since these first discoveries, more directly detecting and weighing BHs has become possible via several methods—it proves to be a challenging undertaking, but tidal disruption events should offer an important new approach.

The BH in the center of our Galaxy can be studied most directly, by monitoring (using adaptive optics) the proper motion of stars around an unseen central object (almost certainly a BH) of mass $M_{\rm BH} \approx 4 \times 10^6 M_\odot$ (e.g., Ghez et al. 2008; Genzel et al. 2010). In external galaxies, however, direct imaging of individual stars in this way is not possible. A technique similar in spirit is to image the central regions of moderately massive nearby galaxies at very high spatial resolution, so that the BH's radius of influence can be resolved. The BH's radius of influence, $r_{\rm inf} \sim GM_{\rm BH}/\sigma_{\rm b}^2$, is the location inside which the gravity of the BH dominates the gravity of the surrounding stars ($\sigma_{\rm b}$ refers to the stellar velocity dispersion in the bulge). This photometric information is accompanied by a long-slit spectrum across the center of the galaxy, which gives the velocity dispersion as a function of radius. This can be used to estimate a BH mass very simply [$GM_{\rm BH}/r = \sigma^2(r)$], or to calculate $M_{\rm BH}$ more exactly by fitting families of stellar orbits to the surface brightness profile and velocity dispersion data (e.g., Gebhardt et al. 2000b). This same technique can also be performed using observations of gas rather than starlight (e.g., Atkinson et al. 2005). Most recently, BH mass measurements are beginning to be undertaken using two-dimensional velocity dispersion data with integrated field units (e.g., Shapiro et al. 2006; McConnell et al. 2011). Most of these studies require the *Hubble Space Telescope* or adaptive optics, and are only possible for our nearest dozens of moderately massive neighbor galaxies, because only in these galaxies can we spatially resolve $r_{\rm inf}$.

Another technique to weigh BHs employs active galactic nuclei (AGN). (AGN are similar to quasars, but less luminous relative to their host galaxy so that the host galaxy is actually visible.) One method is called reverberation mapping (e.g., Peterson et al. 2004). AGN

light curves often exhibit time variability, brightening temporarily presumably as the mass accretion rate rises due to some instability. The variability is observed to occur at different times in different emission components: the optical/UV/X-ray continuum emission (thought to come from an accretion disk close to the BH) brightens first, followed later in time by the brightening of broad emission lines. The time lag is interpreted as light travel time from the accretion disk out to a location in the broad line region (BLR); in combination with the width of the broad line (which gives the velocity), these measurements can be used to estimate the BH mass.[2] Reverberation mapping was used to discover an empirical relation between BLR line luminosity and location in the BLR, which allows a BH mass measurement from a single epoch of spectroscopy (e.g., Kaspi et al. 2005). And finally, observations of water masers in galactic nuclei can also yield BH mass measurements (e.g., Greene et al. 2010): the orbital motion of water masers can be measured very precisely with radio interferometry, and then fit to a model potential.

All of these observational BH studies have led to several important conclusions: (almost) all moderately massive galaxies host a massive BH at their center (e.g., Richstone et al. 1998), and the mass of the BH correlates with the host galaxy[3] bulge's stellar mass, luminosity, and velocity dispersion (e.g., Ferrarese & Merritt 2000; Gebhardt et al. 2000a; Häring & Rix 2004). However, several interesting caveats to these conclusions are in order. First, these correlations hold with significantly larger scatter for lower-mass BHs in the $\sim 10^5 - 10^7 M_\odot$ range (especially those hosted by "pseudobulges," galactic nuclei that are flatter and more rotation-dominated than classical bulges) (e.g., Greene et al. 2008); indeed a few low-mass galaxies have been found to host no massive BH at all (e.g., Gebhardt et al. 2001). Second, the above techniques for measuring $M_{\rm BH}$ are possible for only a small number of galaxies: those that are very nearby and moderately massive (so that we can resolve the radius of influence), and those that host an AGN (or water masers). If the correlations are different for more distant galaxies, lower-mass galaxies, or non-AGN, there is little way we would know currently.

As I show in Chapters 2 and 3, the luminosities, peak wavelengths, evolution timescales, and spectral lines of tidal disruption events all depend on the mass of the BH. TDEs turn out to be bright at optical wavelengths even for $\sim 10^5 - 10^6 M_\odot$ BHs, and may be visible as far away as $z \sim 1$. Thus, observationally studying the tidal disruption of stars offers an exciting new technique for estimating BH masses, even in fairly low-mass or distant galaxies, and does not depend on the presence of an AGN.

1.2.2 The orbits of stars in galactic nuclei

Not only can we measure BH masses directly in only a few dozen galaxies, we can only measure the distribution of stars (their number density and velocities as a function of location) close to the BH in an even more limited set of galaxies. Yet the structure

[2]Note that the zero-point in this method is calibrated to the dynamically measured $M_{\rm BH}$–σ relation, to resolve geometrical ambiguities.

[3]A "bulge" means an entire elliptical galaxy, or the bulge in the center of a spiral galaxy.

of the nucleus of our Milky Way galaxy is richly complex: there is a circumnuclear disk of molecular gas, an ionized gas structure called the "mini-spiral," dense stellar "superclusters," and either one or two disks of stars right in the central parsec (e.g., Lu et al. 2009; Genzel et al. 2010). Our neighbor the Andromeda galaxy (M31) harbors an interesting nuclear region as well, with a disk of stars orbiting the central BH on aligned eccentric orbits (e.g., Peiris & Tremaine 2003). These tantalizing observations, which likely carry imprints of the galaxies' and BHs' histories, suggest that the nuclei of many galaxies have interesting stories to tell, even though we cannot measure such detail in distant galaxies. Observing how often BHs tidally disrupt stars can offer us a new window into the structure of galactic nuclei, which can inform our understanding of how they formed.

I will now quickly review observations of the nuclei of the dozens of galaxies nearby enough for high-resolution photometric and kinematic studies. The nuclei of nearby "classical" galaxy bulges typically exhibit a broken power-law surface brightness profile that breaks at a radius of a few to tens of parsecs (e.g., Faber et al. 1997). There may be a dichotomy between galaxies with a shallow inner slope ("core galaxies") and a steeper inner slope ("cusp galaxies") (e.g., Lauer et al. 1995). Integral field studies show that bulge galaxies appear to comprise both "slow rotators" dominated by random stellar motions, which often show misaligned photometric and kinematic axes indicating that their shape is triaxial, and "fast rotators" with significant stellar orbital angular momentum that tend to be axisymmetric in shape (e.g., Cappellari et al. 2007). The disks of disk galaxies are supported by rotation, and often show large-scale asymmetric features such as a bar or spiral arms. In the nuclei of many disk galaxies ($\sim 75\%$ of local late-type spirals), the surface brightness profile rises sharply at the innermost radii, indicating the presence of a nuclear star cluster: these are massive ($\sim 10^6 - 10^7 M_\odot$), compact (several pc across), and can show a high degree of rotational support (e.g., Böker et al. 2002; Seth et al. 2008b). Tens of nearby galactic nuclei also appear to be "pseudobulges," observationally distinguished from classical bulges by their more flattened shapes, more ordered stellar velocities relative to random, exponential surface brightness profiles, and often nuclear structure such as a bar or spiral arms (Kormendy & Kennicutt 2004). Pseudobulges range from a prominent galaxy component to tiny, containing just a few percent of the mass in giant virtually pure-disk galaxies (Kormendy et al. 2010). What processes produce this diversity of galaxy structures?

The hierarchical clustering picture of galaxy formation theorizes that galaxies grow by merging repetitively (White & Rees 1978). Major galaxy mergers scramble the galactic potential: any pre-existing galactic disk that had grown by gas accretion or minor mergers violently relaxes into a classical bulge. Large-scale gravitational instability (for example, a galactic bar) drives gas to the galactic nucleus, where it forms stars and feeds the central black hole(s) (Barnes & Hernquist 1991). Dynamical friction causes the BHs from both galaxies to make their way to the center of the merging galaxies. Through interactions with the gas and stars in the nucleus, the BHs give up their angular momentum, and eventually can merge via the emission of gravitational waves (e.g., Holz & Hughes 2005). The structure in the nucleus of the merging galaxies must affect the ability of BHs to lose angular momentum, and the merging BHs must also leave their mark on the nuclear structure of the merged galaxy. For

example, BHs likely lose angular momentum by kicking stars out of the nuclear region, which may leave the nucleus relatively empty, in line with observations of core galaxies (e.g., Lauer et al. 2005). Meanwhile, gas flowing to the galaxy's center and feeding the BH may form a massive nuclear star cluster (see Ferrarese et al. 2006; Wehner & Harris 2006; Seth et al. 2008a), and/or leave behind an eccentric disk of gas that forms into stars like what is seen in the nucleus of M31 (e.g., Hopkins & Quataert 2010). Later on, after the last major merger, it is thought that continued gas accretion and/or minor mergers can grow a galactic disk around the classical bulge. On the other hand, galaxies containing a pseudobulge (rather than a classical bulge) may have experienced *no* major mergers at all: their much slower secular evolution is likely instead driven by interactions between gas clouds and stars with galaxy-scale structures like a bar or spiral, which funnel matter to the center triggering star formation (Kormendy & Kennicutt 2004).

This wide variety of orbital properties of stars in the nuclei of galaxies should lead to a variety of rates of tidal disruption as a function of galaxy type. The basic mechanism for putting stars on orbits bound for the BH's disruption zone is gravitational encounters with other stars: two-body relaxation (e.g., Frank & Rees 1976). This mechanism is likely dominant in spherically symmetric and isotropic nuclei. Other possible mechanisms include resonant relaxation (if stars deep in the BH's potential well dominate the rate: Hopman & Alexander 2006) or gravitational encounters with giant molecular clouds (if there are enough GMCs close to / inside the BH's sphere of influence: Perets et al. 2007). Thirdly, triaxial or asymmetrical galactic potentials (such as is produced by a bar, spiral, or eccentric disk) produce chaotic stellar orbits which can carry stars to the BH's disruption zone without requiring gravitational scattering (Merritt & Poon 2004). Stars in the vicinity of two merging BHs can be kicked onto chaotic orbits bound for disruption as well (e.g., Chen et al. 2009). Observing the rate of tidal disruption in various galaxy types can therefore offer an important probe of the structure of galactic nuclei—even in galaxies much too far away to measure the structure directly—which can help us learn about the galaxies' and BHs' histories. Chapters 2 and 3 describe my work on predicting observable properties of TDEs in order to help transient surveys begin to make these rate measurements. Chapter 4 describes my work on predicting the disruption rate as a function of distance from the BH, which should be an even more sensitive probe of galaxy structure than the overall disruption rate alone.

Measuring the rate of tidal disruption in different galaxy types can also indicate whether consumption of stars makes an important contribution to BH growth in these galaxies. As discussed in the next section, many BHs probably grow primarily by accreting nearby gas (e.g., Yu & Tremaine 2002). The consumption of stars may be significant for the growth of lower-mass BHs, however: if the rate of disruption is $\sim 10^{-5}\,\mathrm{yr}^{-1}$ (as estimated by the *ROSAT* All-Sky Survey: Donley et al. 2002), a $10^5 M_\odot$ may be able to double its mass over a Hubble time by disrupting stars. Note that an important question is whether or not the BH can consume a sizable fraction of the stellar mass fed to it following disruption, or whether most of the gas is blown away in an outflow (discussed further in the next section). In any case, studying the rates of tidal disruption events can give us insight into the orbital properties of stars in galactic nuclei, thereby giving us another tack for understanding the

evolution of the stars and BHs in galactic nuclei.

1.2.3 The growth of black holes

The tidal disruption of stars can also offer insights into how all of these massive BHs formed and grew. It is believed that massive BHs began their lives as smaller BHs ("seed BHs"), and over time have grown by consuming nearby material: gas, stars, and other BHs. In this subsection, we focus on BH growth via the accretion of gas: TDEs can help us understand this process by providing opportunities to observe accretion physics in relatively clean conditions.

A variety of mechanisms have been proposed for forming seed BHs (e.g., van der Marel 2004). Seed BHs of mass $\sim$ few $\times\, 100 M_\odot$ may be the remnants of stellar evolution from the first generation of stars (the zero-metallicity Population III stars), since the lack of metals allowed more massive stars to form and diminished the rate of stellar mass loss. Another possibility is that seed BHs could form via runaway stellar mergers in the dense central regions of galactic nuclei or globular clusters. A third idea is that seed BHs formed primordially in the early Universe.

Once formed, at least some fraction of these seed BHs must have grown substantially to produce the massive $\sim 10^6 - 10^{10} M_\odot$ BHs we observe today. Observations of quasars and AGN show that at least some of that growth proceeded via the accretion of gas: in fact, by using the quasar luminosity function to estimate how much mass must have been accreted, and comparing with the inferred mass density of BHs today, Soltan (1982) and Yu & Tremaine (2002) have shown that gas accretion must account for the bulk of BH growth (at least for fairly massive BHs).

Gas with even a relatively tiny amount of angular momentum must lose much of that angular momentum before it can accrete onto a central BH. To begin with, gas just falls towards the BH, radiating away energy while conserving angular momentum; eventually the gas falls far enough that its angular momentum corresponds roughly to that of a circular orbit. The gas can fall no further until it loses angular momentum, and it settles into a rotationally-supported disk structure (e.g., Pringle 1981). Losing angular momentum is a complicated process. Simple molecular or particle viscosity is orders of magnitude too weak to affect the angular momentum (because the mean free path for gas particles is so short). Instead, turbulent viscosity, where bulk motions on the scale of the accretion disk, appears to be responsible. A simple commonly-used model to parametrize this viscosity is $\nu = \alpha c_\mathrm{s} H$, where c_s is the gas sound speed, H is the disk scale height, and $\alpha \lesssim 1$ is an unknown dimensionless number (Shakura & Sunyaev 1973).

The leading idea for the physical mechanism to produce the turbulence is the magnetorotational instability (MRI) (Balbus & Hawley 2002), which requires a weak magnetic field threading the disk and that the angular velocity decreases with radius (as in a Keplerian potential around a BH). Consider two radially adjacent fluid elements, which are connected by the magnetic field: the inner element moves more quickly while the outer element moves more slowly, increasing the distance between them. This increasing distance is opposed by

the force of magnetic tension (since field lines connect the two elements), which slows the inner element down and speeds the outer element up. The slower inner element then sinks deeper into the BH's potential, losing angular momentum, while the outer element moves outward, gaining angular momentum: this further increases their separation, and the process runs away.

The MRI has been and continues to be investigated by numerical simulations of increasing realism and complexity (e.g., Stone & Pringle 2001; Sharma et al. 2007). A major subtlety is the presence of radiation: close to the BH (at $\sim$ tens of Schwarzschild radii), the radiation pressure in the accretion flow far exceeds the gas pressure (for thin disks). One complication that has plagued the field is whether the sound speed $c_{\rm s}$ in the viscosity $\nu \sim \alpha c_{\rm s} H$ should be due the combination of radiation and gas pressure, or to gas pressure alone. In addition, Lightman & Eardley (1974) showed that under the Shakura & Sunyaev (1973) model, a radiation-pressure dominated (vertically thin) accretion disk is subject to thermal and viscous instabilities. Hirose et al. (2009) recently used numerical simulations to show that a thin disk undergoing the MRI actually *is* thermally stable, and that the bulk viscosity is best predicted by including radiation and gas pressure both. Verifying the viscous instability is more challenging, but it appears that the viscous instability may remain (Blaes et al. 2011): gas may pile up in particular annuli while other annuli are empty, likely leading to sharp swings in the accretion rate. Accretion disks may be unstable to convection and the photon bubble instability as well (e.g., Gammie 1998).

How well accretion flows can radiate away their energy has a large impact on the resulting dynamics (see, e.g., Frank et al. 1992; Krolik 1999). For a range of mass feeding rates, the situation is fairly simple: the time it takes for gas at a given radius to be transported inward is substantially longer than the time for photons to be created (typically by bremsstrahlung) and diffuse vertically out of the disk (which is typically optically thick to bremsstrahlung and electron scattering). The disk can therefore cool efficiently and so is geometrically thin (i.e., the vertical scale height is much less than the radius from the BH). The disk is expected to emit as a multicolor blackbody (or modified blackbody, if the disk opacity is dominated by scattering). The comparison of advection time to radiation time corresponds to a comparison of the mass feeding rate to the Eddington rate, $\dot{M}_{\rm Edd} = L_{\rm Edd}/\epsilon c^2 = 4\pi G M_{\rm BH}/\epsilon \kappa_{\rm es} c$, where $\epsilon \approx 0.1$ is a typical radiative efficiency and $\kappa_{\rm es}$ is the electron scattering opacity. This thin disk model applies when the feeding rate is $\sim 0.01 - 1 \dot{M}_{\rm Edd}$.

However, when the feeding rate is greater or much less than the Eddington rate, the situation is more complicated: the flow may not be able to cool efficiently, and so it becomes hot and geometrically thick. When the feeding rate exceeds the Eddington rate, photons aren't able to escape from the flow on less than an advection time: instead, some trapped photons are probably carried down into the BH along with the gas, and others push on low-angular momentum gas to drive an outflow away from the BH (e.g., King & Pounds 2003). Abramowicz et al. (1988) developed the "slim disk" model to describe the accretion flow at moderately super-Eddington rates. Ohsuga et al. (2005) numerically simulated BH feeding at $100 \dot{M}_{\rm Edd}$ and found that about 10% of the gas was unbound in an outflow. The dynamics and observational appearance of the gas during super-Eddington accretion remain

important unsolved questions.

When the feeding rate is below $\sim 0.01\dot{M}_{\rm Edd}$, the flow can be radiatively inefficient as well, due to its very low density. If the flow is hot, Coulomb collisions happen too infrequently to produce the photons necessary to cool the gas, and so it remains hot, geometrically thick and optically thin (e.g., Ichimaru 1977; Narayan & Yi 1994). The ions and electrons have different temperatures (ions are hotter), and photons are Compton upscattered to produce hard X-rays. Variations on this "advection-dominated accretion flow" (ADAF: Narayan & Yi 1994) idea allow for gas to be driven back out from the BH at the same time: because the hot gas is only tenuously bound to the BH, it should be easy to unbind some of it using some fraction of the energy released when even a small amount of gas accretes onto the BH. Ideas in this vein include the "advection-dominated inflow-outflow solution" (ADIOS: Blandford & Begelman 1999), in which much of the gas is driven out in a wind from small radii, and the "convection-dominated accretion flow" (CDAF: Quataert & Gruzinov 2000), in which the liberated accretion energy drives gas out to large radii via convection.

Observational studies of accreting objects provide important motivation and tests of these accretion theories. X-ray binary systems (XRBs) are especially important (see Remillard & McClintock 2006, and references therein). These systems comprise a compact object emitting X-rays as it accretes gas from a donor star (which may be on the main sequence, a red giant, or a white dwarf): either the compact object intercepts a fraction of the donor star's stellar wind, or tidal forces from the compact object rip gas directly off the donor star (as it overflows its Roche lobe). Many XRBs are observed to transition abruptly between two states of emission, the "high soft" state, in which the emission is relatively bright and the spectrum is close to thermal, and the "low hard" state, in which the emission is fainter and peaks in the hard X-rays. Another state sometimes observed is the "steep power-law" state, in which the emission is even brighter and softer than the high soft state. These observations have been interpreted as follows (e.g., Esin et al. 1997): the high soft state is the radiatively efficient thin disk during periods of high feeding, and the low hard state is the radiatively inefficient optically thin flow during periods of low feeding. The steep power-law state may arise from super-Eddington feeding rates. Radio emission is often observed to accompany the hard X-rays of the low hard state: this has been interpreted as synchrotron emission from a highly collimated, relativistic jet driven by magnetic fields close to the BH, perhaps tapping into the BH's spin.

Active galactic nuclei show many similarities to XRBs. Seyfert galaxies and quasars show prominent thermal emission (though also X-rays and radio emission), which is probably produced by radiatively efficient accretion at somewhat sub-Eddington feeding rates (see Krolik 1999, and references therein). Many more galactic nuclei host low-luminosity AGN (including our own Galactic nucleus), where the bolometric luminosity may be as low as $10^{-5}L_{\rm Edd}$ ($\lesssim 10^{-8}L_{\rm Edd}$ for the Milky Way); much of the energy in these AGN is released in the X-rays, and radio emission is prominent as well (e.g., Ho 2008; Genzel et al. 2010). These are likely galactic nuclei with a very sub-Eddington mass feeding rate. Quasars, by contrast, shine at a high fraction of their Eddington luminosities, and thus are likely being fed at super-Eddington rates (e.g., Kollmeier et al. 2006). Many bright AGN/quasars also

emit strongly in the radio (see Krolik 1999). Blueshifted absorption lines in the spectra of bright AGN are likely produced by outflowing gas obscuring a central accretion disk (e.g., Weymann et al. 1991; Pounds et al. 2003; Murray et al. 1995).

The tidal disruption of stars offers another opportunity to study accretion physics—perhaps easier to interpret than XRBs and AGN because we have an idea of the mass feeding rate and inflowing gas geometry *a priori*. TDEs let us study the accretion onto a BH through a wide range of feeding rates, from highly super-Eddington through highly sub-Eddington, over a period of only months to years. We may be able to learn about the speed and mass flux of outflows, in particular teaching us about what fraction of gas can accrete onto a BH and contribute to its growth during super-Eddington feeding. We may also be able to learn about the sub-Eddington transition from radiatively efficient to inefficient flow, and about the conditions required to produce a radio jet.

1.3 Previous studies of the tidal disruption of stars

In this section, we describe previous research on the tidal disruption of stars by massive black holes. The tidal disruption of stars was first studied in the 1970s as a source of fuel for BHs, in the hopes of explaining observations of quasars[4] (e.g., Hills 1975; Young et al. 1977; Frank 1978). This explanation was soon abandoned, as it was realized that the rate of tidal disruptions necessary to explain the abundance of quasars required unrealistically high stellar densities in nuclei of galaxies. (As we have said, the leading idea today to explain quasars is galaxy-scale instabilities related to galaxy mergers that funnel gas to the center, where it is accreted by the central massive BH.) Later on, Rees (1988) revived interest in studying the tidal disruption of stars: he pointed out that even if it cannot explain quasar observations, the process must nevertheless happen in any galaxy hosting a moderately massive BH, and so could be used to find BHs and constrain their prevalence in the Universe.

Studies of the tidal disruption of stars are generally focused either on predicting the rate of such events in galactic nuclei, or on predicting the observational appearance and effects on the BH's environs. My thesis work includes both types of studies, and the physics involved in each is quite different: gravitational dynamics to understand disruption rates, and hydrodynamics and accretion physics to understand observational properties. We describe previous research in each subtopic in turn.

1.3.1 Stellar dynamical studies of the tidal disruption of stars

In this section, we describe previous calculations of the dynamics of stars orbiting a black hole, as bears on the tidal disruption rate. We begin with order-of-magnitude estimates, then discuss more precise calculations using the distribution function and Fokker-Planck equation (the background for both of these is discussed in much more detail in Chapter 4). We then describe other dynamical effects.

[4]This has the wonderful name, the "black tide" model.

The basic work on tidal disruption rates considers a very simple situation, a BH embedded in a cluster of stars that is spherically symmetric and whose velocities are distributed (at least mostly) isotropically. In the absence of gravitational interactions, stars that are on orbits aimed at the BH's disruption zone would be destroyed in a dynamical time, and all other stars would be safe "forever." Instead, gravitational interactions between stars occasionally alters stellar orbits, providing a continuing supply of stars on orbits aimed at the disruption zone (e.g., Frank & Rees 1976). (Such orbits are said to be in the "loss cone," the region of velocity space where stars can be lost to the BH. If you draw a sphere around a star, the set of velocity vectors aimed inside the disruption region fills a cone-shaped region.) In a gravitational interaction, two stars passing each other at a distance b change each other's orbital velocity by

$$\delta v \sim \frac{Gm}{bv} \tag{1.1}$$

(where m is the stellar mass and v is a typical stellar velocity), and so during a "relaxation time" $t_{\rm rel}$, stellar velocities are changed by order unity,

$$t_{\rm rel} \sim \frac{v^3}{G^2 m^2 n} \frac{1}{\ln \Lambda} \tag{1.2}$$

(where n is the stellar number density and Λ accounts for integration over all possible separations b) (see Binney & Tremaine 1987). Simple estimates[5] of tidal disruption rates assume that gravitational relaxation happens efficiently enough to keep the loss cone "full" (e.g., Rees 1988), and so the rate of disruption is simply

$$\gamma \sim \frac{N(<r)}{t_{\rm dyn}(r)} \theta_{\rm lc}^2(r)\,, \tag{1.3}$$

where N is the number of stars inside r, $t_{\rm dyn} \sim (r^3/GM_{\rm BH})^{1/2}$ is the dynamical time, and $\theta_{\rm lc}^2$ is the solid angle of the loss cone. Frank & Rees (1976) and Lightman & Shapiro (1977) pointed out, however, that at sufficiently small distances from the BH (sufficiently large negative energies), the fractional velocity change over a dynamical time due to gravitational encounters is insufficient to completely refill the loss cone: in this limit, the disruption rate from a starting radius r is

$$\gamma \sim \frac{N(<r)}{\ln(\sqrt{r/r_{\rm T}})\, t_{\rm rel}(r)} \tag{1.4}$$

(e.g., Alexander 2005). It turns out that an integration over orbital energy (roughly corresponding to a star's starting radius) demonstrates that most disrupted stars come from the junction between the full loss cone regime and this diffusive regime, at an energy dubbed $E_{\rm crit}$ (e.g., Magorrian & Tremaine 1999). Since $E_{\rm crit}$ is much greater (much less negative) than the energy of a circular orbit inside the disruption zone, stars on course to disrupt typically approach the BH on approximately parabolic orbits. Furthermore, it turns out that

[5]Other simple estimates ignore the loss cone completely, and assume that diffusion in energy space is responsible for disrupting stars (e.g., Bahcall & Wolf 1976; Shapiro & Lightman 1976).

$E_{\rm crit}$ typically corresponds to a radius close to the radius of influence of the BH; using $r_{\rm inf}$ in equation (1.4) gives a typical disruption rate per galaxy of $10^{-5} - 10^{-4}\,{\rm yr}^{-1}$ (e.g., Alexander 2005).

Work beyond these order-of-magnitude estimates requires calculating the distribution function of stars, i.e., the spatial density and distribution of velocities (see Binney & Tremaine 1987). In the absence of gravitational interactions, the distribution function would obey the Boltzmann equation. The effect of gravitational interactions, assumed to be weak, is approximated by the Fokker-Planck equation (borrowed from plasma physics, where the Coulomb force on ions/electrons parallels the gravitational force acting on stars). Two-body gravitational interactions cause the distribution function to diffuse over the relaxation timescale; the (spherically symmetric, isotropic) diffusion coefficients have been calculated by Rosenbluth et al. (1957). The tidal disruption rate is found by solving the Fokker-Planck equation for the distribution function, subject to approriate boundary conditions accounting for the presence of the loss cone; then calculating the rate at which the distribution function flows into the loss cone. Solving the Fokker-Planck equation is challenging. One route is direct integration, usually averaging over an orbital period and assuming that gravitational interactions are short enough range to affect only orbital velocity and not orbital position (e.g., Lightman & Shapiro 1977; Cohn & Kulsrud 1978). Another route has been Monte Carlo calculations, where the orbits of stars are directly integrated, occasionally being perturbed randomly (according to a distribution calibrated to the diffusion coefficients) (e.g., Spitzer & Hart 1971; Shapiro & Marchant 1978). Comparison of these two complementary approaches is used to confirm each other's results. Direct N-body calculations of an entire galaxy bulge have been too computationally expensive so far.

In the late 1990s, high-resolution imaging from the *Hubble Space Telescope* gave us the first views of external galactic nuclei inside the BH's radius of influence, in a sample of about thirty nearby elliptical galaxies. Spectroscopic results along with two-integral axisymmetric modeling was used to estimate masses for the stellar distribution and BH (Magorrian et al. 1998). Syer & Ulmer (1999) used these observational results to calculate tidal disruption rates for real galaxies for the first time, assuming spherical symmetry and isotropic velocity distribution. They derived rates of $\sim 10^{-7} - 10^{-4}\,{\rm yr}^{-1}$ per galaxy. Magorrian & Tremaine (1999) performed similar calculations but assuming axisymmetry, and obtained similar (slightly higher) results. Several years later, the observational results for these BH masses were found to be too high; Wang & Merritt (2004) recalculated disruption rates using the $M_{\rm BH} - \sigma_*$ relation for $M_{\rm BH}$, assuming spherical symmetry and isotropy. Despite the increasing number of galaxies with high-resolution imaging of their nuclei and dynamically-measured BH masses, no further data-based disruption rate calculations have been published. (This is a direction I intend to pursue, particularly focusing on non-elliptical galaxies.)

Thus far, all of the calculations mentioned in this section assume that two-body gravitational interactions are the primary process driving stellar orbits into the disruption zone. A variety of other dynamical effects have been proposed and studied as well (as already alluded to in §1.2.2). Merritt & Poon (2004) predicted tidal disruption rates in model galaxies having triaxial shapes, showing that stellar orbits become chaotic and can head for the disruption

zone even without suffering gravitational scatterings. Their rate estimates reach as high as $\sim 10^{-3}\,\mathrm{yr}^{-1}$. A process called resonant relaxation (e.g, Rauch & Tremaine 1996) may also be relevant: because stars close to the BH orbit in an almost-Keplerian potential, the timescale during which they can torque each other's orbits becomes longer and so relaxation proceeds more quickly. This mechanism is probably not that important for tidal disruption rates, since rates are typically set by the stars close to the BH's radius of influence, where the potential is no longer very Keplerian. Zhao et al. (2002) proposed that "massive perturbers" are important for tidal disruption rates: gravitational interactions with giant molecular clouds or a remnant accretion disk may dominate over interactions with stars (GMCs are typically too rare close to E_{crit}, however, so may not be important). The rate at which merging or recently merged BHs disrupt stars may be interesting as well. Merging BHs slingshot stars on chaotic 3-body encounters, perhaps raising the disruption rate as high as $1\,\mathrm{yr}^{-1}$ for $\sim 10^5\,\mathrm{yr}$ in the final stages of a BH merger (Chen et al. 2009). If the merging BHs have large and misaligned spins, their gravitational wave emission can give them a kick that sends the merged BH to a region of stellar phase space where the loss cone is temporarily full again, raising disruption rates significantly (e.g., Komossa & Merritt 2008; Stone & Loeb 2011). Results of these studies are particularly uncertain since the rate of BH mergers is uncertain.

Finally, it is worth noting that there are other phenomena whose rate calculations are closely related to the tidal disruption rate calculations summarized here. The orbits of binary star systems are similarly torqued by interactions with other stars (and here GMCs do seem to play an important role); binary stars can be tidally pulled apart if they approach the BH too closely, sending one star off (perhaps as one of the observed "high-velocity stars") and one star in close to the BH (perhaps as one of the observed "S stars"[6]) (e.g., Perets et al. 2007). The disruption of stars in globular clusters has also received much attention, particularly as a method for determining whether globular clusters do in fact host massive BHs.[7] The disruption rate in globulars is likely lower than galactic nuclei, however, due to the lower concentration of stars (e.g., Sigurdsson & Rees 1997).

[6]The S stars comprise a cluster of tens (observed so far) of mostly B stars in the central 0.04 pc of the Galactic Center. The dynamics of these stars are in good agreement with an isotropic distribution, perhaps with a somewhat higher eccentricity distribution than a relaxed, thermal distribution (e.g., Genzel et al. 2010). The formation of these stars is mysterious, as they are young but may have had difficulty forming *in situ* due to the BH's strong tidal gravity; it has been proposed that they have been delivered to tightly bound orbits by the tidal disruption of binary star systems (e.g., Hills 1988). These stars may not, however, be of great interest for tidal disruption of individual stars: the pericenter distance of even the closest star lies at $\sim 100 r_{\mathrm{T}}$ from the BH, and moreover, the stellar disruption rate is dominated by the far more numerous population of stars much further away at E_{crit} (corresponding to $\sim 1\,\mathrm{pc}$).

[7]Observing the disruption of white dwarfs rather than main sequence stars would be particularly interesting, because this is only possible for $M_{\mathrm{BH}} \lesssim 10^5 M_\odot$ and so would indicate the presence of an intermediate mass BH.

1.3.2 Predictions for the observational appearance of tidal disruption events

Much of the basis for our current understanding of what happens to the gas following disruption comes from Rees (1988) (see also Hills 1975; Lacy et al. 1982). The star typically approaches the BH from great distance on an orbit of approximately zero energy—then following disruption[8] at $\sim r_{\rm T}$, different parts of the star end up with a spread of energy much wider than the star's own binding energy. The (specific) energy spread

$$\Delta\epsilon \sim \frac{GM_{\rm BH}}{r_{\rm T}}\frac{r_\star}{r_{\rm T}} \tag{1.5}$$

is due to the fact that different parcels of gas lie at different depths in the BH's potential well, yet all have approximately the same velocity (the BH's escape velocity). (On top of this, the tidal gravity might spin the approaching star up to break-up, increasing the energy spread by a factor of ≈ 3: see, e.g., Li et al. 2002.) As a result, about half of the stellar gas has positive specific energy, and escapes from the BH on hyperbolic trajectories, while the other half has negative specific energy, and follows its highly eccentric orbits away and then back towards the BH again. The timescale for the most tightly bound material to return to the BH is the orbital period of particles having energy $-\Delta\epsilon$,

$$t_{\rm fallback} \sim \left(\frac{r_{\rm T}^3}{GM_{\rm BH}}\right)^{1/2}\left(\frac{r_{\rm T}}{r_\star}\right)^{3/2} . \tag{1.6}$$

Accretion of bound gas onto the BH powers the tidal disruption flare, and so the bound gas has received the most attention.

Calculating the rate at which bound gas approaches the BH requires knowing how the mass of the star is distributed among the spread in energies $\Delta\epsilon$. Rees (1988) assumed for simplicity that the spread is uniform, $dm/d\epsilon \propto \epsilon^0$, and so the rate of bound gas approaching the BH is

$$\dot{M}_{\rm fallback} \approx \frac{1}{3}\frac{M_\star}{t_{\rm fallback}}\left(\frac{t}{t_{\rm fallback}}\right)^{-5/3} \tag{1.7}$$

(Rees 1988; Phinney 1989).[9] The rate of gas falling back to the BH, $\dot{M}_{\rm fallback}$, can far exceed the Eddington rate early on, so many early studies simply assumed that the emission from a tidal disruption event would be at the Eddington luminosity, eventually declining

[8]The possibility of emission from the tidal disruption process itself has also been studied. It has been proposed that the shock as the star is tidally compressed at pericenter can be strong enough to start thermonuclear reactions for stars on orbits that deeply penetrate the disruption zone (e.g., Carter & Luminet 1982; Brassart & Luminet 2008), but 3-dimensional grid-based calculations have shown that the density in the shock is probably never high enough for this to occur for a solar-type star (Guillochon et al. 2009). (It probably does occur in the disruption of white dwarfs, however; see Rosswog et al. 2009). The breakout of shockwaves may produce bright short-lived X-ray emission (Guillochon et al. 2009).

[9]Rees (1988) published the incorrect exponent, which was corrected by Phinney (1989).

proportional to $t^{-5/3}$. Evans & Kochanek (1989) confirmed the uniform $dm/d\epsilon$ distribution with a smoothed-particle hydrodynamics (SPH) calculation of a tidal disruption. This result has been further confirmed at late times $t \gg t_{\rm fallback}$ by more recent SPH simulations and analytic polytropic calculations, though the fallback rate may decline somewhat more gently at early times (e.g., Lodato et al. 2009; Ramirez-Ruiz & Rosswog 2009). The falling-back gas is expected to shock on itself vertically and radially as it reaches pericenter, due to funneling of orbits into a tight volume, and relativistic precession (e.g., Rees 1988; Evans & Kochanek 1989; Kochanek 1994; Ramirez-Ruiz & Rosswog 2009). (Kochanek 1994 discusses the extreme possibility that stellar debris will not intersect itself at pericenter at all if the BH is spinning rapidly.)

The shock at pericenter should circularize the gas particles' orbits within a few times $t_{\rm fallback}$, forming a torus of stellar debris. The viscous time in the torus is typically shorter than the fallback time at least early on, so at least some of the gas should manage to accrete (Li et al. 2002; Ulmer 1999). Cannizzo et al. (1990) considered the long-term evolution of the torus, suggesting that eventually (when the fallback rate and so density are low), the viscous time becomes longer than the fallback time; accretion onto the BH thus must wait for the disk to viscously spread, so the accretion rate declines more gently, and the light curve may fall more gently as well. (We show in Chapter 2 that the flow may become radiatively inefficient before this point, which leads to very different observational predictions.)

Early on, radiation pressure may inhibit accretion while the fallback rate exceeds the Eddington rate however (e.g., Ulmer 1999). Ulmer (1999) proposed that the gas forms a thick disk that should be bright in the UV and soft X-rays, while Loeb & Ulmer (1997) proposed a lower-energy outflow that never becomes completely unbound from the BH; it rather settles into a hydrostatic atmosphere surrounding the BH, like a star, and would be bright at optical wavelengths. Most recently, Giannios & Metzger (2011) suggested that the super-Eddington fallback rate could give rise to a relativistic jet that would shock on the interstellar medium and produce radio emission.

The half of the gas that becomes unbound during the process of stellar disruption has been studied by several authors as well. Khokhlov & Melia (1996) estimated its dimensions (though we disagree: see §2.3) and predicted that it would sweep up material in the interstellar medium (similar to a supernova); they propose that the structure Sagittarius A East in our Galactic Center was produced in this way. Bogdanović et al. (2004) performed an SPH simulation of disruption; they then used the photoionization code *Cloudy* to calculate the Hα emissivity of individual unbound gas particles and predict a (fairly faint) Hα luminosity. After our paper Strubbe & Quataert (2009) was published, Kasen & Ramirez-Ruiz (2010) suggested that recombination in the unbound debris could produce a days-long optical transient. Clausen & Eracleous (2011) used our results for the photoionization of unbound debris in Strubbe & Quataert (2009) to make spectroscopic predictions for the unbound debris of a white dwarf disrupted by an intermediate mass BH.

1.3.3 Observations of tidal disruption candidates

A modest number of events have been observed that may potentially be tidal disruptions—TDE candidates. All of these candidates were found as galaxies that exhibited a single large-amplitude swing in luminosity during a period of multiple observations. AGN may appear similar to TDEs, so two observational cuts are typically made: requiring a *single* large-amplitude outburst, rather than multiple outbursts, and a follow-up optical spectrum to look for AGN emission lines. (It is not that TDEs cannot be present in active galaxies, but rather that they would be significantly more difficult to identify and interpret.) Here we review how the candidates were detected and identified, and their observational properties.

A handful of tidal disruption candidates were found in the late 1990s by the *ROSAT* All-Sky Survey (RASS), which imaged the entire sky in the energy band $0.1 - 2.4\,\mathrm{keV}$ over a period of six months, and about 20% of the sky at least twice during that period. These events were discovered by comparing multiple epochs of data within the RASS, or RASS detections with later pointed observations, looking for galaxies with a brightness difference of at least a factor of 20. A longer list of candidates was followed up with optical spectroscopy, and a handful of Seyfert nuclei discarded. Komossa (2002) reviews the candidate TDEs, which comprise NGC 5905[10] (Bade et al. 1996; Komossa & Bade 1999), RXJ1642+7554 (Grupe et al. 1999), RXJ1242-1119 (Komossa & Greiner 1999) and RXJ1420+5334 (Greiner et al. 2000). The former two galaxies are spirals, and the latter[11] two are early-type galaxies. These candidates are at redshifts $z \sim 0.1$, show peak X-ray luminosities typically $\sim 10^{44}\,\mathrm{erg\,s^{-1}}$, and have very soft X-ray spectra. The *ROSAT* light curves of all of these candidates (except for NGC 5905) consist only of an outburst point and a later upper limit. No radio emission was detected from these galaxies (except NGC 5905) in the FIRST[12] (Faint Images of the Radio Sky at Twenty centimeters) Survey (Komossa 2002). Follow-up in the X-rays with the *Chandra* X-ray Observatory a decade after RASS found that all candidates had dimmed by factors of hundreds to thousands (Halpern et al. 2004). Donley et al. (2002) estimated the tidal disruption rate per galaxy based on these RASS candidates to be $\sim 10^{-5}\,\mathrm{yr^{-1}}$. These events are tantalizing, but had so little data during the flare that they are very difficult to interpret unambiguously.

A handful of additional candidates have been found at X-ray wavelengths in other surveys. The *XMM-Newton* Slew Survey images the sky as the telescope slews between pointed observations; comparison of galaxies detected in this survey with the RASS uncovered two more tidal disruption candidates, NGC 3599 and SDSS J132341.97+482701.3 (although later detailed optical spectroscopy of the former led to its reclassification as a low-luminosity AGN) (Esquej et al. 2007, 2008). The amplitude of each of these flares was

[10]NGC 5905, previously known to contain star formation, was later shown to contain a weak Seyfert nucleus as well by Gezari et al. 2003, and so may be a less viable TDE candidate. Furthermore, the X-ray luminosity of the flare was fainter, prompting Li et al. 2002 to interpret the flare as disruption of a brown dwarf or planet, rather than solar-type star.

[11]RXJ1242-1119 is actually a pair of (probably interacting) early-type galaxies.

[12]Neither RXJ1242-1119 nor RXJ1420+5334 lies in the FIRST Survey field.

≈ 80, their X-ray luminosities were $\sim 10^{41}\,\mathrm{erg\,s^{-1}}$ and $10^{43}\,\mathrm{erg\,s^{-1}}$, and their X-ray spectra were very soft. Follow-up observations with *XMM-Newton* and the *Swift* X-ray Telescope show that each event dimmed by a factor of tens over several years. These events were used to estimate a disruption rate per galaxy of $\sim 2 \times 10^{-4}\,\mathrm{yr^{-1}}$ (Esquej et al. 2008). Tidal disruption candidates have additionally been found in galaxy clusters: in Abell 3571 with *ROSAT* (Cappelluti et al. 2009), and in the spiral galaxy SDSS J131122.15-012345.6 in Abell 1689 with *XMM-Newton* / *Chandra* (Maksym et al. 2010). Both of these candidates showed peak X-ray luminosities of few $\times\, 10^{42}\,\mathrm{erg\,s^{-1}}$ and very soft X-ray spectra. A study of the *Chandra* Deep Field (containing $\approx 30,000$ galaxies) found no TDE candidates (Luo et al. 2008).

Candidate disruptions have been found at ultraviolet wavelengths as well. The first was in NGC 4552 (Renzini et al. 1995) (found serendipitously by comparing two epochs of *HST* observations), though the later detection of variable hard X-ray emission with *Chandra* makes a flaring low-luminosity AGN a more likely interpretation (Xu et al. 2005). Another candidate called "PALS-1" was found by a UV-optical survey for Lyman Break galaxies in the galaxy cluster Abell 267, possibly a gravitationally lensed TDE at $z \sim 3.3$ (Stern et al. 2004). Two tidal disruption candidates were found in the *GALEX* Deep Imaging Survey (Gezari et al. 2006, 2008), which covered 80 $\mathrm{deg^2}$ in the far and near UV ($\approx 1300 - 2800\,\text{Å}$) over several years, of which 1.2 $\mathrm{deg^2}$ were imaged multiple times. The FUV[13] *GALEX* data were co-added into 1-year bins and searched for sources showing a single swing of variability. Regions of the DIS overlap the optical Canada-France-Hawaii Telescope Legacy Survey (CFHTLS) fields, and so TDE candidates were required to have optically-resolved galaxy hosts. These regions also had prior *XMM-Newton* or *Chandra* data, and candidates were required not to contain a bright compact X-ray source (which would be interpreted as an AGN). Potential candidates were then followed up with optical spectroscopy and discarded if they showed [OIII]/Hβ ratios indicative of an AGN. The two candidates identified this way are labelled "D1-9" and "D3-13." A third event, labelled "D23H-1," was later found in DIS observations of a field called DEEP2 23H (which does not overlap the CFHTLS fields) (Gezari et al. 2009). Candidates D1-9 and D3-13 each have several *GALEX* data points and tens of CFHTLS optical points, spanning a few years, and are fairly similar. The peak UV luminosities for both are $\sim$ few $\times\, 10^{43}\,\mathrm{erg\,s^{-1}}$, and the peak optical luminosities are $\sim$ few $\times\, 10^{41}\,\mathrm{erg\,s^{-1}}$; both light curves decay relatively steeply for the first year, then flatten. These candidates appear to have two-temperature blackbody spectral energy distributions, at $T \sim$ few $\times\, 10^4$ K and $T \sim$ few $\times\, 10^5$ K. *Chandra* follow-up 1–3 years after the peaks yielded X-ray detections, with luminosities of $\sim$ few $\times\, 10^{41}\,\mathrm{erg\,s^{-1}}$ for D1-9 and $\sim 10^{43}\,\mathrm{erg\,s^{-1}}$ for D3-13. Both of these candidates are hosted by red (non-star-forming) galaxies located at redshifts $z \sim 0.3 - 0.4$. The third candidate, D23H-1, was identified in close to real time and followed up with optical photometry 2 and 8 weeks after the observed UV peak of the flare. The peak UV luminosity was $\sim 10^{43}\,\mathrm{erg\,s^{-1}}$. The event was followed up with *Chandra* a few days and a few months after the UV peak, but no X-ray emission was detected. Unlike

[13]FUV was chosen because the host galaxy is fainter than in NUV.

the other two candidates, D23H-1's spectral energy distribution appears consistent with a single-temperature blackbody at $T \sim$ few $\times 10^5$ K, and the light curve appears to decay as a single power-law. The host galaxy of D23H-1 is a star-forming galaxy located at $z \sim 0.2$. Possible identification of these events as other types of transients has been considered but judged unlikely: (1) the lack of prior hard X-rays, previous variability, and [OIII] emission contra-indicates AGN; and (2) the candidates are likely too blue in color to be Type Ia supernovae, gamma-ray bursts, or AGN. Type II supernovae (bluer than Type Ia's) are not expected in red non-star-forming hosts like D1-9 or D3-13; although D23H-1 is in a star-forming galaxy, the long decay timescale of the observed flare makes it unlikely to be a Type II supernova (which should fade in the UV over the course of weeks, or display emission lines in the case of a Type IIn supernova). These UV-selected events comprise the most comprehensively studied tidal disruption candidates to date.

A few candidates have been published on the basis of unusual emission lines. The low-luminosity Seyfert galaxy NGC 5548 displayed a brightening at optical wavelengths accompanied by the appearance of a strong, abnormally broad He II 4686 Å emission line, which the authors suggested was due to an accretion event such as the tidal disruption of a star (Peterson & Ferland 1986). The galaxy SDSS J095209.56+214313.3 exhibited a very bright high-ionization iron line accompanied by bright He II emission and unusually shaped Balmer lines, all of which faded over several years (Komossa et al. 2008, 2009). Archival NUV, optical and near-infrared data show continuum variability on the same timescale. The faint post-flare X-ray luminosity of $\sim 10^{41}\,\mathrm{erg\,s^{-1}}$ measured by *Chandra* suggests that the galaxy does not host a typical AGN, though it may be a low-luminosity AGN. While the observed event could be an extreme Type IIn supernova, the authors suggest that the event is the "light echo" of a tidal disruption event as photons from the flare pass through and ionize circumnuclear material.

One of the most signficant results of this thesis is that tidal disruption events may be particularly bright at optical wavelengths. Prior to our paper Strubbe & Quataert (2009), virtually no candidate events had been selected by their optical emission (with the exception of UV/optical candidate PALS-1 by Stern et al. 2004). van Velzen et al. (2010) then announced two optically-selected candidates in 2010, culled from the Sloan Digital Sky Survey's Stripe 82. Stripe 82 is a 300 deg^2 that was imaged ~ 70 times over 9 years in the u, g, r, i, z wavebands, and contains $\sim 3 \times 10^6$ galaxies within $z < 0.3$, many of which have been observed spectroscopically as well. These authors identified galaxies from this set that showed a single flare over the observing epoch. In order to remove contamination from supernovae, they measured the distance of each flare from the host galaxy's center and kept only those located within $0.2''$, arguing that this distance is sufficiently small for contamination to be low. They identify AGN spectrocopically where they can, and photometrically otherwise, and remove those as well. This procedure leads to the identification of two tidal disruption candidates, which they label "TDE1" and "TDE2." TDE1 shows a maximum optical luminosity of $\sim$ few $\times 10^{42}\,\mathrm{erg\,s^{-1}}$, and its color is very blue; the host is located at $z \sim 0.1$ and is red (not forming stars). TDE2 is also very blue in color, but brighter with a maximum optical luminosity of $\sim$ few $\times 10^{43}\,\mathrm{erg\,s^{-1}}$. The host is located at $z \sim 0.3$ and is forming stars. Based

on observed galaxy luminosities, the authors estimate that the galaxies host BHs of masses $\sim 10^7 M_\odot$ and few $\times\, 10^7 M_\odot$, respectively. Although it is not clear that these events are not in fact supernovae, their observational appearances are broadly in line with the predictions we make in Chapter 2 (as described in §3.5.2). Another optically-selected TDE candidate has been found in the *ROTSE* supernova survey, though has not yet been published (J.C. Wheeler, personal communication). As described in §6, we found the first optically-selected TDE candidate in real time with the Palomar Transient Factory last summer (Cenko et al. 2011)—my work was instrumental in the analysis of this event.

1.4 Summary of chapters

Here I briefly summarize the work presented in each chapter.

Chapter 2 is entitled "Optical Flares from the Tidal Disruption of Stars by Massive Black Holes" (published as Strubbe & Quataert 2009). We were motivated by the advent of new and upcoming wide-field rapid-cadence surveys to make predictions of the observable properties of tidal disruption events. While previous theoretical studies focused on UV/X-ray emission, we studied potential sources of *optical* emission, with the aim of helping optical transient surveys like the Palomar Transient Factory, Pan-STARRS, and the Large Synoptic Survey Telescope (e.g., Magnier 2007; Rau et al. 2009) find and study TDEs at much higher cadence than had previously been possible. We identified two important sources of optical emission in TDEs: super-Eddington outflows, and the unbound material. As described in §1.3.2, the rate of mass falling back to the BH following disruption can initially be well above the Eddington rate; as described in §1.2.3, radiation pressure may then drive gas back away from the BH. Photons are trapped by electron scattering in the expanding flow, which adiabatically stretches their wavelengths—from X-rays into the optical/UV. We calculate the location and temperature of the photosphere where these cooled photons emerge, and predict their luminosity and (blackbody) spectral energy distribution: $\sim 10^{43} - 10^{44}\,\mathrm{erg\,s^{-1}}$, as bright as a supernova, and peaking in the near UV. We use these results to predict the rate of TDEs that may be detectable to optical transient surveys: tens to hundreds per year! We also calculate the emission properties of the accretion disk, which should last beyond the period of super-Eddington outflow, and the half of the gas that becomes unbound when the star is disrupted. The surface of the unbound gas is photoionized by emission from the accretion disk; it then re-radiates in very broad permitted lines (like Hα). The spectroscopic appearance of the unbound material is similar to that of an AGN's broad line region, but where the lines have been blue- or red-shifted away from the galactic lines, and with no associated narrow line region. We make predictions for the detection rates of TDEs due to this emission as well. Emission from super-Eddington outflows and the unbound material is particularly prominent for BHs in the mass range $M_{\rm BH} \sim 10^5 - 10^6 M_\odot$, and so new optical transient surveys may be particularly sensitive to this population of BHs which is otherwise very difficult to study.

In Chapter 3, entitled "Spectroscopic Signatures of the Tidal Disruption of Stars by Massive Black Holes" (and published as Strubbe & Quataert 2011), we study in more detail the super-Eddington outflow produced in a TDE. The layers of gas outside the continuum photosphere are photoionized by the continuum photosphere below. These outer layers absorb photons at discrete wavelengths, producing a spectrum of absorption lines on top of the blackbody spectrum from the continuum photosphere. These lines should be strongly blueshifted relative to the host galaxy, and typically be very broad ($0.01 - 0.1c$). We use the photoionization code *Cloudy* to predict the lines and line strengths, finding that lines are most prominent at ultraviolet wavelengths (e.g., C IV, Lyman α, O VI) at early times ($\lesssim 1$ month for a $\sim 10^6\ M_\odot$ BH). There may also be optical absorption lines of hydrogen and He II if there is a lower velocity component to the outflow ($\lesssim 0.01$ c). We also discuss the ability of the shock (at pericenter, where the falling back gas returns to the BH) to reach thermal equilibrium: when the density falls too low (e.g., after a few weeks for a $10^6 M_\odot$ BH), the gas cannot thermalize and instead likely produces a spectrum of hard X-rays. We additionally discuss how supernovae will likely contaminate optical transient searches for TDEs: both types of events can be similar in brightness and last weeks to months. A discriminant can be imaging to determine whether a putative TDE lies truly at the center of the galaxy. We estimate that, unfortunately, the rate of central supernovae, to within the resolution of a ground-based survey at $z \sim 0.1$, can be 100 times the rate of TDEs—high-resolution follow-up imaging with *HST* or adaptive optics will be crucial in telling the difference. The color evolution of TDEs (becoming bluer with time) is also distinct from that of supernovae, and should be an important discriminant in optical transient surveys.

Having focused much of my thesis on the accretion physics of tidal disruption events, I decided to strike out in a new direction for my last project, which I plan to continue into my postdoctoral research. In Chapter 4, entitled "The Rate of Tidal Disruption as a Function of Pericenter Distance," I study the stellar dynamics in galactic nuclei, with the aim of calculating the disruption rate as a function of pericenter distance, making the simplest standard assumptions. A star's final orbit towards the BH's disruption zone may have its pericenter just inside the disruption zone at $\sim r_{\rm T}$, or its pericenter may lie deep inside the disruption zone as far in as $\sim r_{\rm S}$ (any deeper in, and the star is swallowed directly without disruption, providing no observable trace). Previous dynamical studies have focused only on the overall rate of disruption, and not how the rate varies with pericenter distance—and yet, we show in Chapters 2 and 3 that the observable properties of TDEs *depend* on this pericenter distance. This chapter represents work in progress, and as such has a different tone from the other chapters. I spend much of the chapter reviewing in detail the standard framework for calculating disruption rates using the Fokker-Planck equation—not new results, but I provide many more explicit details in the derivation than are typically presented. I use this foundation to solve the Fokker-Planck equation inside the tidal disruption zone, allowing me to derive an expression for the disruption rate as a function of pericenter for a generic spherically symmetric and isotropic galactic nucleus. I then calculate the disruption rate as a function of pericenter for the galaxy NGC 4467, using real data from Faber et al. (1997). I close by describing my future plans to calculate these rates for a variety of other galaxies,

and extend this theory to more complicated galactic nuclei geometries.

The penultimate chapter, called "Dust Dynamics, Surface Brightness Profiles, and Thermal Spectra of Debris Disks: The Case of AU Mic" (published as Strubbe & Chiang 2006), describes my earlier theoretical work on a very different topic. Debris disks are optically thin disks of dust (and a little gas) surrounding young stars ($\sim 10\,\mathrm{Myr} - 1\,\mathrm{Gyr}$ old). Debris disks can be observed in several ways: as an infrared excess in the spectral energy distribution of a star, through its thermal emission in resolved radio observations, or in *scattered* light at optical wavelengths. An important question has been the origin of the dust: Is the dust primordial (left over from star formation), is it produced in steady state through collisions of rocks, or is it produced in catastrophic bursts when a giant rocky mass is somehow destroyed? Understanding the origin of the dust can offer a probe of the late stages of planet formation. We chose to study the debris disk surrounding the M star AU Microscopii (AU Mic) because of its intriguing scattered-light surface brightness profile (observed with *HST*): at radii less than $\approx 43\,\mathrm{AU}$ from the star, the profile falls gently, and then outside this radius it falls much more quickly. We proposed that a ring of rocks orbits the star at $\approx 43\,\mathrm{AU}$, and that these rocks collide in steady state to produce the dust seen as the debris disk. Although the rocks essentially feel only the gravity from the star, smaller dust particles produced in collisions feel additionally the outward forces of radiation pressure and stellar wind pressure from the star. Freshly born dust grains, now feeling this reduced gravity, are sent onto eccentric orbits away from the star[14] (sharing pericenter at $\approx 43\,\mathrm{AU}$). Smaller grains feel a smaller effective gravity and so have larger apocentric distances—since grains spend most of their time at apocenter, the size distribution of grains dictates the surface brightness profile of the outer regions of the debris disk. Meanwhile, Poynting-Robertson and stellar wind drag degrade the dust grains' orbits over time, and would eventually cause the grains to spiral into the star. Collisions with other grains, however, act too quickly in the AU Mic system: collisions grind down grains so small that they become unbound from the star before they would have time to spiral in. As a result, the inner region of the debris disk (inside $\approx 43\,\mathrm{AU}$) is empty. We develop these ideas, then use them to calculate model surface brightness profiles, color profiles, and thermal spectra; we compare these with the data and find reasonable agreement. In the time since we published this research, many more debris disks have revealed broken surface brightness profiles, and our work has been instrumental in understanding the dust dynamics in these systems.

The final chapter is an Epilogue, returning to tidal disruptions: I describe two recent observational discoveries that build on results in my thesis. During the final year of my thesis, two ground-breaking tidal disruption candidates were discovered by teams led by Berkeley's Dr. S. B. Cenko and Prof. J. S. Bloom: the first optically-selected candidate found in real time, labelled "PTF10iya" (Cenko et al. 2011), and the first TDE candidate found in the γ-rays, labelled "Swift 1644+57" (Bloom et al. 2011). I contributed to the analysis in both of these discoveries, and describe the discoveries and interpretation in this final chapter.

[14]For a surprising moment, this work parallels the dynamics in a tidal disruption event! I considered titling my thesis "Eccentric orbits in Keplerian potentials."

Chapter 2

Optical Flares from the Tidal Disruption of Stars by Massive Black Holes

Abstract

A star that wanders too close to a massive black hole (BH) is shredded by the BH's tidal gravity. Stellar gas falls back to the BH at a rate initially exceeding the Eddington rate, releasing a flare of energy. In anticipation of upcoming transient surveys, we predict the light curves and spectra of tidal flares as a function of time, highlighting the unique signatures of tidal flares at optical and near-infrared wavelengths. A reasonable fraction of the gas initially bound to the BH is likely blown away when the fallback rate is super-Eddington at early times. This outflow produces an optical luminosity comparable to that of a supernova; such events have durations of ~ 10 days and may have been missed in supernova searches that exclude the nuclear regions of galaxies. When the fallback rate subsides below Eddington, the gas accretes onto the BH via a thin disk whose emission peaks in the UV to soft X-rays. Some of this emission is reprocessed by the unbound stellar debris, producing a spectrum of very broad emission lines (with no corresponding narrow forbidden lines). These lines are the strongest for BHs with $M_{\rm BH} \sim 10^5 - 10^6 M_\odot$ and thus optical surveys are particularly sensitive to the lowest mass BHs in galactic nuclei. Calibrating our models to ROSAT and GALEX observations, we predict detection rates for Pan-STARRS, PTF, and LSST and highlight some of the observational challenges associated with studying tidal disruption events in the optical. Upcoming surveys such as Pan-STARRS should detect at least several events per year, and may detect many more if current models of outflows during super-Eddington accretion are reasonably accurate. These surveys will significantly improve our knowledge of stellar dynamics in galactic nuclei, the physics of super-Eddington accretion, the demography of intermediate mass BHs, and the role of tidal disruption in the growth of massive BHs.

2.1 Introduction

Stellar orbits in the center of a galaxy are not static, and sometimes stars walk into trouble. If an unlucky star passes within $R_{\rm T} \sim R_\star (M_{\rm BH}/M_\star)^{1/3}$ of the galaxy's central black hole (BH), the BH's tidal gravity exceeds the star's self-gravity, and the star is disrupted. For BHs with $M_{\rm BH} \leq 10^8 M_\odot$, the disruption of a solar-type star occurs outside the horizon and is likely accompanied by a week- to year-long electromagnetic flare (e.g., Rees 1988).

Gravitational interactions between stars ensure that all supermassive BHs tidally disrupt nearby stars (e.g., Magorrian & Tremaine 1999). The scattering process might be accelerated by resonant relaxation very close to the BH (Rauch & Tremaine 1996), or interactions with "massive perturbers" like a massive accretion disk (Zhao et al. 2002) or giant molecular clouds (Perets et al. 2007). In addition, the galactic potential may be triaxial so stars need not be scattered at all: they may simply follow their chaotic orbits down to $\sim R_{\rm T}$ (Merritt & Poon 2004). Given these uncertainties, predictions for the timescale between tidal disruptions in a given galaxy range from 10^3 to 10^6 years. The rate remains uncertain, but tidal disruption must occur.

Indeed, a handful of candidate events have been detected to date. The accreting stellar debris is expected to emit blackbody radiation from very close to the BH, so X-ray and UV observations probe the bulk of the emission. Several candidate tidal disruption events were discovered in the ROSAT All-Sky Survey (see Komossa 2002) and the XMM-Newton Slew Survey (Esquej et al. 2007); the GALEX Deep Imaging Survey has so far yielded three candidates (Gezari et al. 2006, 2008, 2009). For ROSAT, these detections are consistent with a rate $\sim 10^{-5}\,{\rm yr}^{-1}$ per galaxy (Donley et al. 2002), but the data are sparse. However, we are entering a new era of transient surveys: in the optical, surveys like Pan-STARRS (PS1, then all four telescopes) (e.g., Magnier 2007), the Palomar Transient Factory (Rau et al. 2009), and later the Large Synoptic Survey Telescope will have fast cadence, wide fields of view, and unprecedented sensitivity. Wide-field transient surveys with rapid cadence are also planned at other wavelengths, including the radio (e.g., LOFAR and the ATA), near-infrared (e.g., SASIR), and hard X-rays (e.g., EXIST). How many tidal flares these surveys find depends on their luminosity and spectra as a function of time.

In this paper, we predict the light curves and spectra of tidal disruption events as a function of time. Since the early work on tidal disruption (e.g., Rees 1988), it has been well-appreciated that the bulk of the emission occurs in the UV and soft X-rays, with a possible extension to harder X-rays.[1] Taking into account only this emission, optical wavelengths are not the most promising for detecting tidal flares, because the blackbody temperature of the inner accretion disk is $\sim 3 \times 10^5\,{\rm K}$. We show, however, that there are two additional sources of optical emission that likely dominate the optical flux in many, though not all, cases: (1)

[1]Such a hard X-ray component may be detectable with upcoming all-sky X-ray surveys like the proposed EXIST mission (Grindlay 2004). However, we choose not to include predictions for hard X-rays in our calculations: one could draw analogy to the hard X-ray power-law tail observed in AGN spectra, but since the origin of this feature is uncertain, it is difficult to make firm theoretical predictions for tidal disruption events.

emission produced by a super-Eddington outflow at early times and (2) emission produced by the irradiation and photoionization of unbound stellar debris (see also the earlier work of Bogdanović et al. 2004). In the latter case, much of the optical emission is in the form of very broad emission lines, while in the former it is primarily continuum (although some lines may also be present). Throughout this paper, we typically discuss these two sources of emission separately, largely because the physics of the photoionized stellar debris is more secure than that of the super-Eddington outflows.

The remainder of this paper is organized as follows. In §§2.2.1, 2.2.2 and 2.3, we describe our models for the polar super-Eddington outflow, accretion disk and the equatorial unbound material, respectively; then in §2.4 we calculate the luminosity and spectral signatures of tidal disruption events. We predict detection rates in §2.5, and summarize and discuss our results in §2.6. §§2.5.2 and 2.6 include a discussion of our models in the context of ROSAT and GALEX observations of tidal flare candidates.

2.2 The Initially Bound Material

We consider a star approaching the BH on a parabolic orbit with pericenter distance $R_{\rm p} \leq R_{\rm T}$. Once the star reaches the vicinity of the tidal radius ($R_{\rm T}$), the tidal gravity stretches it radially and compresses it vertically and azimuthally. The acceleration is $a \sim (GM_{\rm BH}/R_{\rm p}^2)(R_\star/R_{\rm p})$ and acts for a dynamical time $t_{\rm p} \sim (GM_{\rm BH}/R_{\rm p}^3)^{-1/2}$ near pericenter, resulting in velocity perturbations $\Delta v_{\rm p} \sim a t_{\rm p} \sim v_\star (R_{\rm T}/R_{\rm p})^{3/2}$, where $R_\star$ is the star's radius and $v_\star$ is the star's escape velocity. The change in velocity $\Delta v_{\rm p}$ is smaller than the star's orbital velocity at pericenter, $v_{\rm p} \equiv (2GM_{\rm BH}/R_{\rm p})^{1/2}$, by a factor of $R_\star/R_{\rm p}$.

Because $\Delta v_{\rm p}$ is at least as large as the sound speed inside the star, the stellar gas may shock vertically and azimuthally (e.g., Brassart & Luminet 2008; Guillochon et al. 2009). Once the shredded star passes through pericenter, the compression subsides and the star re-expands, cooling adiabatically; thermal pressure becomes negligible and the particles travel away from the BH ballistically. We assume that the particle trajectories become ballistic when the star passes through pericenter. At that time, the particles have perturbed azimuthal, vertical, and radial velocities $\sim \Delta v_{\rm p}$.

The particles have a range in specific energy $\mathcal{E} \sim \pm 3(GM_{\rm BH}/R_{\rm p})(R_\star/R_{\rm p})$ (e.g., Lacy et al. 1982; Li et al. 2002), due to their relative locations in the BH's potential well and differences in their azimuthal speeds. Initially, approximately half of the stellar mass is bound and half is unbound (Lacy et al. 1982; Evans & Kochanek 1989). After a time

$$\begin{aligned} t_{\rm fallback} &\sim \frac{2\pi}{6^{3/2}} \left(\frac{R_{\rm p}}{R_\star}\right)^{3/2} t_{\rm p} \\ &\sim 20 M_6^{5/2} R_{\rm p,3R_S}^3 r_\star^{-3/2} \,{\rm min}\,, \end{aligned} \tag{2.1}$$

the most bound material returns to pericenter. (Here we have defined $M_6 \equiv M_{\rm BH}/10^6 M_\odot$,

$R_{\rm p,3R_S} \equiv R_{\rm p}/3R_{\rm S}$, and $r_\star \equiv R_\star/R_\odot$.) Less bound gas follows, at a rate

$$\dot{M}_{\rm fallback} \approx \frac{1}{3}\frac{M_\star}{t_{\rm fallback}}\left(\frac{t}{t_{\rm fallback}}\right)^{-5/3} \tag{2.2}$$

(Rees 1988; Phinney 1989). There will be some deviations from this canonical $t^{-5/3}$ scaling at early times, depending on the precise structure of the star (Lodato et al. 2009; Ramirez-Ruiz & Rosswog 2009), but we use equation (2.2) for simplicity. As matter returns to pericenter, it shocks on itself, converting most of its bulk orbital energy to thermal energy (see Kochanek 1994). The viscous time is typically shorter than the fallback time, so at least some of the matter begins to accrete.

For $M_{\rm BH} \lesssim$ few $\times\, 10^7 M_\odot$, the mass fallback rate predicted by equations (2.1) & (2.2) can be much greater than the Eddington rate $\dot{M}_{\rm Edd}$ for a period of weeks to years; here $\dot{M}_{\rm Edd} \equiv 10 L_{\rm Edd}/c^2$, $L_{\rm Edd}$ is the Eddington luminosity, and 0.1 is the assumed efficiency of converting accretion power to luminosity. The fallback rate only falls below the Eddington rate at a time

$$t_{\rm Edd} \sim 0.1\, M_6^{2/5} R_{\rm p,3R_S}^{6/5} m_\star^{3/5} r_\star^{-3/5}\,{\rm yr}, \tag{2.3}$$

where $m_\star \equiv M_\star/M_\odot$. While the fallback rate is super-Eddington, the stellar gas returning to pericenter is so dense that it cannot radiate and cool. In particular, the time for photons to diffuse out of the gas is longer than both the inflow time in the disk and the dynamical time characteristic of an outflow. The gas is likely to form an advective accretion disk accompanied by powerful outflows (e.g., Ohsuga et al. 2005), although the relative importance of accretion and outflows in this phase is somewhat uncertain (see §2.6). Later, when $\dot{M}_{\rm fallback} < \dot{M}_{\rm Edd}$ ($t > t_{\rm Edd}$), the outflows subside, and the accretion disk can radiatively cool and becomes thin.

In §2.2.1, we describe our model for the super-Eddington outflows, and in §2.2.2, we describe our model for the accretion disk. We discuss uncertainties in these models in §2.6.

2.2.1 Super-Eddington Outflows

When the fallback rate to pericenter is super-Eddington, radiation produced by the shock and by viscous stresses in the rotating disk is trapped by electron scattering. By energy conservation, this material is initially all bound to the BH, but it is only weakly bound because the radiation cannot escape and because the material originated on highly eccentric orbits. Some fraction of the returning gas is thus likely unbound (see, e.g., the simulations of Ayal et al. 2000), with energy being conserved as other gas accretes inward (Blandford & Begelman 1999). If the outflow's covering fraction is high, most of the radiated power will be emitted from the outflow's photosphere, which can be far outside $\sim R_{\rm p}$ (Loeb & Ulmer 1997). We now estimate the properties of this outflowing gas (see Rossi & Begelman 2009 for related estimates in the context of short-duration gamma-ray bursts).

In our simplified scenario, stellar debris falls back at close to the escape velocity and shocks at the launch radius $R_{\rm L} \sim 2R_{\rm p}$, converting bulk kinetic energy to radiation:

$$aT_{\rm L}^4 \sim \frac{1}{2}\rho_{\rm fallback,L} v_{\rm esc,L}^2 \,, \tag{2.4}$$

where $T_{\rm L}$ is the temperature at $R_{\rm L}$, $\rho_{\rm fallback,L} \sim \dot{M}_{\rm fallback}/(4\pi R_{\rm L}^2 v_{\rm esc,L})$ is the density of gas at $R_{\rm L}$, and $v_{\rm esc,L} \equiv (2GM_{\rm BH}/R_{\rm L})^{1/2}$. Outflowing gas is launched from $R_{\rm L}$ at a rate

$$\dot{M}_{\rm out} \equiv f_{\rm out}\dot{M}_{\rm fallback} \tag{2.5}$$

and with terminal velocity

$$v_{\rm wind} \equiv f_v v_{\rm esc}(R_{\rm L}). \tag{2.6}$$

We approximate the outflow's geometry as spherical, with a density profile

$$\rho(r) \sim \frac{\dot{M}_{\rm out}}{4\pi r^2 v_{\rm wind}} \tag{2.7}$$

inside the outflow where $r \lesssim R_{\rm edge} \equiv v_{\rm wind}t$; the density falls quickly to zero at $\sim R_{\rm edge}$. We define the trapping radius $R_{\rm trap}$ via $R_{\rm trap}\rho(R_{\rm trap})\kappa_{\rm s} \sim c/v_{\rm wind}$ (where $\kappa_{\rm s}$ is the opacity due to electron scattering): inside $R_{\rm trap}$, the gas is too optically thick for photons to escape and so the outflowing gas expands adiabatically. Because the outflow remains supported by radiation pressure, $T \propto \rho^{1/3}$. The photosphere of the outflow $R_{\rm ph}$ is where $R_{\rm ph}\rho(R_{\rm ph})\kappa_{\rm s} \sim 1$. Because $v_{\rm wind}$ is likely not much smaller than c, $R_{\rm trap} \sim R_{\rm ph}$; we thus neglect any deviations from adiabaticity between $R_{\rm trap}$ and $R_{\rm ph}$.

At the earliest times for small $M_{\rm BH}$ and $R_{\rm p}$, the fallback rate can be so large and the density so high that the edge of the outflow limits the location of the photosphere to be just inside $R_{\rm edge}$. In that case, the density of the photosphere is still given by $\rho(R_{\rm ph}) \sim (\kappa_{\rm s}R_{\rm edge})^{-1}$; lacking a detailed model, we assume that the photospheric gas near the edge is on the same adiabat as the rest of the gas, so that

$$\begin{aligned} T_{\rm ph} &\sim T_{\rm L}\left[\frac{\rho(R_{\rm ph})}{\rho_{\rm fallback,L}}\right]^{1/3} \\ &\sim 3\times10^4 f_v^{-1/3} M_6^{1/36} R_{\rm p,3R_S}^{-1/8} m_\star^{-1/12} r_\star^{1/12} \left(\frac{t}{\rm day}\right)^{-7/36} {\rm K}\,. \end{aligned} \tag{2.8}$$

Note that the photospheric temperature during the edge-dominated phase is essentially independent of all parameters of the disruption (e.g., $M_{\rm BH}$, $R_{\rm p}$, etc.), and is only a weak function of time. The total luminosity during this phase grows as $L \propto t^{11/9}$ while the luminosity on the Rayleigh-Jeans tail increases even more rapidly, $\nu L_\nu \propto t^{65/36}$. After a time

$$t_{\rm edge} \sim 1\ f_{\rm out}^{3/8} f_v^{-3/4} M_6^{5/8} R_{\rm p,3R_S}^{9/8} m_\star^{3/8} r_\star^{-3/8}\,{\rm day}\,, \tag{2.9}$$

the density falls sufficiently that the photosphere lies well inside $R_{\rm edge}$; the photosphere's radius is then

$$R_{\rm ph} \sim 4 f_{\rm out} f_v^{-1} \left(\frac{\dot{M}_{\rm fallback}}{\dot{M}_{\rm Edd}} \right) R_{\rm p,3R_S}^{1/2} R_{\rm S} \tag{2.10}$$

and its temperature is

$$T_{\rm ph} \sim 2 \times 10^5 f_{\rm out}^{-1/3} f_v^{1/3} \left(\frac{\dot{M}_{\rm fallback}}{\dot{M}_{\rm Edd}} \right)^{-5/12} M_6^{-1/4} R_{\rm p,3R_S}^{-7/24} \ {\rm K}\,. \tag{2.11}$$

The adiabatically expanding outflow preserves the photon distribution function generated in the shock and accretion disk close to the BH. Estimates indicate that this gas is likely to be close to thermal equilibrium and thus we assume that the escaping photons have a blackbody spectrum

$$\nu L_\nu \sim 4\pi^2 R_{\rm ph}^2 \nu B_\nu(T_{\rm ph})\,. \tag{2.12}$$

When the photosphere lies inside the edge of the outflow (i.e., $t > t_{\rm edge}$ so $R_{\rm ph} < v_{\rm wind} t$), equations (2.10) and (2.11) imply that the total luminosity of the outflow is

$$L \sim 10^{44} f_{\rm out}^{2/3} f_v^{-2/3} M_6^{11/9} R_{\rm p,3R_S}^{1/2} m_\star^{1/3} r_\star^{-1/3} \left(\frac{t}{\rm day} \right)^{-5/9} {\rm erg\,s^{-1}}. \tag{2.13}$$

The total luminosity of the outflow is thus of order the Eddington luminosity: see Figure 2.4, discussed in §2.4.1. Note that the total luminosity decreases for lower outflow rates, $L \propto f_{\rm out}^{2/3}$, because the photosphere's surface area is smaller. The luminosity on the Rayleigh-Jeans tail (generally appropriate for optical and near-infrared wavelengths) declines even faster for lower $\dot{M}_{\rm out}$, scaling as

$$\nu L_\nu \propto f_{\rm out}^{5/3} f_v^{-5/3}\,. \tag{2.14}$$

These relations only apply if $R_{\rm ph} \gtrsim R_{\rm L}$ because otherwise the outflow is optically thin; we impose this lower limit to $R_{\rm ph}$ in our numerical solutions described later.

2.2.2 The Accretion Disk

We now consider the bound stellar debris that accretes onto the BH. After shocking at pericenter, this gas circularizes and viscously drifts inward, forming an accretion disk. The disk extends from $\sim 2R_{\rm p}$ down to the last stable orbit, $R_{\rm LSO}$. We expect the viscous time in the disk to be substantially shorter than the fallback time for at least a few years (see Ulmer 1999 for the case of $R_{\rm p} = R_{\rm T}$, assuming a thick disk), and check this expectation at the end of §2.2.2; we thus assume that accretion during this period proceeds at $\dot{M} \simeq (1 - f_{\rm out})\dot{M}_{\rm fallback}$. During the super-Eddington phase, the time for photons to diffuse out of the disk is longer than the viscous time, and so the disk is thick and advective. In contrast, at later times when $\dot{M}_{\rm fallback} \lesssim \dot{M}_{\rm Edd}$, the disk is thin and can cool by radiative diffusion. We derive an

analytic "slim disk" model (similar to the numerical work of Abramowicz et al. 1988) to describe the structure of the disk in both regimes.

To calculate the disk's properties, we solve the equations of conservation of mass, momentum, and energy:

$$\dot{M} = -4\pi R H \rho v_r \,, \tag{2.15}$$

$$v_r = -\frac{3}{2}\frac{\nu}{R}\frac{1}{f} \,, \tag{2.16}$$

$$q^+ = q^- - \rho T v_r \frac{s}{R} \,, \tag{2.17}$$

where we have approximated the radial entropy gradient as $\partial s/\partial R \sim -s/R$. Here $\dot{M}$ is the accretion rate, R is the cylindrical distance from the BH, H is the disk scale height, ρ is the density, v_r is the radial velocity, and T is the midplane temperature. The no-torque boundary condition at the inner edge of the disk implies $f \equiv 1-(R_{\rm LSO}/R)^{1/2}$. We neglect gas pressure, since radiation pressure is dominant throughout the disk for at least a few years; we further assume that the viscous stress is proportional to the radiation pressure, so that (Shakura & Sunyaev 1973) $\nu = \alpha c_{\rm s} H$ with sound speed $c_s = (aT^4/3\rho)^{1/2}$ and $H = c_{\rm s}/\Omega_{\rm K}$, where $\Omega_{\rm K} \equiv (GM_{\rm BH}/R^3)^{1/2}$. Simulations indicate that this assumption is reasonable and that such disks are thermally stable (Hirose et al. 2009). The vertically integrated heating and cooling rates are given by $2Hq^+ = 3GM_{\rm BH}\dot{M}f/4\pi R^3$ and $2Hq^- = 8\sigma T^4/3\tau$, where the half-height optical depth is $\tau = H\rho\kappa_{\rm s}$ and $\kappa_{\rm s}$ is the electron scattering opacity. These relations form a quadratic equation for the dimensionless quantity $\kappa_{\rm s} a T^4/c\Omega_{\rm K} = 3\tau(c_{\rm s}/c)$,

$$0 = \left(\frac{\kappa_{\rm s} a T^4}{c\Omega_{\rm K}}\right)^2 - \frac{4}{3\alpha}\left(\frac{\kappa_{\rm s} a T^4}{c\Omega_{\rm K}}\right) - \frac{8f}{3\alpha^2}\left(\frac{10\dot{M}}{\dot{M}_{\rm Edd}}\right)^2 \left(\frac{R}{R_{\rm S}}\right)^{-2} . \tag{2.18}$$

Solving equation (2.18) yields the effective temperature of the disk,

$$\sigma T_{\rm eff}^4 = \frac{4\sigma T^4}{3\tau} = \frac{3GM_{\rm BH}\dot{M}f}{8\pi R^3} \times$$

$$\left[\frac{1}{2} + \left\{\frac{1}{4} + \frac{3}{2} f \left(\frac{10\dot{M}}{\dot{M}_{\rm Edd}}\right)^2 \left(\frac{R}{R_{\rm S}}\right)^{-2}\right\}^{1/2}\right]^{-1} . \tag{2.19}$$

Combining this relation with equation (2.2), we calculate the luminosity and spectrum of the disk as a function of time, modeling it as a multicolor blackbody.

The solution to (2.18) also yields the disk scale height ratio,

$$\frac{H}{R} = \frac{3}{4} f \left(\frac{10\dot{M}}{\dot{M}_{\rm Edd}}\right)\left(\frac{R}{R_{\rm S}}\right)^{-1} \times$$

$$\left[\frac{1}{2}+\left\{\frac{1}{4}+\frac{3}{2}f\left(\frac{10\dot{M}}{\dot{M}_{\rm Edd}}\right)^2\left(\frac{R}{R_{\rm S}}\right)^{-2}\right\}^{1/2}\right]^{-1}. \tag{2.20}$$

The scale height $H \sim R$ while $\dot{M}_{\rm fallback} \gtrsim \dot{M}_{\rm Edd}$, and decreases as $t^{-5/3}$ at fixed R at later times. The viscous time at a radius R in the disk is

$$t_{\rm visc} \sim \alpha^{-1}\left(\frac{GM_{\rm BH}}{R^3}\right)^{-1/2}\left(\frac{H}{R}\right)^{-2}, \tag{2.21}$$

which is $\sim \alpha^{-1}$ times the local dynamical time during the super-Eddington phase, and later increases as $t^{10/3}$ at fixed R. For $\alpha \sim 0.1$, the viscous timescale evaluated at the disk's outer edge is shorter than the time t since disruption for $\sim 1-3\,{\rm yr}$; our assumption of steady-state accretion during this period is thus consistent.

2.3 The Equatorial Unbound Material

While half of the initial star becomes bound to the BH during the disruption, the other half gains energy and escapes from the BH on hyperbolic trajectories. From the viewpoint of the BH, this unbound material subtends a solid angle $\Delta\Omega$, with a dispersion $\Delta\phi$ in azimuth and a dispersion Δi in orbital inclination. This material absorbs and re-radiates a fraction of the luminosity from the accretion disk.[2] We now estimate the dimensions of the unbound wedge.

In the orbital plane at a fixed time $t \gtrsim t_{\rm fallback}$, the unbound stellar debris lies along an arc, as the spread in specific energy produces a spread in radius and azimuthal angle (see Fig. 2.1). The most energetic particles escape on a hyperbolic orbit with eccentricity $e_{\rm max} \sim 1 + 6R_\star/R_{\rm p}$. These particles race away from the BH at a substantial fraction of the speed of light,

$$\frac{v_{\rm max}}{c} \sim \left(\frac{3R_\star}{R_{\rm p}}\right)^{1/2}\frac{v_{\rm p}}{c} \sim 0.3M_6^{-1/2}R_{\rm p,3R_S}^{-1} \tag{2.22}$$

(ignoring relativistic effects) and lie furthest from the BH at a distance

$$R_{\rm max} \sim 0.01M_6^{-1/2}R_{\rm p,3R_S}^{-1}r_\star^{1/2}\left(\frac{t}{0.1\,{\rm yr}}\right)\,{\rm pc}\,. \tag{2.23}$$

They also have the smallest angle away from stellar pericenter, $\phi_{\rm min} \sim f_\infty$, where f_∞ obeys $\cos f_\infty = -1/e_{\rm max}$ so that $\phi_{\rm min} \sim \pi - (12R_\star/R_{\rm p})^{1/2}$ (see also Khokhlov & Melia 1996). Particles with lower energies and thus smaller eccentricities are closer to the BH and make a larger angle relative to pericenter, up to $\phi \sim \pi$. This produces an azimuthal dispersion $\Delta\phi \sim (12R_\star/R_{\rm p})^{1/2}$.

[2]The polar outflow could also irradiate the unbound material, but it will have less of an effect because its spectrum is softer and its luminosity declines more rapidly.

Particles having the maximum vertical velocity $\Delta v_{\rm p}$ have vertical specific angular momentum $j_z = R_{\rm p} v_{\rm p}$, and total specific angular momentum

$$j \sim R_{\rm p} v_{\rm p} \left[1 + \frac{1}{2} \left(\frac{\Delta v_{\rm p}}{v_{\rm p}} \right)^2 \right] \sim R_{\rm p} v_{\rm p} \left[1 + \frac{1}{2} \left(\frac{R_\star}{R_{\rm p}} \right)^2 \right] \tag{2.24}$$

to lowest order in $\Delta v_{\rm p}/v_{\rm p}$. The orbital inclination i is given by $\cos i = j_z/j \sim 1 - (1/2)(R_\star/R_{\rm p})^2$, so $i \sim \pm R_\star/R_{\rm p}$. The resulting inclination dispersion is $\Delta i \sim 2R_\star/R_{\rm p}$ (our result is consistent with Evans & Kochanek 1989 but we disagree with Khokhlov & Melia 1996).

The finite inclination dispersion produces a vertical wall of debris whose inside face scatters, absorbs, and re-radiates a fraction of the disk's emission. This face subtends a solid angle

$$\begin{aligned} \Delta\Omega = \Delta i \Delta\phi &\sim 48^{1/2} \left(\frac{R_\star}{R_{\rm p}} \right)^{3/2} \\ &\sim 0.2 M_6^{-3/2} R_{\rm p,3R_S}^{-3/2} r_\star^{3/2} \, {\rm sr} \, . \end{aligned} \tag{2.25}$$

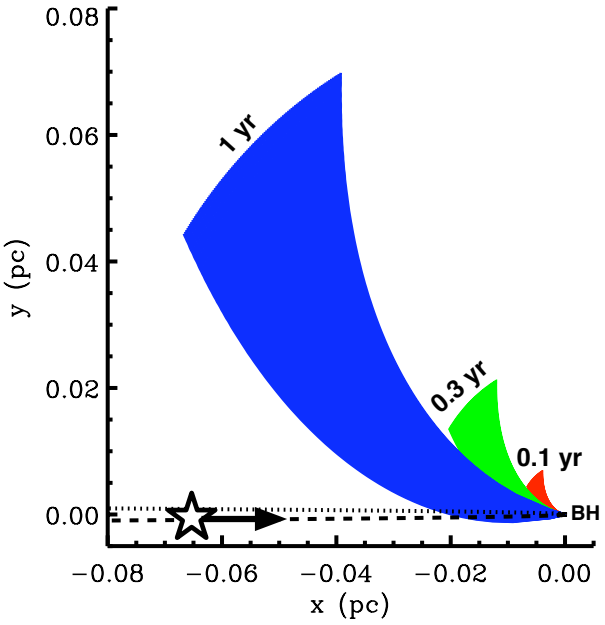

Figure 2.1: Spatial diagram of the equatorial stellar debris in the plane defined by the original orbit of the star. The unbound material is shown 0.1 yr, 0.3 yr, and 1 yr after the tidal disruption of a solar-type star by a $10^6 M_\odot$ BH at $R_{\rm p} = 3R_{\rm S}$. The dashed and dotted curves indicate the incoming parabolic trajectory of the star and its continuation if the star were not disrupted. The debris also has an inclination dispersion perpendicular to this plane of $\Delta i \sim 2R_\star/R_{\rm p}$.

The number density of particles in the unbound wedge is $n \sim (M_\star/2m_p)/(R^2\Delta R\Delta\Omega/3)$, where ΔR is the radial dispersion of the material at fixed ϕ. This dispersion is due to differences in the particles' radial velocities and azimuthal positions when the star passes through pericenter. Particles at $\sim R_{\rm max}$ travel on orbits whose pericenter is shifted from the star's pericenter by an angle $\sim \pm 3(R_\star/R_{\rm p})$, which produces a spread in radial position $(\Delta R/R)_{\rm max} \sim (3R_\star/R_{\rm p})^{1/2}$. The number density is then

$$n \sim 10^9 M_6^{7/2} R_{\rm p,3R_S}^5 m_\star r_\star^{-7/2} \left(\frac{t}{0.1\,{\rm yr}}\right)^{-3} {\rm cm}^{-3} \tag{2.26}$$

and the radial column density seen by the black hole is

$$N \sim 10^{25} M_6^{5/2} R_{\rm p,3R_S}^{7/2} m_\star r_\star^{-5/2} \left(\frac{t}{0.1\,{\rm yr}}\right)^{-2} {\rm cm}^{-2}\,. \tag{2.27}$$

As the unbound material expands, it cools very quickly; after at most a few weeks, the gas would all be neutral if not for the disk's ionizing radiation. This radiation ionizes the surface layer of the unbound material. The ionized gas in turn emits via bremsstrahlung, radiative recombination, and lines. The physical conditions and processes here are similar to those in the broad line region of an active galactic nucleus (AGN).

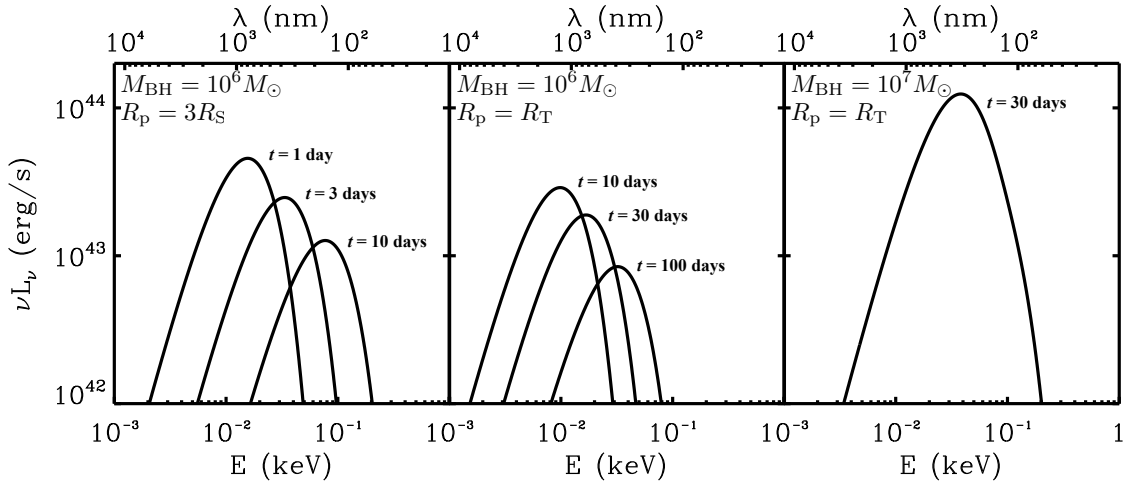

Figure 2.2: Spectral energy distributions for our three fiducial tidal disruption flares at several different times after disruption. These spectra include only the emission from the super-Eddington outflows (for $f_{\rm out} = 0.1$ and $f_v = 1$; see eqns [2.5] & [2.6]), which dominate the emission at early times (see Fig. 2.3). For $M_{\rm BH} = 10^7 M_\odot$ and $R_{\rm p} = R_{\rm T}$ (right panel), the disk dominates the emission for $t \gtrsim 50$ days (Fig. 2.3); this is why we do not plot the outflow emission at later times.

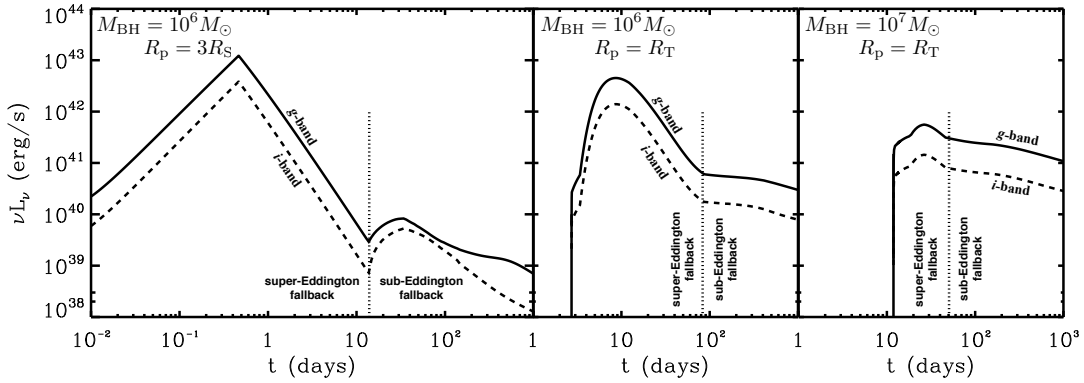

Figure 2.3: Light curves at g- (solid) and i-band (dashed) for our three fiducial models. In each panel, times to the left of the vertical dotted line ($\sim t_{\rm Edd}$; eq. [2.3]) have super-Eddington fallback rates and an outflow dominates the optical emission; at later times, the fallback rate is sub-Eddington and the emission is produced by the accretion disk and the photoionized unbound material (see §2.4.2). In the leftmost panel, the emission rises at early times because the edge of the outflow limits the size of the photosphere. The optical emission then declines until the end of the outflow phase as the photosphere recedes and the photospheric temperature rises (Fig. 2.2).

The ionized gas can reach photoionization equilibrium provided conditions change more slowly than the hydrogen recombination rate $t_{\rm rec}^{-1} \sim n_{\rm e}\alpha_{\rm rec}$. The recombination coefficient for hydrogen is $\alpha_{\rm rec} \approx 4 \times 10^{-13}\,{\rm cm^3\,s^{-1}}$, and $n_{\rm e}$ is the electron number density. In the ionized region, $n_{\rm e}/n \approx 1$, as we show below. The material can remain in equilibrium for at least a few years, until $t_{\rm rec}/t \gtrsim 1$:

$$\frac{t_{\rm rec}}{t} \sim (n\alpha_{\rm rec}t)^{-1} \sim 10^{-3} M_6^{-7/2} R_{\rm p,3R_S}^{-5} m_\star^{-1} r_\star^{7/2} \left(\frac{t}{0.1\,{\rm yr}}\right)^2 . \quad (2.28)$$

The column depth of the ionization front is $N_{\rm ion} \sim 10^{23} U\,{\rm cm^{-2}}$, where $U \equiv L_{\rm disk}/4\pi R_{\rm max}^2 c\langle h\nu\rangle n$ is the ionization parameter,

$$U \sim \quad (2.29)$$
$$0.3 \left(\frac{L_{\rm disk}}{L_{\rm Edd}}\right) \left(\frac{\langle h\nu\rangle}{0.1\,{\rm keV}}\right)^{-1} M_6^{-3/2} R_{\rm p,3R_S}^{-3} m_\star^{-1} r_\star^{5/2} \left(\frac{t}{0.1\,{\rm yr}}\right) .$$

The electron density in the ionized layer is $n_{\rm e} \approx n(1 - 10^{-6}U^{-1}) \approx n$ and the fractional depth of the ionization front is

$$\frac{\Delta R_{\rm ion}}{\Delta R} = \frac{N_{\rm ion}}{N} \sim$$
$$3 \times 10^{-3} \left(\frac{L_{\rm disk}}{L_{\rm Edd}}\right) \left(\frac{\langle h\nu\rangle}{0.1\,{\rm keV}}\right)^{-1} M_6^{-4} R_{\rm p,3R_S}^{-13/2} m_\star^{-2} r_\star^{5} \left(\frac{t}{0.1\,{\rm yr}}\right)^3 ,$$

so the ionized layer is typically thin and highly ionized.

2.4 Predicted Emission

We use the results of §§2.2 and 2.3 to calculate the emission due to the tidal disruption of a solar-type star as a function of time and wavelength. We consider a solar-type star because the stellar mass-radius relation and typical stellar mass functions imply that these stars should dominate the event rate. The two key parameters we vary are the star's pericenter distance $R_{\rm p}$ and the BH mass $M_{\rm BH}$. We consider the mass range $M_{\rm BH} \sim 10^5 - 10^8 M_\odot$.

2.4.1 Super-Eddington Outflows

Early on, when $\dot{M}_{\rm fallback} \gtrsim \dot{M}_{\rm Edd}$ ($t < t_{\rm Edd}$), outflowing gas likely dominates the emission. We calculate its properties using results from §2.2.1.

In Figure 2.2 we plot the spectral energy distribution at various times during the outflow phase, for three fiducial models: $M_{\rm BH} = 10^6 M_\odot$ and $R_{\rm p} = 3R_{\rm S}$; $M_{\rm BH} = 10^6 M_\odot$ and $R_{\rm p} = R_{\rm T}$; and $M_{\rm BH} = 10^7 M_\odot$ and $R_{\rm p} = R_{\rm T}$. We take nominal values of $f_v = 1$ and $f_{\rm out} = 0.1$; we discuss the uncertainties in these parameters in §§2.5.3 and 2.6. The photosphere lies well inside the edge of the outflow at all times shown in Figure 2.2. The emission from the outflow has a blackbody spectrum, initially peaking at optical/UV wavelengths. As time passes and the density of the outflow subsides, the photosphere recedes and the emission becomes hotter but less luminous.

In Figure 2.3, we plot g- (4770Å) and i- (7625Å) band light curves for the three fiducial models. In the leftmost panel at $t \lesssim 1\,{\rm day}$, the edge of the outflow limits the size of the photosphere, so the photosphere initially expands, following the edge of the outflow. After a time $t_{\rm edge}$ (eq. [2.9]), however, the photosphere begins to recede inside the edge of the outflow and the luminosity declines. In the middle and rightmost panels, the photosphere lies well inside $R_{\rm edge}$ for virtually the entire outflow phase. The optical emission decreases as the photosphere's emitting area decreases and the temperature rises only slowly. As Figures 2.2 & 2.3 demonstrate, the peak optical luminosity of the outflow is substantial, $\sim 10^{43}\,{\rm erg\,s^{-1}} \sim 10^9 L_\odot$, comparable to the optical luminosity of a supernova. The color of the emission is quite blue ($g - r \approx -0.8$). To illustrate how the peak luminosity depends on the parameters of the disruption event, Figure 2.4 shows the peak bolometric and g-band luminosities of the outflow as a function of $M_{\rm BH}$, for $R_{\rm p} = 3R_{\rm S}$ and $R_{\rm p} = R_{\rm T}$. For sources at cosmological distances (which *are* detectable; §2.5), the negative k-correction associated with the Rayleigh-Jeans tail implies that the rest-frame g-band luminosity in Figure 2.4 underestimates the peak optical luminosity visible at Earth.

2.4.2 Disk and Photoionized Unbound Debris

When $\dot{M}_{\rm fallback} \gtrsim \dot{M}_{\rm Edd}$, a fraction of the falling-back gas is blown away while the remainder likely accretes via an advective disk (§2.2.2). As the fallback rate declines below Eddington, the photons are able to diffuse out of the region close to the BH and the disk cools efficiently, but also becomes less luminous. The vertical dotted line in Figure 2.3 delineates the super-Eddington fallback (and outflow) phase from the sub-Eddington fallback phase.

The accretion disk irradiates the surface of the equatorial unbound stellar material (§2.3). In this section we calculate the combined emission produced by the accretion disk and the irradiated stellar debris. In order to isolate the more theoretically secure emission by the disk and photoionized material, we do *not* consider the emission from super-Eddington outflows in this section. We show results for the disk and photoionized material at both $t < t_{\rm Edd}$ and $t > t_{\rm Edd}$; depending on the geometry of the outflow, and the viewing angle of the observer to the source, it is possible that all three emission components could be visible at early times. Because the mass driven away by outflows during the super-Eddington phase can also be photoionized by the central source at times $t > t_{\rm Edd}$, our emission line predictions are likely a lower limit to the total emission line fluxes (§2.6).

We calculate the photoionization properties of the unbound material using version 07.02.02 of the publicly available code Cloudy, last described by Ferland et al. (1998). We simplify the geometry: the unbound spray traces out a widening spiral shape with most of

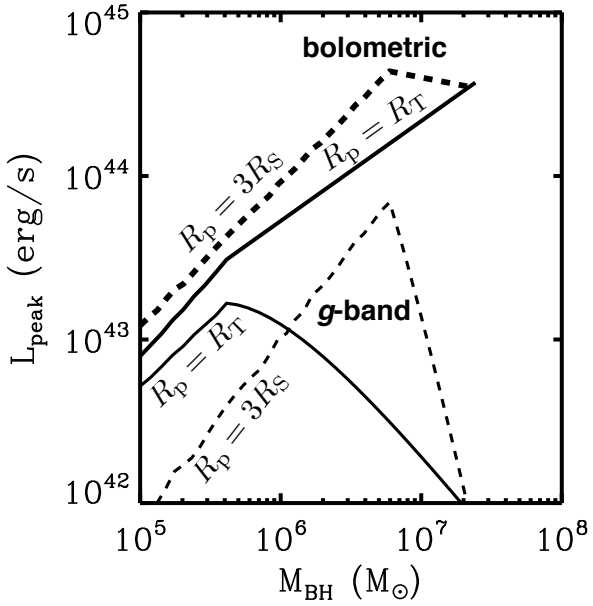

Figure 2.4: Peak bolometric (heavy lines) and g-band (light lines) luminosities of the early-time super-Eddington outflows as functions of $M_{\rm BH}$, for $R_{\rm p} = 3R_{\rm S}$ (dashed) and $R_{\rm p} = R_{\rm T}$ (solid), assuming that $f_{\rm out} = 0.1$ and $f_v = 1$. Figure 2.11 shows the duration of this phase.

the area coming from close to $\sim R_{\rm max}$, so we approximate it as a cloud of area $R_{\rm max}^2\Delta\Omega$ located a distance $R_{\rm max}$ from the ionizing source. Our model cloud has constant density n (eq. [2.26]), column depth N (eq. [2.27]), and is irradiated by the accretion disk having the luminosity and spectrum described in §2.2.2. The total emission calculated here is the sum of the emission from this photoionized layer and the emission from the central accretion disk. We focus on non-rotating BHs ($R_{\rm LSO} = 3R_{\rm S}$), although we quote results for rapidly rotating holes ($R_{\rm LSO} = R_{\rm S}$) as well.

In Figure 2.5 we plot the spectral energy distribution 30 days, 100 days, 300 days, and 1000 days after disruption, for our three fiducial models: $M_{\rm BH} = 10^6 M_\odot$ and $R_{\rm p} = 3R_{\rm S}$; $M_{\rm BH} = 10^6 M_\odot$ and $R_{\rm p} = R_{\rm T}$; and $M_{\rm BH} = 10^7 M_\odot$ and $R_{\rm p} = R_{\rm T}$. The early-time short-wavelength peaks at $\sim 0.1\,$keV with luminosity $\sim L_{\rm Edd}$ are emission from the disk. After a time $t_{\rm Edd}$, the mass fallback rate declines below the Eddington rate, and the disk begins to cool and fade. For $R_{\rm p} \sim R_{\rm LSO}$ and $M_{\rm BH} \sim 10^5 - 10^6 M_\odot$, the optical light is dominated by lines and continuum from the photoionized material. For larger $M_{\rm BH}$ (and larger $R_{\rm p}/R_{\rm S}$), the equatorial debris subtends a smaller solid angle (see eq. [2.25]) and the disk's luminosity is larger, so the disk dominates the optical emission.

Figure 2.6 zooms in on the UV/optical/near-infrared spectra for our three fiducial models. The emission lines characteristic of the broad line region of an AGN are typically the strongest lines here as well: e.g., Lyα, CIV 1548+1551, Hβ, and Hα. In most cases, these

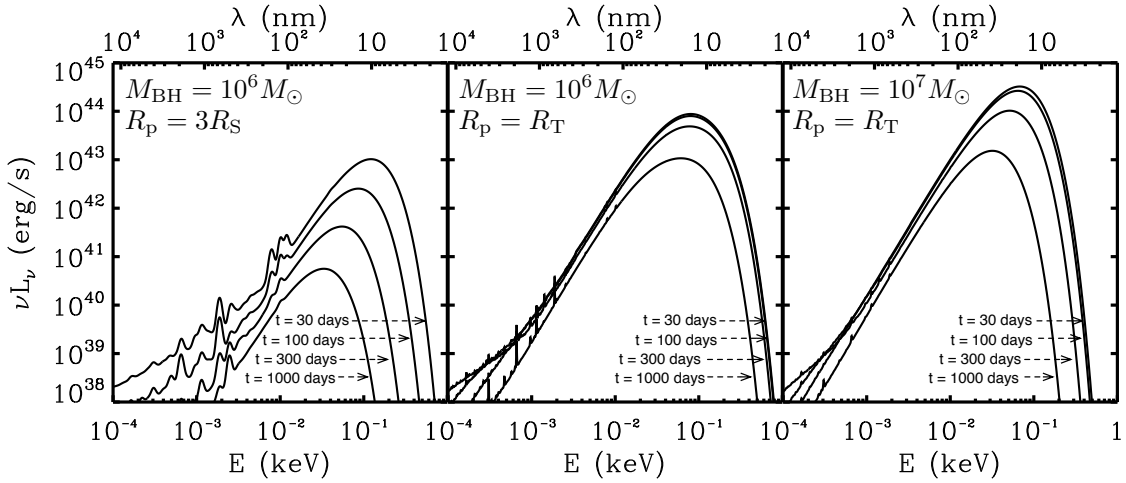

Figure 2.5: Spectral energy distributions for tidal flares around a non-rotating BH, 30, 100, 300, and 1000 days after disruption. Emission from the accretion disk dominates at short wavelengths. The photoionized unbound stellar debris absorbs and re-radiates some of the disk's emission, producing optical-infrared emission. These spectra do not include the emission from super-Eddington outflows at early times; see Figs. 2.2 & 2.3 for this emission.

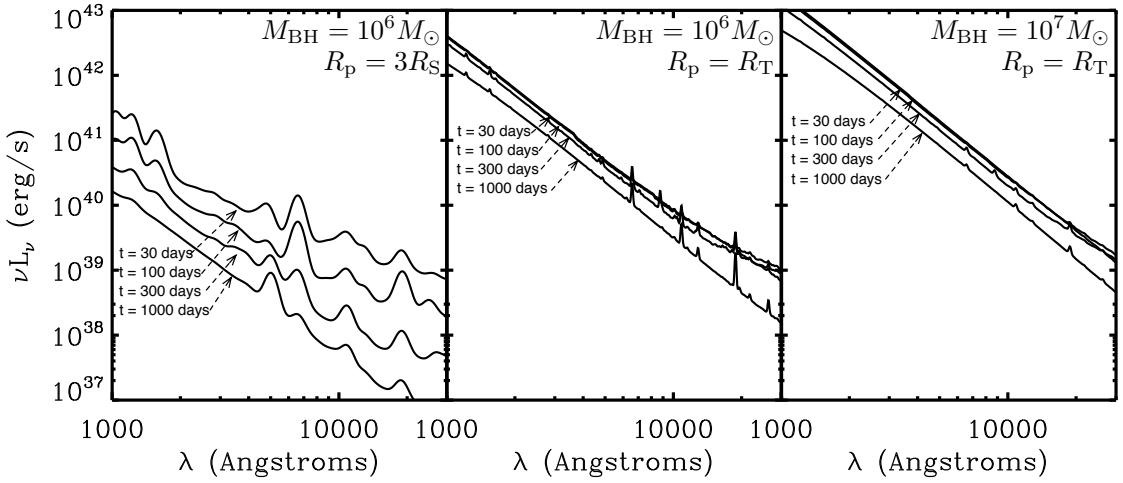

Figure 2.6: UV to near-infrared spectra for tidal flares around a non-rotating BH, 30, 100, 300, and 1000 days after disruption. The spectra are the sum of contributions from the accretion disk and the photoionized unbound material, but do not include the emission from super-Eddington outflows, which likely dominate at early times (Fig. 2.3). The linewidths and line strengths are both larger for smaller $R_{\rm p}/R_{\rm S}$ and smaller $M_{\rm BH}$ (eq. [2.22]).

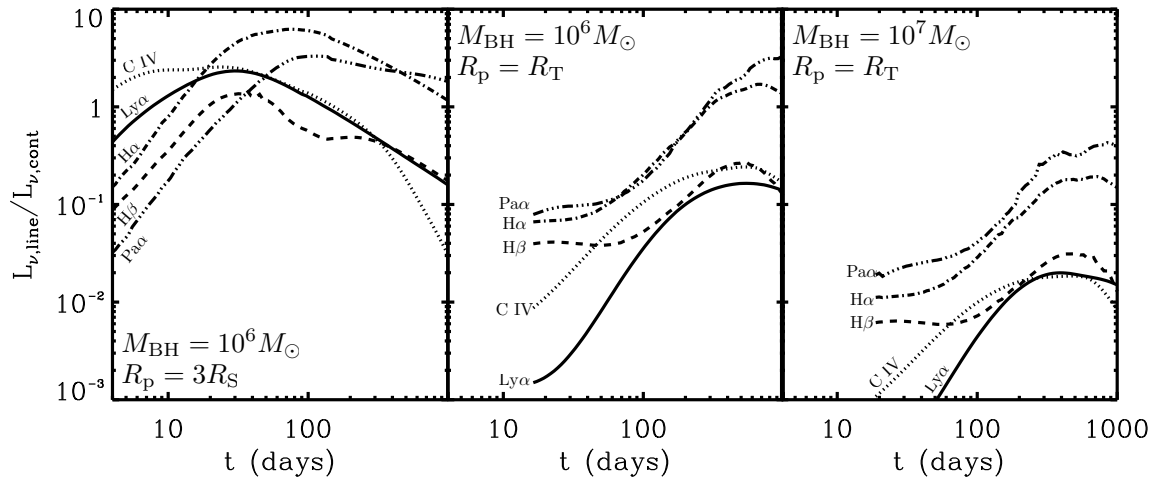

Figure 2.7: Line strength evolution for the three fiducial models. Results are shown for Lyα (solid), CIV 1548+1551 (dotted), Hβ (dashed), Hα (dot-dashed), and Paα (triple-dot-dashed). The quantity $L_{\nu,\rm line}/L_{\nu,\rm cont}$ is the ratio at line center of the line intensity to continuum intensity, taking into account emission from both the disk and the photoionized material, but not the early-time super-Eddington outflows.

Table 2.1: Assumed parameters for transient surveys[4] and predicted rates. Our results can be scaled to other survey parameters and model assumptions using eq. (2.31).

Survey	$f_{\rm lim}$	$f_{\rm sky}$	Cadence	D+UB[a] ($\rm yr^{-1}$)	Outflows[b] ($\rm yr^{-1}$)
Pan-STARRS 3π Survey	23 AB mag (g, i-band)	0.75	6 months	$4-12$	200
Pan-STARRS Medium Deep Survey	25 AB mag (g-band)	2×10^{-3}	4 days	$0.2-1$	20
Palomar Transient Factory	21 AB mag (g-band)	0.2	5 days	$0.3-0.8$	300
Large Synoptic Survey Telescope	24.5 AB mag (g-band)	0.5	3 days	$60-250$	6000
Synoptic All-Sky Infrared Survey[c]	23.5 AB mag (Y-band)	0.03?	10 days?	$0.1-0.5$	100
ROSAT All-Sky Survey[d]	$2\times10^{-12}\,\rm erg\,s^{-1}\,cm^{-2}$	1	e	$2-100$	N/A[f]
GALEX Deep Imaging Survey	25 AB mag (2316 Å)	7×10^{-5}	e	$0.05-0.2$	N/A[f]

[a] Rates for the emission from the disk and unbound equatorial debris; the range corresponds to $R_{\rm LSO}=3R_{\rm S}$ (low), $R_{\rm LSO}=1R_{\rm S}$ (high). This emission is relatively faint in the optical/infrared and may be difficult to detect relative to the host bulge (see §2.6).

[b] Rates for the emission from super-Eddington outflows, restricted to $z<1$, for $f_{\rm out}=0.1$ and $f_v=1$ (see Fig. 2.13).

[c] The survey strategy for SASIR has not yet been finalized.

[d] These parameters are for comparison with the all-sky rate calculation by Donley et al. (2002).

[e] ROSAT and GALEX do not have regular cadences.

[f] ROSAT and GALEX have insufficient cadence and/or sky coverage to detect flares from super-Eddington outflows.

lines are optically thick for more than a year. The lines are extremely broad, since the marginally bound gas has a speed close to zero while the most energetic gas leaves the BH at $v_{\rm max} \sim 0.4c$, $0.09c$, and $0.2c$ for $M_{\rm BH} = 10^6 M_\odot$, $R_{\rm p} = 3R_{\rm S}$; $M_{\rm BH} = 10^6 M_\odot$, $R_{\rm p} = R_{\rm T}$; and $M_{\rm BH} = 10^7 M_\odot$, $R_{\rm p} = R_{\rm T}$, respectively (see eq. [2.22]). In addition, the mean velocity along our line of sight will usually be substantial, so the lines should have a large redshift or blueshift on top of the galaxy's redshift. For clarity, we plot the spectra with a mean redshift of zero.

Figure 2.7 focuses on the evolution of five strong lines, plotting the ratio $L_{\nu,\rm line}/L_{\nu,\rm cont}$ at line center for each.[3] The quantity $L_{\nu,\rm line}$ is the line intensity at line center accounting for the significant broadening. As the surface area of the equatorial wedge grows in time, line luminosities grow until $\dot{M}_{\rm fallback} \lesssim \dot{M}_{\rm edd}$ and irradiation by the disk subsides. The quantity $L_{\nu,\rm cont}$ is the continuum intensity, which includes the contributions of both the disk (blackbody) and the photoionized unbound material (bremsstrahlung and radiative recombination)—again, the emission from the super-Eddington outflows is not included in $L_{\nu,\rm cont}$. The lines remain prominent for a few years, and are strongest and broadest for small $M_{\rm BH}$ and small $R_{\rm p}/R_{\rm S}$. The UV lines are the strongest lines when the unbound material dominates the continuum (left panel), while the near-infrared lines are the strongest when the disk dominates the continuum (middle and right panels).

We next describe the broadband optical evolution of a tidal disruption event. Figure 2.3, also discussed in §2.4.1, plots the optical light curve for each fiducial model, showing the total emission at both g- and i-bands. For $t \lesssim t_{\rm Edd}$ (left of the dotted lines), the emission is dominated by the super-Eddington outflows, while for $t \gtrsim t_{\rm Edd}$ the emission is dominated by the accretion disk and photoionized equatorial debris. Once $t > t_{\rm Edd}$, i.e., $\dot{M}_{\rm fallback} \lesssim \dot{M}_{\rm edd}$, the disk's optical luminosity falls off gently, approximately as $t^{-5/12}$: although the bolometric luminosity is declining as $t^{-5/3}$, the optical emission lies on the Rayleigh-Jeans tail. Increasing $R_{\rm p}/R_{\rm S}$ and/or $M_{\rm BH}$ increases the disk's luminosity by up to two orders of magnitude because of the disk's larger emitting area and/or because $L_{\rm Edd}$ rises. At all times, the disk emission is quite blue ($g - r \approx -1$).

For large $M_{\rm BH}$ and/or large $R_{\rm p}/R_{\rm S}$ (middle and right panels in Fig. 2.3), the disk outshines the photoionized material at optical wavelengths, and the light curves and color evolution are determined by the disk emission alone. By contrast, for $M_{\rm BH} = 10^6 M_\odot$ and $R_{\rm p} = 3R_{\rm S}$ (left panel), the photoionized material's optical line emission is initially an order of magnitude brighter than the disk. As the illuminating power of the disk declines but the unbound debris becomes less dense, different lines wax and wane. The significant redshift or blueshift of the unbound material further complicates the photometry by altering which lines contribute in which wavebands (again, our figures assume a mean redshift of zero). These effects can produce a non-monotonic light curve and a complicated color evolution, depending on the exact redshift of the source and the velocity of the equatorial debris.

[3]By comparing the results of different versions of Cloudy, we find that the results for line strengths can be uncertain by up to factor few.

2.5 Predicted Rates

We use our calculated spectra and light curves to predict the number of tidal disruption events detectable by observational surveys. We focus on an (almost) all-sky optical survey like the Pan-STARRS PS1 3π survey, but we also predict results for surveys with more rapid cadence (e.g., PTF and LSST) and discuss the results of our models compared to ROSAT and GALEX observations. Our assumed survey parameters are listed in Table 2.1, along with some of our results.[4] Our results can readily be scaled to other surveys using equation (2.31) discussed below.

To predict rates, we use the redshift-dependent BH mass function given by Hopkins et al. (2007). At $z \sim 0$, the BH density is $\simeq 10^{-2}\,\mathrm{Mpc}^{-3}$ for $\sim 10^6 M_\odot$ and gently falling at higher masses; as z rises to 3, the BH number density falls by ~ 30. We assume that the BH number density for $10^5 - 10^6 M_\odot$ is the same as for $\sim 10^6 M_\odot$, although it is poorly constrained observationally. We do not consider tidal disruption events beyond $z \sim 3$. (Our results can easily be scaled to other assumed BH mass densities; see eq. [2.31]).

The rate of tidal disruptions within a single galaxy is $\gamma(M_{\rm BH})$. To predict detection rates, we assume that γ is independent of BH mass. We adopt $\gamma = 10^{-5}\,\mathrm{yr}^{-1}$ as found by Donley et al. (2002) using the ROSAT All-Sky Survey, which is also in line with conservative theoretical estimates. We further assume that this rate is distributed equally among logarithmic bins of stellar pericenter distance $R_{\rm p}$, so that $d\gamma/d\ln R_{\rm p} = \gamma/\ln(R_{\rm T}/R_{\rm p,min})$. In the limit of $z \ll 1$, the equation for the predicted rate is

$$\frac{d\Gamma}{d\ln M_{\rm BH}} = \int_{R_{\rm p,min}}^{R_{\rm T}} \frac{4\pi}{3} d_{\rm max}^3 f_{\rm sky} \frac{dn}{d\ln M_{\rm BH}} \frac{d\gamma}{d\ln R_{\rm p}}\, d\ln R_{\rm p} \tag{2.30}$$

where $f_{\rm sky}$ is the fraction of sky surveyed; when necessary we use the generalization of equation (2.30) that includes cosmological effects. When the duration of a flare $t_{\rm flare}$ is shorter than the cadence of the survey $t_{\rm cad}$, we approximate the probability of detection as $t_{\rm flare}/t_{\rm cad}$.

We start by considering emission from only the accretion disk and photoionized equatorial debris. Then in §2.5.3, we include the emission from super-Eddington outflows, where the physics is somewhat less certain, but the observational prospects are particularly promising.

2.5.1 Disk and Photoionized Material

For all but the largest $M_{\rm BH}$, the duration of peak optical emission for the accretion disk and photoionized material is $t_{\rm flare} \sim t_{\rm Edd}$ (eq. [2.3]). This timescale depends on the BH's mass and the star's pericenter distance, as shown in Figure 2.8. For $R_{\rm p} \sim R_{\rm T}$, the flare lasts for $t_{\rm Edd} \sim 0.3 - 1\,\mathrm{yr}$ and then decays only gently since the disk dominates the optical emission. However, for $M_{\rm BH} \sim 10^5 - 10^6 M_\odot$ and $R_{\rm p} \sim R_{\rm LSO}$, the optical flare is

[4] These are intended to be illustrative, and may not correspond precisely to the true observational survey parameters, although we have attempted to be as accurate as possible.

shorter, $t_{\rm Edd} \sim 0.03 - 0.1\,{\rm yr}$, and then the emission decays more quickly since irradiation of the unbound material—the dominant source of optical emission—subsides. For $M_{\rm BH} \gtrsim 8 \times 10^7 M_\odot$, $t_{\rm flare} \sim t_{\rm fallback}$ (eq. [2.1]) because the fallback rate in these systems is never super-Eddington.

Figure 2.9 shows our calculated rates for optically-detected tidal flares (for a survey like the Pan-STARRS 3π survey), for both non-rotating and rapidly rotating BHs. For $M_{\rm BH} \gtrsim 10^6\,M_\odot$, the disk contributes most of the emitted power, so the rates increase with $M_{\rm BH}$ as $L_{\rm disk} \sim L_{\rm Edd}$ increases. The rates are dominated by $R_{\rm p} \sim R_{\rm T}$ and $M_{\rm BH} \sim 2 \times 10^7 M_\odot$ (non-rotating BHs) and $M_{\rm BH} \sim 10^8 M_\odot$ (rapidly rotating BHs). Since most of the flares that dominate the rates have relatively long durations (Fig. 2.8), imperfect survey cadence only modifies the detection rates by $\sim 50\%$. At $10^5 - 10^6 M_\odot$ and small $R_{\rm p}$, the photoionized material re-emits a relatively large fraction of the disk's power in the optical and boosts the detection rates significantly.

Integrated over $M_{\rm BH} = 10^6 - 10^8 M_\odot$, our estimated rates for the Pan-STARRS 3π survey, assuming non-rotating BHs, are $4\,{\rm yr}^{-1}$ and $2\,{\rm yr}^{-1}$ in g-band and i-band, respectively. The mass range $10^5 - 10^6 M_\odot$ contributes another $0.4\,{\rm yr}^{-1}$ (both g-band and i-band), assuming (probably optimistically) that $dn/d\ln M_{\rm BH}$ and γ are the same at $10^5 M_\odot$ as at $10^6 M_\odot$. If the BH is rotating faster, $R_{\rm p}/R_{\rm S}$ can be smaller. This allows an accretion disk to form for even $M_{\rm BH} \sim$ few $\times\, 10^7 - 10^8 M_\odot$, widens the disk for all $M_{\rm BH}$, and increases the solid angle of the unbound material. Indeed for $M_{\rm BH} \sim 10^5 M_\odot$ and $R_{\rm p} \sim R_{\rm S}$, the unbound material covers a quarter of the sky! (At this point $R_{\rm S} \sim R_\odot$ so our approximations begin to break down.) These effects raise the total predicted rates for rapidly rotating BHs to $\sim 12\,{\rm yr}^{-1}$.

Figure 2.10 plots the detection rates as a function of $R_{\rm p}/R_{\rm S}$ for $M_{\rm BH} = 10^5 M_\odot$, $10^6 M_\odot$, and $10^7 M_\odot$, for the disk alone (light lines) and for the disk plus photoionized material (heavy lines). The photoionized material enhances detection rates significantly for most $R_{\rm p}/R_{\rm S}$ at $10^5 M_\odot$ and $10^6 M_\odot$, but has little effect for $10^7 M_\odot$. The rates decrease substantially for $R_{\rm p}/R_{\rm S} \to 1.5$ because then the outer radius of the disk $\simeq 2R_{\rm p} = 3R_{\rm S}$ is at the last stable orbit; our disk model assumes a no-torque boundary condition at $R_{\rm LSO}$, implying that there is essentially no emission from the disk when $R_{\rm p} \sim R_{\rm LSO}$.

Although the rates quoted above and in Figures 2.9 and 2.10 are for a survey covering 3/4 of the sky, assuming constant $\gamma(M_{\rm BH})$ and constant BH mass density below $\simeq 10^6 M_\odot$, our predicted rates can be scaled to other assumed parameters:

$$\frac{d\Gamma}{d\ln M_{\rm BH}} \propto f_{\rm lim}^{-3/2} f_{\rm sky} f_{\rm cad} \frac{dn}{d\ln M_{\rm BH}} \gamma(M_{\rm BH}) \tag{2.31}$$

assuming that the sources are at $z \ll 1$, where $f_{\rm cad} \equiv \min(t_{\rm flare}/t_{\rm cad}, 1)$.

The Pan-STARRS MDS, PTF, and LSST will have cadences of only a few days, giving them sensitivity to all events within their survey volumes. However, for detecting this relatively long-lived emission, the advantage of fast cadence is only minor; more significant is the spatial volume probed by the survey (see Table 2.1). The MDS will deeply ($m_{\rm AB} \sim 25$) image a relatively small (84-deg^2) region, and so will detect $\sim 5 - 10\%$ as many events as the 3π Survey, $\sim 0.2 - 1$ per year. PTF will image a larger region ($8000\,{\rm deg}^2$) but less deeply

($m_{\rm AB} \sim 21$), and so will have detection rates similar to the MDS. The emission from early-time super-Eddington outflows may significantly increase these rates, as we discuss in §2.5.3. In the next decade, LSST will image a large region (20,000 deg^2) deeply ($m_{\rm AB} \sim 24.5$), and so will discover hundreds of tidal flares. MDS and LSST will detect events at cosmological distances ($z_{\rm max} \sim 0.3 - 0.6$), where the negative k-correction of the disk's blackbody peak enhances rates by a factor of a few. By co-adding images up to ~ 1 month, these short-cadence surveys will also be able to raise their detection rates of events having $M_{\rm BH} \sim 10^6 - 10^8 M_\odot$ by a factor of a few. Also in the next decade, SASIR plans to deeply image 140 deg^2 each night in the near infrared (to $m_{\rm AB} \sim 23.5$ at Y-band; Bloom et al. 2009). Their observing strategy is not yet finalized; assuming a 10-day cadence covering 1400 deg^2 (a good strategy for detecting flares during the super-Eddington outflow phase; see §2.5.3), this survey should detect a flare every few years from the accretion disk plus photoionized debris.

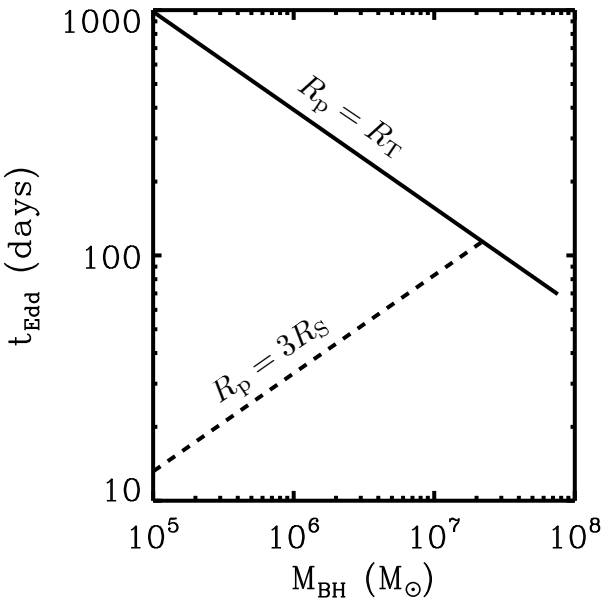

Figure 2.8: Duration of maximum luminosity during the late-time accretion disk phase, plotted as a function of $M_{\rm BH}$ for $R_{\rm p} = 3R_{\rm S}$ and $R_{\rm p} = R_{\rm T}$. Most flares last longer than $\sim$ a month. The super-Eddington outflow at early times produces a shorter flare that should precede this emission (Figs. 2.3 & 2.11–2.13). (The fallback rates for $M_{\rm BH} \gtrsim 8 \times 10^7 M_\odot$ are never super-Eddington, so the flare duration in these systems is $\sim t_{\rm fallback}$.)

2.5.2 Current Observational Constraints

As a check on our model, we have calculated rates for the ROSAT All-Sky Survey for comparison with Donley et al. (2002)'s result of 42 events per year over the whole sky for $f_{\rm lim} = 2 \times 10^{-12}\,{\rm erg\,s^{-1}\,cm^{-2}}$ $(0.2 - 2.4$ keV).[5] Considering blackbody emission alone, we predict $2\,{\rm yr^{-1}}$ ($R_{\rm in} = 3R_{\rm S}$) or $40\,{\rm yr^{-1}}$ ($R_{\rm in} = R_{\rm S}$). This strong sensitivity to $R_{\rm in}$ arises because the ROSAT band is on the Wien tail of the disk emission. If we assume that 10% of the emission is in an X-ray power-law tail with a photon index $\Gamma = 3$ (not unreasonable assumptions for X-ray emission from accreting BHs; e.g., Koratkar & Blaes 1999), our predicted rates are $10\,{\rm yr^{-1}}$ ($R_{\rm in} = 3R_{\rm S}$) and $100\,{\rm yr^{-1}}$ ($R_{\rm in} = R_{\rm S}$). Given the large uncertainties in the X-ray emission, our predictions are consistent with the observational results. We also compare with detection rates in the GALEX Deep Imaging Survey (Gezari et al. 2008). They search an area of 2.882 square degrees, observed at FUV (1539 Å) and NUV (2316 Å) down to $f_{\rm lim} \sim 25$ AB magnitudes. Gezari et al. detect 2 events[6] in this region over 3 years. This

[5]The cadence is ~ 1 year but irregular; we assume it is perfect for simplicity. The rates we predict thus may be slightly high.

[6]The candidate of Gezari et al. (2009) is in a different field.

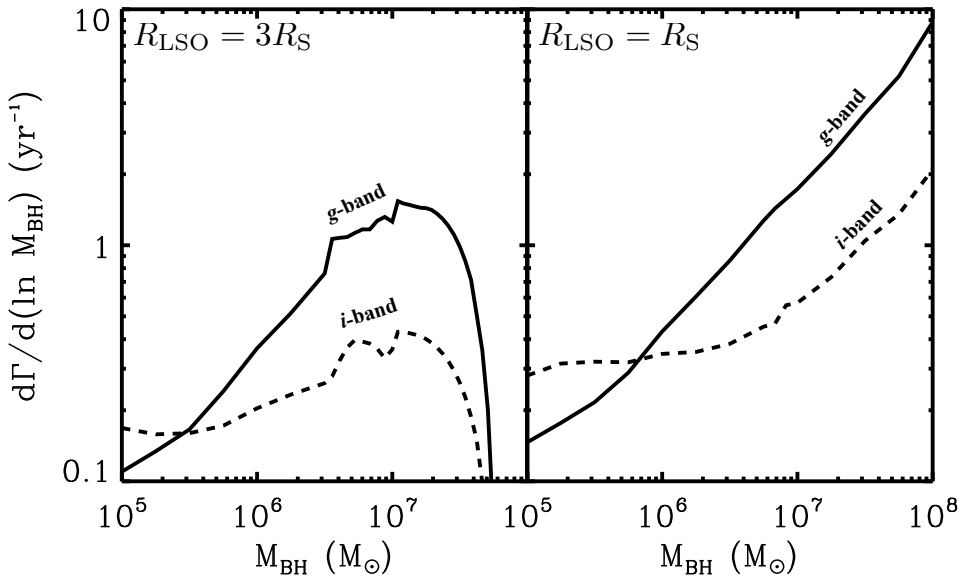

Figure 2.9: Predicted detection rates as a function of BH mass for the Pan-STARRS 3π survey (see Table 2.1). Results are shown for non-rotating BHs (left panel) and rapidly rotating BHs (right panel). The rates shown here can be scaled to other surveys and other model parameters using eq. (2.31). These rates do not include the emission from super-Eddington outflows at early times; see Figs. 2.12 & 2.13 for these results.

is somewhat higher than our predicted rates in the NUV, $0.05\,\mathrm{yr}^{-1}$ if $R_{\rm in} = 3R_{\rm S}$ and $0.2\,\mathrm{yr}^{-1}$ if $R_{\rm in} = R_{\rm S}$ (assuming perfect cadence for simplicity), and may suggest that the disruption rate per galaxy γ is a factor of a few higher than we have assumed here.

As the above estimates demonstrate, consistency with GALEX and ROSAT constraints prefers a rate per galaxy of $\gamma \sim (1-3)\times 10^{-5}\,\mathrm{yr}^{-1}$. Significantly larger disruption rates, as some calculations predict (e.g., Merritt & Poon 2004), are inconsistent with current observational limits unless dust obscuration has significantly biased the ROSAT and GALEX results or the large disruption rates are confined to brief epochs in a galaxy's life (e.g., a merger). Note also that this constraint only applies to massive BHs with $M_{\rm BH} \sim 10^7 M_\odot - 10^8 M_\odot$, because UV and X-ray surveys select for these systems (§2.6).

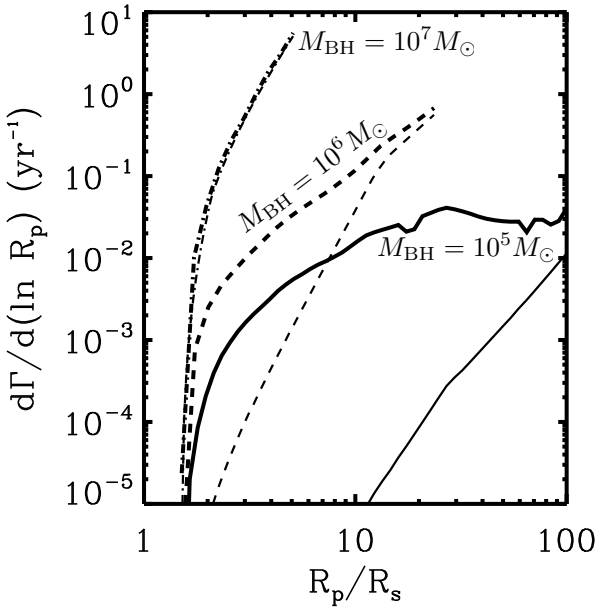

Figure 2.10: Predicted detection rates as a function of pericenter distance $R_{\rm p}/R_{\rm S}$ for the Pan-STARRS 3π survey at g-band (see Table 2.1). Results are shown for $M_{\rm BH} = 10^5 M_\odot$ (solid), $10^6 M_\odot$ (dashed), and $10^7 M_\odot$ (dot-dashed), assuming a non-rotating BH. The thin/light lines are for the disk emission alone, while the thick/heavy lines include the emission from both the disk and the photoionized unbound material. The photoionized material significantly increases the rates for low $M_{\rm BH}$ and small $R_{\rm p}/R_{\rm S}$. These rates do not include emission from super-Eddington outflows at early times; those results are shown in Figs. 2.12 & 2.13. The small fluctuations in the results for $M_{\rm BH} = 10^5 M_\odot$ are due to difficulties in performing Cloudy calculations at very high densities.

2.5.3 Super-Eddington Outflows

We now calculate optical detection rates accounting for emission from the luminous but shorter-lived super-Eddington outflows. We begin by plotting the duration of peak emission for the outflow phase, $t_{\rm flare} \sim t_{\rm outflow}$, in Figure 2.11 as a function of $M_{\rm BH}$ for $R_{\rm p} = 3R_{\rm S}$ and $R_{\rm p} = R_{\rm T}$. For $R_{\rm p} = 3R_{\rm S}$ and $M_{\rm BH} \lesssim 6 \times 10^6 M_\odot$, the duration of the outflow is set by the time at which the photosphere recedes inside the edge of the outflow ($t_{\rm outflow} \sim t_{\rm edge}$; eq. [2.9]) while for larger $M_{\rm BH}$, the duration is set by the timescale for the most bound material to return to pericenter ($t_{\rm outflow} \sim t_{\rm fallback}$; eq. [2.1]); for $R_{\rm p} = R_{\rm T}$, the transition from $t_{\rm edge}$ to $t_{\rm fallback}$ occurs at a somewhat lower BH mass of $M_{\rm BH} \lesssim 4 \times 10^5 M_\odot$. Figure 2.11 shows that most flares last longer than the few-day cadences of surveys like PTF, Pan-STARRS MDS, and LSST, but are much shorter than the months-long cadence of the Pan-STARRS 3π survey. ROSAT and GALEX are unlikely to have detected events during this phase due to insufficient cadence and sky coverage.

In Figure 2.12, we plot detection rates as a function of $R_{\rm p}/R_{\rm S}$ for $M_{\rm BH} = 10^5 M_\odot$, $10^6 M_\odot$, and $10^7 M_\odot$, all for the Pan-STARRS 3π survey at g-band. At small $R_{\rm p}/R_{\rm S}$, the edge of the

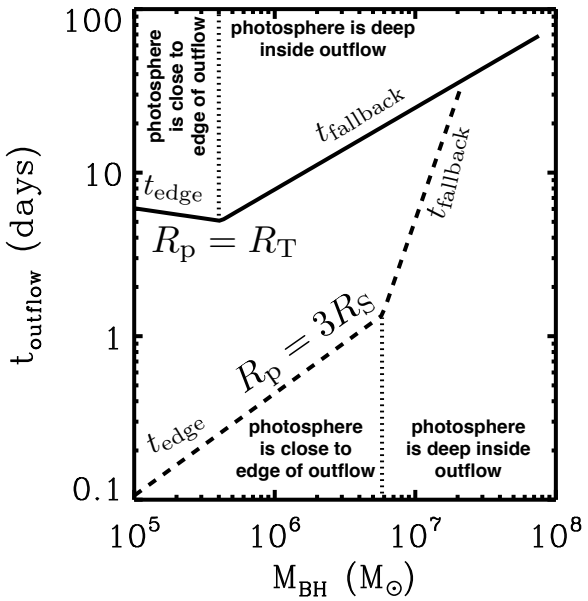

Figure 2.11: Duration of peak luminosity during the early super-Eddington outflow phase, as a function of $M_{\rm BH}$ for $R_{\rm p} = 3R_{\rm S}$ and $R_{\rm p} = R_{\rm T}$ (for $f_{\rm out} = 0.1$ and $f_v = 1$; see eqs. [2.5] & [2.6]). The vertical dotted lines mark the boundary between events where the edge of the outflow limits the size of the photosphere (lower BH masses) and where it does not (higher BH masses). The flares from super-Eddington outflows typically last longer than the few-day cadence of surveys like PTF, Pan-STARRS MDS, and LSST, but they are often short enough that they would not be detected in surveys optimized solely for supernovae.

outflow limits the size of the photosphere. As $R_{\rm p}/R_{\rm S}$ increases, the radius of the photosphere at $t_{\rm edge}$ increases and so the rates increase. For $M_{\rm BH} = 10^6 M_\odot$ and $10^7 M_\odot$ at the largest $R_{\rm p}/R_{\rm S}$, the photosphere is no longer limited by the edge of the outflow, and the maximum luminosity occurs at $t_{\rm fallback}$. For large $R_{\rm p}/R_{\rm S}$, the rate declines as the photosphere recedes inward.

In Figure 2.13, we plot overall detection rates at g-band for Pan-STARRS 3π and MDS, PTF, and LSST. In the leftmost panel, we assume that 10% of the falling back material flows out in the wind ($f_{\rm out} = 0.1$), as we have previously. Here we restrict detections to redshifts $z < 1$, where our assumed tidal disruption rate per galaxy is appropriate. The Pan-STARRS 3π survey should detect $200\,{\rm yr}^{-1}$, while the MDS should detect $20\,{\rm yr}^{-1}$ because of its smaller spatial volume. PTF should detect $300\,{\rm yr}^{-1}$ as well, since its fast cadence makes up for its smaller spatial volume relative to the Pan-STARRS 3π survey. LSST's large spatial volume and rapid cadence should allow it to detect $6000\,{\rm yr}^{-1}$! Assuming the survey parameters and strategy described in §2.5.1 and Table 2.1, SASIR should detect $\sim 100\,{\rm yr}^{-1}$ as well.

In the central panel of Figure 2.13, we plot detection rates for redshifts $z > 1$ to highlight the possibility of studying tidal disruption events at cosmological distances. Deep surveys like MDS will be sensitive to events far beyond $z \sim 1$. Even the shallower 3π survey could detect ~ 30 events per year at $z > 1$. Our predicted rates at $z > 1$ are particularly uncertain:

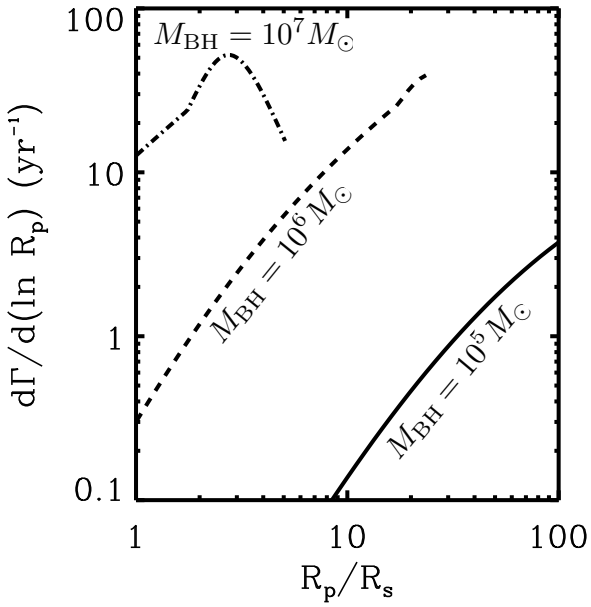

Figure 2.12: Predicted detection rates for emission from super-Eddington outflows at early times (for $f_{\rm out} = 0.1$ and $f_v = 1$; see eqs. [2.5] & [2.6]). Results are shown as a function of $R_{\rm p}/R_{\rm S}$ for $M_{\rm BH} = 10^5 M_\odot$, $10^6 M_\odot$, and $10^7 M_\odot$, all for a Pan-STARRS 3π-like survey at g-band (see Table 2.1).

higher redshift sources are more likely to be obscured, and the lower mass BHs of interest for tidal disruption are still growing significantly in mass at these redshifts (Heckman et al. 2004) so the tidal disruption rate and mass function become less certain. Nonetheless, the fact that tidal disruption flares will be detectable at $z > 1$ with forthcoming surveys highlights that these sources may become a strong probe of the evolution of $\sim 10^6 - 10^8 M_\odot$ BHs.

In the rightmost panel of Figure 2.13, we show the sensitivity of our predictions to uncertainty in the outflow model by plotting the rates for the Pan-STARRS 3π survey for different assumptions about the fraction of the material that is blown away in the outflow, $f_{\rm out}$. For $f_{\rm out} \sim 0.3$, the detection rate is $600\,{\rm yr}^{-1}$, while for $f_{\rm out} \sim 0.01$ it falls to $8\,{\rm yr}^{-1}$. The rate falls rapidly at the highest $M_{\rm BH}$ because the outflow is optically thin. Figure 2.13 shows that even if we very conservatively assume that only 1% of the material is blown away when the fallback rate is super-Eddington, upcoming optical surveys like Pan-STARRS should still be able to detect a significant number of tidal disruptions during the super-Eddington phase.

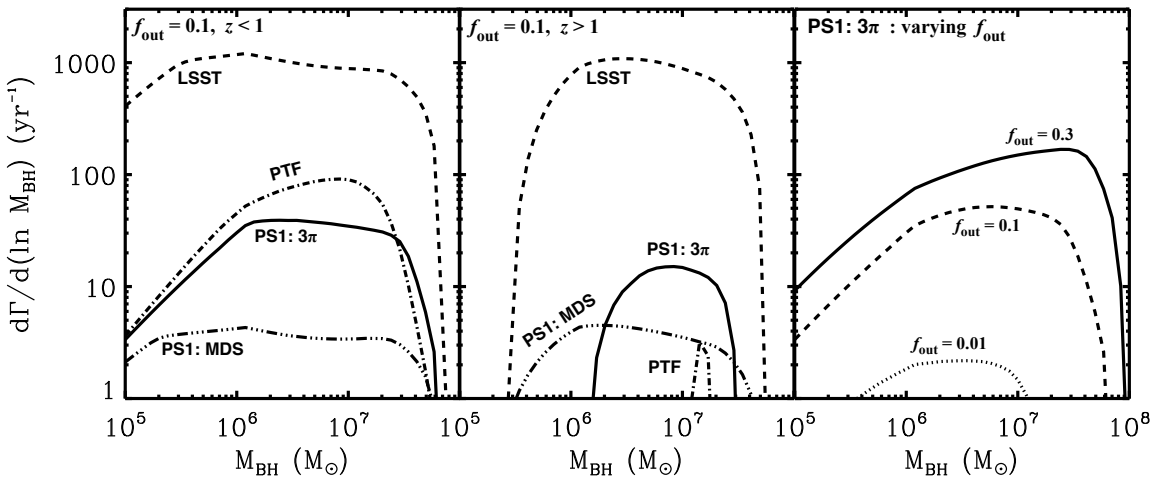

Figure 2.13: Predicted detection rates for emission at g-band from super-Eddington outflows for various optical transient surveys. In the leftmost panel, we use our standard outflow model in which $f_{\rm out} = 0.1$ and $f_v = 1$ (see eqns [2.5] & [2.6]), and restrict detections to $z < 1$. In the central panel, we plot detection rates for $z > 1$ to illustrate the potential for surveys to be sensitive to the cosmological evolution of BHs; note that PTF is not deep enough to detect flares beyond $z \sim 1$. In the rightmost panel, we vary $f_{\rm out}$ from 0.3 to 0.01 to illustrate the sensitivity of our results to uncertainties in the outflow physics.

2.6 Discussion

We have calculated the spectra and light curves produced by the tidal disruption of a solar-type star by a massive black hole. Upcoming optical transient surveys should detect many such events (§2.5). Our results demonstrate that there are at least three different emission components that are important during tidal flares: (1) outflows at early times when the fallback rate is super-Eddington, (2) a compact ($\lesssim 10 - 100 R_{\rm S}$) accretion disk around the BH, and (3) stellar debris that is unbound during the disruption and forms an outflowing "wedge" in the equatorial plane (see Fig. 2.1). It is also possible that the super-Eddington fallback powers a lower-density magnetically-dominated jet, but the properties of such a jet are difficult to predict so we do not consider this potential source of emission.

Each of these three components contributes to the total emission from tidal disruption flares. At early times, the super-Eddington outflows likely dominate, producing a few– to 10–day optical-infrared flare with a luminosity comparable to that of a supernova (Figs. 2.2-2.4 & 2.11). As the fallback rate decreases below the Eddington rate, these outflows will diminish, revealing the underlying accretion disk that emits primarily in the UV to soft X-rays (Fig. 2.5); at this time, the optical emission is likely to be much less than that of a typical AGN—and well below that of the super-Eddington phase (Fig. 2.3)—because the accretion disk is not very spatially extended. The central UV and soft X-ray source photoionizes the inner edge of equatorial stellar debris, producing a spectum of broad emission lines (Figs. 2.5, 2.6, & 2.7) whose "rest" wavelength should be either blueshifted or redshifted with respect to the host galaxy depending on the line of sight of the observer relative to the escaping material. We find that this spectroscopic signature of tidal flares is the strongest for low mass BHs because the equatorial stellar debris occupies the largest solid angle in these systems (eq. [2.25]).

Although the above stages are the focus of this paper, for completeness we briefly discuss the rest of the evolution of a tidal disruption event. As the fallback rate continues to decrease below the Eddington rate, the viscous time in the thin disk (eq. [2.21]) increases and becomes comparable to the time t since disruption; at this point, matter begins to build up rather than rapidly accreting onto the BH. For disruption at $R_{\rm p} \sim R_{\rm T}$, which is likely to produce a significant fraction of the events (Figs. 2.10 & 2.12), we estimate that this occurs $\sim 3\,\alpha_{0.1}^{3/7}$ years after disruption, when the fallback rate has decreased to $\dot{M}_{\rm fallback} \sim 0.2\,\alpha_{0.1}^{-5/7}\,M_6^{-2/3}\,\dot{M}_{\rm Edd}$ (where $\alpha \equiv 0.1\alpha_{0.1}$ is the dimensionless viscosity). Separately, we expect a significant change in the thermodynamics of the disk when $\dot{M}_{\rm fallback} \simeq \alpha^2 \dot{M}_{\rm Edd} \sim 10^{-2}\dot{M}_{\rm Edd}$. Below this accretion rate, the material will no longer cool efficiently when it circularizes and shocks upon returning to pericenter. Instead of cooling to form a thin disk, the material will be shock heated to form a geometrically thick, radiatively inefficient accretion flow. In general, both geometrically thin/optically thick and geometrically thick/radiatively inefficient disks appear to be stable accretion solutions for a given $\dot{M} \lesssim 10^{-2}\dot{M}_{\rm Edd}$. However, in this case, the boundary condition that matter shocks up to the virial temperature upon returning to pericenter picks out the radiatively inefficient solution once $\dot{M}_{\rm fallback} \lesssim 10^{-2}\dot{M}_{\rm Edd}$. Because the

viscous time in a thick disk is $\sim \alpha^{-1}$ times the dynamical time, once the accretion becomes radiatively inefficient, the viscous time is always much shorter than the orbital period of matter returning to pericenter. Moreover, the transition to radiatively inefficient accretion happens at a time comparable to when matter would otherwise begin accumulating in a thin disk, particularly for more massive BHs. This suggests that there is typically only a limited range of accretion rates (and time) during which the "spreading disk" solution of Cannizzo et al. (1990) applies. Instead, at late times matter will rapidly accrete via a thick disk and the accretion rate will decay as $\sim \dot{M}_{\rm fallback} \propto t^{-5/3}$. As in X-ray binaries (Remillard & McClintock 2006), we expect that the thermodynamic transition at $\sim 10^{-2}\dot{M}_{\rm Edd}$ will be accompanied by a significant change in the luminosity and spectrum of the disk, and perhaps also by the production of relativistic jets. This should be explored in more detail in future work.

Having summarized our key results and the timeline of a tidal disruption event, we now discuss some uncertainties in our models, observational challenges to detecting tidal flares, and the astrophysical applications of studies of tidal disruption events.

2.6.1 Super-Eddington Outflows

In §2.2.1, we described our simple model for outflows driven when the fallback rate is super-Eddington. Energy conservation implies that the falling back material initially remains bound after returning to pericenter and circularizing, but even small amounts of accretion can release additional energy and drive a powerful outflow. There is, however, a significant uncertainty in precisely how much of the falling back material is blown away, and in the kinematics of the outflow. We assume that the gas expands roughly spherically from the BH, but the flow is probably somewhat collimated along the pole, due to the original angular momentum of the stellar debris. Some photons can then leak out through the sides of the outflow rather than continuing to drive the expansion; in this case, the overall emission would be somewhat hotter and fainter, with a dependence on viewing angle.

We have parameterized the terminal velocity of the outflow using $v_{\rm wind} = f_v v_{\rm esc}(2R_{\rm p})$, and the mass outflow rate using $\dot{M}_{\rm out} \equiv f_{\rm out}\dot{M}_{\rm fallback}$; in all of our calculations, we have assumed that $f_v \sim 1$. If the gas actually expands more slowly ($f_v < 1$), its density will be larger, so the photosphere will be larger, increasing the optical fluxes and detection rates. In the extreme case in which there is no unbound outflow, but super-Eddington fallback leads to a radiation-pressure-supported atmosphere around the BH that slowly expands until the photons can diffuse out, we also expect significant optical luminosities during the super-Eddington phase (e.g., Loeb & Ulmer 1997).

It is worth noting that our predictions for the radiation from super-Eddington outflows are particularly uncertain for low $M_{\rm BH}$ and small $R_{\rm p}/R_{\rm S}$, when the edge of the outflow limits the radius of the photosphere and determines both the peak luminosity (Fig. 2.3) and duration (Fig. 2.11) of the flare; this does not, however, significantly influence our total predicted rates (Fig. 2.12).

Figure 2.13 shows that even if the outflow rate is just a few percent of the fallback rate

($f_{\rm out} \sim 0.01 - 0.1$), the outflowing gas is sufficiently bright in the optical that forthcoming surveys should detect a significant number of tidal disruption flares. This makes early-time optical flares from the tidal disruption of stars an extremely promising candidate for current and future optical/infrared transient surveys. (We discuss some practical issues associated with detecting these sources in §2.6.3.) In this context, we note that in the radiation hydrodynamic simulations of accretion at $\dot{M} = 100\dot{M}_{\rm Edd}$ carried out by Ohsuga et al. (2005), $\sim 10\%$ of the gas becomes unbound, $\sim 10\%$ accretes, and the remaining $\sim 80\%$ is marginally bound and may (or may not) eventually accrete as well. These precise values will depend on the pericenter of the star, with smaller $R_{\rm p}/R_{\rm S}$ likely leading to smaller $f_{\rm out}$, i.e., a smaller fraction of the gas being blown away. Future observational constraints on the luminosity, spectrum, and timescale of the super-Eddington outflow phase should be able to strongly constrain the value of $f_{\rm out}$ in individual events. These results will have important implications for how massive BHs grow. In particular, if $f_{\rm out}$ is typically modest, this would imply that black holes can accrete at rates far above the Eddington rate, perhaps helping to explain how supermassive BHs ($M_{\rm BH} \gtrsim 10^8 M_\odot$) can be observable as luminous quasars as early as $z \sim 6$.

Figure 2.13 also demonstrates that deep optical surveys such as the Pan-STARRS MDS and LSST will be sensitive to tidal flares at high redshift. These surveys may thus provide a powerful probe of the BH mass function and stellar dynamics in galactic nuclei as a function of redshift. For example, at $z \sim 0.1$, BHs having $M_{\rm BH} \lesssim 10^7 M_\odot$ are still growing significantly in mass (Heckman et al. 2004) and thus their disruption rates may evolve significantly with redshift. In addition, galaxy mergers, which are more common at $z \sim 1 - 2$, could substantially increase the tidal disruption rate: Chen et al. (2009) find rates of up to $\sim 1\,{\rm yr}^{-1}$ for $\sim 10^5$ years after the merger due to three-body interactions between stars and a binary BH.

2.6.2 The Accretion Disk, Photoionized Gas, & Broad Emission Lines

We now consider several aspects of our model for the accretion disk, broad emission lines, and the material unbound during the disruption (§§2.2.2 and 2.3). Our accretion disk model is designed to describe the emission from the time when the disk first forms through the following few years. During much of this period, the fallback rate is super-Eddington, and we expect the disk to be optically and geometrically thick, with radiation pressure dominating gas pressure. Once the fallback rate becomes sub-Eddington, the disk becomes geometrically thin and may be subject to viscous instabilities (although it is thermally stable; Hirose et al. 2009). These instabilities may lead to additional time dependence not captured in our models, particularly at late times when the viscous time in the thin disk becomes comparable to the orbital period of the material falling back to pericenter. As described above, once $\dot{M}_{\rm fallback} \lesssim \alpha^2 \dot{M}_{\rm Edd}$, the density is sufficiently low that the flow becomes radiatively inefficient and our model is no longer appropriate. The disk will then heat up and its spectrum will

become significantly harder. This phase may be detectable by hard X-ray transient surveys like EXIST.

It is also unclear how much tidal forces will spin up the rotation of the star as it approaches pericenter. We have assumed that the star is maximally spun up, so that stellar debris is accelerated to relative velocities $\Delta v \sim v_{\rm p}(R_\star/R_{\rm p})^{1/2}$ in the azimuthal direction. If in fact the spin-up is less effective, the onset of the flare, which occurs at the fallback time (eq. [2.1]), will be later by a factor of few and the solid angle subtended by the unbound equatorial debris will be somewhat smaller. This will not change our qualitative conclusions, only some of our quantitative results.

It is important to stress that the line emission we predict may well be an underestimate in all cases: the accretion disk will also photoionize the *back edge* of the material that was blown away during the super-Eddington phase, which is far from the BH once the outflows subside. Simple estimates indicate that the density and velocity of this outflowing gas are similar to that of the gas unbound at the time of disruption; as a result, irradiation of this gas will produce additional broad hydrogen lines. The equivalent width of these lines depends on the solid angle subtended by the super-Eddington winds, which, although uncertain, is likely to be significant. These lines are unlikely to depend as sensitively on $M_{\rm BH}$ and $R_{\rm p}/R_{\rm S}$ as the emission lines from the equatorial debris (see Fig. 2.6 for the latter). As a result, observations of the line emission will help constrain the geometry of the outflowing gas created during the tidal disruption event.

In addition to emission lines from the back edge of the outflowing gas at late times, the photosphere of the super-Eddington outflow may at early times show strong *absorption lines*, particularly in the ultraviolet (much like the photosphere of a star); these lines would likely be highly blueshifted relative to the lines of the host galaxy. Finally, we reiterate that we expect very little narrow forbidden line emission from tidal disruption events: the outflowing stellar debris is too dense to produce forbidden lines, and there is insufficient time to photoionize ambient lower density gas far from the BH. It is possible that there is ambient gas in the galactic nucleus sufficiently close to the BH to produce forbidden lines on a $\lesssim 1\,{\rm yr}$ timescale, but the prevalence of such gas is currently poorly understood.

2.6.3 Observational Considerations

Candidate detections of tidal disruption flares have thus far been selected by their UV and soft X-ray emission (predominantly via GALEX, ROSAT and XMM-Newton). The emission at these wavelengths is primarily produced by the accretion disk, which is brighter for larger $M_{\rm BH}$. As a result, these surveys are most sensitive to BHs having $M_{\rm BH} \sim 10^7 - 10^8 M_\odot$. UV and X-ray selected events are likely to be discovered somewhat after the initial period of super-Eddington fallback, because the outflow during that phase probably precludes direct observation of the underlying accretion disk from many viewing angles. This outflowing material could also be a significant source of obscuration even at late times when the fallback rate is sub-Eddington.

The accretion disk emission we predict for UV-selected events is broadly consistent

with the GALEX candidates: UV luminosities of $\sim$ few $\times\, 10^{43}\,\mathrm{erg\,s^{-1}}$, optical luminosities of $\sim$ few $\times\, 10^{41}\,\mathrm{erg\,s^{-1}}$, blackbody temperatures of $T \sim$ few $\times\, 10^4 -$ few $\times\, 10^5\,\mathrm{K}$, and bolometric luminosities of $L_{\rm bol} \sim 10^{45}\,\mathrm{erg\,s^{-1}}$. The events selected from soft X-rays have less data, but typically have soft X-ray luminosities of $\sim 10^{43} - 10^{44}\,\mathrm{erg\,s^{-1}}$. This emission may be from the accretion disk, at energies just above the blackbody peak, or may be from an X-ray power-law tail with $1-10\%$ of the bolometric luminosity. In addition, as discussed in §2.5.2, our model is consistent with ROSAT and GALEX rate estimates, provided that the tidal disruption rate per galaxy for BHs with $M_{\rm BH} \sim 10^7 M_\odot - 10^8 M_\odot$ is $\gamma \sim 10^{-5}\,\mathrm{yr^{-1}}$. This constraint already suggests that galactic nuclei in the nearby universe are relatively spherical, rather than triaxial, because the expected disruption rate is significantly higher in the latter case (Merritt & Poon 2004).

As described in §2.4, the spectral signature of the equatorial stellar debris is a transient spectrum of broad emission lines shifted in wavelength relative to the host galaxy. We do not expect forbidden lines (e.g. [NII], [SII], [OI], [OIII]) to be present, because the density in the unbound material is too high.[7] For several reasons, it is not surprising that this spectral signature has yet to be seen. First, the tidal flare candidates are likely from relatively high-mass BHs; in those events, the unbound stellar debris subtends a small solid angle (eq. [2.25]) and so the emission lines should be $\lesssim 1\%$ of the bulge luminosity. Future optically-selected tidal flares are more likely to show detectable lines. It is also important to note that most standard searches for AGN in optical/infrared surveys use forbidden lines to identify nuclear activity, and have not specifically looked for faint, broad lines offset from the host galaxy's lines. Tidal disruption events may yet be hiding in archival spectroscopic data.

We predict that outflows during the super-Eddington fallback phase have peak optical luminosities of $\sim 10^{43} - 10^{44}\,\mathrm{erg\,s^{-1}}$ and characteristic decay timescales of ~ 10 days (Figs. 2.4 & 2.11). These events are sufficiently bright that a natural concern is whether our predictions can already be ruled out by optical supernova searches such as the Supernova Legacy Survey and Stripe 82 in the Sloan Digital Sky Survey. Although a careful search of archival data is clearly warranted, we do not believe that current observations are necessarily that constraining, for two reasons. First, the outflow phase can be relatively brief and many survey cadences may be insufficient to find these events. Most importantly, however, tidal flares could be readily mistaken for AGN and thus discarded. Indeed, most supernova searches discard galactic nuclei in order to avoid confusion with AGN and optimize their probability of detecting supernovae.

Optically detecting a tidal flare may require disentangling the flare emission from that of the BH's host galaxy. For example, at a distance of 300 Mpc, a ground-based optical survey with a resolution ~ 1" should just be able to resolve a kiloparsec-sized bulge. Bulges are found to be ~ 700 times more massive than their central BHs (Häring & Rix 2004). Super-Eddington outflows typically shine at $10^{43} - 10^{44}\,\mathrm{erg\,s^{-1}}$ (see Fig. 2.4), so this phase should be at least as bright as the host galaxy and readily detectable given sufficient attention to

[7] The 5007 Å line of [OIII] does appear at late times for the lowest $M_{\rm BH}$ and $R_{\rm p}$, where the densities fall below this ion's critical density after about a year.

sources in galactic nuclei and careful screening to rule out an unsteady AGN. By contrast, the typical optical luminosity of the accretion disk itself is $10^{40} - \text{few} \times 10^{41}\,\text{erg}\,\text{s}^{-1}$ (see Fig. 2.3). The accretion disk would thus brighten the host bulge by only a few percent. Photometric detections of late-time flares will require very careful bulge subtraction. As a result, shallow, wide-area surveys such as PTF are more likely to find the late-time disk emission than narrow deep surveys such as the Pan-STARRS MDS. As an additional complication to finding tidal flares, optical extinction in galactic nuclei can be significant (although less than at UV or soft X-rays); as a result, some fraction of optical tidal flares may not be detectable due to obscuration. Infrared surveys such as SASIR, which are also very sensitive to tidal disruption events (Table 2.1), will be particularly immune to the effects of obscuration.

Type II supernovae in the nuclear regions of galaxies may be confused with tidal disruption events, as both have quite blue colors. For sources at ~ 300 Mpc, we estimate that such supernovae will occur within ~ 1" of the galactic nucleus at a rate of $\sim 10^{-4}\,\text{yr}^{-1}$, perhaps an order of magnitude more often than tidal disruption events; at higher redshift the contamination from supernovae will be more significant, but follow-up imaging at high spatial resolution and/or spectroscopic follow-up should help classify these events and distinguish tidal flares from nuclear supernovae.

2.6.4 Astrophysical Applications

Theoretical calculations of the tidal disruption rate per galaxy, γ, vary substantially and can have complicated dependences on BH mass and pericenter distance (e.g., Magorrian & Tremaine 1999). The rate model we implement is consistent with theoretical estimates and is sufficiently simple that the reader can easily scale our results to different model parameters (eq. [2.31]). We have assumed that the rate at which stars enter the disruption zone ($R_\text{S} < R_\text{p} < R_\text{T}$) is independent of BH mass, and constant with $\ln R_\text{p}$. A star may venture deep into the disruption zone ($R_\text{p} \sim R_\text{S}$) on its last orbit if its change in angular momentum over one dynamical time is large enough—at least of order the maximum angular momentum for disruption. This condition is satisfied in the full loss cone regime, and marginally satisfied in the outskirts of the diffusive regime. For realistic stellar density profiles, the disruption rate is dominated by the boundary between these two regimes (e.g., Alexander 2005), so many stars probably do take large enough angular momentum steps to arrive at $R_\text{p} \ll R_\text{T}$. In the diffusive regime, the disruption rate per $\ln R_\text{p}$ varies weakly with $\ln R_\text{p}$, consistent with our assumption in §2.5. Given the sensitivity of the optical-infrared emission from tidal flares to R_p, upcoming surveys should significantly improve our knowledge of the stellar dynamics in galactic nuclei.

Our results demonstrate that optical transient surveys will be quite sensitive to the lowest mass BHs in galactic nuclei, both because of the outflows produced when the fallback rate is super-Eddington and because of the large angle subtended by the equatorial stellar debris. Such BHs are otherwise difficult to detect because their host galaxies are faint, it is difficult to resolve their small spheres of influence, and even when they are active, their Eddington luminosities are low. The space density of $10^5 - 10^6 M_\odot$ BHs and the stellar

density profiles in the galaxies they inhabit are only moderately well-constrained at present (e.g., Greene & Ho 2007), as is the role of tidal disruption in growing these BHs. Optical searches for tidal flares should thus prove to be a powerful probe of low-mass BHs and their host galaxies.

Acknowledgments

We thank Josh Bloom, Phil Chang, Eugene Chiang, Luis Ho, and Enrico Ramirez-Ruiz for helpful discussions; we also thank Phil Hopkins for providing the black hole mass function in tabular form; and we thank Gary Ferland, Ryan Porter and Peter van Hoof at the Cloudy discussion board for rapid and helpful replies to our questions. LES and EQ are supported in part by the David & Lucile Packard Foundation and NASA Grant NNG06GI68G. LES dedicates this work to the memory of two shining stars, Sandra Strubbe and Doug Baker.

Chapter 3

Spectroscopic Signatures of the Tidal Disruption of Stars by Massive Black Holes

Abstract

During the tidal disruption of a main sequence star by a massive black hole (BH) having mass $M_{\rm BH} \lesssim 10^7 M_\odot$, the stellar debris is expected to fall back to the BH at a rate well above the Eddington rate. Some fraction of this gas is predicted to be blown away from the BH, producing an optically bright flare of radiation. We predict the spectra and spectral evolution of tidal disruption events, focusing on the signatures produced by photoionized gas outside the photosphere of this super-Eddington outflow. We show that the spectrum of such an outflow should show absorption lines that are strongly blueshifted relative to the host galaxy, are typically very broad ($0.01 - 0.1c$), and are most prominent at ultraviolet wavelengths (e.g., C IV, Lyman α, O VI) at early times ($\lesssim$ 1 month for a $\sim 10^6$ $M_\odot$ BH). There may also be optical absorption lines of hydrogen and He II if there is a lower velocity component to the outflow ($\lesssim$ 0.01 c). At later times, the outflow falls out of thermal equilibrium and the continuum emission likely hardens—the absorption lines will then primarily be in the soft X-rays.

Supernovae in galactic nuclei are a significant source of confusion in optical surveys for tidal disruption events: we estimate that nuclear Type Ia supernovae are two orders of magnitude more common than tidal disruption events at $z \sim 0.1$ for ground-based surveys. Nuclear Type II supernovae occur at a comparable rate but can be excluded by pre-selecting red galaxies. The contamination from nuclear supernovae can be reduced to a manageable level by using high-resolution follow-up imaging with adaptive optics or the Hubble Space Telescope. Our predictions should help optical transient surveys capitalize on their potential for discovering tidal disruption events.

3.1 Introduction

A massive black hole (BH) at the center of a galaxy can tidally disrupt stars that pass within a radius $R_{\rm T} \sim R_\star (M_{\rm BH}/M_{\rm star})^{1/3}$ of it, where $M_{\rm BH}$ and $M_{\rm star}$ are the mass of the BH and star[1], respectively, and $R_\star$ is the radius of the star. For solar-mass stars, $R_{\rm T}$ lies outside the BH's event horizon for $M_{\rm BH} \lesssim 10^8 M_\odot$; in these systems, a fraction of the stellar debris is expected to flow back towards the BH following disruption, releasing a flare of radiation. Although the rate of tidal disruption events per galaxy is uncertain, it is likely $\sim 10^{-6} - 10^{-3}$ per year (e.g., Magorrian & Tremaine 1999; Wang & Merritt 2004; Donley et al. 2002).

Observing and studying such flares has the potential to inform our understanding of accretion physics, the mass function of BHs, and the dynamics of stars in the nuclei of galaxies. To date, several candidate events have been discovered, and many more are likely to be found in the coming years. A handful of candidates were discovered in soft X-rays by the ROSAT All-Sky Survey and XMM-Newton Slew Survey, and several more candidates have been discovered in the ultraviolet (UV) by GALEX (Komossa 2002; Gezari et al. 2008, 2009); these observations likely probe emission from an accretion disk close to the BH. Searches with GALEX are ongoing, and several new wide-field, high-cadence optical transient surveys have recently started or are planned: the Palomar Transient Factory (PTF), Pan-STARRS, and the Large Synoptic Survey Telescope (LSST).

In Strubbe & Quataert (2009), we argued that optical surveys have the potential to discover tens to hundreds of tidal disruption events per year. Bright optical emission occurs when stellar debris is unbound by the intense radiation pressure produced by the debris falling back to the BH at a super-Eddington rate. We predicted that this outflow produces a flare as bright as a supernova, $\sim 10^{43} - \text{few} \times 10^{44}\,\text{erg}\,\text{s}^{-1}$, that lasts for days to weeks. These optically luminous flares may be detectable out to $z \sim 1$ (and perhaps beyond). However, optical transient surveys are finding and will find *many* bright transients close to the centers of galaxies (e.g., active galactic nuclei and supernovae). Identifying tidal disruption events amid an array of far more common transient phenomena thus poses a substantial challenge. Observational follow-up is crucial: detailed multi-wavelength light curves, high-resolution imaging (to determine that events are truly nuclear), and spectroscopy are all required. In the long term, the last of these has the potential to be the most definitive signature of a tidal disruption event.

In this paper, we predict the optical–X-ray spectroscopic signatures of tidal disruption events as a function of time, focusing on the outflows produced when the fallback rate is super-Eddington. In such outflows, gas outside the electron scattering photosphere emits photons and absorbs photons from deeper in, producing a spectrum that can contain emission and absorption features. A separate source of spectroscopic features can arise at late times, after the outflow subsides, from the half of the star that gained energy upon disruption and is escaping from the BH in the star's original orbital plane. The surface of that equatorial material is irradiated by the accretion disk, producing broad emission lines (mostly

[1]We reserve the symbol M_* for the stellar mass of a galaxy (§3.4).

hydrogen) offset in velocity from the galactic lines (Strubbe & Quataert 2009). Detecting these lines would also be a strong confirmation of a tidal disruption event, but they are usually substantially fainter than the spectral diagnostics presented here and so will be more difficult to observe.

The remainder of the paper is organized as follows: in §3.2, we review the physics of super-Eddington outflows produced during tidal disruption events and describe how we use the photoionization code Cloudy to calculate the spectral lines of the outflow and how we calculate the line profiles. We also critically assess when the assumption of thermal equilibrium for the outflow's emission employed by Strubbe & Quataert (2009) is valid (§3.2.2). In §3.3 we describe our primary spectroscopic predictions. We then briefly estimate the rate of supernovae in the nuclei of galaxies (§3.4), since nuclear supernovae are one of the primary sources of confusion in optical searches for tidal disruption events. Finally, in §3.5 we discuss our results and their implications for observing and identifying tidal disruption events.

3.2 Super-Eddington Outflows

3.2.1 Summary of Basic Properties

We summarize theoretical expectations for the physics of tidal disruption events. Following a star's disruption, roughly half of the stellar debris becomes bound to the BH, falls back to pericenter, and shocks; the rate of fallback is (Rees 1988; Phinney 1989)

$$\dot{M}_{\rm fallback} \simeq \frac{1}{3}\frac{M_{\rm star}}{t_{\rm fallback}}\left(\frac{t}{t_{\rm fallback}}\right)^{-5/3} \tag{3.1}$$

where

$$t_{\rm fallback} \simeq 20 M_6^{5/2} R_{\rm p,3R_S}^3 r_\star^{-3/2}\,{\rm min}$$

is the period of the most bound debris, the BH mass is $M_{\rm BH} \equiv M_6 \times 10^6 M_\odot$, the pericenter distance of the star's orbit is $R_{\rm p}$, $R_{\rm p,3R_S} \equiv R_{\rm p}/3R_{\rm S}$ (where $R_{\rm S}$ is the Schwarzschild radius), and the stellar radius $r_\star \equiv R_\star/R_\odot$. For $M_{\rm BH} \lesssim$ few $\times 10^7 M_\odot$, the fallback rate predicted by equation (3.1) can be much greater than the Eddington rate $\dot{M}_{\rm Edd}$ for a period of weeks to years; here $\dot{M}_{\rm Edd} \equiv 10 L_{\rm Edd}/c^2$, $L_{\rm Edd}$ is the Eddington luminosity, and 0.1 is the fiducial efficiency of converting accretion power to luminosity.

While the fallback rate is super-Eddington, the stellar gas returning to pericenter is so dense that the photons produced in the shock are unable to escape and cool the gas; in particular, the time for photons to diffuse out of the gas is longer than both the inflow time in the disk and the dynamical time characteristic of an outflow. The gas is likely to form an advective accretion disk accompanied by powerful outflows (e.g., King & Pounds 2003; Ohsuga et al. 2005).

In Strubbe & Quataert (2009), we developed a simple model to describe the outflowing gas (see also related estimates in King & Pounds 2003; Rossi & Begelman 2009). We assume

the outflowing gas is launched from $\sim R_{\rm L} \equiv 2R_{\rm p}$ at a rate

$$\dot{M}_{\rm out} \equiv f_{\rm out}\dot{M}_{\rm fallback} \tag{3.2}$$

with a terminal velocity

$$v_{\rm wind} \equiv f_v v_{\rm esc}(R_{\rm L}), \tag{3.3}$$

which is typically $1-10\%$ of the speed of light. Radiation hydrodynamical simulations of super-Eddington accretion show that the density and velocity structure of the outflowing gas varies with angle, with higher speed outflows along the pole (e.g., Ohsuga et al. 2005); in the tidal disruption context, the outflow properties may also vary with time. To account for variations with viewing angle, we consider values of $f_{\rm out}$ ranging from 0.01 to 0.3, with $f_{\rm out} = 0.1$ as our fiducial value, and values of f_v ranging from 0.1 to 1, with $f_v = 1$ as our fiducial value. We approximate the outflow's geometry as spherical, with a density profile

$$\rho(r,t) \simeq \frac{\dot{M}_{\rm out}(t - r/v_{\rm wind})}{4\pi r^2 v_{\rm wind}} \tag{3.4}$$

inside the outflow where $r \lesssim R_{\rm edge} \equiv v_{\rm wind}t$. For $r \ll R_{\rm edge}$, the density varies as $\rho(r,t) \sim \dot{M}_{\rm out}(t)/4\pi r^2 v_{\rm wind}$. When $t \gtrsim$ few $\times\, t_{\rm fallback}$, the density increases with radius approaching $R_{\rm edge}$: most of the mass is near the edge, within a shell of thickness $\Delta r_{\rm shell}$, so that

$$\rho(R_{\rm edge},t) \sim \frac{\frac{1}{2}f_{\rm out}M_{\rm star}}{4\pi R_{\rm edge}^2 \Delta r_{\rm shell}}\,. \tag{3.5}$$

Since most of the gas was expelled during a period lasting $\sim t_{\rm fallback}$, $\Delta r_{\rm shell}$ is at least $\sim v_{\rm wind}t_{\rm fallback}$; to account for a possible variation in outflow velocity during the period when most of the wind is launched, we assume that the wind speed varies by $\Delta v_{\rm wind}/v_{\rm wind} \sim 10\%$, so that $\Delta r_{\rm shell} \sim \max(v_{\rm wind}t_{\rm fallback}, 0.1 v_{\rm wind}t)$. The exact magnitude of $\Delta v_{\rm wind}$ is uncertain, but accounting for this systematic variation is important because otherwise the shell is unphysically narrow and dense at late times.

At most wavelengths, the dominant opacity in the outflow is electron scattering. The outflow is optically thick to electron scattering out to a radius $R_{\rm ph,es}$, the electron scattering photosphere, at which $R_{\rm ph,es}\rho(R_{\rm ph,es})\kappa_{\rm es} \sim 1$, where $\kappa_{\rm es}$ the opacity to electron scattering:

$$R_{\rm ph,es} \simeq 10 f_{\rm out} f_v^{-1} \left(\frac{\dot{M}_{\rm fallback}}{\dot{M}_{\rm Edd}}\right) R_{\rm p,3R_S}^{1/2} R_{\rm S}\,. \tag{3.6}$$

Because they are trapped by electron scattering, photons produced in the shock cool adiabatically as the gas expands in the outflow. In Strubbe & Quataert (2009) we assumed that the gas and photons would be in thermal equilibrium at the shock so that the outflowing photons would have a blackbody spectrum, given by

$$\nu L_\nu = 4\pi^2 R_{\rm ph,es}^2 \nu B_\nu(T_{\rm ph,es}) \tag{3.7}$$

where $T_{\rm ph,es}$ is the temperature at the electron scattering photosphere. The flow remains supported by radiation pressure and thus adiabatic expansion causes the temperature in the outflow to scale as $T \propto \rho^{1/3}$. In thermal equilibrium, the temperature of the gas and radiation at the shock ($T_{\rm eq}$) are determined by $aT_{\rm eq}^4 \simeq u_{\rm pre,gas}$, i.e., the post-shock photon energy density is approximately equal to the bulk kinetic energy density of the pre-shock gas. We approximate that the gas falls back to pericenter spherically, so that $u_{\rm pre,gas} \sim \dot{M}_{\rm fallback} v_{\rm esc,L}/4\pi R_{\rm L}^2$, where $v_{\rm esc,L}$ is the escape velocity of the gas at $R_{\rm L}$. The temperature at $R_{\rm ph,es}$ in thermal equilibrium is thus

$$T_{\rm ph,es} \sim 2 \times 10^5\,{\rm K} \left(\frac{f_v}{f_{\rm out}}\right)^{1/3} \left(\frac{\dot{M}_{\rm fallback}}{\dot{M}_{\rm Edd}}\right)^{-5/12} M_6^{-1/4} R_{\rm p,3R_S}^{-7/24}. \quad (3.8)$$

After weeks to months, the outflow finally becomes optically thin to electron scattering, revealing the accretion disk close to the BH. The accretion disk's spectrum is a multicolor blackbody with temperatures $\sim 10^5\,{\rm K}$, described in more detail in Strubbe & Quataert (2009). Eventually, after a time

$$t_{\rm Edd} \simeq 0.1\, M_6^{2/5} R_{\rm p,3R_S}^{6/5} m_\star^{3/5} r_\star^{-3/5}\,{\rm yr} \quad (3.9)$$

(where $m_\star \equiv M_{\rm star}/M_\odot$), the mass fallback rate decreases below the Eddington rate, and radiation pressure is no longer strong enough to unbind new gas. The previously expelled gas continues to expand outwards, becoming a thin shell located at $\sim R_{\rm edge}$ with a thickness $\Delta r_{\rm shell}$ and a density given in equation (3.5). From some viewing angles, the accretion disk will continue to be seen through this shell, with the exact covering fraction of the shell depending on the geometry of the outflow at early times, which is somewhat uncertain.

3.2.2 The Applicability of Thermal Equilibrium

Equations (3.7) and (3.8) assume that the gas and radiation are thermally well-coupled from the shock at $\sim R_{\rm p}$ to the outflow's electron scattering photosphere at $R_{\rm ph,es}$. However, the post-shock gas and radiation may not have time to reach thermal equilibrium before advecting away from the shock. Here we quantitatively assess the applicability of thermal equilibrium drawing an analogy to the radiation-mediated shocks present during supernovae and shock-breakout (e.g., Katz et al. 2010).

In local thermal equilibrium (LTE), the temperature of the gas and radiation are given by $T_{\rm eq}$, where $aT_{\rm eq}^4 \simeq u_{\rm pre,gas}$ (see the text before eq. [3.8]). The dominant continuum emission process is free-free emission. The time to reach thermal equilibrium $t_{\rm LTE}$ is determined by the timescale for free-free emission in the post-shock plasma to produce the number density of photons required for thermal equilibrium. Prior to $\sim t_{\rm LTE}$, the gas and radiation are instead in Compton equilibrium at a temperature $T_{\rm shock}$ that is substantially larger than $T_{\rm eq}$ (Katz et al. 2010). The shock jump conditions imply that the velocity falls and the density of gas rises by a factor of 7 as the gas moves from pre-shock to post-shock. Using equation (13)

from Katz et al. (2010), we then find that the time for the post-shock plasma to thermalize, in units of the local dynamical time $t_{\rm dyn} = R_{\rm L}/v_{\rm esc,L}$, is given by[2]

$$\begin{aligned}\frac{t_{\rm LTE}}{t_{\rm dyn}} &\sim 400\, M_6^{-5/8} R_{\rm p,3R_S}^{-47/16} \left(\frac{r_\star}{m_\star}\right)^{9/8} \left(\frac{t}{10\,{\rm day}}\right)^{15/8} \\ &\sim 0.9\, M_6^{109/48} \left(\frac{R_{\rm p}}{R_{\rm T}}\right)^{43/16} m_\star^{-9/8} r_\star^{-27/16} \left(\frac{t}{t_{\rm fallback}}\right)^{15/8}. \end{aligned} \quad (3.10)$$

If $t_{\rm LTE} < t_{\rm dyn}$, the assumption of blackbody emission in equations (3.7) and (3.8) is reasonable. Equation (3.10) shows that this is generally true at early times for $M_{\rm BH} \lesssim 10^6 M_\odot$ and any stellar pericenter distance, and for $M_{\rm BH} \lesssim$ few $\times\, 10^6 M_\odot$ and $R_{\rm p} \sim 3R_{\rm S}$. However, for more massive BHs ($M_{\rm BH} \sim 10^7 M_\odot$), the assumption of thermal equilibrium is probably poor for $t \gtrsim t_{\rm fallback}$, when most of the stellar debris returns to pericenter. Moreover, for a given BH mass and stellar pericenter distance, the post-shock plasma is not in thermal equilibrium after a time

$$\begin{aligned} t_{\rm non-therm} &\sim 0.5\, M_6^{1/3} R_{\rm p,3R_S}^{47/30} \left(\frac{m_\star}{r_\star}\right)^{3/5} {\rm day} \\ &\sim 10\, M_6^{-32/45} \left(\frac{R_{\rm p}}{R_{\rm T}}\right)^{47/30} \left(\frac{m_\star}{r_\star}\right)^{3/5} {\rm day}. \end{aligned} \quad (3.11)$$

Equation (3.11) shows that the assumption of thermal blackbody emission is likely reasonable for a few weeks for $M_{\rm BH} \sim 10^6 M_\odot$ and $R_{\rm p} \sim R_{\rm T}$. For smaller $R_{\rm p}$, thermal equilibrium breaks down earlier, but events with $R_{\rm p} \sim R_{\rm T}$ are predicted to dominate the rates and are thus in practice probably the most important (Fig. 12 of Strubbe & Quataert 2009). At times $t \gtrsim t_{\rm non-therm}$, the temperature at the shock, $T_{\rm shock}$, is tens to hundreds of keV, scaling as $R_{\rm p,3R_S}^{-4}$ for mildly relativistic fallback speeds. The radiation emitted at the electron scattering photosphere will be cooler than this by a factor of $\sim (R_{\rm ph,es}/R_{\rm L})^{2/3}$ due to adiabatic expansion. Compton upscattering also likely gives the radiation a power-law spectrum. We will discuss the effects of this non-blackbody emission in §§3.3.1 and 3.5, but defer a detailed calculation of the non-LTE spectrum to future work.

It is important to note that if the gas and radiation are not able to thermalize close to the shock (i.e., for $t \gtrsim t_{\rm non-therm}$), they are unlikely to thermalize further out in the outflow instead: the equilbrium photon number density falls with radius, as ρ, but the equilibrium free-free emissivity falls faster, as $\rho^{11/16}$, so there is even less time to come into thermal equilibrium at larger radii.

[2]This estimate of $t_{\rm LTE}$ is about 100 times shorter than the most naïve estimate of the thermalization time, $\sim (\alpha_{\rm ff}^R c)^{-1}$, where $\alpha_{\rm ff}^R$ is the Rosseland mean absorption coefficient for free-free interactions. The time $t_{\rm LTE}$ is that associated with waiting for the gas to emit photons rather than waiting for it to absorb photons already present. The large numerical difference between $t_{\rm LTE}$ and $\sim \alpha_{\rm ff}^R c$ is primarily due to different weighting of frequencies in the averaging; in the correct calculation, emission of low-frequency photons dominates (Katz et al. 2010), while in $\alpha_{\rm ff}^R$, absorption of photons close to the blackbody peak dominates.

3.2.3 Spectroscopic Calculations

The spectrum of the outflow will be imprinted with spectral lines produced by the outer layers of gas between the photosphere and the edge of the outflow at $R_{\rm edge}$. The photosphere is initially determined by the outflow itself ($R_{\rm source} = R_{\rm ph,es}$) but at later times as the outflow subsides and becomes optically thin, the photosphere is set by the accretion disk, with $R_{\rm source} = R_{\rm disk}$. The gas outside $R_{\rm source}$ absorbs photons released deeper in, through photoionization and bound-bound transitions, creating absorption and emission features. The outer gas is highly ionized by the central source, and maintains photoionization equilibrium so long as the recombination time is shorter than the expansion time: $t_{\rm rec} \sim (n_e \alpha_{\rm rec})^{-1} < t$. Here $\alpha_{\rm rec}$ is the recombination coefficient, $\sim 2 \times 10^{-13}\,{\rm cm^3\,s^{-1}}$ for hydrogen at $30,000\,{\rm K}$ and typically larger for heavier species.

Early on, most absorption takes place at $r \sim R_{\rm ph,es}$, where the gas is always in photoionization equilibrium, since

$$\begin{aligned} \frac{t_{\rm rec}(R_{\rm ph,es})}{t} &\sim [n_e(R_{\rm ph,es})\alpha_{\rm rec}]^{-1} \\ &\sim 10^{-5}\frac{f_{\rm out}}{f_v} M_6^{5/3} R_{\rm p,3R_S}^{5/2} \frac{m_\star}{r_\star} \left(\frac{t}{10\,{\rm day}}\right)^{-8/3} . \end{aligned} \tag{3.12}$$

At late times, most of the mass in the outflow resides in a shell at $r \sim R_{\rm edge}$, which dominates the absorption. There, the gas falls out of photoionization equilibrium after a few months to a few years, since

$$\begin{aligned} \frac{t_{\rm rec}(R_{\rm edge})}{t} &\sim [n_e(R_{\rm edge})\alpha_{\rm rec}]^{-1} \\ &\sim 3 \times 10^{-3}\frac{f_v^3}{f_{\rm out}} \frac{M_6^{5/2} R_{\rm p,3R_S}^{3/2}}{m_\star r_\star^{3/2}} \left(\frac{t}{10\,{\rm day}}\right) , \end{aligned} \tag{3.13}$$

when $\Delta r_{\rm shell} \sim v_{\rm wind} t_{\rm fallback}$; $t_{\rm rec}$ increases even more later when $\Delta r_{\rm shell} \sim 0.1 v_{\rm wind} t$.

We determine the ionization and opacity structure of the gas outside $R_{\rm source}$ by performing photoionization calculations with version 08.00 of the publicly available code Cloudy, last described by Ferland et al. (1998). To determine the spectrum, we then post-process Cloudy's output to account for Doppler shifts by the outward motion of the gas. We will only show results below for times at which $t_{\rm rec} \lesssim t$ so that photoionization equilibrium is a reasonable approximation.

For calculating line profiles, it is useful to divide the outflow into two parts: at times $t \lesssim t_{\rm Edd}$, when the outflow is being continuously driven, there is a radially extended outflow from $R_{\rm source}$ to $\sim R_{\rm edge}$. Because $R_{\rm edge}$ is generally much larger[3] than $R_{\rm source}$, the line-of-sight

[3] In Strubbe & Quataert (2009), we describe an early ∼day-long phase for small $M_{\rm BH}$ and small $R_{\rm p}$ during which $R_{\rm ph,es} \sim R_{\rm edge}$; although there may be interesting spectroscopic features during this phase, we focus on later times when the physics of the escaping photons is more secure.

velocities of the gas span a wide range, which causes absorption lines to be strongly velocity-broadened. At times $t \gtrsim$ few $\times\, t_{\rm fallback}$, there is also a narrow, denser shell at $r \sim R_{\rm edge}$, which contains most of the mass (because most of the mass is unbound at $\sim t_{\rm fallback}$). In the shell, thermal broadening may dominate over velocity broadening. We first qualitatively describe the evolution of the spectrum produced by these two parts of the outflow, and then explain in more detail how we calculate the absorption and emission line profiles.

Three phases of evolution

For $M_{\rm BH} \lesssim$ few $10^7\, M_\odot$, the fallback rate is super-Eddington and the outflow is optically thick to electron scattering for a few weeks to months after disruption. Photons released from $R_{\rm source} = R_{\rm ph,es}$ with the blackbody spectrum in equation (3.7) (perhaps with an additional X-ray power-law tail; §3.4) photoionize the outer layers of gas between $R_{\rm source} = R_{\rm ph,es}$ and $R_{\rm edge}$, which have a density profile given by equation (3.4). This gas spans a wide range in radii, and so produces a spectrum of broad absorption lines, whose profiles are described in §3.2.3; when $t \gtrsim$ few $\times\, t_{\rm fallback}$, there are also narrower absorption lines, described in §3.2.3. The emission lines are calculated as described in §3.2.3.

At later times, the fallback rate diminishes and the electron scattering photosphere of the outflow moves inward. The entire outflow becomes optically thin to electron scattering $\sim$ weeks to months after disruption, but it continues to be driven until $\dot{M}_{\rm fallback}$ falls below $\dot{M}_{\rm Edd}$, which can be somewhat later ($t_{\rm Edd}$; eq. 3.9). Deep inside the outflow, accretion onto the BH proceeds via a thin disk, which emits a multicolor blackbody spectrum peaking close to $\sim 10^5\,{\rm K}$ (described in Strubbe & Quataert 2009). In our calculations for these times, our input spectrum to Cloudy is the spectrum of the accretion disk (whose size is $R_{\rm source} = R_{\rm disk}$). The outflow continues to span a wide range in radii, $R_{\rm source} = R_{\rm disk} \lesssim r \lesssim R_{\rm edge}$, and so we calculate absorption line profiles as in §3.2.3, with additional absorption lines from the shell (§3.2.3) when appropriate. The emission lines are again calculated as in §3.2.3.

For $t > t_{\rm Edd}$, $\dot{M}_{\rm fallback} < \dot{M}_{\rm Edd}$ and the shocked gas at pericenter can cool efficiently; essentially all of the gas thus accretes through the disk rather than being blown away. The previously expelled material continues to expand out as a thin shell, with a density given by equation (3.5) and a radial thickness $\Delta r_{\rm shell}$. The shell is irradiated by the blackbody emission from the accretion disk. In many cases, the outflow is no longer in photoionization equilibrium (see eq. 3.13), but if there are places where the outflow velocity is low ($f_v \sim 0.1$), the shell can be dense enough to remain in equilibrium for up to several years. In such cases, the absorption lines are all *narrow* (§3.2.3), while the emission lines are broad (§3.2.3) and very faint.

We now describe how we calculate the line profiles for the extended part of the outflow and the shell (see also related calculations in Castor 1970, for line profiles in Wolf-Rayet star winds).

Velocity-broadened absorption lines

Cloudy outputs a table of absorption lines: each entry contains the line frequency ν_0, the species (element and ionization stage) producing the transition, and the total optical depth $\tau_{\rm stat}$ through the (stationary) layer of gas. Cloudy also outputs the density distribution $n_{\rm species}(r)$ for each species, and the temperature profile $T(r)$. The stationary optical depth is

$$\tau_{\rm stat} = \int_{R_{\rm source}}^{R_{\rm edge}} n_{\rm species}(r)\sigma_0(r)\,dr \tag{3.14}$$

$$= (\sigma_0 v_{\rm th}) \int_{R_{\rm source}}^{R_{\rm edge}} \frac{n_{\rm species}(r)}{v_{\rm th}(r)}\,dr \tag{3.15}$$

$$\equiv (\sigma_0 v_{\rm th}) I_{\rm species}\,, \tag{3.16}$$

where $\sigma_0(r)$ is the cross section of the transition at line center and $v_{\rm th}(r)$ is the thermal velocity of the gas. Because the lines provided by Cloudy are thermally broadened, the quantity $(\sigma_0 v_{\rm th})$ is independent of radius.

For simplicity, we assume that the gas flows out radially with a spatially and temporally constant velocity, $v = v_{\rm wind}$ (eq. 3.3), superposed by small thermal motions. Since the gas is optically thin at most frequencies, its temperature regulates to $T \sim 10^4 - 10^5\,{\rm K}$, leading to thermal velocities $v_{\rm th} \sim 10 - 30\,{\rm km\,s^{-1}} \ll v_{\rm wind} \sim 0.01c - 0.1c$. Because the photoionizing source—the electron scattering photosphere or accretion disk—is spatially extended, its radiation originates from impact parameters b ranging from 0 (center of the source) to $R_{\rm source}$ (edge of the source). At a given impact parameter b, our line of sight passes through gas moving at projected line-of-sight velocities $v_{\rm LOS} = v_{\rm wind}\sqrt{1-(b/r)^2}$, where r ranges from $R_{\rm source}$ to $R_{\rm edge}$.

A transition of frequency ν_0 can absorb photons of rest frequency ν at places in the wind where $v_{\rm LOS}$ satisfies $\nu = \nu_0(1 + v_{\rm LOS}/c)$. These locations are centered at radii

$$r_{\rm abs} = \frac{b}{\sqrt{1-(v_{\rm LOS}/v_{\rm wind})^2}} \tag{3.17}$$

with a small spread along the line of sight, $\Delta\ell$, due to random thermal motion of the gas:

$$\Delta\ell = r_{\rm abs}\left(\frac{v_{\rm th}(r_{\rm abs})}{v_{\rm wind}}\right)\left(\frac{r_{\rm abs}}{b}\right)^2\,. \tag{3.18}$$

Thus, for a given rest frequency and impact parameter, the optical depth to a given transition is[4]

$$\tau_b \sim (n_{\rm species}\sigma_0\Delta\ell)|_{r_{\rm abs}} \sim \frac{\tau_{\rm stat} r_{\rm abs}^3 n_{\rm species}(r_{\rm abs})}{b^2 v_{\rm wind} I_{\rm species}}\,. \tag{3.19}$$

[4]We use $\tau_{\rm stat}$ and $I_{\rm species}$ because Cloudy does not output line opacities as a function of radius.

Approximating the source as a spherical isotropic emitter, we find the overall transmitted power:

$$\nu L_\nu^{\rm trans} = \nu L_\nu^{\rm source} \times \int_0^{\pi/2} 2e^{-\tau_b} \sin\theta\cos\theta\, d\theta\,, \tag{3.20}$$

where $\sin\theta \equiv b/R_{\rm source}$. When multiple transitions contribute absorption at frequency ν, we replace τ_b above with the sum of their corresponding optical depths. We account for continuous absorption processes as well; these are generally important only for $h\nu \gtrsim 0.3\,{\rm keV}$ since the gas is so highly ionized.

Thermally-broadened absorption lines

At times $t \gtrsim$ few $\times\, t_{\rm fallback}$, the bulk of the previously expelled gas forms a thin shell at $r \sim R_{\rm edge}$, as described above in §3.2.1. While velocity broadening is the dominant broadening mechanism for absorption at $R_{\rm source} \lesssim r \lesssim R_{\rm edge}$, the line-of-sight velocity's variation with impact parameter at $r \sim R_{\rm edge}$ may become less than $v_{\rm th}$ after at most a few months if the wind velocity is close to constant in time. For example, at times when $R_{\rm source} = R_{\rm ph,es}$,

$$\frac{\Delta v_{\rm LOS}}{v_{\rm th}} \sim \left(\frac{R_{\rm ph,es}}{R_{\rm edge}}\right)^2 \left(\frac{v_{\rm wind}}{v_{\rm th}}\right)$$
$$\sim 0.03\, \frac{f_{\rm out}^2}{f_v^3} M_6^{16/3} R_{\rm p,3R_S}^{11/2} \frac{m_\star^2}{r_\star^2} \left(\frac{v_{\rm th}}{30\,{\rm km\,s^{-1}}}\right)^{-1} \left(\frac{t}{10\,{\rm day}}\right)^{-16/3}. \tag{3.21}$$

(The variation in $v_{\rm LOS}$ along the line of sight through the narrow shell is even smaller than this, by a factor of $\Delta r_{\rm shell}/R_{\rm edge}$.) Consequently, the random thermal motion may dominate the broadening of absorption lines produced in the shell; such lines are therefore *narrow*, with a linewidth $\Delta\nu = \nu_0(v_{\rm th}/c)$, and are blueshifted to $\sim \nu_0(1 + v_{\rm wind}/c)$.

If the wind speed varies in time by more than $\sim 0.1\%$, velocity broadening instead dominates over thermal broadening, leading to wider and shallower absorption lines. The wind speed variation $\Delta v_{\rm wind}$ could be substantial, e.g., $\sim 0.1 v_{\rm wind}$, but is highly uncertain, so we consider thermal broadening in the shell as a lower limit.

We run separate Cloudy calculations for the narrow shells, which give the thermally-broadened optical depth $\tau_{\rm th}(\nu)$ as a function of ν, which we blueshift by $v_{\rm wind}/c$. At times $t \lesssim t_{\rm Edd}$, we multiply the velocity-broadened spectrum described above by $e^{-\tau_{\rm th}(\nu)}$; at later times, we multiply the continuum produced at $R_{\rm disk}$ by this factor.

Emission lines

The gas at $r \gtrsim R_{\rm source}$ can also produce emission via radiative recombination and radiative decay of (collisionally or radiatively) excited atoms/ions. Because of the large velocities in the outflow, the gas is effectively optically thin to all of these photons, even at the energies of resonance lines. As a result, we can observe emission from gas having line-of-sight velocities $v_{\rm LOS} \sim -v_{\rm wind}$ up to $v_{\rm LOS} \sim +v_{\rm wind}(1 - R_{\rm source}^2/R_{\rm edge}^2)^{1/2}$; we approximate this with a

Gaussian line profile centered on the rest energy of the line, and slightly truncated on the red side. This approximation is based on analogy to Monte Carlo calculations of emission from expanding Lyman alpha blobs (Verhamme et al. 2006). We treat emission lines produced in the narrow shell the same way, since line photons emitted from essentially any part of the shell can reach us.

The large velocities in the outflow imply that the resulting emission lines are extremely broad; in most of our calculations, the emission is so spread out that the lines will be orders of magnitude fainter than the transmitted spectrum. The overall emission $\nu L_\nu^{\rm emis}$ then consists of faint continuum and very broad emission lines centered on the rest frequencies of the transitions. The observable spectrum is the sum of this emission and the transmitted light from equation (3.20), i.e.,

$$\nu L_\nu^{\rm out} = \nu L_\nu^{\rm trans} + \nu L_\nu^{\rm emis} \,. \tag{3.22}$$

Although the physical processes are similar in tidal disruption events and broad absorption line quasars (BAL QSOs), we note that tidal disruption events have substantially smaller emission line equivalent widths; this comparison is discussed further in §3.5.

3.3 Predicted Spectra

We now use the methodology of §3.2 to calculate spectra as a function of time due to the disruption of a solar-type star, varying the BH mass and pericenter distance of the stellar orbit. We assume solar abundances. We focus on solar type stars because they are among the most abundant stars at $\sim 1-10$ pc in galactic bulges, which is where most of the disrupted stars originate. The three fiducial models we consider are: $M_{\rm BH} = 10^6 M_\odot$ and $R_{\rm p} = 3R_{\rm S}$; $M_{\rm BH} = 10^6 M_\odot$ and $R_{\rm p} = R_{\rm T}$; and $M_{\rm BH} = 10^7 M_\odot$ and $R_{\rm p} = R_{\rm T}$. Our fiducial model for the outflow takes $f_v = 1$ and $f_{\rm out} = 0.1$, but later we vary these values.

To start, we assume that the outflow produces a thermal blackbody spectrum that photoionizes the surrounding gas; in §3.3.1 we consider the effects of (harder) non-thermal emission on the predicted spectra. The thermalization time estimate in §3.2.2 implies that thermal equilibrium in the outflow is maintained for $t \lesssim 0.5$ and 10 days for $M_{\rm BH} = 10^6 M_\odot$, $R_{\rm p} = 3R_{\rm S}$ and $R_{\rm p} = R_{\rm T}$, while it fails at later times; the outflow is never in thermal equilibrium for $M_{\rm BH} = 10^7 M_\odot$. Given, however, the uncertainties in the precise thermalization time we show thermal outflow models for a range of timescales.

Figure 3.1 shows our predicted spectra at various times after disruption, from the optical to the extreme ultraviolet (EUV). Significant lines in the far ultraviolet (FUV) to optical are labeled in the top and bottom panels. The top panel of Figure 3.2 shows a zoomed-in version of the $1000-2000$ Å region of the spectrum for our fiducial $M_{\rm BH} = 10^6 M_\odot$ and $R_{\rm p} = R_{\rm T}$ model. For the latter, we plot the luminosity density L_λ normalized to its maximum value over the wavelength interval $1000-2000$ Å and vertically offset different curves for clarity.

In Figures 3.1 and 3.2, we show results from $t \sim t_{\rm fallback}$, the peak of fallback and

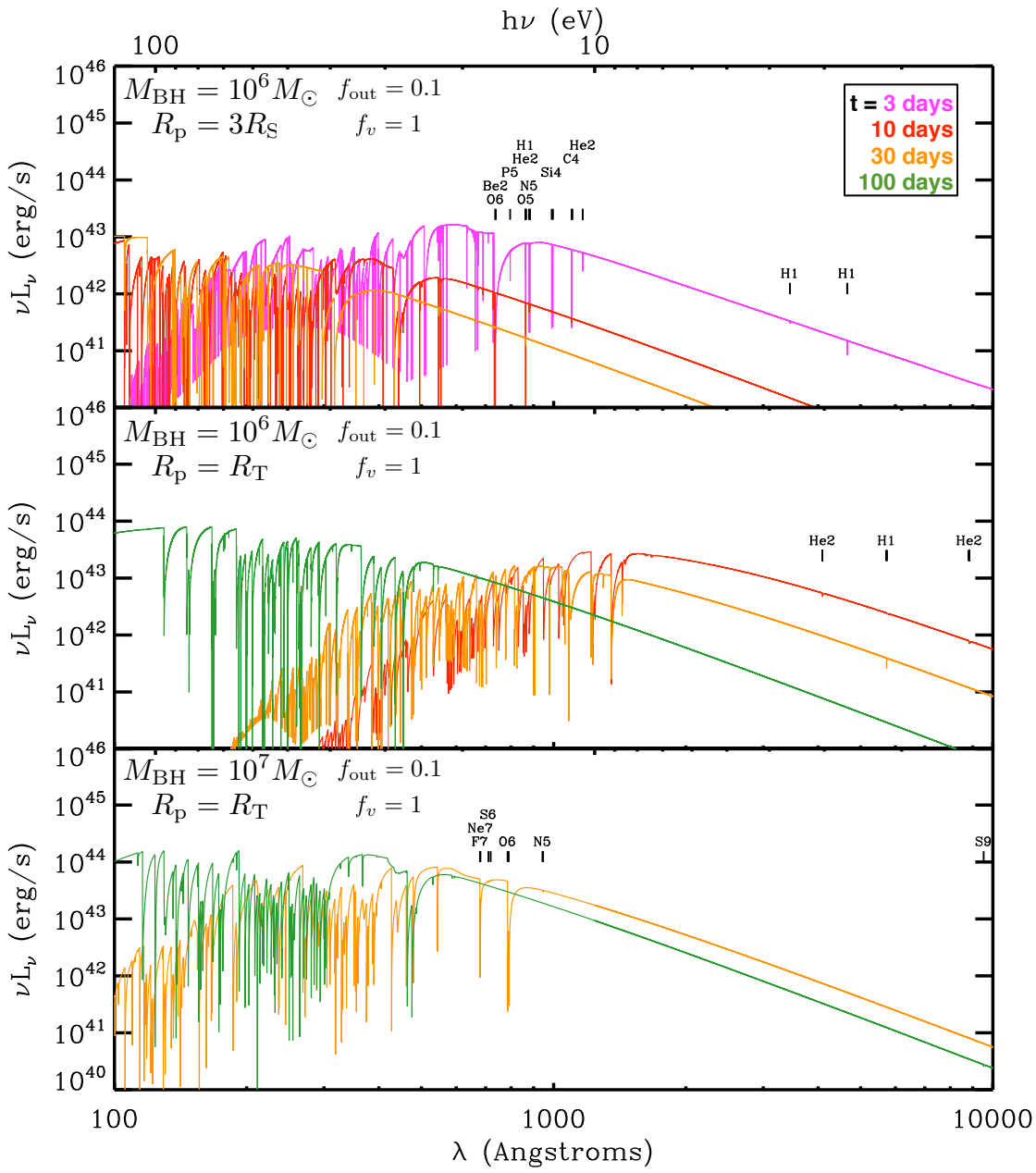

Figure 3.1: Predicted spectra for our three fiducial tidal disruption flares at several different times after disruption. Labeled tickmarks identify the blueshifted positions of the strongest long-wavelength lines. A zoomed in view of the FUV region of the middle panel is in Figure 3.2. At early times, the continuum emission in these calculations is produced by a super-Eddington outflow while at later times it is produced by the accretion disk close to the black hole. These calculations assume that the outflow is able to thermalize completely (§3.2.2); Fig. 3.4 shows results for incomplete thermalization.

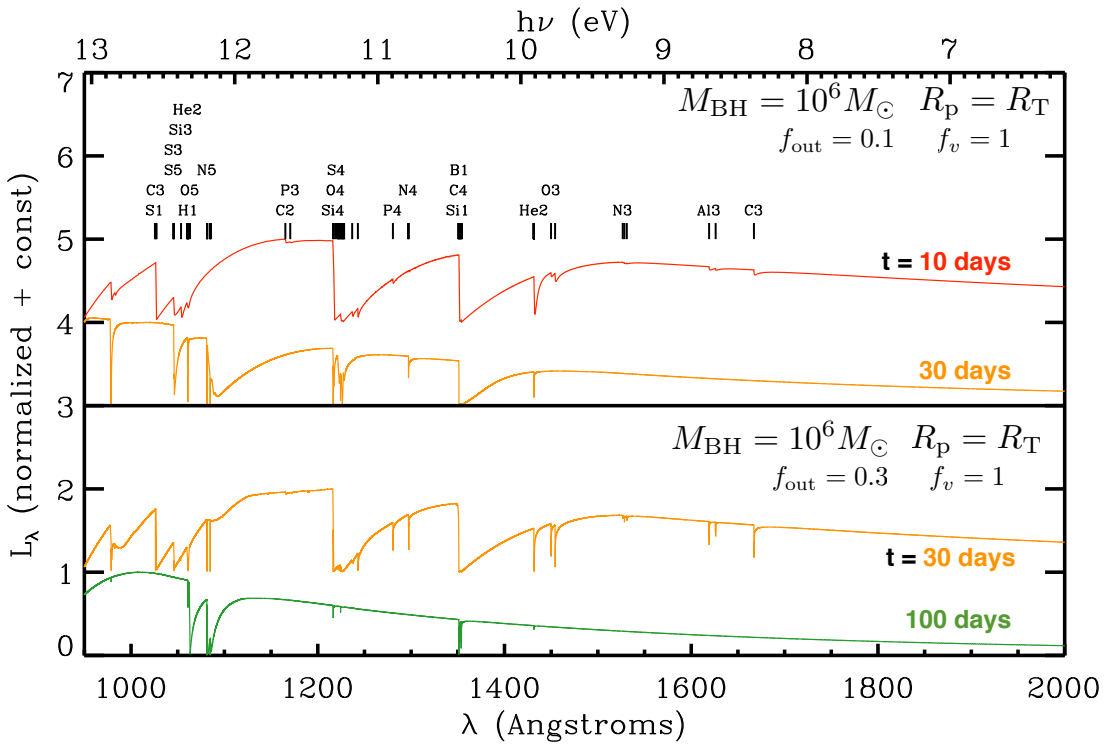

Figure 3.2: Predicted spectra varying the mass-loss rate in the outflow (via $f_{\rm out}$; eq. 3.2), focusing on the wavelength region $1000 - 2000$ Å. Each spectrum is portrayed as L_λ, normalized by its maximum value on that wavelength range, with an added integer constant to offset curves for clarity. Labeled tickmarks identify the blueshifted positions of the lines. Top panel: $M_{\rm BH} = 10^6 M_\odot$, $R_{\rm p} = R_{\rm T}$, $f_{\rm out} = 0.1$, $f_v = 1$ at $t = 10$ days and 30 days; bottom panel: same as top panel, except $f_{\rm out} = 0.3$, and $t = 30$ days and 100 days. Lines tend to be stronger for larger mass outflow rates (larger $f_{\rm out}$), because the continuum emission has a lower temperature ($T_{\rm ph,es}$).

outflow, to when the outflow shell falls out of photoionization equilibrium.[5] (The outflow's photosphere $R_{\rm ph,es}$—where most absorption takes place while the fallback rate is super-Eddington—is always in photoionization equilibrium; see beginning of §3.2.3.) Photoionization equilibrium in the shell typically fails when, or somewhat before, the fallback rate reaches the Eddington rate. More precisely, it fails at ~ 30 days for $M_{\rm BH} = 10^6 M_\odot$, $R_{\rm p} = 3R_{\rm S}$, $f_{\rm out} = 0.1$; 100 days for $M_{\rm BH} = 10^6 M_\odot$, $R_{\rm p} = R_{\rm T}$, $f_{\rm out} = 0.1$, and 200 days for $M_{\rm BH} = 10^6 M_\odot$, $R_{\rm p} = R_{\rm T}$, $f_{\rm out} = 0.3$; while $t_{\rm Edd} \sim 30$, 400 and 400 days for these three models respectively. For $M_{\rm BH} = 10^7 M_\odot$, $R_{\rm p} = R_{\rm T}$, the shell of gas at $\sim R_{\rm edge}$ is never in photoionization equilibrium, and so we do not include any contribution from the shell.

The spectral features visible in Figure 3.1 are exclusively absorption lines; the emission lines are so broadened by the large range in line-of-sight velocity that they become unde-

[5]For $M_{\rm BH} = 10^6 M_\odot$, $R_{\rm p} = 3R_{\rm S}$ (top panel), the earliest time we depict is $t = 3$ days because $R_{\rm ph,es} \sim R_{\rm edge}$ until ~ 1 day (see footnote 3).

tectable above the blackbody continuum. The outflow as a whole and the dense thin shell at $R_{\rm edge}$ typically both contribute to the absorption lines. For $M_{\rm BH} = 10^6 M_\odot$, $R_{\rm p} = 3R_{\rm S}$, the shell dominates the absorption lines at $\lambda \gtrsim 800\,\text{Å}$; the shell and outflow as a whole both contribute at a wide range of wavelengths for $10^6 M_\odot$, $R_{\rm p} = R_{\rm T}$; and the shell does not contribute for $10^7 M_\odot$, $R_{\rm p} = R_{\rm T}$ because it is never in photoionization equilibrium. The absorption lines from the extended part of the outflow are strongly blueshifted and typically (while $t < t_{\rm Edd}$) very broad[6], with linewidths of $\sim v_{\rm wind} \sim 0.01 - 0.1\,c$. Superimposed on these broad lines are the thermally-broadened narrow lines produced in the outer shell of gas, with linewidths of $\sim 10 - 30\,{\rm km\,s^{-1}}$.

Most of the absorption lines are in the UV ($\lambda \lesssim 2000\,\text{Å}$; $h\nu \gtrsim 10\,{\rm eV}$), with few features in the optical. The reason for this has two parts. First, consider the ionization parameter $U_{h\nu}$ for a species whose ionization energy is $\xi_{\rm ion} = h\nu$: because the gas density is relatively low while the incident spectrum is luminous and peaks at energy $h\nu_{\rm peak} \sim 10\,{\rm eV}$ or higher, $U_{10\,{\rm eV}} \gg 1$ and so species having $\xi_{\rm ion} \lesssim 10\,{\rm eV}$ are almost fully ionized. (For example, the ionization parameter for hydrogen is typically $U_{\rm H} \sim 10^3 - 10^5$, and hydrogen's neutral fraction is typically $10^{-8} - 10^{-10}$.) Secondly, most atoms/ions are in the ground state: the radiative decay rates are fast compared to the rates of photoionization and collisional excitation. As a result, almost all of the species present in the flow have $\xi_{\rm ion} \gtrsim h\nu_{\rm peak} \gtrsim 10\,{\rm eV}$, and members of those species are in the ground state. Transitions from the ground state have energies similar to $\xi_{\rm ion}$, which is $\gtrsim 10\,{\rm eV}$, so most spectral lines have energies $\gtrsim 10\,{\rm eV}$, i.e., in the UV rather than optical. In particular, some common prominent lines in the UV at $\lambda > 1000\,\text{Å}$ are He II (1640 Å), C IV (1548 + 1551Å), Si IV (1394 + 1403Å), O IV (1400 + 1401 + 1405 + 1407Å), N V (1239 + 1243Å), Lyman α (1216Å), and O VI (1032 + 1038Å). These are similar to the lines observed in the spectra of BAL QSOs—this is not surprising given that the physical conditions are similar. When the density is high enough for optical lines to be present (because U and $h\nu_{\rm peak}$ are lower), these optical lines are mostly the lines of H I and He II.

Figure 3.1 shows that the minimum energy/maximum wavelength of the absorption lines in the optical–UV depends both on time and on the parameters of the tidal disruption (e.g., $M_{\rm BH}$ and $R_{\rm p}$). For example, the typical absorption lines shift to shorter wavelengths at later times. The physical origin of these dependencies can be understood as follows. For all times and outflow parameters that we consider, $U_{h\nu}$ in the outflow is $\gg 1$ for $h\nu \lesssim h\nu_{\rm peak}$, and so the approximate minimum energy[7] of significant absorption lines present in the spectra is $\sim h\nu_{\rm peak}$/few. So long as the outflow is optically thick (most times depicted), the peak energy of the incident spectrum is set by the temperature of the electron scattering photosphere $T_{\rm ph,es}$. We can thus understand the variation in the typical energy of spectral lines by considering the scalings for $T_{\rm ph,es}$ in equation (3.8). For example, at a fixed time after disruption, a model with $M_{\rm BH} = 10^6 M_\odot$, $R_{\rm p} = 3R_{\rm S}$ has a hotter electron scattering

[6]The sawtooth shape of the absorption lines at early times in Figure 3.1 is a result of our assumption of spatially constant velocity (see §3.2.3); a more realistic velocity gradient would shift some absorption from $\sim h\nu_0(1 + v_{\rm wind}/c)$ towards $h\nu_0$, leading to a less abrupt change in the spectrum at $\sim h\nu_0(1 + v_{\rm wind}/c)$.

[7]High-n lines of hydrogen at wavelengths of tens of microns are also typically optically thick due to l-mixing collisions with ions.

photosphere than a model with $M_{\rm BH} = 10^6 M_\odot$, $R_{\rm p} = R_{\rm T}$. This is why the spectra for the former situation have fewer low-energy lines in Figure 3.1; $M_{\rm BH} = 10^7 M_\odot$, $R_{\rm p} = R_{\rm T}$ is yet hotter at fixed time, and so has even fewer longer wavelength lines.

These arguments also help to explain the time evolution of the spectra in Figure 3.1. During the optically thick phase (§3.2.3), the continuum radiation produced by the outflow becomes harder with time as $R_{\rm ph,es}$ moves inward, while the luminosity remains high. As a result, the lines present in the spectrum tend to have shorter wavelengths (higher energies) at later times. Once the outflow becomes optically thin, the continuum spectrum is $\sim 30\,{\rm eV} - 100\,{\rm eV}$ emission from the accretion disk, and most absorption lines have $h\nu \gtrsim 30\,{\rm eV}$ and remain very broad (§3.2.3). In some cases, narrow lines produced in the shell (§3.2.3) are superimposed on these broad lines. The lines would become purely narrow after $t_{\rm Edd}$ because nearly all of the outflow is then in a thin shell, but for our fiducial outflow parameters, the outflow falls out of photoionization equilibrium before $t_{\rm Edd}$.

As mentioned in §3.2.1, numerical simulations suggest that the velocity and density of the outflow will vary with latitude, with higher speed outflows along the pole relative to the equator (e.g., Ohsuga et al. 2005). To consider how the spectrum of a tidal disruption event may vary with viewing angle, Figure 3.3 shows spectra for different values of $f_{\rm out}$ and f_v (eqs. [3.2] and [3.3]). Significant NUV/optical lines are labeled; the lower panel of Figure 3.2 highlights the $\lambda = 1000 - 2000\,{\rm \AA}$ part of the spectrum for the $f_{\rm out} = 0.3$, $f_v = 1$ model. Because the density at $r \sim R_{\rm edge}$ is larger if the outflow is slower (smaller f_v) the shell remains in photoionization equilibrium longer for the models with $f_v = 0.1$ in Figure 3.3, for 4000 days ($M_{\rm BH} = 10^6 M_\odot$, $R_{\rm p} = R_{\rm T}$) and 1000 days ($M_{\rm BH} = 10^7 M_\odot$, $R_{\rm p} = R_{\rm T}$).

The ionization parameter $U_{h\nu}$ is large for all of these variations about our fiducial models. It is thus again the temperature of the continuum radiation $T_{\rm ph,es}$ that determines the approximate minimum energy of the spectral lines. For $f_{\rm out} = 0.3$, $T_{\rm ph,es}$ is lower than for $f_{\rm out} = 0.1$, and so there are more and deeper FUV-optical lines when $f_{\rm out}$ is larger (compare the top panel of Figure 3.3 with the middle panel of Figure 3.1, or the two panels of Figure 3.2); for $f_{\rm out} = 0.01$ (not shown), there are virtually no lines with $\lambda \gtrsim 1500\,{\rm \AA}$. Similarly, $T_{\rm ph,es}$ is lower for lower outflow velocities. For $M_{\rm BH} = 10^6 M_\odot$, $R_{\rm p} = R_{\rm T}$, $f_v = 0.1$, there are in fact many optical absorption lines (mostly hydrogen Balmer and He II) early on; for $M_{\rm BH} = 10^7 M_\odot$, $R_{\rm p} = R_{\rm T}$, $f_v = 0.1$, there are many lines at $\sim 1000 - 2000\,{\rm \AA}$, though no lines in the optical. Additionally, Hα and He II λ6560 (blended together) can be seen in emission at late times for $M_{\rm BH} = 10^6 M_\odot$, $R_{\rm p} = R_{\rm T}$, $f_v = 0.1$. Since the outflow velocity is lower, the density at $r \sim R_{\rm edge}$ is larger and so recombination happens more frequently, leading to emission lines; furthermore, the lower outflow velocity produces less broadening and so the emission lines are brighter above the blackbody continuum.

3.3.1 Implications of an X-ray Power-law

The candidate tidal disruption events discovered in the ROSAT All-Sky Survey and GALEX Deep Imaging Survey all show soft X-ray spectra (Komossa 2002; Gezari et al. 2008, 2009). However, by analogy to the observed spectra of AGN, it is possible that some

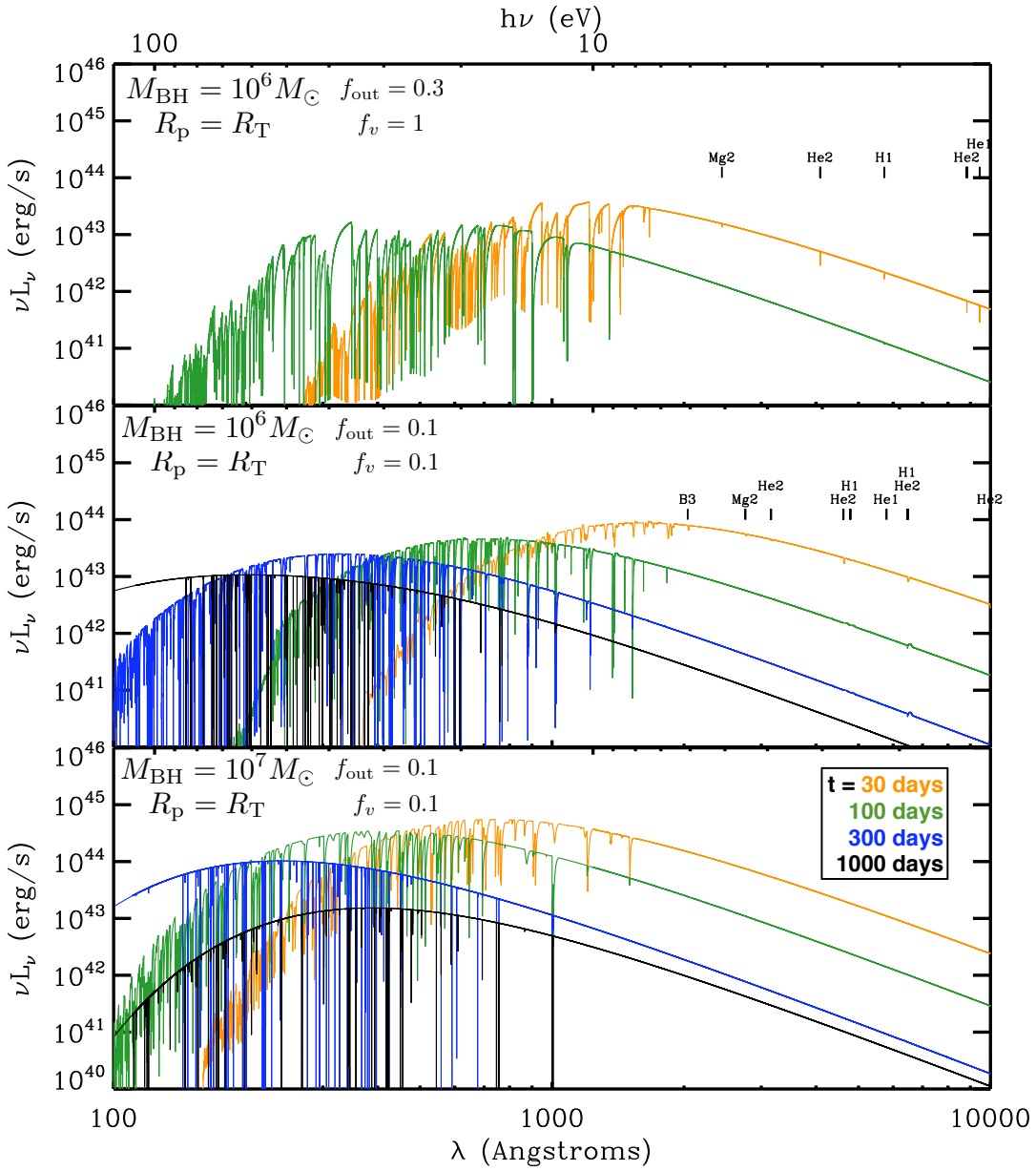

Figure 3.3: Predicted spectra showing the effects of varying the mass-loss rate (via f_{out}; eq 3.2) and outflow speed (via f_v; eq. 3.3) in the super-Eddington wind. Labeled tickmarks identify the blueshifted positions of the strongest long-wavelength lines. Slower and/or higher mass-loss rate winds have softer continuum emission and are thus more likely to produce optical or near-UV lines (compare these results with Fig. 3.1). Top panel: $M_{BH} = 10^6 M_\odot$, $R_p = R_T$, $f_{out} = 0.3$, $f_v = 1$, $t = 30$ days, 100 days; middle panel: $M_{BH} = 10^6 M_\odot$, $R_p = R_T$, $f_{out} = 0.1$, $f_v = 0.1$, $t = 30$ days, 100 days, 300 days, 1000 days; bottom panel: $M_{BH} = 10^7 M_\odot$, $R_p = R_T$, $f_{out} = 0.1$, $f_v = 0.1$, $t = 30$ days, 100 days, 300 days, 1000 days. A zoomed in view of the FUV region of the middle panel is in Figure 3.2.

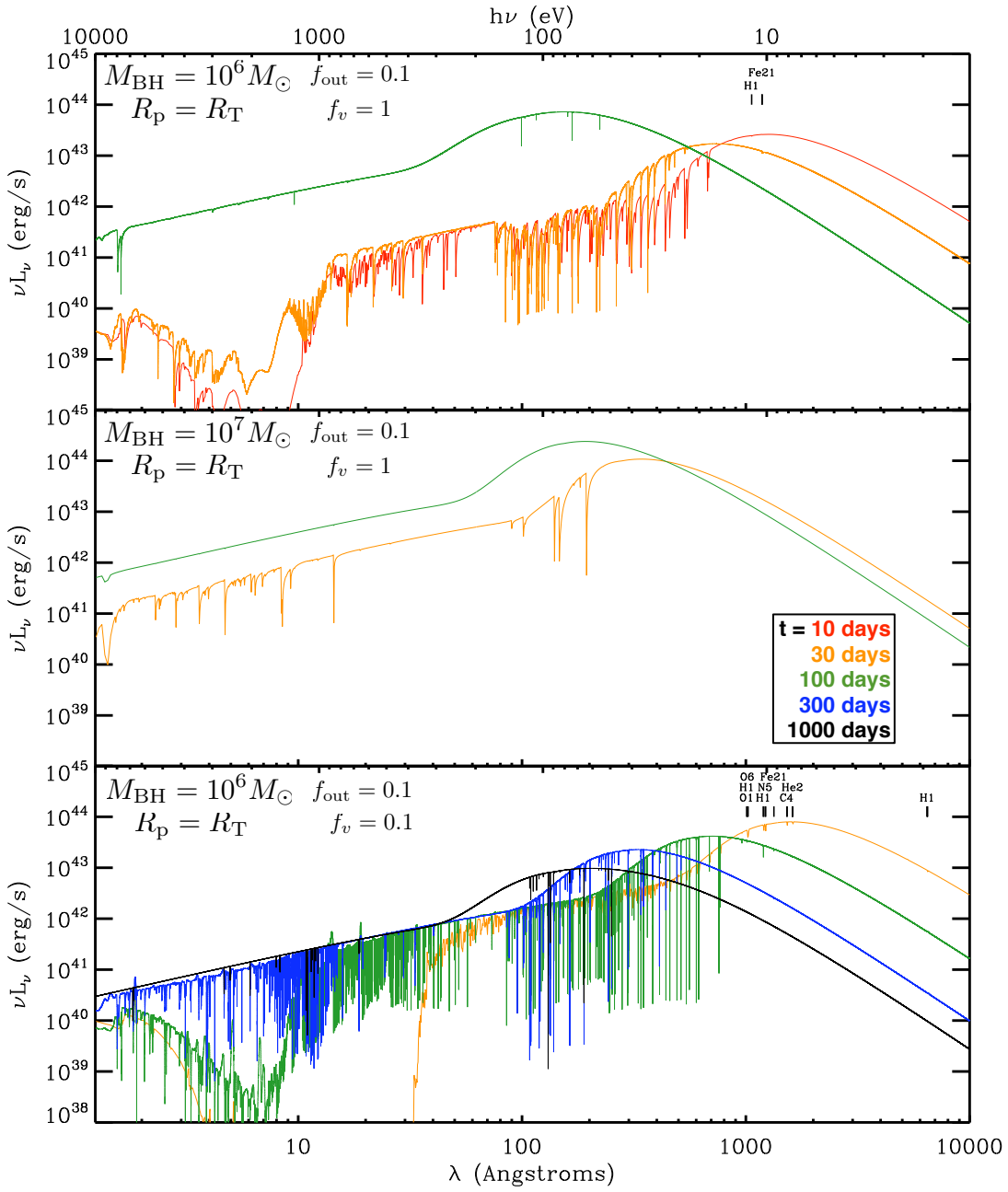

Figure 3.4: Predicted spectra, including the presence of an X-ray power-law tail with photon index $\Gamma = 3$ that carries 10% of the blackbody luminosity (appropriate when the shock at pericenter does not have time to thermalize completely). Optical and UV lines are mostly absent because the gas is so highly ionized (cf. pure blackbody continuum in Figs. 3.1 and 3.3), although there is typically significant absorption in the EUV and soft X-rays. When $\Gamma = 2$, there are even fewer lines and little continuum absorption.

tidal disruption spectra will contain a high-energy power-law tail extending from the peak in the blackbody continuum to hard X-rays. Such an X-ray power-law component might also be produced as a result of incomplete thermalization at the shock at pericenter where matter falls back to the BH (§3.2.2). To consider the observational effects of such X-rays, we carried out Cloudy calculations using an input spectrum that consists of the blackbody spectrum described in §3.2.3 plus a power-law tail that has 10% of the blackbody luminosity, a photon index of 3 ($\nu L_\nu \propto \nu^{-1}$), and that begins at the frequency where its emission equals the blackbody emission. (Such a spectrum may be appropriate for partial thermalization; in a moment, we consider the even harder spectrum expected from Compton equilibrium if the shock is not thermalized.)

Figure 3.4 shows the 10 keV to 1 μm spectra for several of our models including this X-ray power-law: $M_{\rm BH} = 10^6 M_\odot$, $R_{\rm p} = R_{\rm T}$, $f_v = 1$ (top panel); $M_{\rm BH} = 10^7 M_\odot$, $R_{\rm p} = R_{\rm T}$, $f_v = 1$ (middle panel); and $M_{\rm BH} = 10^6$, $R_{\rm p} = R_{\rm T}$, $f_v = 0.1$ (bottom panel). Due to the different peak energies of the blackbody components, the actual power-law luminosity above 1 keV varies for the different models as a function of time, with $\nu L_\nu(> 1\,{\rm keV})/L_{\rm bol} = 10^{-4} - 2\times10^{-2}$ (top panel), $6 \times 10^{-3} - 10^{-2}$ (middle panel), and $5 \times 10^{-5} - 10^{-2}$ (bottom panel). These models are thus reasonably conservative in terms of the contribution of the X-ray emission to the bolometric luminosity. Nonetheless, the presence of the hard X-ray emission significantly changes the resulting spectra.

The hard incident spectrum photoionizes the gas to a higher degree than the pure blackbody incident spectrum. Species that have ionization energies $\xi_{\rm ion} < 10\,{\rm eV}$ are thus more scarce, and so the optical absorption lines seen in the previous section disappear (except for $M_{\rm BH} = 10^6 M_\odot$, $R_{\rm p} = R_{\rm T}$, $f_v = 0.1$, where Hα still has optical depth ~ 1). Most of the FUV lines disappear as well; the Lyα line and a few others can still be faintly visible early on for $M_{\rm BH} = 10^6 M_\odot$, especially if $f_v \sim 0.1$. Fe XXI λ1354 is sometimes the longest wavelength UV/optical line.

So long as the outflow is optically thick to electron scattering, the X-ray tail can show many absorption features. These include both continuum absorption and individual absorption lines. Figure 3.4 shows that for $M_{\rm BH} = 10^6 M_\odot$, $R_{\rm p} = R_{\rm T}$, there is a deep continuum absorption trough, extending from ~ 1 keV up to ~ 5 keV; for $f_v = 0.1$ the outflow is denser and the trough extends down to ~ 0.3 keV. This feature is somewhat weaker for $M_{\rm BH} = 10^6 M_\odot$, $R_{\rm p} = 3R_{\rm S}$ and absent for $M_{\rm BH} = 10^7 M_\odot$. There are also many absorption lines superposed on the power-law tail and absorption trough, provided by highly ionized Ar, Ca, Fe, Mg, Mn, Ni, and Si (among others). The specific lines and line strengths vary significantly between the different models, so it is difficult to predict exactly which lines will be in the spectrum. As the electron scattering photosphere moves inward and becomes hotter, Figure 3.4 shows that the X-ray luminosity actually increases in time given our assumption of a fixed power-law with a photon index of 3. Once the outflow becomes optically thin to electron scattering and the accretion disk provides the incident spectrum with $h\nu_{\rm peak} \sim 0.1\,{\rm keV}$ (typically after a few months), the gas is so highly ionized that most of the absorption and emission features in the spectrum disappear.

If instead of $\nu L_\nu \propto \nu^{-1}$, the X-ray power-law tail has a flatter spectrum with a photon

index of 2 (extending up to ~ 100 keV), the gas is even more highly ionized. There are thus fewer X-ray lines (though still a significant number) and little continuum absorption. There are no lines at all in the FUV/optical (apart from very faint Lyα and Fe XXI λ1354 for $f_v = 0.1$).

3.4 Supernova Rates in Galactic Nuclei

Tidal disruption flares are expected to be similar to supernovae in their overall brightness and timescale. Supernovae thus represent a significant source of contamination when trying to discover and study tidal disruption flares in optical transient surveys. In particular, tidal disruption flares may be confused with supernovae that appear coincident with the galactic nucleus within the spatial resolution of the observations. To quantify this source of confusion, we estimate the rate of Type II and Type Ia supernovae that take place within a distance $R_{\rm res}$ of a galaxy's nucleus. To do so, we first estimate the disk and bulge stellar mass within

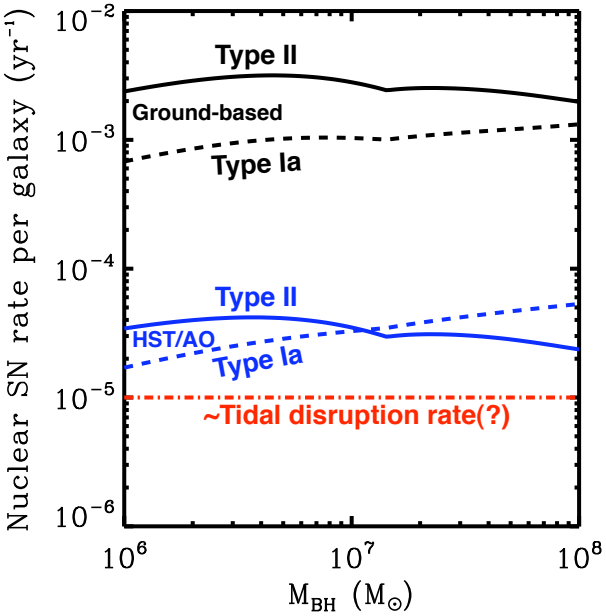

Figure 3.5: Supernova rates within 0.5" (black) and 0.05" (blue) of the galactic nucleus at $z = 0.1$, for Type II supernovae (solid) and Type Ia supernovae (dashed); 0.5" is the typical astrometric accuracy of ground-based transient surveys (J. Bloom, personal communication) while 0.05" is the spatial resolution of HST or ground-based adaptive optics. If the rate of tidal disruption per galaxy is $10^{-5}\,{\rm yr}^{-1}$ (Donley et al. 2002, red dot-dashed line), then nuclear supernovae will outnumber tidal disruption events by about two orders of magnitude for ground-based optical transient surveys. For HST/AO, the nuclear supernova rate will be comparable to the tidal disruption rate, reducing the contamination dramatically.

$R_{\rm res}$ as a function of BH mass.

For a BH of mass $M_{\rm BH}$, the stellar mass of the bulge is $M_{*,B} \sim 700 M_{\rm BH}$ (Häring & Rix 2004). We estimate the stellar mass of the disk using the ratio of bulge (B) to total mass (T) from Figure 3 of Hopkins et al. (2009), which is based on data from Balcells et al. (2007): if $M_{*,B} < 10^{10} M_\odot$, $B/T \sim 0.1$; for larger masses, $B/T \sim 3 \log(M_{*,B}/10^{10} M_\odot) - 2.9$ (where total mass $M_{*,T}$ = disk mass $M_{*,D}$ + bulge mass $M_{*,B}$). We determine the half-light radius of the disk $R_{1/2,D}$ using the results from SDSS in Shen et al. (2003) (their eq. 18) and convert to scale radius via $R_{{\rm scale},D} = R_{1/2,D}/1.68$. We then find the mass of the stellar disk inside $R_{\rm res}$ by assuming that the surface density profile is exponential:

$$M_{*,D}(< R_{\rm res}) \simeq M_{*,D} \int_0^{R_{\rm res}/R_{{\rm scale},D}} x e^{-x}\, dx\,. \tag{3.23}$$

Similarly, we calculate the half-light radius of the bulge $R_{1/2,B}$ hosting a given BH using[8] equation (17) in Shen et al. (2003) and convert it to the scale radius of the de Vaucouleurs profile using $R_{{\rm scale},B} = R_{1/2,B}/3461$ (Binney & Merrifield 1998). We then find the mass of the bulge inside $R_{\rm res}$ using

$$M_{*,B}(< R_{\rm res}) \simeq \frac{M_{*,B}}{20160} \int_0^{R_{\rm res}/R_{{\rm scale},B}} x e^{-x^{1/4}}\, dx\,. \tag{3.24}$$

The rate of Type II supernovae depends on the instantaneous star formation rate (SFR) in the galaxy. For galaxies that are actively forming stars, the galaxy-integrated SFR as a function of galaxy stellar mass ($M_* = M_{*,D} + M_{*,B}$) is $\log SFR = 0.67 \log(M_*/10^{10} M_\odot) - 6.19$, where SFR is in $M_\odot\,{\rm yr}^{-1}$ (Noeske et al. 2007)[9]. Assuming that the spatial distribution of star formation tracks stellar mass, the SFR within $R_{\rm res}$ is $SFR(< R_{\rm res}) \sim [M_{*,D}(< R_{\rm res})/M_{*,D}] \times SFR$. The nuclear Type II supernova rate is then

$$\Gamma_{\rm II}(< R_{\rm res}) \simeq 10^{-2} f_D \frac{SFR(< R_{\rm res})}{M_\odot\,{\rm yr}^{-1}}\,{\rm yr}^{-1}. \tag{3.25}$$

To account for the fact that only disk galaxies typically form stars, equation (3.25) includes a multiplicative factor given by the fraction of disk galaxies at the given M_*,

$$f_D \simeq 1 - \frac{dn_E/d\ln M_*}{dn_{\rm tot}/d\ln M_*} \tag{3.26}$$

where $dn/d\ln M_*$ is the number density of elliptical galaxies (E) or all galaxies (tot) from Bernardi et al. (2010) locally[10] and Drory et al. (2009, their Table 3) at higher redshift.

[8] Note the erratum in Shen et al. (2003)'s Table 1, so that $b = 2.88 \times 10^{-6}$.

[9] We extend the relation down to $M_* \sim 10^9 M_\odot$, and we suppose that the relation is proportional to $(1+z)^{3.4}$, using the redshift dependence of the volume-integrated star formation rate in Yüksel et al. (2008) and in agreement with the approximate redshift dependence reported by Noeske et al. (2007).

[10] Parameters for mass functions of ellipticals and total are from Table B2 in Bernardi et al. (2010), defining ellipticals by a concentration index larger than 2.86 as recommended by these authors.

With this factor of f_D, our estimate of the supernova rate per galaxy statistically takes into account that some systems of a given M_* are already passive and thus will not have significant numbers of Type II supernovae.

Following recent galaxy integrated results, we estimate the rate of nuclear Type Ia supernovae given both the nuclear stellar mass and the nuclear star formation rate:

$$\begin{aligned} \Gamma_{\rm Ia}(< R_{\rm res}) &\simeq A\left(\frac{[M_{*,B}+M_{*,D}](< R_{\rm res})}{10^{10}M_\odot}\right) \\ &+ B\left(f_D\frac{SFR(< R_{\rm res})}{10M_\odot\,{\rm yr}^{-1}}\right), \end{aligned} \tag{3.27}$$

where $A = 4.4\times10^{-4}\,{\rm yr}^{-1}$ and $B = 2.6\times10^{-2}\,{\rm yr}^{-1}$ (Scannapieco & Bildsten 2005).

The typical accuracy to which ground-based optical transient surveys can determine the location of a transient is ~ 0.5" (J. Bloom, personal communication), which corresponds to $R_{\rm res} = 0.9$ kpc at $z = 0.1$ and $R_{\rm res} = 4.1$ kpc at $z = 1$. Figure 3.5 shows the Type II and Type Ia supernova rates per galaxy within 0.9 kpc of the galactic nucleus, as a function of BH mass; this choice of $R_{\rm res}$ corresponds to a ground-based survey observing at $z \simeq 0.1$. Predicted tidal disruption rates depend on BH mass and galaxy structure and typically range from $\sim 10^{-6} - 10^{-3}$ yr^{-1} per galaxy. Using candidate detections in the ROSAT All-Sky Survey, Donley et al. (2002) estimated a rate of $\sim 10^{-5}$ tidal disruptions per year per galaxy. For the latter, Figure 3.5 shows that nuclear supernova rates are typically several orders of magnitude larger than tidal disruption rates. High resolution photometry with the Hubble Space Telescope (HST) or ground-based adaptive optics (AO) can decrease the nuclear SN rates to few $\times\,10^{-5}\,{\rm yr}^{-1}$ per galaxy, reducing confusion to order unity. We discuss the implications of these estimates of nuclear supernova rates in the next section.

3.5 Discussion

We have calculated the spectroscopic signatures of outflows produced by super-Eddington accretion during the tidal disruption of stars by massive black holes. Although there are some uncertainties in the continuum emission, mass outflow rate and kinematics, we find a number of reasonably robust conclusions: 1) the spectrum will show strong absorption lines that are blueshifted relative to the host galaxy, 2) the absorption lines will typically be very broad ($\sim 0.01 - 0.1\,c$), though often with a narrow thermally-broadened ($\sim 30\,{\rm km\,s}^{-1}$) component that dominates as the outflow subsides and becomes a thin shell at later times, 3) if the continuum spectrum is largely a blackbody, the absorption lines will be most prominent at UV wavelengths (e.g., C IV, Si IV, O IV, N V, Lyman α and O VI). In addition, if there is a lower velocity component to the outflow, which is plausible based on simulations of radiatively inefficient accretion (e.g., Ohsuga et al. 2005), we find that there will also be optical absorption (and possibly emission) lines, in particular Hα, Hβ, He II λ6560, and He II λ4860 (Fig. 3.3). The optical/UV lines will, however, be largely absent from the spectrum if the continuum emission is harder or contains an X-ray power-law tail (either because

of non-thermal processes or incomplete thermalization)—the gas would then be too highly ionized. In that case, the dominant absorption lines are in the soft X-rays (Fig. 3.4). This highlights the importance of X-ray observations of tidal disruption events coeval with optical and UV spectroscopic observations, in order to properly interpret the presence or absence of optical/UV lines.

Having summarized our key results, we now describe several uncertainties in our spectroscopic predictions. Our calculations assume a blackbody spectrum of photons released from the electron scattering photosphere of the outflow, with an 'optional' phenomenologically motivated X-ray power-law tail. We find, however, that when gas returning to pericenter shocks at $\sim 2R_{\rm p}$, the thermalization between the photons and gas is a strong function of BH mass, stellar pericenter distance, and time since disruption (§3.2.2). The thermalization is often incomplete. This would harden the continuum spectrum, eliminating many of the optical-UV spectroscopic signatures of tidal disruption events. Moreover, the prominent optical continuum emission predicted by Strubbe & Quataert (2009) from tidal disruption outflows requires reasonable thermalization in the post-shock plasma. Such thermalization is the most likely for tidal disruptions around lower mass BHs with $M_{\rm BH} \lesssim$ few $10^6 M_\odot$ and at early times after disruption, $t \lesssim 2$ weeks (eq. 3.10). This estimate assumes spherical fallback and is thus somewhat conservative, since stellar debris is focused into a thin stream as it falls back after disruption (Kochanek 1994); a higher density at the shock would lead to a longer period of thermal blackbody emission, perhaps up to a month for $M_{\rm BH} \sim 10^6 M_\odot$. Nonetheless, these results emphasize the importance of high cadence observations with rapid follow-up in optical searches for tidal disruption flares. In the future, observing the spectrum of a tidal disruption event change as the outflow falls out of thermal equilibrium would provide strong constraints on the physics of radiation-dominated shocks, which are important in other astrophysical environments such as shock break-out in supernovae.

Another uncertainty in our spectroscopic predictions is related to the mass loading and speed of the outflow (parameterized by $f_{\rm out}$ [eq. 3.2] and f_v [eq. 3.3] in our calculations), and the outflow's geometry. Radiation hydrodynamic simulations of super-Eddington black hole feeding suggest reasonable values for $f_{\rm out}$ and f_v: Ohsuga et al. (2005)'s simulation at $100\dot{M}_{\rm Edd}$ obtains $f_{\rm out} \sim 0.1$ and $f_v \sim 1$ (our fiducial values). Ohsuga (2007)'s similar simulations of feeding at $\dot{M}_{\rm Edd} - 300\dot{M}_{\rm Edd}$ imply $f_{\rm out} \sim 0.1-0.4$ (depending on viscous parameter α) and outflow velocities of $\sim 0.1c-0.3c$; Takeuchi et al. (2009)'s similar simulations at $100\dot{M}_{\rm Edd}$ and $300\dot{M}_{\rm Edd}$ imply $f_{\rm out} \sim 0.8$. Dotan & Shaviv (2011) calculate a super-Eddington accretion model in which instabilities make the gas inhomogeneous, and find that $f_{\rm out} \sim 0.5-0.7$ for feeding rates $5\dot{M}_{\rm Edd} - 20\dot{M}_{\rm Edd}$. We note that Lodato & Rossi (2011) calculate tidal disruption light curves using our super-Eddington outflow model (eqs. [3.6] - [3.8]) with Dotan & Shaviv (2011)'s $f_{\rm out}$ results and a more detailed model for $\dot{M}_{\rm fallback}(t)$ (Lodato et al. 2009); they find similar results to those in Strubbe & Quataert (2009) (optical luminosities are similar, and emission from the outflow lasts a factor of few times longer). In §3.3, we used fiducial values of $f_{\rm out} \sim 0.1$ and $f_v \sim 1$ and showed the results of varying those parameters: larger mass outflow fractions lead to more absorption lines at longer wavelengths, and slower outflow velocities lead to narrower absorption lines, the presence of optical lines, and even

the presence of some emission lines. In reality, the mass-loading and outflow kinematics may vary with viewing angle; the geometry of the outflow is uncertain, and we do not capture this effect with our simple spherical models. Ohsuga & Mineshige (2007) and Takeuchi et al. (2009) find outflow opening (half) angles of ~ 30 degrees, suggesting that from some viewing angles, accretion disk and outflow may both be visible.

3.5.1 Observational Prospects

The prominent UV lines predicted here are challenging to observe for several reasons. First, the UV emission can be obscured by dust, particularly along lines of sight through the host galaxy's disk; however, observations of similar absorption lines in BAL QSO spectra suggest that at least some lines of sight will have low obscuration. Second, observations at extreme UV wavelengths ($1000\,\text{Å} \lesssim \lambda \lesssim 100\,\text{Å}$), where most of the predicted spectral features lie, must take place from space and are technically difficult. Encouragingly, the Space Telescope Imaging Spectrograph and the Cosmic Origins Spectrograph aboard the Hubble Space Telescope (HST) should be able to observe spectroscopic features like those predicted here in the far UV.

The optical to X-ray spectra predicted here apply to tidal disruption flares having early-time super-Eddington outflows, which requires $M_{\rm BH} \lesssim \text{few} \times 10^7 M_\odot$. To detect such flares in the first place using optical transient surveys, significant contaminants such as variable active galactic nuclei (AGN) and supernovae must be excluded. Luminous AGN fueled by other means are $\gtrsim 10^3$ times more common than tidal disruption events and could in principle produce optically bright 'flares.' Typically, however, AGN show optical emission lines in their spectra (like the Balmer lines and [O III]). We have shown that during the super-Eddington outflow phase, tidal disruption events are unlikely to show such optical lines; furthermore, if tidal disruption events do show optical lines, Balmer and He II lines are the only reasonable candidates (perhaps also very faint He I and S IX), because the densities are too high for collisionally excited lines like [O III] which almost always appear in AGN spectra. These conclusions about Balmer versus [O III] lines also hold during the later phase of a tidal disruption event (described in Strubbe & Quataert 2009) in which the accretion disk irradiates the unbound stellar debris.

BAL QSOs (a subset of quasars) are more physically and spectroscopically similar to tidal disruption events, both involving a bright central continuum source driving an outflow, which gives rise to blueshifted UV absorption lines. However, BAL QSOs show strong emission lines while tidal disruption events likely will not, for the following two-part reason, which draws on Murray et al. (1995)'s theoretical work on BAL QSOs. First, the tidal disruption outflow is typically much more ionized than a BAL QSO wind, so optical depths for resonance lines in tidal disruption events are at most comparable to, and are often much less than, optical depths in BAL QSOs. (The optical depth to true absorption—rather than scattering—by resonance transitions is typically much less than one in both cases; the emission is thus effectively thin and so the smaller optical depth for tidal disruption outflows implies less emission.) Secondly, BAL QSO winds are thought to originate well outside

the source of continuum radiation (the gas is not as highly ionized at larger radii, so UV resonance lines are optically thick enough for radiation pressure to drive the wind). Thus, although we see the hot continuum source through the cooler wind, the wind can produce significant emission lines (in addition to strong absorption) because the wind's emitting area is much larger than the area of the continuum source (Murray et al. 1995). In tidal disruption events, by contrast, those emitting areas are typically the same: the region where most line emission occurs and the outer edge of the continuum source are both typically at the electron scattering photosphere. This, along with the small true optical depth, implies that tidal disruption outflows are expected to show little or no line emission. The situation may be more complicated if the outflow does not fully thermalize, as there could be additional line emission inside the electron scattering photosphere that we have not considered here.[11] In addition to this important difference in the presence of emission lines, note that BAL QSOs are generally associated with higher-mass BHs ($M_{\rm BH} \gtrsim 10^8 M_\odot$), which cannot tidally disrupt solar-type stars outside the horizon.

Another significant contaminant in optical searches for tidal disruption events is supernovae that take place in the nuclei of galaxies, because the luminosities and timescales are similar, and because supernovae are initially blue like tidal disruption events. Spectroscopy will help: supernovae typically show a forest of deep optical absorption lines, quite unlike our predictions for tidal disruption events. Type IIn supernovae may still pose a particular challenge: the supernova plows into surrounding circumstellar medium, shock-heating the gas to high enough temperatures to suppress the optical lines. However, these supernovae begin to cool after several months, becoming redder and producing optical emission lines at late times. Tidal disruption events, by contrast, become *hotter* with time and are not expected to produce similar optical emission lines.

To quantify how much nuclear supernovae will 'contaminate' searches for tidal disruption events, we estimated the rate of supernovae within the spatial resolution (~ 0.5") of ground-based optical transient surveys (§3.4 and Fig. 3.5): at $z \sim 0.1$ the nuclear Type II rate is a few $\times\, 10^{-3}\,{\rm yr}^{-1}$ per galaxy, of which $\sim 10\%$ are probably Type IIn (Li et al. 2011); the Type Ia rate is a factor of $2-3$ smaller than the Type II rate. These rates of Type II and Type IIn supernovae are $\gtrsim 2$ and 1 order(s) of magnitude greater than the tidal disruption rate per galaxy inferred by Donley et al. (2002) using ROSAT. The ROSAT constraints, however, are largely on more massive black holes (which are both more luminous and more likely to be prominent in the X-rays) so it is possible that the tidal disruption rate is different in the lower mass systems most likely to produce optically luminous emission from super-Eddington outflows. The high rate of nuclear supernovae estimated in Figure 3.5 emphasizes the importance of high-resolution follow-up imaging with HST or adaptive optics, which can reduce the rate of nuclear supernovae 'false positives' in optical tidal disruption searches by a factor of $\gtrsim 50$ (Fig. 3.5).

Although the super-Eddington outflows produced during the tidal disruption of stars are

[11] If the outflow runs into relatively dense circumnuclear gas, additional line emission may be possible there as well.

in principle readily detectable out to $z \gtrsim 1$ (Strubbe & Quataert 2009), restricting candidate events to hosts with $z \sim 0.1$ is likely a good strategy for minimizing interference from supernovae: the rate of nuclear supernovae increases rapidly with redshift, to $\sim 10^{-1}\,\mathrm{yr}^{-1}$ per galaxy at $z \sim 1$. This increase is due to both the increase in star formation at high redshift and the increasing fraction of a galaxy that lies within the point-spread function of the observation.

The fiducial outflow model in Strubbe & Quataert (2009) ($f_{\rm out} = 0.1$; $f_v = 1$; disruption rate per galaxy $= 10^{-5}\,\mathrm{yr}^{-1}$) predicts that ~ 8 tidal disruptions per year can be detected at $z \lesssim 0.1$ for a survey like the Palomar Transient Factory. Relatively nearby events have the additional advantages that they are less expensive to follow up spectroscopically and it is easier to characterize their host galaxies. For these comparatively nearby events, we predict that the detection probability in optical surveys is relatively independent of $M_{\rm BH}$ for $M_{\rm BH} \lesssim$ few $\times\, 10^7 M_\odot$, so it should help to restrict candidates to bulges less massive than $\sim 10^{10} M_\odot$ (the weak dependence of the detection probability on $M_{\rm BH}$ is also important because tidal disruption flares from lower mass BHs $\sim 10^6 M_\odot$ are the most likely to be in thermal equilibrium and thus to have prominent optical continuum emission in the first place). Restricting follow-up to systems with little ongoing star formation and/or old stellar populations would help further minimize the number of nuclear supernovae. Observationally, the star formation rate in galaxies, and hence the supernova rate, is relatively bimodal, and thus some galaxies will have nuclear supernova rates (particularly type II rates) smaller than estimated in Figure 3.5. This is especially true for more massive BHs, but $\sim 10\%$ of lower massive systems ($M_{\rm BH} \lesssim 10^7 M_\odot$) are likely to be relatively passive as well (e.g., Bernardi et al. 2010). If these can be identified in advance (via, e.g., prior Sloan Digital Sky Survey observations), they may well be the most promising systems in which to follow up nuclear transients; this selection would, however, decrease the predicted detection rate to $\sim 1\,\mathrm{yr}^{-1}$ at $z \lesssim 0.1$ for a survey like PTF.

Given the recent plethora of luminous supernovae (e.g., Quimby et al. 2009), it is unclear how well single-band photometry alone will be able to distinguish tidal disruption events from nuclear supernovae. If this proves difficult, as we suspect is likely, the spectroscopic predictions for tidal disruption events presented here, and the color evolution predicted in Strubbe & Quataert (2009) (the outflow photosphere becomes hotter with time—becoming bluer if the observing band is close to the peak, or showing no color evolution if the observing band is on the Rayleigh-Jeans tail), may prove particularly useful for identifying and characterizing tidal disruption flares.

3.5.2 Optically-selected candidates

The first two optically-selected tidal disruption candidates were announced shortly after the submission of this paper, found in Stripe 82 of the Sloan Digital Sky Survey (van Velzen et al. 2010). These candidates have observed properties broadly consistent with our predictions, with observed g-band luminosities of $\sim 10^{43}\,\mathrm{erg\,s}^{-1}$ and no color evolution. The optical data for candidate "TDE1" is reasonably approximated by our model for the super-

Eddington outflow due to the disruption of a solar-type star by a BH of mass $\sim 10^7 M_\odot$ at $R_\mathrm{p} \sim R_\mathrm{T}$, with $f_\mathrm{out} \sim 0.1$ [eq. 3.2] and $f_v \sim 0.1$ [eq. 3.3]. In detail, the optical data for candidate "TDE2" is harder to approximate with our simple model: although the luminosity can be reproduced by a relatively large f_out or relatively small f_v, the optical colors and only gentle fading of the event are less consistent with our model. These properties may be more consistent with a model like that of Loeb & Ulmer (1997) in which falling-back gas settles into a steady hydrostatic atmosphere rather than becoming unbound in a true outflow; this may be appropriate if the fallback rate is never highly super-Eddington. The large optical luminosity of these two candidate events suggests that outflows may have relatively low velocities, and is encouraging for the optical detection of future tidal disruption candidates.

Acknowledgments

We thank Josh Bloom, Kevin Bundy, Phil Chang, Weidong Li, Norm Murray, Kristen Shapiro, and Nathan Smith for helpful conversations; we also especially thank David Strubbe for help with C++ calculations. Support for EQ was provided in part by the Miller Institute for Basic Research in Science, University of California, Berkeley and the David and Lucile Packard Foundation. Support for program number AR 12151 was provided by NASA through a grant from the Space Telescope Science Institute, which is operated by the Association of Universities for Research in Astronomy, Inc., under NASA contract NAS5-26555.

Chapter 4

The Rate of Tidal Disruption as a Function of Pericenter Distance

Abstract

The tidal disruption of a star by a massive black hole (BH) is predicted to produce an electromagnetic flare whose observational appearance depends on the BH mass $M_{\rm BH}$ and on stellar properties—and also on the pericenter distance $r_{\rm p}$, the star's distance of closest approach to the BH on its last orbit (where $r_{\rm p} \leq r_{\rm T}$). As data and models improve, we expect robust identification of $r_{\rm p}$ in individual tidal disruption events to be possible, enabling calculation of an observed disruption rate as a function of $r_{\rm p}$ and host galaxy properties. Many authors have made predictions of the tidal disruption rate per galaxy, but have focused on the overall rate γ integrated over all pericenter distances, rather than the rate as a function of pericenter distance, $d\gamma/d\ln r_{\rm p}$. In this work, we review the Fokker-Planck formalism for calculating tidal disruption rates, and then derive an expression for $d\gamma/d\ln r_{\rm p}$ by extending the solution to the Fokker-Planck equation inside the tidal disruption region, assuming a spherically symmetric and isotropic stellar distribution surrounding the BH. We use our result to calculate $d\gamma/d\ln r_{\rm p}$ for the nearby elliptical galaxy NGC 4467: as expected, the rate rises proportional to $r_{\rm p}$ for small $r_{\rm p}$ and then turns up more quickly at $r_{\rm p} \sim r_{\rm T}$. We then examine how this form for $d\gamma/d\ln r_{\rm p}$ affects predictions for the optical detection rate of tidal disruption events. We close by describing future research plans based on this work as a foundation: calculating $d\gamma/d\ln r_{\rm p}$ for a variety of individual galaxies, extending our derivation to a wider range of geometries, and investigating other dynamical effects not accounted for here. In the future, comparison of the observed disruption rate as a function of $r_{\rm p}$ with predictions for $d\gamma/d\ln r_{\rm p}$ for a variety of galaxy types should provide an important probe of the dynamics of galactic nuclei, offering insights into the formation and evolution of BHs and their surrounding stars.

4.1 Introduction

The tidal gravity of a massive black hole (BH) in the center of a galaxy will disrupt stars that pass closer than $r_{\rm T} \sim r_*(M_{\rm BH}/m_*)$, where r_* and m_* are the radius and mass of the star, and $M_{\rm BH}$ is the mass of the BH. Gas from the disrupted star flows towards the BH, powering an electromagnetic flare that should be detectable by new and upcoming transient surveys. In Chapters 2 and 3 (Strubbe & Quataert 2009, 2011), we predicted the photometric and spectroscopic evolution of tidal disruption events (TDEs). When gas falls back to the BH at a super-Eddington rate, radiation pressure likely drives a significant fraction back outwards in a super-Eddington outflow that is optically bright, superposed with broad, blueshifted absorption lines. There is also expected to be a longer-lasting accretion disk, and emission from the disk should photoionize the surface of the stream of stellar gas that became unbound during the disruption, producing broad emission lines.

Our predicted observational signatures depend on $M_{\rm BH}$ and orbital pericenter distance $r_{\rm p}$, the distance between the BH and the star at closest approach on the star's last fateful orbit. A smaller pericenter distance leads to a more extreme event in which timescales and velocities are faster, and the rate at which mass feeds the BH is higher. As a result, the flares from events at $r_{\rm p} \ll r_{\rm T}$ are predicted to look substantially different from those at $r_{\rm p} \sim r_{\rm T}$: the former evolve more quickly (on timescales of hours to days instead of weeks to months), and show spectral lines that are broader and can comprise different lines. Additionally, the accretion disk should be fainter because it is narrower, while the super-Eddington outflow can be brighter or fainter (depending on $M_{\rm BH}$ and viewing time). Events at low $r_{\rm p}$ also are less able to thermalize, likely producing hard X-rays. More speculative, we have proposed that the emission from Swift J164449.3+573451 may come from a relativistic jet produced by a TDE at very low $r_{\rm p}$, feeding the BH at a highly super-Eddington rate (Bloom et al. 2011). While not yet possible today, we may be able before long to identify $r_{\rm p}$ robustly for individual events based on their observed multi-waveband light curves and spectra. Observationally measuring the rate of TDEs as a function of $M_{\rm BH}$ and $r_{\rm p}$ should offer a statistical probe of the structure and dynamics of galactic nuclei. Theoretical studies of the disruption rate per galaxy as a function of $r_{\rm p}$ (which we call $d\gamma/d\ln r_{\rm p}$) will be an important foundation for interpreting the *observed* rates of TDEs as a function of $r_{\rm p}$.

This quantity $d\gamma/d\ln r_{\rm p}$ has not previously been investigated in detail, but much work has been devoted to theoretically calculating the *overall* ($r_{\rm p}$-integrated) rate at which BHs should tidally disrupt stars (which we call γ). The basic process that converts safe stellar orbits into dangerous ones that enter the BH's disruption zone (sometimes called the "loss cone" due to its shape in velocity space: see footnote 5) is 2-body scattering events in which one star's orbit is perturbed by a gravitational interaction with another star. (Stellar orbits may also be changed by other processes, but we will discuss these only in §4.6 and defer deeper investigation of their effects on $d\gamma/d\ln r_{\rm p}$ to future work.) Repeated scattering events cause stellar orbits to diffuse in phase space. The tidal disruption rate implied by this diffusion process can be estimated through simple approximations (e.g., Frank & Rees 1976) which we review in §4.2. The diffusion process is described more exactly by the Fokker-Planck

equation (e.g., Lightman & Shapiro 1977; Cohn & Kulsrud 1978), first derived in the context of plasma physics: in both circumstances, interactions via a $1/r^2$ force (gravity or Coulomb collisions) alter particle trajectories (stars or electrons/ions). Solutions of the Fokker-Planck equation under various approximations have been calculated for generic model galaxies (e.g., Frank & Rees 1976; Rees 1988), and using observational data for real galaxies (Syer & Ulmer 1999; Magorrian & Tremaine 1999; Wang & Merritt 2004). This formalism is reviewed in detail in §4.3. This previous work, however, focuses only on finding solutions to the Fokker-Planck equation *outside* the disruption region and at the boundary—and therefore only on the overall tidal disruption rate γ.

In this chapter, we derive $d\gamma/d\ln r_{\rm p}$ for a spherically symmetric stellar profile by extending the solution to the Fokker-Planck equation *inside* the disruption region (§§4.3.6 and 4.3.8). This Fokker-Planck solution is based on unpublished work by M. Milosavljević (personal communication). We provide a detailed derivation of this solution, show how $d\gamma/d\ln r_{\rm p}$ depends on it, and then in §4.4 calculate $d\gamma/d\ln r_{\rm p}$ as a function of orbital energy for a Keplerian potential and power-law stellar density profile. Next in §4.4.2 we extend the results to general spherical (non-Keplerian) potentials, and in §4.5 calculate the tidal disruption rate as a function of pericenter distance for the elliptical galaxy NGC 4467, based on its observed surface brightness profile, mass-to-light ratio, and inferred $M_{\rm BH}$. We conclude by showing how an accurate form for $d\gamma/d\ln r_{\rm p}$ affects predictions of optical detection rates of TDEs (§4.5.1), and in §4.6 discuss plans for future work in the context of studying the co-evolution of BHs and their surrounding stars.

4.2 Tidal disruption rate basics

In this section, we review the order-of-magnitude framework for estimating tidal disruption rates in galaxies, based on Frank & Rees (1976); Lightman & Shapiro (1977); Binney & Tremaine (1987); Rees (1988); Alexander (2005). Our set-up is a BH of mass $M_{\rm BH}$ surrounded by a population of stars all of mass m having a density distribution $n(r) \propto r^{-\alpha}$, where r is the radius measured from the BH.[1] The radius of influence $r_{\rm h}$ is the location where the interior mass of stars equals $M_{\rm BH}$, i.e., $n(r)r^3 \sim M_{\rm BH}/m$. The stars have an isotropic velocity distribution, which means that stars at a given r have equal probability of their velocity vector $\vec{v}$ pointing in any direction. For $r < r_{\rm h}$, $v \sim (GM_{\rm BH}/r)^{1/2}$, and for $r > r_{\rm h}$, $v \sim \sigma$, where $\sigma \sim (GM_{\rm BH}/r_{\rm h})^{1/2}$ is the (assumed constant) velocity dispersion of the stellar bulge.[2]

[1]Note that throughout this chapter, we assume for simplicity that all stars have mass m, and in §4.5 we assume that stars are solar-type so that $m \sim M_\odot$ and $r_* \sim r_\odot$. We also assume that the background distribution of stars is distributed spherically and isotropically (despite evidence to the contrary in particular stellar populations in galactic nuclei, including the disk(s) of stars in our own Galactic Center). Thirdly, we assume that the stars and BH are the only dynamically important masses; we ignore possible contributions from gas or dark matter. See §4.6 for discussion of these assumptions.

[2]As an aside, note that if the stellar distribution outside $r_{\rm h}$ is that of an isothermal sphere, then the velocity distribution will be Maxwellian. The velocity distribution inside $r_{\rm h}$ is not Maxwellian due to the

Stars are occasionally gravitationally scattered by interactions with other stars. During a single gravitational scatter at impact parameter b, a star's velocity is deflected by

$$\delta v \sim f_{\rm grav}\delta t \sim \frac{Gm}{b^2}\frac{b}{v_{\rm rel}} \sim \frac{Gm}{bv_{\rm rel}} \sim \frac{Gm}{bv}\,, \tag{4.1}$$

where we have employed the impulse approximation: $f_{\rm grav} \sim Gm/b^2$ is the gravitational force per mass, $\delta t \sim b/v_{\rm rel}$ is the timescale for the interaction, and $v_{\rm rel} \sim v$ is the relative velocity of the two stars. Multiple scatters are approximately uncorrelated, and so lead to zero mean change in velocity: the velocity executes a random walk. To change a star's velocity by order unity therefore requires $N_{\rm scat} \sim (v/\delta v)^2 \sim (bv^2/Gm)^2$ scatters. The frequency of gravitational interactions at impact parameter b is

$$\frac{d\nu_{\rm scat}}{d\ln b} \sim nb^2 v_{\rm rel} \sim nb^2 v\,, \tag{4.2}$$

and so the time to change a star's velocity by order unity is the relaxation time,

$$t_{\rm rel} \sim N_{\rm scat}\frac{1}{nb^2 v}\frac{1}{\ln\Lambda} \sim \frac{v^3}{G^2m^2n}\frac{1}{\ln\Lambda}\,, \tag{4.3}$$

where $\ln\Lambda \approx \ln(r_{\rm bulge}/b_{\rm min})$ is the Coulomb logarithm, accounting for integration over all impact parameters b from a minimum $b_{\rm min}$ to the size of the stellar bulge $r_{\rm bulge}$.

Note that we have $b_{\rm min} \sim Gm/v^2$ because closer gravitational scatterings lead to velocity changes $\delta v \gtrsim v$, so this perturbative analysis breaks down (in particular, the Fokker-Planck equation requires $\delta v \ll v$ to be valid). Tidal disruption rate calculations typically ignore the strong gravitational scatterings at $b < b_{\rm min}$, since the results depend only logarithmically on b and there are many more decades in b at $b > b_{\rm min}$. However, strong gravitational scatterings at $b < b_{\rm min}$ may be more important for producing tidal disruption events at $r_{\rm p} \ll r_{\rm T}$. We will investigate this further in future work.

We will see later that most tidally disrupted stars come from radii far from the BH on orbits of specific energy $\ll GM_{\rm BH}/r_{\rm T}$. A star on track to be tidally disrupted thus has orbital angular momentum (per mass) at most $J_{\rm lc} \sim (2GM_{\rm BH}r_{\rm T})^{1/2}$. The angular momentum of a star on a circular orbit at $r < r_{\rm h}$ is $J_{\rm c} \sim (GM_{\rm BH}r)^{1/2}$, and at $r > r_{\rm h}$ is $J_{\rm c} \sim \sigma r$. Assuming an isotropic velocity distribution, the fraction of stars at a given r with low enough angular momentum to be disrupted is[3]

$$\theta_{\rm lc}{}^2 \sim \frac{J_{\rm lc}{}^2}{J_{\rm c}{}^2} \sim \begin{cases} \frac{2GM_{\rm BH}r_{\rm T}}{GM_{\rm BH}r} \sim \frac{r_{\rm T}}{r}\,, & r < r_{\rm h} \\ \\ \frac{2GM_{\rm BH}r_{\rm T}}{(\sigma r)^2} \sim \frac{r_{\rm T}r_{\rm h}}{r^2}, & r > r_{\rm h}\,. \end{cases} \tag{4.4}$$

presence of the BH.

[3]The reader can visualize this in the following way. Around the point P a distance r from the BH, the set of all possible velocity directions trace out a sphere in velocity space. The stars whose angular momenta are low enough to be disrupted trace out a cone in velocity space whose vertex is at the point P, whose base is $J_{\rm lc}/r$, and whose opening angle is $\theta_{\rm lc}$. The fraction of stars in the cone compared to the total within the sphere is therefore $\sim \theta_{\rm lc}{}^2$: the space of velocities tangent to the BH is two-dimensional.

(In future sections we will often call this quantity $R_{\rm lc}$ instead of ${\theta_{\rm lc}}^2$.) Typical values for $r_{\rm T}$ and $r_{\rm h}$ are AU and pc, respectively: therefore, $r_{\rm T} \ll r_{\rm h}$ and so the fraction of stars on track to be disrupted is ${\theta_{\rm lc}}^2 \ll 1$ (and this is true even for giant stars and particularly compact nuclei). Since we wish to consider stellar disruptions at pericenter distances $r_{\rm p} < r_{\rm T}$, we can also calculate the fraction of stars having (at most) the corresponding angular momentum $J_{r_{\rm p}<r_{\rm T}} \sim 2GM_{\rm BH}r_{\rm p}$,

$$\theta^2_{r_{\rm p}<r_{\rm T}} \sim \frac{J^2_{r_{\rm p}<r_{\rm T}}}{{J_{\rm c}}^2} \sim \begin{cases} \frac{2GM_{\rm BH}r_{\rm p}}{GM_{\rm BH}r} \sim \frac{r_{\rm p}}{r}\,, & r < r_{\rm h} \\ \\ \frac{2GM_{\rm BH}r_{\rm p}}{(\sigma r)^2} \sim \frac{r_{\rm p}r_{\rm h}}{r^2}, & r > r_{\rm h}\,. \end{cases} \tag{4.5}$$

Since a star can survive on an orbit with $J \leq J_{\rm lc}$ for at most a dynamical time, it is useful to calculate the typical change in angular momentum over a dynamical time. During one dynamical time, a star experiences $t_{\rm dyn}(d\nu_{\rm scat}/d\ln b) \sim nb^2vt_{\rm dyn}$ scatters, which change v by $\Delta v_{\rm dyn} \sim v(t_{\rm dyn}/t_{\rm rel})^{1/2}$, and so the orbital angular momentum (relative to $J_{\rm c} \sim vr$) therefore changes by

$$\theta_{\rm dyn} \sim \frac{\Delta v_{\rm dyn} r}{J_{\rm c}} \sim \left(\frac{t_{\rm dyn}}{t_{\rm rel}}\right)^{1/2}\,. \tag{4.6}$$

Comparison of $\theta_{\rm dyn}$ and $\theta_{\rm lc}$ reveals two regimes. In the "diffusive regime," $\theta_{\rm dyn} < \theta_{\rm lc}$, and so stars can only diffuse into the disruption zone a distance $\Delta J \sim J_{\rm c}(t_{\rm dyn}/t_{\rm rel})^{1/2}$ in angular momentum space: deeper inside, the disruption zone is empty. A given star has a reasonable probability of entering the disruption zone only after a relaxation time, and so the rate of tidal disruption in this regime is

$$\frac{d\gamma}{d\ln r_0} \sim \frac{n(r_0)r_0^3}{t_{\rm rel}(r_0)}\ \text{(diffusive regime)}\,, \tag{4.7}$$

where r_0 is the initial orbital radius of the star. (In future sections, we will more precisely consider this as an initial orbital *energy* of the star rather than orbital radius.) In the "full loss cone regime" (also called the "pinhole regime"), $\theta_{\rm dyn} > \theta_{\rm lc}$, and so stars can repeatedly enter and exit the disruption region during a single dynamical time: the presence of the disruption region has little effect on the dynamics. Each dynamical time, the BH disrupts a small fraction (${\theta_{\rm lc}}^2$) of the stars, so that the rate of tidal disruption is

$$\frac{d\gamma}{d\ln r_0} \sim \frac{n(r_0)r_0^3}{t_{\rm dyn}}{\theta_{\rm lc}}^2\ \text{(full loss cone regime)}\,. \tag{4.8}$$

Similarly, (using eq. 4.5) the rate—now as a function of $r_{\rm p}$—is

$$\frac{d^2\gamma}{d\ln r_0\, d\ln r_{\rm p}} \sim \frac{n(r_0)r_0^3}{t_{\rm dyn}}\theta^2_{r_{\rm p}<r_{\rm T}} \propto r_{\rm p}\,. \tag{4.9}$$

The ratio $(\theta_{\rm dyn}/\theta_{\rm lc})^2$ is often called q. At small radii from the BH, $q \ll 1$ and the regime is diffusive; at large radii from the BH, $q \gg 1$ and the regime is full loss cone. The special

location where $\theta_{\rm dyn} = \theta_{\rm lc}$ is called $r_{\rm crit}$. The full tidal disruption rate is the integral over all initial radii (or all q). The behavior of $d\gamma/d\ln r_0$ clearly changes at $r_0 \sim r_{\rm crit}$ and $r_0 \sim r_{\rm h}$. Examination of power-law scalings for typical density profiles shows that $r_{\rm crit} \sim r_{\rm h}$, and that $r \sim r_{\rm crit}$ (or $q \sim 1$) dominates the rate integral. Figure 4.1 demonstrates the difference between the diffusive and full loss cone regimes (using the language of §4.3): the horizontal axis is proportional to J^2, and the vertical axis shows the (normalized) fraction of stars that have orbits inside the disruption region after one dynamical time. For $q \gg 1$, the fraction is independent of angular momentum, while for $q \ll 1$, the fraction drops by half when one compares stars at the boundary of the disruption region with stars that have wandered in a distance of $q^{1/2}/2 \sim \theta_{\rm dyn}/2\theta_{\rm lc}$ in angular momentum space.

Therefore, based on these approximate considerations, we expect that the tidal disruption rate as a function of pericenter distance will have the following shape: At $r_{\rm p} \ll r_{\rm T}$, $d\gamma/d\ln r_{\rm p} \propto r_{\rm p}$ (by eq. 4.9), because only stars having $\theta_{\rm dyn} \gg \theta_{\rm lc}$ can take such a large angular momentum step in a single dynamical time. At $r_{\rm p} \sim r_{\rm T}$, $d\gamma/d\ln r_{\rm p}$ will be enhanced above this linear scaling, due to the contribution from stars in the diffusive regime: the closer to $r_{\rm T}$, the more stars at $q \ll 1$ can contribute. The more precise result for $d\gamma/d\ln r_{\rm p}$ that we present for NGC 4467 in Figure 4.4 follows this expected shape.

4.3 The Fokker-Planck formalism: Review & derivation of $d\gamma/d\ln r_{\rm p}$

With the previous section's order-of-magnitude results in mind, we now derive the tidal disruption rate as a function of pericenter distance using the Fokker-Planck formalism. We spend much of this section reviewing the derivation and solution of the Fokker-Planck equation in the context of stellar dynamics, synthesizing results from Cohn & Kulsrud (1978); Spitzer (1987); Binney & Tremaine (1987); Magorrian & Tremaine (1999) and making explicit steps that these works leave implicit. These papers calculate the tidal disruption rate integrated over $r_{\rm p}$ by solving the Fokker-Planck equation outside and at the boundary of the tidal disruption region. In §§4.3.6 and 4.3.8, we derive the solution to the Fokker-Planck equation *inside* the disruption region: this derivation is due to M. Milosavljević (personal communication), and we have again made more steps in the derivation explicit. Associating the solution inside the disruption region with $d\gamma/d\ln r_{\rm p}$ (eqs. 4.71, 4.73), and finding the limiting form for $\xi(q)$ (eq. 4.85) are my primary original contributions in this section.

4.3.1 The distribution function and coordinate systems

Consider the (number) distribution function of stars $f(\mathbf{r}, \mathbf{v})$ in the gravitational potential of a black hole of mass $M_{\rm BH}$. We start by discussing coordinate systems. In full generality, we would use the 6-dimensional coordinate system $(\mathbf{r}, \mathbf{v})$—however, we make several simplifying assumptions about symmetry: first, we assume that the distribution function is (spatially) spherically symmetric, so that the only spatial coordinate is r. The spatial volume element

is therefore $d^3\mathbf{r} = 4\pi r^2\,dr$. Second, we make the following assumption about the symmetry in velocity space. For a star at a given spatial location $\mathbf{r}$, there could in principle be three independent velocity coordinates: v_r parallel to $\mathbf{r}$, v_t perpendicular to $\mathbf{r}$, and the angle ϕ between v_t and a reference direction. We assume that the distribution function is independent of ϕ. (Note that this is different from the assumption of isotropic velocity distribution, because we still have two velocity coordinates, rather than only one.) So the velocity space volume element is $d^3\mathbf{v} = 2\pi v_t\,dv_t\,dv_r$, a thin ring of height dv_r, radius v_t and thickness dv_t. The full coordinate system can thus be written (r, v_r, v_t).

We can now transform the two velocity coordinates into two new coordinates, (E, R), where $E \equiv \psi(r) - \frac{1}{2}(v_r^2 + v_t^2)$ is (minus) the specific energy ("dynamicists' sign convention") and ψ is (minus) the gravitational potential; $R \equiv J^2/J_{\rm c}(E)^2$, where $J = v_t r$ is the specific angular momentum, and $J_{\rm c}(E)$ is the specific angular momentum of a circular orbit of energy E (equal to $GM_{\rm BH}/(2E)^{1/2}$ for a Keplerian potential). This coordinate system is useful because the relaxation time (see §4.3.3 and eq. [4.36]) is typically much longer than an orbital period ($t_{\rm rel} \gg t_{\rm dyn}$), so E and R change little over an orbital period (i.e., are approximately independent of r), and thus can treated as action variables, while r is the angle variable (in which the motion is periodic).

The transformation from velocity $\mathbf{v} = (v_r, v_t\cos\phi, v_t\sin\phi)$ to $\mathbf{v} = (E, R, \phi)$ is made via

$$v_r = \sqrt{2[\psi(r) - E] - \frac{J^2}{r^2}} \tag{4.10}$$

$$v_t\cos\phi = \frac{J}{r}\cos\phi \tag{4.11}$$

$$v_t\sin\phi = \frac{J}{r}\sin\phi\,. \tag{4.12}$$

(We include both eqs. 4.11 and 4.12 just to emphasize the three dimensions of v.) The differential velocity element is

$$d^3\mathbf{v} = (\det\mathcal{J})\,dE\,dR\,d\phi = -\frac{{J_{\rm c}}^2 dE\,dR\,d\phi}{2v_r r^2}\,, \tag{4.13}$$

where $\mathcal{J}$ is the Jacobian matrix for the transformation. Since $d^3\mathbf{v}$ is independent of ϕ, we integrate $\int_0^{2\pi} d\phi$. We also multiply by 2 because there are two radial velocities of opposite sign that correspond to the same $(E, R; r)$ (and drop the minus sign, which is present because r increases outwards and E increases inwards). Thus we obtain

$$d^3\mathbf{v} = \frac{2\pi {J_{\rm c}}^2\,dE\,dR}{v_r r^2}\,. \tag{4.14}$$

(We could also have derived this using $d^3\mathbf{v} = 2\pi v_t\,dv_t\,dv_r$, along with $v^2 = v_r^2 + v_t^2$ and $dE = v\,dv$.)

We now can write the phase space volume element

$$d\mathcal{V} = d^3\mathbf{r}\,d^3\mathbf{v} = \frac{8\pi^2 {J_{\rm c}}^2}{v_r}\,dE\,dR\,dr\,. \tag{4.15}$$

The differential number of stars having coordinates $(E, R; r)$ is thus

$$\frac{d^3N}{dE\,dR\,dr} = \frac{8\pi^2 {J_c}^2}{v_r} f(E, R; r)\,; \tag{4.16}$$

We can calculate the differential number having coordinates (E, R) by integrating from pericenter r_- to apocenter r_+ (alternatively called the radial turning points if the potential is non-Keplerian),

$$\frac{d^2N}{dE\,dR} = \int_{r_-}^{r_+} \frac{8\pi^2 {J_c}^2}{v_r} f(E, R; r)\,dr\,. \tag{4.17}$$

If we take the orbital velocity of an imaginary star and project it onto the radial direction, we find that a star spends an amount of time $2dr/v_r$ per orbit at radii between r and $r + dr$ (the 2 appears because stars pass the same r twice each orbit), and so

$$2\int_{r_-}^{r_+} \frac{dr}{v_r} = P(E)\,, \tag{4.18}$$

where $P(E)$ is the orbital period at energy E. In general, P could be a function of E and R, but for almost-radial orbits close to the disruption zone, we may approximate $P(E, R)$ by $P(E) \equiv P(E, 0)$. Thus,

$$\frac{d^2N}{dE\,dR} = 4\pi^2 {J_c}^2(E) P(E) f(E, R)\,, \tag{4.19}$$

where $f(E, R)$ is the distribution function averaged over an orbital period.

When calculating diffusion coefficients in §4.3.3, we will make the useful assumption that the stellar velocity distribution is isotropic: i.e., f depends only on v^2 or E, but not on R. Under this approximation, the relationship between number density n and distribution function f is simple, since $d^3\mathbf{v} = 4\pi v^2\,dv$ and $dE = -v\,dv$ with $v = \sqrt{2(\psi - E)}$, and $(0, \sqrt{2\psi})$ are the limiting values for the velocity v of a bound[4] star:

$$\begin{aligned} n(r) &= \int_0^{\sqrt{2\psi}} f(v)\,d^3\mathbf{v} = 4\pi \int_0^{\sqrt{2\psi}} f(v) v^2\,dv \\ &= 4\pi \int_0^{\psi} f(E)\left[2\,(\psi - E)\right]^{1/2}\,dE\,. \end{aligned} \tag{4.20}$$

The distribution function can be inferred from the density by differentiating this equation with respect to ψ to obtain

$$\frac{1}{\sqrt{8}\pi}\frac{d\rho}{d\psi} = m\int_0^{\psi} \frac{f(E)}{\sqrt{\psi - E}}\,dE\,, \tag{4.21}$$

[4]Any unbound stars originally present are expected to have left the region close to the disruption zone long ago; new unbound stars could be gravitationally scattered into this region, but we assume that this rate is negligible.

which is an Abel integral equation with solution (called Eddington's formula)

$$f(E) = \frac{1}{\sqrt{8}\pi^2 m}\frac{d}{dE}\int_0^E \frac{d\rho}{d\psi}\frac{d\psi}{\sqrt{E-\psi}}\,. \tag{4.22}$$

We now use equation (4.20) to show for a Keplerian potential ($r \ll r_{\rm h}$ or $E \gg \sigma_{\rm h}^2$; see below) that if the distribution function is

$$f(E) = (2\pi\sigma_{\rm h}^2)^{-3/2} n_0 \frac{\Gamma(\alpha+1)}{\Gamma(\alpha-\frac{1}{2})}\left(\frac{E}{\sigma_{\rm h}^2}\right)^{\alpha-\frac{3}{2}}, \frac{1}{2} < \alpha < 3\,, \tag{4.23}$$

then the number density of stars is $n(r) = n_0(r/r_{\rm h})^{-\alpha}$ (where $r_{\rm h}$ is the radius of influence of the BH, and $\sigma_{\rm h}^2 = GM_{\rm BH}/r_{\rm h}$ is the velocity dispersion there). We show this by integrating $f(E)$ in equation (4.20) using the substitution $t = 1 - rE/GM_{\rm BH}$ and the result

$$\int_0^1 t^{1/2}(1-t)^{\alpha-3/2}\,dt = B\left(\frac{3}{2}, \alpha-\frac{1}{2}\right) = \frac{\Gamma(\frac{3}{2})\Gamma(\alpha-\frac{1}{2})}{\Gamma(\alpha+1)}\,, \tag{4.24}$$

where B is the Euler Beta function, Γ is the Gamma function, and $\Gamma(3/2) = \sqrt{\pi}/2$. Note also the relation

$$n_0 = \frac{M_{\rm BH}}{m}\frac{3-\alpha}{4\pi}\left(\frac{{\sigma_{\rm h}}^2}{GM_{\rm BH}}\right)^3\,, \tag{4.25}$$

where m is the mass of an individual star.

4.3.2 Deriving the Fokker-Planck equation for $(E, R; r)$ space

In the absence of collisions, the distribution function f changes while satisfying the continuity equation in the 6 phase-space coordinates w_α (any coordinate system): f changes locally due only to the divergence of the flow of f (through all 6 dimensions), $\partial f/\partial t = -\nabla_{\mathbf{w}}\cdot\mathbf{F}(\mathbf{w}) = -\nabla_{\mathbf{w}}\cdot(f\dot{\mathbf{w}})$. This is the Boltzmann equation. When stars gravitationally scatter each other, their locations in phase space change discontinuously, and so the flow of the distribution function changes discontinuously. We employ the usual trick of separating how the distribution function changes due to the smooth background potential and that due to stellar encounters (the "graininess" of the potential): the total derivative of the distribution function is instead is equal to the rate of change of f due to encounters, the collision term $\Gamma[f]$. This is the Vlasov equation (BT chapter 8.3),

$$\frac{df}{dt} = \frac{\partial f}{\partial t} + \sum_{\alpha=1}^{6}\frac{\partial(f\dot{w}_\alpha)}{\partial w_\alpha} = \frac{\partial f}{\partial t} + \nabla_{\mathbf{w}}\cdot(f\dot{\mathbf{w}}) \tag{4.26}$$

$$= \frac{\partial f}{\partial t} + \sum_{\alpha=1}^{6}\dot{w}_\alpha\frac{\partial f}{\partial w_\alpha} = \frac{\partial f}{\partial t} + (\dot{\mathbf{w}}\cdot\nabla_{\mathbf{w}})(f) \tag{4.27}$$

$$= \Gamma[f]\,. \tag{4.28}$$

The second line follows from the fact that gravitational acceleration depends only on spatial location and not velocity, so that

$$\sum_{\alpha=1}^{6} \frac{\partial \dot{w}_\alpha}{\partial w_\alpha} = 0\,. \tag{4.29}$$

We now write out the above in the coordinate system (r, E, R) (where terms like $\partial f/\partial\phi$ are assumed to equal zero by symmetry),

$$\frac{df}{dt} = \frac{\partial f}{\partial t} + v_r\frac{\partial f}{\partial r} + \dot{E}\frac{\partial f}{\partial E} + \dot{R}\frac{\partial f}{\partial R} = \Gamma[f] \tag{4.30}$$

We will look for steady-state solutions, so $\partial f/\partial t = 0$. Additionally, since R is a constant of motion for a spherical potential and E is a constant of motion for any static potential, we have $\dot{R} = \dot{E} = 0$, and so

$$\frac{df}{dt} = v_r\frac{\partial f}{\partial r}\,. \tag{4.31}$$

To evaluate the collision term $\Gamma[f]$, we make the approximation that most gravitational encounters are weak, meaning that most encounters have impact parameter $b \gg b_{\rm min}$, where $b_{\rm min} \equiv Gm/v^2$ is the impact parameter which produces an order-unity velocity change. Then we can Taylor expand $\Gamma[f]$ in small $\mathbf{r}$ and small $\mathbf{v}$. We make an additional approximation that $b \ll L$, where L is a typical length-scale of the system (say, the BH's radius of influence, or radius of the bulge). This is the "local approximation," meaning that encounters are short compared to an orbital period, and so we can use the impulse approximation. This means that we can say that $\mathbf{v}$ (which is a function of E and R) changes in an encounter, but $\mathbf{r}$ does not. (Note that the weak encounters approximation is required to obtain the Fokker-Planck equation, but the local approximation is not.) Neglecting diffusion in r, the collision term $\Gamma[f]$ can be written

$$\begin{aligned}\Gamma[f] \;=\; & -\frac{\partial}{\partial E}[\langle\Delta E\rangle f] - \frac{\partial}{\partial R}[\langle\Delta R\rangle f] + \frac{1}{2}\frac{\partial^2}{\partial E^2}[\langle(\Delta E)^2\rangle f] \\ & + \frac{1}{2}\frac{\partial^2}{\partial E\partial R}[\langle\Delta E\Delta R\rangle f] + \frac{1}{2}\frac{\partial^2}{\partial R^2}[\langle(\Delta R)^2\rangle f]\,,\end{aligned} \tag{4.32}$$

where the diffusion coefficient $\langle\Delta E\rangle$ is defined as the expectation per unit time of the change in E (and corresponding definitions for the other diffusion coefficients).

Next we recognize that although stars diffuse in both E and J^2 with the same characteristic timescale $t_{\rm rel}$, diffusion in J^2 is the dominant contributor to consumption by the BH: for all but the most tightly bound stars (of which there are very few), the boundary of the tidal disruption zone (loss cone[5], "lc") is almost independent of E,

$$J_{\rm lc}^2 \equiv 2GM_{\rm BH}r_{\rm T}\left(1 - \frac{E}{GM_{\rm BH}/r_{\rm T}}\right) \approx 2GM_{\rm BH}r_{\rm T} \tag{4.33}$$

[5] The shape of the disruption region is a cone in velocity space, but close to a cylinder in (E, R) space.

since $E \ll GM_{\rm BH}/r_{\rm T}$ for all but the closest-in stars. The geometry of the velocity space we are considering is a solid of revolution, having circular cross-sections of varying radius: the vertical coordinate is E, radial coordinate is J^2 with maximum radius ${J_{\rm c}}^2(E)$, and azimuthal coordinate ϕ is the angle between v_t and a reference direction (again, the distribution function is assumed to be independent of ϕ). The disruption zone is a vertical tube in the middle of the cylinder with an almost constant radius $J_{\rm lc}^2$. Therefore, another way to say the argument is that for almost all stars, E has to grow by much more than unity for a star to enter the disruption zone, which thus takes much longer than $t_{\rm rel}$ (rather, it takes $\sim t_{\rm rel}(GM_{\rm BH}/Er_{\rm T})$); by contrast, a star needs to lose only order unity of its angular momentum to be disrupted, which takes only $t_{\rm rel}$. Most disrupted stars therefore originate from large radii ($r \gg r_{\rm T}$), having a large orbital apocenter and entering the disruption zone on a near-radial orbit: $R_{\rm lc} \equiv J_{\rm lc}^2/{J_{\rm c}}^2 \ll 1$ for most stars.

Therefore, we neglect energy diffusion in the Fokker-Planck equation (4.32), and only consider diffusion in R. Dropping $\partial/\partial E$ terms, we obtain:

$$\frac{df}{dt} = \frac{\partial}{\partial R}\left[-\langle \Delta R\rangle f + \frac{1}{2}\frac{\partial}{\partial R}(\langle (\Delta R)^2\rangle f)\right] . \tag{4.34}$$

4.3.3 Diffusion coefficients

Next we consider the diffusion coefficients, $\langle \Delta R\rangle$ and $\langle (\Delta R)^2\rangle$, which measure the expectation value per time of changes in the stellar velocities. The basic diffusion coefficients (the components of $\langle \Delta v\rangle$ and $\langle \Delta v^2\rangle$, from which other diffusion coefficients can be calculated) are calculated by considering how a single interaction between a test star and field star (both of mass m for simplicity) changes their relative velocity V_0. This velocity change is averaged over different angular orientations to obtain $(\overline{\Delta v_i})_\theta$; then it is integrated over all possible field star velocities $\mathbf{v_a}$ and impact parameters b—weighted by the frequency $\nu_{\rm scat}$ of such encounters[6], $n\sigma V_0 = (f\,\mathbf{d^3 v_a})(2\pi b\,db)V_0$,

$$\langle \Delta v_i\rangle = \int (\overline{\Delta v_i})_\theta (f\,\mathbf{d^3 v_a})(2\pi b\,db)V_0\,. \tag{4.35}$$

To simplify the calculations, two assumptions are made about the background distribution function f. First, we assume that f is spatially homogeneous[7] , i.e., does not depend on spatial location, and so is independent of b. Second, we assume that the background distribution function is isotropic, which means f depends only on $|v|$ (or equivalently on E), but not on R. To justify this, we will look ahead to a result from §4.3.5, equation (4.56) for $f(E,R)$. For angular momenta far outside the disruption zone[8] $R \gg R_{\rm lc}$, with $R_{\rm lc} \ll 1$

[6]Note that σ here is a cross section for gravitational scattering, not a velocity dispersion; we use that symbol in this way only here, to clarify the scattering frequency.

[7] This is equivalent to assuming that most encounters are short-range enough that the densities at the locations of the test star and perturbing star are not very different.

[8]Note that at the same time as we assume an isotropic *background* distribution function, we will still be taking the limit of $R \ll 1$ for the *test* star to simplify calculations.

(so ${R_{\rm lc}}^{-1} \gg 1$), we have $\ln(R/R_{\rm lc}) = \ln R + \ln {R_{\rm lc}}^{-1} \approx \ln {R_{\rm lc}}^{-1}$, so $f(E,R) \approx f(E,R=1)$, independent of R; additionally, we find that $f(E,R=1)$ is approximately equal to the distribution function averaged over R. We call this average background distribution function $\bar{f}(E)$, and use it for all diffusion coefficient calculations.

In a single (weak) encounter, most of the velocity change is perpendicular to the direction of motion: the acceleration is $\sim Gm/b^2$ and the duration of the encounter is $\sim b/V_0$, so $\delta v_\perp \sim V_0(Gm/bV_0^2)$. The velocity change along the direction of motion is smaller because the interaction is almost symmetric: the test star spends almost as much time being pulled forward by the field star (while it approaches) as it does being pulled backward (as it recedes). The time *difference*, due to the test star's slightly longer path away because of $\delta v_\perp$, leads to a slowing of $\delta v_\parallel \sim \delta v_\perp (Gm/bV_0^2) \sim V_0(Gm/bV_0^2)^2$. However, averaged over many encounters at random orientations, $\langle \Delta v_\perp \rangle = 0$, while $\langle \Delta v_\parallel \rangle$ is not. The squared velocity change $\delta v_\perp^2 \sim V_0^2(Gm/bV_0^2) \sim V_0 \delta v_\parallel$ is also non-zero. Another way to say this is that since the distribution function is isotropic, there is only one unique direction in velocity space: the velocity vector of the test star being scattered; there are thus only three (non-zero) independent velocity diffusion coefficients, $\langle \Delta v_\parallel \rangle$, $\langle \Delta v_\parallel^2 \rangle$, and $\langle \Delta v_\perp^2 \rangle$. The quantities $v_\parallel$, $v_\parallel^2$ and $v_\perp^2$ diffuse on a similar timescale, the relaxation timescale $t_{\rm rel}$,

$$t_{\rm rel} \sim \nu_{\rm scat}^{-1} \left(\frac{bV_0^2}{Gm}\right)^2 \sim \frac{v^3}{G^2 m^2 n}\,, \tag{4.36}$$

as we already saw in equation (4.3). Therefore both first- and second-order diffusion coefficients have similar magnitudes (i.e., the second-order diffusion coefficients cannot be dropped relative to the first-order terms in the Fokker Planck equation [4.32 and 4.34]); third-order quantities like $v_\perp^3$, however, diffuse on a timescale that is longer by (bV_0^2/Gm), and so can be neglected. BT (8-64) evaluates the first- and second-order diffusion coefficients; for example,

$$\langle \Delta v_\perp^2 \rangle = \frac{32}{3}\pi^2 G^2 m^2 \ln\Lambda \left(3I_{1/2} - I_{3/2} + 2I_0\right) \sim \frac{v^2}{t_{\rm rel}}\,, \tag{4.37}$$

where

$$\begin{aligned} I_0 &\equiv \int_v^{\sqrt{2\psi(r)}} v_a \bar{f}(v_a)\, dv_a \\ I_{n/2} &\equiv v^{-n} \int_0^v v_a^{n+1} \bar{f}(v_a)\, dv_a\,. \end{aligned} \tag{4.38}$$

The integrals here can be written[9]

$$\begin{aligned} I_0 &\equiv \int_0^E \bar{f}(E')\, dE' \\ I_{n/2} &\equiv [2(\psi(r)-E)]^{-\frac{n}{2}} \int_E^{\psi(r)} [2(\psi(r)-E')]^{\frac{n}{2}}\, \bar{f}(E')\, dE'\,. \end{aligned} \tag{4.39}$$

[9]Note that we assume stars are bound, so that $v < \sqrt{2\psi}$; this assumption is not made in Binney & Tremaine (1987) (8-64), where the upper bound for I_0 is instead ∞.

The quantities $v\langle\Delta v_\parallel\rangle$ and $\langle\Delta v_\parallel^2\rangle$ are the same order of magnitude as $\langle\Delta v_\perp^2\rangle$, but with different velocity-weighted distribution function integrals (which are $\sim n/v$).

We start by calculating $\langle\Delta v_t^2\rangle$, since $\langle\Delta R\rangle = r^2\langle\Delta v_t^2\rangle/{J_\mathrm{c}}^2$. (Remember that the diffusion coefficients for R are defined holding E and r constant, because our coordinate system is $(E, R; r)$). Because $\bar{f}$ is isotropic, $v_t^2 = v_x^2 + v_y^2$ with v_x and v_y the (normal) velocity components in an *arbitrary* plane; therefore,

$$\begin{aligned}\Delta v_t^2 &= \Delta(v_x^2 + v_y^2) \\ &= 2v_x\Delta v_x + 2v_y\Delta v_y + 2\Delta v_x\Delta v_x + 2\Delta v_y\Delta v_y\,. \end{aligned} \tag{4.40}$$

We evaluate this using Binney & Tremaine (1987) (8-65)[10], which gives the velocity diffusion coefficents with respect to an arbitrarily oriented coordinate system in terms of $\langle\Delta v_\parallel\rangle$, $\langle\Delta v_\parallel^2\rangle$, and $\langle\Delta v_\perp^2\rangle$:

$$\begin{aligned}\langle\Delta v_t^2\rangle &= \langle\Delta v_\perp^2\rangle + \frac{v_t^2}{v^2}\left[2v\langle\Delta v_\parallel\rangle + \langle\Delta v_\parallel^2\rangle - \frac{1}{2}\langle\Delta v_\perp^2\rangle\right] \\ &\approx \langle\Delta v_\perp^2\rangle \end{aligned} \tag{4.41}$$

because $R \ll 1$ implies that $v_t^2 \ll v^2$. Physically, the assumption of low angular momentum means that almost all of the test star's velocity is in the radial direction, and so v_t is almost perpendicular to the test star's velocity; thus $\langle\Delta v_t^2\rangle \approx \langle\Delta v_\perp^2\rangle$.

Next we consider the diffusion coefficient $\langle(\Delta R)^2\rangle \equiv \langle\Delta R\Delta R\rangle = r^4\langle\Delta v_t^2\Delta v_t^2\rangle/{J_\mathrm{c}}^4$. Using equation (4.40) and dropping terms third-order and higher,

$$\Delta v_t^2\Delta v_t^2 = 4v_x^2(\Delta v_x)^2 + 4v_y^2(\Delta v_y)^2 + 8v_xv_y\Delta v_x\Delta v_y\,, \tag{4.42}$$

and so (using BT 8-65 again)

$$\begin{aligned}\Delta v_t^2\Delta v_t^2 &= 2v_t^2\left[\langle\Delta v_\perp^2\rangle + \frac{4v_t^2}{v^2}\left[\langle\Delta v_\parallel^2\rangle - \frac{1}{2}\langle\Delta v_\perp^2\rangle\right]\right] \\ &\approx 2v_t^2\langle\Delta v_\perp^2\rangle\,, \end{aligned} \tag{4.43}$$

again because $v_t^2 \ll v^2$ for low-angular momentum orbits. Therefore,

$$\langle(\Delta R)^2\rangle \approx 2R\langle\Delta R\rangle \tag{4.44}$$

and

$$\langle\Delta R\rangle = \frac{1}{2}\frac{\partial}{\partial R}\langle(\Delta R)^2\rangle\,. \tag{4.45}$$

We then define μ, which is thus a function of E and r but not R:

$$\mu \equiv \lim_{R\to 0}\frac{\langle(\Delta R)^2\rangle}{2R} = \langle\Delta R\rangle = \frac{r^2\langle\Delta v_\perp^2\rangle}{{J_\mathrm{c}}^2} \sim \frac{1}{t_\mathrm{rel}}\,. \tag{4.46}$$

[10]Note that Binney & Tremaine (1987) uses the notation $D(\Delta v)$ where Cohn & Kulsrud (1978),Magorrian & Tremaine (1999) (and we) use $\langle\Delta v\rangle$.

4.3.4 The Fokker-Planck equation, continued

Using the above results for the diffusion coefficients, equation (4.34) becomes

$$\frac{df}{dt} = v_r \frac{\partial f}{\partial r} = \Gamma[f] = \mu \frac{\partial}{\partial R}\left(R \frac{\partial f}{\partial R}\right) . \tag{4.47}$$

It is now useful to change variables from r to the time-like coordinate τ:

$$\tau \equiv \left[\int_{r_-}^{r} \frac{\mu\, dr}{v_r}\right] \Big/ 2\left[\int_{r_-}^{r_+} \frac{\mu\, dr}{v_r}\right] \equiv \left[\int_{r_-}^{r} \frac{\mu\, dr}{v_r}\right] \Big/ P(E)\bar{\mu}(E) \tag{4.48}$$

where $r_\pm$ are the apocenter and pericenter of an orbit of energy E and angular momentum R, $\bar{\mu}(E)$ is orbit-averaged normalized diffusion coefficient[11], and we have again assumed $R \ll 1$ in estimating the orbital period (see eq. 4.18). (The factor of 2 accounts for the orbital motion from pericenter to apocenter and back to pericenter again.) The values $\tau = 0, 1, 2, ...$ correspond to successive pericenter passages of an imaginary star of energy E and angular momentum R. Note that in a Keplerian potential,

$$r_\pm = \frac{GM}{2E}\left[1 \pm \sqrt{1-R}\right] \tag{4.49}$$

because the orbital semi-major axis is $a = GM_{\rm BH}/2E$ and the orbital eccentricity is $e = \sqrt{1-R}$. We now transform variables using

$$\frac{d\tau}{dr} = \frac{1}{P\bar{\mu}} \frac{d}{dr} \int_{r_-}^{r} \frac{\mu\, dr'}{v_r} = \frac{1}{P\bar{\mu}} \frac{\mu}{v_r} \tag{4.50}$$

(by the Fundamental Theorem of Calculus), so that

$$\frac{\partial f}{\partial \tau} = P\bar{\mu} \frac{\partial}{\partial R}\left(R \frac{\partial f}{\partial R}\right) . \tag{4.51}$$

Additionally, using equation (4.50), note that the differential volume element can be written

$$d\mathcal{V} = 4\pi^2 {J_{\rm c}}^2(E) P(E) \frac{\bar{\mu}(E)}{\mu(\tau, E)}\, d\tau\, dR\, dE\, . \tag{4.52}$$

We now introduce another variable, $y \equiv R/P\bar{\mu}$:

$$\frac{\partial f}{\partial \tau} = \frac{\partial}{\partial y}\left(y \frac{\partial f}{\partial y}\right) , \tag{4.53}$$

[11] Despite the assumption of homogeneous background distribution made in calculating the diffusion coefficients like $\langle \Delta v_\perp^2 \rangle$, orbit-averaging is required to calculate $\bar{\mu}$ because $\bar{\mu} \propto r^2$ and the integral bounds in $\langle \Delta v_\perp^2 \rangle$ (eq. 4.37) contain r as well.

and then make one more variable change, $x \equiv \sqrt{y}$, so we have

$$\frac{\partial f}{\partial \tau} = \frac{1}{4x}\frac{\partial}{\partial x}\left(x\frac{\partial f}{\partial x}\right) = \frac{1}{4}\nabla_x^2 f\,, \tag{4.54}$$

where the Laplacian is in cylindrical coordinates, and changes in f are independent of both azimuthal coordinate ϕ and vertical coordinate E. (We have made many variable changes at this point, but note that x simply is proportional to the orbital angular momentum.) This equation now has the form of the heat equation, where x is the radial coordinate and τ is the time coordinate. Note that over one orbit ($\tau = 0-1$), f diffuses by order unity in x, i.e., R changes by $P\bar{\mu}$, or J changes by $(P\bar{\mu})^{1/2}J_{\rm c} \sim (t_{\rm dyn}/t_{\rm rel})^{1/2}J_{\rm c}$, as expected by our simpler analysis (§4.2).

4.3.5 The distribution function outside the tidal disruption zone

We start by solving equation (4.51) for f outside the tidal disruption zone $R > R_{\rm lc}$. Since f changes with respect to R on timescales much longer than an orbital period, we can consider in $\partial f/\partial\tau$ only changes due to orbital motion. Far outside the loss region ($R_{\rm lc} \ll R \sim 1$), orbits are close to circular, and so $\partial f/\partial\tau \approx 0$ (stars spend similar fractions of time at all phases of their orbit, so f does not vary much with τ). We therefore solve equation (4.51) setting $\partial f/\partial\tau = 0$, which gives the correct limiting behavior for $R \sim 1$. However, we will extend this solution down to $R_{\rm lc} \ll 1$ where it may no longer be valid.

So now we solve

$$0 = P\bar{\mu}\frac{\partial}{\partial R}\left(R\frac{\partial f}{\partial R}\right) \tag{4.55}$$

on $R := (R_{\rm lc}, 1)$ and find

$$f(E,R) = f(E,R_{\rm lc}) + \frac{f(E,1)-f(E,R_{\rm lc})}{\ln R_{\rm lc}^{-1}}\ln(R/R_{\rm lc})\,,\quad R_{\rm lc} \le R \le 1\,. \tag{4.56}$$

We can calculate $f(E,1)$ from the mean R-integrated distribution function,

$$\begin{aligned}
\bar{f}(E) &\approx \frac{\int_{R_{\rm lc}}^1 f(E,R)\,dR}{\int_{R_{\rm lc}}^1 dR} \\
&= (1-R_{\rm lc})^{-1}\left[f(E,R_{\rm lc})(1-R_{\rm lc}) + \frac{f(E,1)-f(E,R_{\rm lc})}{\ln {R_{\rm lc}}^{-1}}\left(\ln {R_{\rm lc}}^{-1} - 1 + R_{\rm lc}\right)\right] \\
&\approx f(E,1)\,,
\end{aligned} \tag{4.57}$$

since $R_{\rm lc} \ll 1$. The mean distribution function $\bar{f}(E)$ can be calculated for real galaxies; e.g., for a galaxy with a power-law density profile, we can use equation (4.23) (inside the radius of influence).

4.3.6 The distribution function inside the tidal disruption zone

Inside the tidal disruption zone, orbit-averaging is not appropriate, because stars survive until pericenter and are then removed (disrupted). So we separately solve equation (4.54) on $x := (0, x_{\rm lc})$, where $x_{\rm lc} \equiv (R_{\rm lc}/P\bar{\mu})^{1/2}$. The initial condition is

$$f(E, x, \tau = 0) = 0\,, \tag{4.58}$$

because a star whose orbital pericenter falls below $r_{\rm T}$ (i.e., x falls below $x_{\rm lc}$) is removed when the star reaches pericenter. In the mathematical language of this section, the region inside $x < x_{\rm lc}$ is empty ($f = 0$) at $\tau = 0$; as τ increases, stars can diffuse into the region so f increases; but when $\tau = 1$, all stars in the region are removed so that $f = 0$ again, and the process repeats. So we solve the equation on the time interval $\tau := (0, 1^-)$.

The boundary conditions use the solution from the previous section, equation (4.56), saying that f is continuous at $R_{\rm lc}$, and that the time-averaged (i.e., orbit-averaged) flow rate through $R_{\rm lc}$ (see the next section §4.3.7) is continuous. The problem is mathematically equivalent to the transfer of heat in a solid cylinder of radius $x_{\rm lc}$ where the outer radius is held at a constant value $f(E, x_{\rm lc})$ (to be determined later), and the inner region $x < x_{\rm lc}$ has $f = 0$ for $\tau = 0$. We will however, be starting by solving the problem with simpler boundary and initial conditions, and then transforming it to our actual problem of interest.

We begin by separating equation (4.54), so that $f(\tau, x) = T(\tau)X(x)$, and

$$\frac{4}{T}\frac{dT}{d\tau} = \frac{1}{X}\frac{d^2X}{dx^2} + \frac{1}{xX}\frac{dX}{dx} = -\beta^2\,, \tag{4.59}$$

where β is an eigenvalue. This becomes separate equations for T and for X:

$$-\frac{\beta^2}{4}T = \frac{dT}{d\tau} \tag{4.60}$$

$$0 = \frac{d^2X}{dx^2} + \frac{1}{x}\frac{dX}{dx} + \beta^2 X\,. \tag{4.61}$$

The former equation is easily solved: $T = c_1\, e^{-\beta^2\tau/4}$, where c_1 is a constant (that will be absorbed into our constants a_m later). The latter equation is a form of Bessel's differential equation (of order zero); it is simplified by the substitution $z = \beta x$,

$$0 = \frac{d^2X}{dz^2} + \frac{1}{z}\frac{dX}{dz} + X\,. \tag{4.62}$$

The eigenfunctions for Bessel's equation (of order zero) are $J_0(z)$ and $Y_0(z)$, Bessel functions of the first and second kind; since we are interested in the domain including $z \to 0$, but $Y_0(z) \to \infty$ as $z \to 0$, we reject the $Y_0(z)$ eigenfunctions. The solution is therefore a linear combination of terms $J_0(\beta x)$, for various values of β.

To determine the eigenvalues β, we start by considering *homogeneous* boundary conditions (essentially the opposite of our actual boundary conditions): $f(x_{\rm lc}) = 0$ for all τ and

$f(x < x_{\rm lc}) = C$ at $\tau = 0$. The first condition tells us that $J_0(\beta x_{\rm lc}) = 0$; we thus obtain an infinite number of the eigenvalues β_m, where $\beta_m x_{\rm lc}$ is the mth zero of J_0. By superposition, we are looking for solutions of the form

$$f(E, x, \tau) = \sum_{m=1}^{\infty} a_m e^{-\beta_m^2 \tau/4} J_0(\beta_m x)\,, \tag{4.63}$$

where the values of a_m are determined by the initial conditions, $f(E, x < x_{\rm lc}, \tau = 0) = C$. The Bessel functions $J_0(\beta_m x)$ form an orthogonal set with weighting x, i.e.,

$$\int_0^{x_{\rm lc}} x J_0(\beta_m x) J_0(\beta_n x)\, dx = \delta_{mn} \frac{{x_{\rm lc}}^2}{2} J_1^2(\beta_m x_{\rm lc}) \equiv N \tag{4.64}$$

(N is the normalization), and so decomposing our initial condition into an infinite series of Bessel functions

$$f(E, x, \tau = 0) = C = \sum_{m=1}^{\infty} a_m J_0(\beta_m x)\,, \tag{4.65}$$

we find the values of a_m,

$$\begin{aligned} a_m &= N^{-1} \int_0^{x_{\rm lc}} C x J_0(\beta_m x)\, dx \\ &= \frac{2}{{x_{\rm lc}}^2 J_1^2(\beta_m x_{\rm lc})} \times \frac{C x_{\rm lc} J_1(\beta_m x_{\rm lc})}{\beta_m} \\ &= \frac{2C}{\beta_m x_{\rm lc} J_1(\beta_m x_{\rm lc})}\,, \end{aligned} \tag{4.66}$$

where we have used the Bessel function property

$$\int_0^u u' J_0(u')\, du' = u J_1(u)\,. \tag{4.67}$$

The solution to the homogeneous boundary value problem is therefore equation (4.63) with the a_m values from equation (4.66).

We can now transform this solution to the *homogeneous* problem into a solution for our actual boundary conditions. We do this by subtracting the homogeneous solution from the solution to the *steady-state* problem with our actual boundary conditions, which is simply $f(E, x < x_{\rm lc}, \tau) = f(E, x_{\rm lc})$. The value of C in our homogeneous problem should likewise be $f(E, x_{\rm lc})$. Our solution is therefore (Özişik 1993, chapter 3, especially p119)

$$f(E, x, \tau) = f(E, x_{\rm lc}) \left[1 - \frac{2}{x_{\rm lc}} \sum_{m=1}^{\infty} \frac{e^{-\beta_m^2 \tau/4}}{\beta_m} \frac{J_0(\beta_m x)}{J_1(\beta_m x_{\rm lc})} \right]\,, \quad 0 \le \tau < 1\,; \quad 0 \le x \le x_{\rm lc}\,. \tag{4.68}$$

4.3.7 Flow rates in phase space

To connect the solutions outside and inside the disruption region, we shall require that flow rates through phase space are continuous at $R_{\rm lc}$. The flow rate at a point $\mathbf{w}$ in phase space is $\mathbf{F}(\mathbf{w}) = f\dot{\mathbf{w}}$, and so the flow rate *through* an entire *surface* of constant $w_\alpha = w^*$ is $\mathbf{F}(\mathbf{w}) \cdot \hat{\mathbf{w}}_\alpha = f\dot{w}_\alpha$ integrated over the five-dimensional surface area. The differential element of surface area of constant w_α is $d\mathcal{V}/dw_\alpha$ (just as $dV = 4\pi r^2\,dr$ is the differential volume element in space, and $dV/dr = 4\pi r^2$ is the surface area at constant r). The flow rate is therefore

$$F_{w_\alpha}(w^*) = \int \left[(f\dot{w}_\alpha)\frac{d\mathcal{V}}{dw_\alpha}\right]_{w_\alpha = w^*} . \tag{4.69}$$

Looking ahead, our ultimate goal is to calculate the flow rate through the surface of constant $\tau = 1^-$, for angular momenta between R and $R + dR$ (with $R < R_{\rm lc}$) and energies between E and $E + dE$: we'll call this rate of stars reaching orbital pericenter $\gamma \equiv F_\tau(1^-)$. This flow rate is thus

$$\gamma = \int_E^{E+dE}\int_R^{R+dR} \left[(f\dot{\tau})\,4\pi^2 {J_{\rm c}}^2 P\frac{\bar{\mu}}{\mu}\,dR'\,dE'\right]_{\tau=1^-} ; \tag{4.70}$$

since $\dot{\tau} = \dot{r}(d\tau/dr) = v_r(\mu/\bar{\mu}Pv_r) = \mu/\bar{\mu}P$, we have simply

$$\frac{d^2\gamma}{dE\,dR} = 4\pi^2 {J_{\rm c}}^2 f(E, R, \tau = 1^-) . \tag{4.71}$$

In terms of the pericenter distance $r_{\rm p}$ corresponding to R,

$$R \approx \frac{2GM_{\rm BH}r_{\rm p}}{{J_{\rm c}}^2} \tag{4.72}$$

(applying our assumption that $E \ll GM_{\rm BH}/r_{\rm p}$), we can re-write equation (4.71)

$$\frac{d^2\gamma}{dE\,d\ln r_{\rm p}} = 8\pi^2 GM_{\rm BH}r_{\rm p}\,f\left(E, R(r_{\rm p}), \tau = 1^-\right) . \tag{4.73}$$

This is the equation we will ultimately use to calculate the tidal disruption rate as a function of pericenter distance in §4.4.

Along the way, we shall also need to calculate the flow rate across the surface of constant $R = R_{\rm lc}$, integrated over all spatial locations r_- to r_+ (i.e., integrated over τ from 0 to 1^-) for energies between E and $E + dE$,

$$\begin{aligned} F_R(R_{\rm lc}) &= \int \left[(\mathbf{F}\cdot\hat{\mathbf{R}})\,\frac{d\mathcal{V}}{dR}\right]_{R=R_{\rm lc}} \\ &= \int_E^{E+dE}\int_0^{1^-} (\mathbf{F}\cdot\hat{\mathbf{R}})\,4\pi {J_{\rm c}}^2 P\frac{\bar{\mu}}{\mu}\,d\tau\,dE' . \end{aligned} \tag{4.74}$$

It is helpful here to use the Divergence Theorem. We draw a closed surface with sides $R = R_{\rm lc}$, $E' = E$, $E' = E + dE$ in velocity space, and $\tau = 0 - 1^-$ spatially: the rate of change of f integrated throughout the enclosed volume is equal to the flux through the closed surface, which is the quantity we seek, $F_R(R_{\rm lc})$,

$$\begin{aligned} F_R(R_{\rm lc}) &= \int (\nabla_{\mathbf{w}} \cdot \mathbf{F})\, d\mathcal{V} \\ &= \int_E^{E+dE} \int_0^{1^-} \int_0^{R_{\rm lc}} (\nabla_{\mathbf{w}} \cdot \mathbf{F})\, 4\pi^2 {J_{\rm c}}^2 P \frac{\bar{\mu}}{\mu}\, dR\, d\tau\, dE' \,. \end{aligned} \tag{4.75}$$

(We continue to assume that flow along $\hat{E}$ into the disruption zone is negligible, so the "endcap" surfaces of constant E and $E+dE$ do not contribute to $(\nabla_{\mathbf{w}} \cdot \mathbf{F})$ inside the region.) The Vlasov equation (4.30) says that the divergence of the flow in phase space is given by the collision rate ($\nabla_{\mathbf{w}} \cdot \mathbf{F} = \Gamma[f]$), so using equation (4.47) for $\Gamma[f]$, we have

$$F_R(R_{\rm lc}) = 4\pi^2 {J_{\rm c}}^2\, dE \int_0^{1^-} \int_0^{R_{\rm lc}} P\bar{\mu} \frac{\partial}{\partial R} \left(R \frac{\partial f}{\partial R} \right) dR\, d\tau \,. \tag{4.76}$$

We can write this result in two ways, integrating first over τ or first over R. To integrate over τ, we rewrite the integrand as $\partial f / \partial \tau$ and use the fact that $f(E, R, \tau = 0) = 0$ for $R < R_{\rm lc}$, so

$$\begin{aligned} F_R(R_{\rm lc}) &= 4\pi^2 {J_{\rm c}}^2\, dE \int_0^{R_{\rm lc}} f(E, R, \tau = 1^-)\, dR \\ &= 8\pi^2 {J_{\rm c}}^2 P\bar{\mu}\, dE \int_0^{x_{\rm lc}} x f(E, x, \tau = 1^-)\, dx \,. \end{aligned} \tag{4.77}$$

(Note that the flow rate to pericenter [equation 4.71] can also be found with equation [4.77], replacing the upper bound with R and differentiating with respect to R.) We can also write equation [4.76] using the fact that $\partial f / \partial R = 0$ at $R = 0$ (because we have required that f be smooth there) and that $R(\partial f / \partial R)$ is (at least approximately) constant with respect to τ at $R_{\rm lc}$:

$$\begin{aligned} F_R(R_{\rm lc}) &= 4\pi^2 {J_{\rm c}}^2 P\bar{\mu}\, dE \int_0^{1^-} \left[R \frac{\partial f}{\partial R} \right]_{R=R_{\rm lc}} d\tau \\ &= 4\pi^2 {J_{\rm c}}^2 P\bar{\mu}\, dE \left[R \frac{\partial f}{\partial R} \right]_{R=R_{\rm lc}} . \end{aligned} \tag{4.78}$$

4.3.8 Calculating $f(R_{\rm lc})$

We now evaluate $f(R_{\rm lc})$ by requiring that $F_R(R_{\rm lc})$ be continuous between the outer solution (eqs. [4.56] and [4.78])

$$F_R({R_{\rm lc}}^+) = 4\pi^2 {J_{\rm c}}^2 P\bar{\mu} \frac{f(E, R = 1) - f(E, R_{\rm lc})}{\ln {R_{\rm lc}}^{-1}} \tag{4.79}$$

and the inner solution (eqs. [4.68] and [4.77]),

$$F_R({R_{\rm lc}}^-) = 8\pi^2 {J_{\rm c}}^2 P\bar{\mu} f(E, R_{\rm lc}) \times \int_0^{x_{\rm lc}} x \left[1 - \frac{2}{x_{\rm lc}} \sum_{m=1}^{\infty} \frac{e^{-\beta_m^2/4}}{\beta_m} \frac{J_0(\beta_m x)}{J_1(\beta_m x_{\rm lc})}\right] dx\,. \tag{4.80}$$

Noting equation (4.67) and $P\bar{\mu}{x_{\rm lc}}^2 = R_{\rm lc}$, the flow rate from the inner solution is

$$\begin{aligned} F_R({R_{\rm lc}}^-) &= 4\pi^2 {J_{\rm c}}^2 R_{\rm lc} f(E, R_{\rm lc}) \left(1 - 4\sum_{m=1}^{\infty} \frac{e^{-\alpha_m^2 q/4}}{\alpha_m^2}\right) \\ &\equiv 4\pi^2 {J_{\rm c}}^2 R_{\rm lc} f(E, R_{\rm lc}) \xi(q)\,, \end{aligned} \tag{4.81}$$

where we have made several new definitions. We have defined $\alpha_m \equiv \beta_m x_{\rm lc}$, and

$$\xi(q) \equiv 1 - 4\sum_{m=1}^{\infty} \frac{e^{-\alpha_m^2 q/4}}{\alpha_m^2}\,. \tag{4.82}$$

We also have defined $q(E) \equiv {x_{\rm lc}}^{-2} = P\bar{\mu}/R_{\rm lc}$, the square of the ratio of a star's angular change over an orbital time $[\theta_{\rm dyn} = (t_{\rm dyn}/t_{\rm rel})^{1/2} \sim (P\bar{\mu})^{1/2}]$ divided by the angular size of the tidal disruption zone ($\theta_{\rm lc} = J_{\rm lc}/J_{\rm c} = {R_{\rm lc}}^{1/2}$),

$$q(E) = \left(\frac{\theta_{\rm dyn}}{\theta_{\rm lc}}\right)^2\,. \tag{4.83}$$

Comparing equations (4.79) and (4.81), we find

$$f(E, R_{\rm lc}) = \frac{f(E, R=1)}{1 + q^{-1}\xi(q) \ln {R_{\rm lc}}^{-1}}\,, \tag{4.84}$$

where $f(E, R=1)$ can be approximated as $\bar{f}(E)$, derivable from observations of galactic nuclei. We also find the limiting behavior of $\xi(q)$,

$$\lim_{q\to 0} \frac{q}{\xi(q)} = \frac{\sqrt{\pi q}}{2}\,. \tag{4.85}$$

As an aside, note that Cohn & Kulsrud (1978) and MT write the flow rate across $R_{\rm lc}$ as[12]

$$F_R({R_{\rm lc}}^+) = 4\pi^2 {J_{\rm c}}^2(E) P(E) \bar{\mu}(E) \frac{f(E, R=1)}{\ln R_0^{-1}}\,, \tag{4.86}$$

[12]Note that the outer distribution function in equation (4.56) extrapolated inside $R_{\rm lc}$ is *not* equal to the actual distribution function inside $R_{\rm lc}$ (eq. 4.68), and so the former cannot be used to calculate the disruption rate there.

where R_0 is the $f = 0$ intercept of the *outside* solution (eq. 4.56) *extrapolated* inside $R_{\rm lc}$. Cohn & Kulsrud (1978) and Magorrian & Tremaine (1999) write an approximate expression for R_0 (a limit of which was first derived by Baldwin et al. 1972 for a plasma mirror machine):

$$R_0 = R_{\rm lc} \times \begin{cases} e^{-q}, & q > 1 \\ e^{-0.186q - 0.824\sqrt{q}}, & q < 1\,. \end{cases} \tag{4.87}$$

Comparing equation (4.86) with (4.79) using (4.84), we find the more exact expression

$$R_0 = R_{\rm lc} e^{-q/\xi(q)}\,, \tag{4.88}$$

so that the overall flow rate is

$$F_R({R_{\rm lc}}^+) = 8\pi^2 G M_{\rm BH} r_{\rm T} \frac{q f(E, R=1)}{\xi^{-1} q + \ln {R_{\rm lc}}^{-1}}\,. \tag{4.89}$$

Equation (4.88) approximately reduces to equation (4.87) in the limits $q \gg 1$ and $q \ll 1$. For $q \gg 1$, $\xi \approx 1$ and so $R_0 \approx R_{\rm lc} e^{-q}$. For $q \ll 1$, $q/\xi \approx \sqrt{\pi q}/2 \approx 0.886\sqrt{q}$, similar to the result in (4.87) for small q: the term $0.186q$ is negligible compared to $0.824\sqrt{q}$ for $q \ll 1$, and is part of the fit to make the function [almost] continuous at $q = 1$).

4.4 Tidal disruption rate as a function of pericenter distance

We now have everything we need to calculate the tidal disruption rate as a function of pericenter distance! The answer is equation (4.73), using equations (4.68) and (4.84), integrated over energy E. We collect those here again for easy reference:

$$\frac{d^2\gamma}{dE\, d\ln r_{\rm p}} = 8\pi^2 G M_{\rm BH} r_{\rm p}\, f\big(q(E), u(r_{\rm p}), \tau = 1^-\big) \tag{4.90}$$

$$f(q, u, \tau = 1^-) = f(q, R_{\rm lc}) \left[1 - 2\sum_{m=1}^{\infty} \frac{e^{-\alpha_m^2 q/4}}{\alpha_m} \frac{J_0(\alpha_m u)}{J_1(\alpha_m)}\right],\ 0 \le u \le 1 \tag{4.91}$$

$$f(q, R_{\rm lc}) = \frac{\bar{f}(E)}{1 + q^{-1}\xi(q) \ln {R_{\rm lc}}^{-1}} \tag{4.92}$$

$$q(E) = \frac{P(E)\bar{\mu}(E)}{R_{\rm lc}(E)} \tag{4.93}$$

$$u(r_{\rm p}) \approx \left(\frac{r_{\rm p}}{r_{\rm T}}\right)^{1/2}, \tag{4.94}$$

where I have defined $u \equiv q^{-1/2} x$, so that $u = 1$ at $r_{\rm p} = r_{\rm T}$. In the limit of $q \gg 1$, $f(\tau = 1^-)$ is

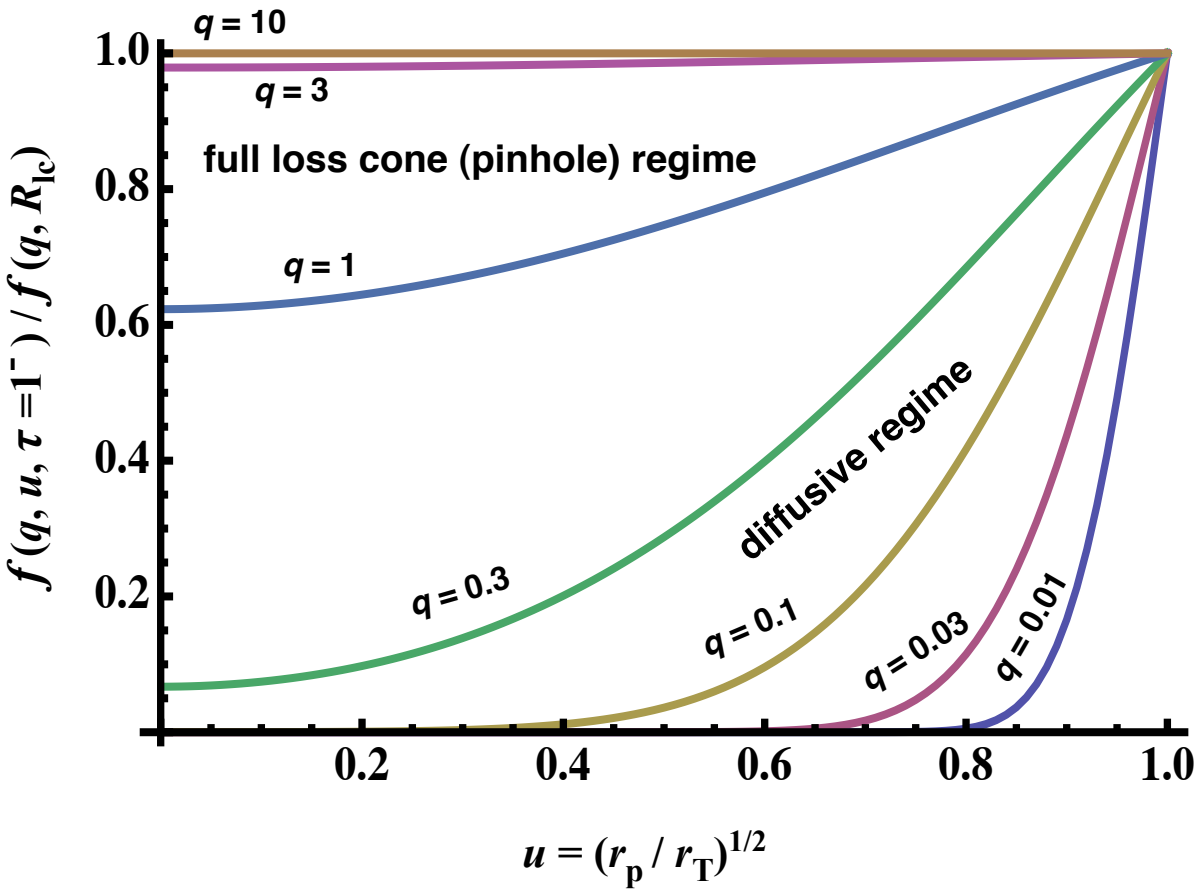

Figure 4.1: Normalized tidal disruption rate as a function of pericenter distance $f(q, u, \tau = 1^-)/f(q, R_{\rm lc})$ for $q = 0.01, 0.03, 0.1, 0.3, 1, 3, 10$. In the diffusive regime ($q \ll 1$), stars can only diffuse a small distance into the loss region; in the full loss cone (pinhole) regime ($q \gg 1$), stars can diffuse all the way across the loss region, so the normalized rate is flat.

independent of u, since $e^{-\alpha_m^2 q/4} \to 0$ and $J_0(\alpha_m u)$ is finite. Therefore $(d^2\gamma/dE\, d\ln r_{\rm p}) \propto r_{\rm p}$, as expected for the pinhole (full loss cone) regime. Figure 4.1 plots the normalized rate $f(q, u, \tau = 1^-)/f(q, R_{\rm lc})$ for various energies corresponding to different values of q, as a function of u which is proportional to the orbital angular momentum. In the diffusive regime ($q \ll 1$), stars can diffuse only a distance $\Delta J \sim (t_{\rm dyn}/t_{\rm rel})^{1/2} J_{\rm c} = q^{1/2} J_{\rm c}$ into the loss region—and so the normalized rate in the figure falls to 1/2 over a normalized angular momentum $\Delta u \sim q^{1/2}/2$. In the full loss cone (pinhole) regime ($q \gg 1$), stars can diffuse in a dynamical time a distance much wider than the loss region, and so the normalized rate is flat.

Calculating $d\gamma/d\ln r_{\rm p}$ requires adding up the curves in Figure 4.1, weighting appropri-

ately by the number of stars at each energy—which is the challenge:

$$\frac{d\gamma}{d\ln r_{\rm p}} = 8\pi^2 G M_{\rm BH} r_{\rm p} \times \int_{E_{\rm min}}^{GM_{\rm BH}/r_{\rm T}} \frac{\bar{f}(E)}{1+q(E)^{-1}\xi(q(E))\ln R_{\rm lc}(E)^{-1}} \left[1 - 2\sum_{m=1}^{\infty} \frac{e^{-\alpha_m^2 q(E)/4}}{\alpha_m} \frac{J_0(\alpha_m u)}{J_1(\alpha_m)}\right] dE\,. \quad (4.95)$$

When evaluating this integral, we must confirm that the integral bound $E_{\rm max}$ does not dominate the rate, because our assumption that stars diffuse only in R (not E) breaks down there. (Additionally, other processes like resonant relaxation may be important at these small radii.) Equation (4.95) shows that the tidal disruption rate requires calculating several quantities: (1) the angular size of the disruption zone $R_{\rm lc}$, (2) the mean (R-averaged) distribution function $\bar{f}(E)$, and (3) the relationship between q and E. We calculate $q(E)$ using equations (4.46) and (4.37) for $\mu(r,E)$ and then orbit-integrating (recalling that ${J_{\rm lc}}^2 = 2GM_{\rm BH}r_{\rm T}$):

$$\begin{aligned} q(E)J_{\rm lc}^2 &= P(E)\bar{\mu}(E){J_{\rm c}}^2(E) = 2\lim_{R\to 0}\int_{r_-}^{r_+} \frac{r^2\langle\Delta v_\perp^2\rangle}{v_r}\,dr \\ &= \frac{64}{3}\pi^2 G^2 m^2 \ln\Lambda \int_0^{r_{\psi=E}} \frac{r^2}{\sqrt{2(\psi(r)-E)}}\left(3I_{1/2} - I_{3/2} + 2I_0\right)\,dr\,, \end{aligned} \quad (4.96)$$

where we have defined $r_{\psi=E}$ such that $\psi(r_{\psi=E}) = E$ (i.e., the orbital apocenter in the limit of low angular momentum $R \to 0$).

4.4.1 Keplerian potential with power-law density profile

In this subsection, we demonstrate the methodology for calculating $d^2\gamma/dE\,d\ln r_{\rm p}$ for the region well inside the radius of influence of the BH $r_{\rm h}$; here, the gravitational potential is approximately Keplerian, so the calculations are simpler and analytic. Because the overall disruption rate is typically dominated by $r \sim r_{\rm h}$, the results of this subsection are not sufficient to fully calculate $d\gamma/d\ln r_{\rm p}$; instead we show them as a simpler warm-up for the more complicated full calculations of §4.4.2.

We will typically want to calculate $d\gamma/d\ln r_{\rm p}$ for a power-law density distribution, $n(r) = n_0(r/r_{\rm h})^{-\alpha}$, so that we have $\bar{f}(E)$ from equation (4.23). To simplify algebra, we define $f_{\rm h} \equiv [\Gamma(\alpha+1)/\Gamma(\alpha-\frac{1}{2})](2\pi\sigma_{\rm h}^2)^{-3/2}n_0$ so that $\bar{f}(E) = f_{\rm h}(E/{\sigma_{\rm h}}^2)^{\alpha-3/2}$. Using the substitution $t = 1 - rE/GM_{\rm BH}$ in equation (4.39), we have

$$I_0 = \frac{f_{\rm h}{\sigma_{\rm h}}^2}{\alpha - 1/2}\left(\frac{E}{{\sigma_{\rm h}}^2}\right)^{\alpha-1/2} \quad (4.97)$$

$$I_{n/2} = f_{\rm h}{\sigma_{\rm h}}^2\left(1-\frac{rE}{GM_{\rm BH}}\right)^{-n/2}\left(\frac{GM_{\rm BH}}{r{\sigma_{\rm h}}^2}\right)^{\alpha-1/2} B\left(1-\frac{rE}{GM_{\rm BH}};\frac{n}{2}+1,\alpha-\frac{1}{2}\right) \quad (4.98)$$

where B is here the Incomplete Euler Beta function. Note that for $\alpha = 3/2$, we have simply

$$I_0 = f_{\rm h} E \tag{4.99}$$

$$I_{n/2} = \left(\frac{n}{2}+1\right)^{-1} f_{\rm h}\left(\frac{GM_{\rm BH}}{r} - E\right) . \tag{4.100}$$

Next we calculate $P\bar{\mu} \equiv 2\int_{r_-}^{r_+} \mu/v_r \, dr$. Recalling equation (4.46), we orbit-integrate I_0 and $I_{n/2}$ weighting by r^2; we take the limit of $R \ll 1$ so that $v_r \approx v = \sqrt{2GM_{\rm BH}/r - E}$, $r_+ \approx GM_{\rm BH}/E$, and $r_- \approx 0$. Therefore,

$$\int_{r_-}^{r_+} \frac{r^2 I_0}{v_r}\, dr = \frac{5\pi}{8\sqrt{2}} \frac{f_{\rm h}\sigma_{\rm h}}{\alpha - 1/2} \left(\frac{GM_{\rm BH}}{{\sigma_{\rm h}}^2}\right)^3 \left(\frac{E}{{\sigma_{\rm h}}^2}\right)^{\alpha-4} \tag{4.101}$$

$$\int_{r_-}^{r_+} \frac{r^2 I_{n/2}}{v_r}\, dr = \frac{f_{\rm h}\sigma_{\rm h}}{\sqrt{2}} \left(\frac{GM_{\rm BH}}{{\sigma_{\rm h}}^2}\right)^3 \left(\frac{E}{{\sigma_{\rm h}}^2}\right)^{\alpha-4} I_B(\frac{n}{2}, \alpha) , \tag{4.102}$$

where we define

$$I_B(\frac{n}{2}, \alpha) \equiv \int_0^1 t^{-\frac{n+1}{2}} (1-t)^{3-\alpha} B(t; \frac{n}{2}+1, \alpha - \frac{1}{2})\, dt , \tag{4.103}$$

which has the special value $I_B(\alpha = 3/2) = \frac{\pi}{16}/(\frac{n}{2}+1)$. Finally we obtain

$$q(E) = \nu \left(\frac{E}{{\sigma_{\rm h}}^2}\right)^{\alpha-4} , \tag{4.104}$$

where (using $R_{\rm lc} = 2GM_{\rm BH} r_{\rm T}$ and replacing $f_{\rm h}$)

$$\nu = \frac{8\sqrt{\pi}}{3}(3-\alpha)\frac{\Gamma(\alpha+1)}{\Gamma(\alpha-\frac{1}{2})} \left[\frac{5}{32(\alpha-\frac{1}{2})} + \frac{3I_B(\frac{1}{2},\alpha) - I_B(\frac{3}{2},\alpha)}{4\pi}\right] \left(\frac{Gm}{{\sigma_{\rm h}}^2 r_{\rm T}}\right) \ln\Lambda , \tag{4.105}$$

and we follow Spitzer & Hart (1971) in taking $\Lambda = 0.4 M_{\rm BH}/m$. The derivative of E is

$$-\frac{dE}{dq} = \frac{{\sigma_{\rm h}}^2}{4-\alpha} \nu^{\frac{1}{4-\alpha}} q^{-\frac{\alpha-5}{\alpha-4}} . \tag{4.106}$$

We now have the ingredients to calculate the tidal disruption rate as a function of pericenter distance and q for energies well inside the radius of influence,

$$\frac{d^2\gamma}{d\ln q\, d\ln r_{\rm p}} = 8\pi^2 GM_{\rm BH} r_{\rm p} \frac{q\bar{f}(E(q))}{1 + q^{-1}\xi(q)\ln R_{\rm lc}(E(q))^{-1}} \left[1 - 2\sum_{m=1}^{\infty} \frac{e^{-\alpha_m^2 q/4}}{\alpha_m} \frac{J_0(\alpha_m u)}{J_1(\alpha_m)}\right] \left(-\frac{dE}{dq}\right) \tag{4.107}$$

In Figure 4.2, we plot $d^2\gamma/d\ln q\, d\ln r_{\rm p}$ as a function of normalized angular momentum u for $M_{\rm BH} = 10^6 M_\odot$, $\sigma_{\rm h} = 100\,{\rm km\,s^{-1}}$ and $\alpha = 2$. This plot is essentially the same as in Figure

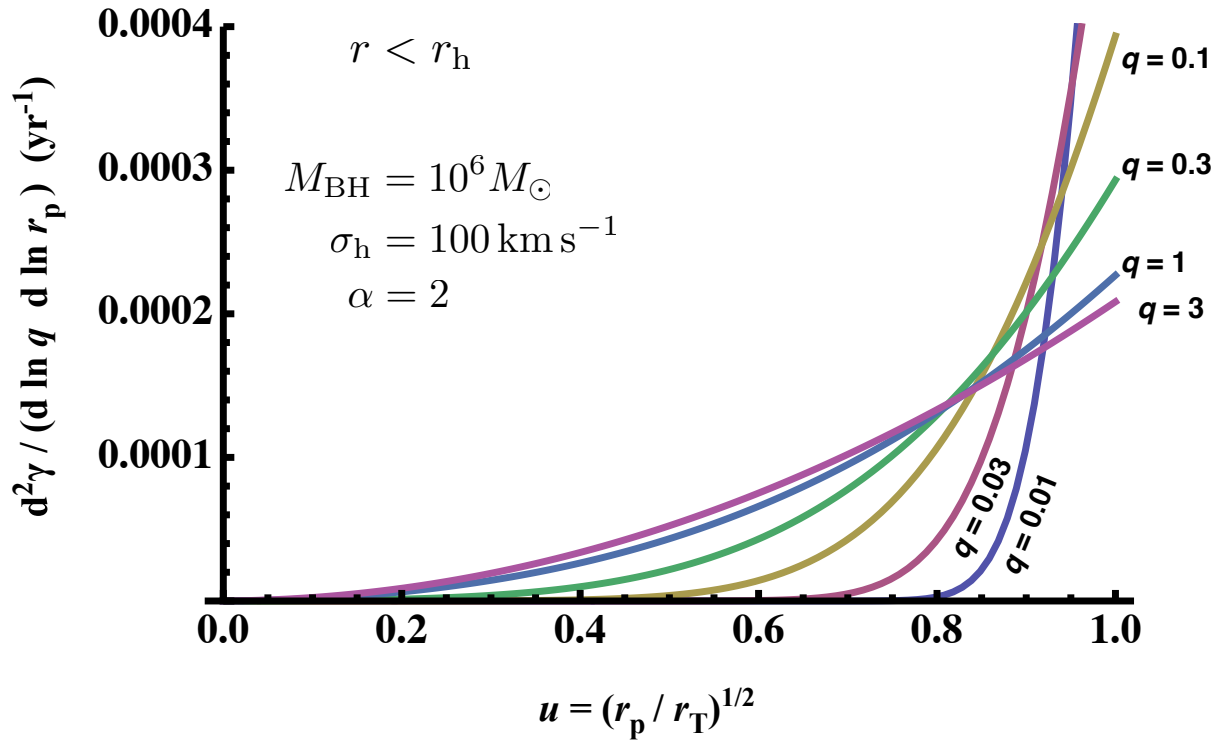

Figure 4.2: Tidal disruption rate per energy as a function of pericenter distance $d^2\gamma/d\ln q\, d\ln r_\mathrm{p}$ for $M_\mathrm{BH} = 10^6 M_\odot$, $\sigma_\mathrm{h} = 100\,\mathrm{km\,s^{-1}}$ and $\alpha = 2$. Results are shown for values of q corresponding to energies inside the BH's radius of influence $q_\mathrm{h} = 3.5$, so that Keplerian approximations can be made. The full loss cone regime dominates $r_\mathrm{p} \ll r_\mathrm{T}$, while the diffusive regime dominates $r_\mathrm{p} \sim r_\mathrm{T}$.

4.1 but with appropriate weighting of the curves according to the number of stars at each value of q. The radius of influence $E = \sigma_\mathrm{h}^2$ is at $q_\mathrm{h} = \nu = 3.5$, so we only plot q values less than this. Values of $q \gtrsim 1$ in the full loss cone regime dominate $d^2\gamma/d\ln q\, d\ln r_\mathrm{p}$ at $r_\mathrm{p} \ll r_\mathrm{T}$, while values of $q \lesssim 1$ in the diffusive regime dominate $r_\mathrm{p} \sim r_\mathrm{T}$. The closer we approach r_T, the smaller the value of q that dominates. The overall rate is $\gamma \sim$ few $\times\, 10^{-4}\,\mathrm{yr}^{-1}$, in line with results in Wang & Merritt (2004). The shape of the curve found by summing these curves is approximately proportional to r_p at $r_\mathrm{p} \ll r_\mathrm{T}$ and rises at $r_\mathrm{p} \sim r_\mathrm{T}$, as expected from §4.2. To calculate $d\gamma/d\ln r_\mathrm{p}$ properly, however, we need to include energies $E < E_\mathrm{h}$ outside the radius of influence, where the potential is no longer Keplerian.

4.4.2 The non-Keplerian potential

In the previous section, we considered radii close to the BH where the gravitational potential is dominated by the BH's gravity—but a considerable fraction of the disrupted stars likely comes from radii outside r_h where the potential is dominated by the stars. We write our results as functions of the stellar density distribution (which can be inferred from

the surface brightness profile; see eq. 4.123), continuing to assume spherical symmetry and isotropic velocity distribution far (in R-space) from the disruption zone.

To calculate the angular size of the disruption zone, we must account for the non-Keplerian potential in calculating the orbital angular momentum ${J_c}^2(E)$,

$$R_{\rm lc}(E) = \frac{J_{\rm lc}^2}{{J_c}^2(E)} = \frac{2GM_{\rm BH}r_{\rm T}}{G\left[M_{\rm BH} + M_{{\rm enc},*}(r_c)\right] r_c}\,, \tag{4.108}$$

where r_c is the radius corresponding to a circular orbit with energy E, i.e., r_c satisfies $E = \psi(r_c) - G(M_{\rm BH} + M_{{\rm enc},*})/2r_c$. The stellar mass enclosed by r is $M_{{\rm enc},*}$, defined below in equation (4.129). We calculate $f(E)$ using equation (4.22). We must also account for the non-Keplerian potential in calculating $q(E)$: equation (4.96) shows that we need to calculate (and then orbit-average) the quantity $\left(3I_{1/2} - I_{3/2} + 2I_0\right)$, using the correct potential and distribution function in equations (4.39).

We spend the rest of this subsection analytically developing numerically tractable formulas for $f(E)$ and $q(E)$, with the aim of applying them to real galaxies with measured surface brightness profiles and measured BH masses. Wang & Merritt (2004) calculated disruption rates γ for the 51 elliptical galaxies presented in Faber et al. (1997) (using more accurate BH masses than Magorrian & Tremaine 1999), assuming spherical symmetry and isotropic velocity dispersion; in the following subsection, we apply our results to one of these galaxies. The overall methodology presented here is far more detailed than in Wang & Merritt (2004), though the spirit is the same. The goal is essentially to calculate $\psi(r)$ and $\bar{f}(E)$ from the data for individual galaxies. Although we use the surface brightness parametrization of Faber et al. (1997) (the "Nuker Law"), the results we present are general to any (radially symmetric) surface brightness profile and need only change the surface brightness derivatives in equation (4.125).

Faber et al. (1997) fit the surface brightness profile $\mathcal{I}$ of each galaxy in units of $\mathrm{erg\,s^{-1}\,cm^{-2}\,sr^{-1}}$ with the function

$$\mathcal{I}(\mathcal{R}) = \mathcal{I}_b 2^{(\beta-\Gamma)/\alpha} \left(\frac{\mathcal{R}}{r_b}\right)^{-\Gamma} \left[1 + \left(\frac{\mathcal{R}}{r_b}\right)^{\alpha}\right]^{-(\beta-\Gamma)/\alpha}\,, \tag{4.109}$$

where $\mathcal{R}$ is the projected radius from the center of the galaxy. The parameters α, β, Γ and r_b are given in Faber et al. (1997) and Wang & Merritt (2004); also given are the dimensionless visual mass-to-light ratio $\Upsilon_V \equiv (M/M_\odot)/(L/L_{\odot,V})$, and μ_b, the surface brightness at r_b in visual magnitudes per arcsec^2, so that

$$\mathcal{I}_b = (206265)^2 \frac{L_{\odot,V}}{(10\,\mathrm{pc})^2}\, 10^{\frac{1}{2.5}(M_{{\rm Sun},V} - \mu_b)}\,, \tag{4.110}$$

where $M_{{\rm Sun},V} = 4.83$ is the visual absolute magnitude of the sun.

To simplify calculations, throughout we: (1) make variable substitutions that remove variables from integral bounds, (2) differentiate analytically within integrands (when necessary) to avoid numerical differentiation (which is much less reliable than numerical integration), and (3) and we non-dimensionalize our variables. In particular, we express densities

in terms of the density scale at r_b,

$$\rho_0 \equiv \frac{\Upsilon_V \mathcal{I}_b M_\odot}{r_b L_{\odot,V}} = \frac{1}{r_b}\frac{M_\odot}{(10\,\mathrm{pc})^2}(206265)^2 \Upsilon_V 10^{\frac{1}{2.5}(M_{\mathrm{sun},V}-\mu_b)}\,. \tag{4.111}$$

The relationships between dimensional and non-dimensional variables are thus:

$$\begin{aligned}
\mathcal{I} &= \mathcal{I}_b\tilde{\mathcal{I}} && (4.112)\\
\mathcal{R} &= r_b\tilde{\mathcal{R}} && (4.113)\\
r &= r_b\tilde{r} && (4.114)\\
\rho(r) &= \rho_0\tilde{\rho}(\tilde{r}) && (4.115)\\
M_{\mathrm{BH}} &= \rho_0 r_b^3 \tilde{M}_{\mathrm{BH}} && (4.116)\\
M_{\mathrm{enc},*}(r) &= \rho_0 r_b^3 \tilde{M}_{\mathrm{enc},*}(\tilde{r}) && (4.117)\\
E &= G\rho_0 r_b^2 \tilde{E} && (4.118)\\
\psi(r) &= G\rho_0 r_b^2 \tilde{\psi}(\tilde{r}) && (4.119)\\
\bar{f}(E) &= \frac{1}{\sqrt{G^3\rho_0} m r_b^3}\tilde{\bar{f}}(\tilde{E}) && (4.120)\\
I_n(E,r) &= \frac{\sqrt{\rho_0}}{m r_b\sqrt{G}}\tilde{I}_n(\tilde{E},\tilde{r}) && (4.121)\\
J_{\mathrm{c}}^2(E) &= G\rho_0 r_b^4 \tilde{J}_{\mathrm{c}}^2(\tilde{E}) && (4.122)
\end{aligned}$$

Assuming spherical symmetry, we can calculate the density profile (which can be re-written conveniently without $\tilde{r}$ in the integral bounds using the dimensionless variable θ),

$$\tilde{\rho}(\tilde{r}) = -\frac{1}{\pi}\int_{\tilde{r}}^{\infty}\frac{d\tilde{\mathcal{I}}}{d\tilde{\mathcal{R}}}\frac{d\tilde{\mathcal{R}}}{\sqrt{\tilde{\mathcal{R}}^2-\tilde{r}^2}} = -\frac{1}{\pi}\int_0^1 \frac{d\tilde{\mathcal{I}}}{d\tilde{\mathcal{R}}}\left(\tilde{\mathcal{R}}=\frac{\tilde{r}}{\theta}\right)\frac{d\theta}{\theta\sqrt{1-\theta^2}}\,. \tag{4.123}$$

Note that for radii $\tilde{r} \ll r_{\mathrm{h}}/r_b$, $\tilde{\rho}(\tilde{r}) \propto \tilde{r}^{-\Gamma-1}$, and for $\tilde{r} \gg 1$, $\tilde{\rho}(\tilde{r}) \propto \tilde{r}^{-\beta-1}$. The derivative of the density is

$$\frac{d\tilde{\rho}}{d\tilde{r}} = -\frac{1}{\pi}\int_0^1 \frac{d\tilde{\mathcal{I}}}{d\tilde{\mathcal{R}}}\left(\tilde{\mathcal{R}}=\frac{\tilde{r}}{\theta}\right)\frac{d\theta}{\theta^2\sqrt{1-\theta^2}}\,. \tag{4.124}$$

and the derivatives of the surface brightness profile are

$$\frac{d\tilde{\mathcal{I}}}{d\tilde{\mathcal{R}}} = -2^{\frac{\beta-\Gamma}{\alpha}}\tilde{\mathcal{R}}^{-\Gamma-1}(1+\tilde{\mathcal{R}}^{\alpha})^{-\frac{\beta-\Gamma}{\alpha}-1}(\Gamma+\beta\tilde{\mathcal{R}}^{\alpha}) \tag{4.125}$$

$$\begin{aligned}\frac{d^2\tilde{\mathcal{I}}}{d\tilde{\mathcal{R}}^2} &= 2^{\frac{\beta-\Gamma}{\alpha}}\tilde{\mathcal{R}}^{-\Gamma-2}(1+\tilde{\mathcal{R}}^{\alpha})^{-\frac{\beta-\Gamma}{\alpha}-2} \\ &\quad\times\left[\beta(1+\beta)\tilde{\mathcal{R}}^{2\alpha}+(\beta-\alpha\beta+\Gamma+\alpha\Gamma+2\beta\Gamma)\tilde{\mathcal{R}}^{\alpha}+\Gamma+\Gamma^2\right]\end{aligned} \tag{4.126}$$

$$\begin{aligned}\frac{d^3\tilde{\mathcal{I}}}{d\tilde{\mathcal{R}}^3} &= 2^{\frac{\beta-\Gamma}{\alpha}}\tilde{\mathcal{R}}^{-\Gamma-3}(1+\tilde{\mathcal{R}}^{\alpha})^{-\frac{\beta-\Gamma}{\alpha}-3}\Big[-\beta(1+\beta)(2+\beta)\tilde{\mathcal{R}}^{3\alpha} \\ &\quad+\left\{(-1+\alpha)\beta(4+\alpha+3\beta)-\left(2+\alpha^2+3\alpha(1+\beta)+3\beta(2+\beta)\right)\Gamma\right\}\tilde{\mathcal{R}}^{2\alpha} \\ &\quad+\left\{(1+\alpha)(-4+\alpha-3\Gamma)\Gamma-\beta\left[2+\alpha^2-3\alpha(1+\Gamma)+3\Gamma(2+\Gamma)\right]\right\}\tilde{\mathcal{R}}^{\alpha} \\ &\quad-\Gamma(1+\Gamma)(2+\Gamma)\Big]\,.\end{aligned} \tag{4.127}$$

The gravitational potential (defined such that $\tilde{\psi}(\tilde{r}\to\infty)=0$) is

$$\begin{aligned}\tilde{\psi}(\tilde{r}) &= \frac{\tilde{M}_{\rm BH}}{\tilde{r}}+\frac{4\pi}{\tilde{r}}\int_0^{\tilde{r}}\tilde{\rho}(\tilde{r}')\tilde{r}'^2\,d\tilde{r}'+4\pi\int_{\tilde{r}}^{\infty}\rho(\tilde{r}')\tilde{r}'\,d\tilde{r}' \\ &\equiv \frac{\tilde{M}_{\rm BH}}{\tilde{r}}+\frac{\tilde{M}_{\rm enc,*}(\tilde{r})}{\tilde{r}}+\tilde{\psi}_2(\tilde{r})\,,\end{aligned} \tag{4.128}$$

where

$$\tilde{M}_{\rm enc,*}(\tilde{r}) = -4\int_0^{\tilde{r}}\int_0^1\frac{d\tilde{\mathcal{I}}}{d\tilde{\mathcal{R}}}\left(\tilde{\mathcal{R}}=\frac{\tilde{r}}{\theta}\right)\frac{\tilde{r}'^2}{\theta\sqrt{1-\theta^2}}d\theta\,d\tilde{r}' \tag{4.129}$$

is the stellar mass enclosed by $\tilde{r}$ and

$$\tilde{\psi}_2(\tilde{r}) = -4\int_0^{\tilde{r}}\int_0^1\frac{d\tilde{\mathcal{I}}}{d\tilde{\mathcal{R}}}\left(\tilde{\mathcal{R}}=\frac{\tilde{r}}{\theta}\right)\frac{\tilde{r}'}{\theta\sqrt{1-\theta^2}}d\theta\,d\tilde{r}' \tag{4.130}$$

Note that Γ must be ≤ 2 for finite $M_{\rm enc,*}$ at any $r>0$; this condition is met for all galaxies in Faber et al. (1997). Additionally, β must be >2 for finite $M_{\rm enc,*}$ as $r\to\infty$, which is *not* met for most of these galaxy models; this is of course unphysical and indicates that the mass distribution steepens at larger radii. However, as long as $\beta>1$ (which is true for almost all of these galaxies), the potential ψ is finite as $r\to\infty$—and the integrals presented below are not dominated by $r\to\infty$, so it is a very good approximation to cut off the mass distribution at finite $r\gg r_b$. The scalings for the behavior of functions at $\tilde{r}\gg 1$ and $\tilde{E}\ll 1$ are given below separately for $\beta\geq 2$ and $1<\beta<2$ with the understanding that the behavior in the latter case ultimately transitions to the behavior in the former case at sufficiently large radii.

The relationship in dimensionless units between the density and (isotropic) distribution function is given by (see eq. 4.22)

$$\tilde{\tilde{f}}(\tilde{E}) = \frac{1}{\sqrt{8}\pi^2}\frac{d}{d\tilde{E}}\int_0^{\tilde{E}}\frac{d\tilde{\rho}}{d\tilde{\psi}}\frac{d\tilde{\psi}}{\sqrt{\tilde{E}-\tilde{\psi}}} \equiv \frac{1}{\sqrt{8}\pi^3}\frac{d\tilde{g}(\tilde{E})}{d\tilde{E}}\,. \tag{4.131}$$

We use equation (4.124) and make the substitution $\tilde{r} = \tilde{r}_{\psi=E}/\varphi$ to obtain

$$\begin{aligned}\tilde{g}(\tilde{E}) &= \pi\int_{\infty}^{\tilde{r}_{\psi=E}}\frac{d\tilde{\rho}}{d\tilde{r}}\frac{d\tilde{r}}{\sqrt{\tilde{E}-\tilde{\psi}(\tilde{r})}} = \int_{\tilde{r}_{\psi=E}}^{\infty}\int_0^1\frac{d^2\tilde{\mathcal{I}}}{d\tilde{\mathcal{R}}^2}\biggl(\tilde{\mathcal{R}}=\frac{\tilde{r}}{\theta}\biggr)\frac{1}{\sqrt{\tilde{E}-\tilde{\psi}(\tilde{r})}}\frac{d\theta\,d\tilde{r}'}{\theta^2\sqrt{1-\theta^2}}\\ &= \tilde{r}_{\psi=E}\int_0^1\int_0^1\frac{d^2\tilde{\mathcal{I}}}{d\tilde{\mathcal{R}}^2}\biggl(\tilde{\mathcal{R}}=\frac{\tilde{r}_{\psi=E}}{\theta\varphi}\biggr)\frac{1}{\sqrt{\tilde{E}-\tilde{\psi}(\tilde{r}_{\psi=E}/\varphi)}}\frac{d\theta\,d\varphi}{\varphi^2\theta^2\sqrt{1-\theta^2}}\,. \qquad (4.132)\end{aligned}$$

Note that for $\tilde{E}\gg\tilde{M}_{\rm BH}/(r_{\rm h}/r_b)$, $\tilde{g}(\tilde{E})\propto\tilde{E}^{\Gamma+1/2}$, and for $\tilde{E}\ll 1$, $\tilde{g}(\tilde{E})\propto\tilde{E}^{\beta+1/2}$ ($\beta\geq 2$) or $\tilde{g}(\tilde{E})\propto\tilde{E}^{\frac{\beta+1}{\beta-1}-\frac{1}{2}}$ ($1<\beta<2$). We can use the latter form of $\tilde{g}(\tilde{E})$ to calculate $\tilde{\tilde{f}}(\tilde{E})$ (which is necessary for calculating $f(R_{\rm lc})$ though not necessary for $q(E)$):

$$\begin{aligned}\tilde{\tilde{f}}(\tilde{E}) &= \frac{1}{\sqrt{8}\pi^3}\int_0^1\int_0^1\frac{1}{\sqrt{\tilde{E}-\tilde{\psi}(\tilde{r}_{\psi=E}/\varphi)}} \qquad (4.133)\\ &\quad\times\Bigl[\frac{\tilde{r}_{\psi=E}}{\theta\varphi}\frac{d\tilde{r}_{\psi=E}}{d\tilde{E}}\frac{d^3\tilde{\mathcal{I}}}{d\tilde{\mathcal{R}}^3}\biggl(\tilde{\mathcal{R}}=\frac{\tilde{r}_{\psi=E}}{\theta\varphi}\biggr)+\frac{d\tilde{r}_{\psi=E}}{d\tilde{E}}\frac{d^2\tilde{\mathcal{I}}}{d\tilde{\mathcal{R}}^2}\biggl(\tilde{\mathcal{R}}=\frac{\tilde{r}_{\psi=E}}{\theta\varphi}\biggr)\\ &\quad-\tilde{r}_{\psi=E}\frac{d^2\tilde{\mathcal{I}}}{d\tilde{\mathcal{R}}^2}\biggl(\tilde{\mathcal{R}}=\frac{\tilde{r}_{\psi=E}}{\theta\varphi}\biggr)\frac{1-\frac{1}{\varphi}\frac{d\tilde{\psi}}{d\tilde{r}}(r=\tilde{r}_{\psi=E}/\varphi)\frac{d\tilde{r}_{\psi=E}}{d\tilde{E}}}{2\left[\tilde{E}-\tilde{\psi}(\tilde{r}_{\psi=E}/\varphi)\right]}\Bigr]\frac{d\theta\,d\varphi}{\varphi^2\theta^2\sqrt{1-\theta^2}}\\ &= -\frac{1}{\sqrt{8}\pi^3}\frac{\tilde{r}^2_{\psi=E}}{\tilde{M}_{\rm BH}+\tilde{M}_{{\rm enc},*}(\tilde{r}_{\psi=E})}\int_0^1\int_0^1\frac{1}{\sqrt{\tilde{E}-\tilde{\psi}(\tilde{r}_{\psi=E}/\varphi)}}\Bigl[\frac{\tilde{r}_{\psi=E}}{\theta\varphi}\frac{d^3\tilde{\mathcal{I}}}{d\tilde{\mathcal{R}}^3}+\frac{d^2\tilde{\mathcal{I}}}{d\tilde{\mathcal{R}}^2}\\ &\quad+\tilde{r}^{-1}_{\psi=E}\frac{d^2\tilde{\mathcal{I}}}{d\tilde{\mathcal{R}}^2}\frac{\tilde{M}_{\rm BH}(\varphi-1)+\varphi\tilde{M}_{{\rm enc},*}(\tilde{r}_{\psi=E}/\varphi)-\tilde{M}_{{\rm enc},*}(\tilde{r}_{\psi=E})}{2\left[\tilde{E}-\tilde{\psi}(\tilde{r}_{\psi=E}/\varphi)\right]}\Bigr]\frac{d\theta\,d\varphi}{\varphi^2\theta^2\sqrt{1-\theta^2}}\,,\end{aligned}$$

where derivatives of $\tilde{\mathcal{I}}$ are evaluated at $\tilde{\mathcal{R}}=\tilde{r}_{\psi=E}/\theta\varphi$, and we have used the derivative

$$\frac{d\tilde{r}_{\psi=E}}{d\tilde{E}} = \biggl[\frac{d\tilde{\psi}}{d\tilde{r}}(\tilde{r}=\tilde{r}_{\psi=E})\biggr]^{-1} = -\frac{\tilde{r}^2_{\psi=E}}{\tilde{M}_{\rm BH}+\tilde{M}_{{\rm enc},*}(\tilde{r}_{\psi=E})}\,. \qquad (4.134)$$

For $\tilde{E}\gg\tilde{M}_{\rm BH}/(r_{\rm h}/r_b)$, $\tilde{\tilde{f}}(\tilde{E})\propto\tilde{E}^{\Gamma-1/2}$, and for $\tilde{E}\ll 1$, $\tilde{\tilde{f}}(\tilde{E})\propto\tilde{E}^{\beta-1/2}$ ($\beta\geq 2$) or $\tilde{\tilde{f}}(\tilde{E})\propto\tilde{E}^{\frac{\beta+1}{\beta-1}-\frac{3}{2}}$ ($1<\beta<2$).

Now we calculate the integrals $\tilde{I}_0$ and $\tilde{I}_{n/2}$, using equation (4.39). The former is simply

$$\tilde{I}_0(E) = \int_0^{\tilde{E}}\tilde{\tilde{f}}(\tilde{E}')\,d\tilde{E}' = \frac{1}{\sqrt{8}\pi^3}\tilde{g}(\tilde{E})\,. \qquad (4.135)$$

Next we calculate $\tilde{I}_{n/2}(\tilde{r},\tilde{E})$: integrating equation (4.39) by parts, and then making the

substitution $\tilde{\psi}(\tilde{r}) - \tilde{E}' = (\tilde{\psi}(\tilde{r}) - \tilde{E})\theta$, we have

$$\begin{aligned}
\tilde{I}_{n/2}(\tilde{r},\tilde{E}) &= \left[2(\tilde{\psi}(\tilde{r})-\tilde{E})\right]^{-\frac{n}{2}} \int_{\tilde{E}}^{\tilde{\psi}(\tilde{r})} \left[2(\tilde{\psi}(\tilde{r})-\tilde{E}')\right]^{\frac{n}{2}} \tilde{\tilde{f}}(\tilde{E}')\, d\tilde{E}' \\
&= \frac{1}{\sqrt{8}\pi^3}\left[2(\tilde{\psi}(\tilde{r})-\tilde{E})\right]^{-\frac{n}{2}} \\
&\quad \times \left\{ \left[2(\tilde{\psi}(\tilde{r})-\tilde{E}')\right]^{\frac{n}{2}} \tilde{g}(\tilde{E}')\Big|_{\tilde{E}}^{\tilde{\psi}(\tilde{r})} + n\int_{\tilde{E}}^{\tilde{\psi}(\tilde{r})} \left[2(\tilde{\psi}(r)-\tilde{E}')\right]^{\frac{n}{2}-1} \tilde{g}(\tilde{E}')\, d\tilde{E}' \right\} \\
&= \frac{1}{\sqrt{8}\pi^3}\left[-\tilde{g}(\tilde{E}) + \frac{n}{2}\int_0^1 \theta^{\frac{n}{2}-1}\, g\Big(\tilde{\psi}(\tilde{r})(1-\theta)+\tilde{E}\theta\Big)\, d\theta\right]. \qquad (4.136)
\end{aligned}$$

Then we combine to obtain $(3\tilde{I}_{\frac{1}{2}} - \tilde{I}_{\frac{3}{2}} + 2\tilde{I}_0)$, and find that the terms proportional to $\tilde{g}(\tilde{E})$ cancel out:

$$3\tilde{I}_{1/2} - \tilde{I}_{3/2} + 2\tilde{I}_0 = \frac{3}{\sqrt{32}\pi^3}\int_0^1 \left(\frac{1}{\sqrt{\theta}} - \sqrt{\theta}\right)\, \tilde{g}\Big(\tilde{\psi}(\tilde{r})(1-\theta)+\tilde{E}\theta\Big)\, d\theta\,. \qquad (4.137)$$

We orbit-integrate weighting by $\tilde{r}^2$ to obtain

$$\int_0^{\tilde{r}_{\psi=E}} \frac{\tilde{r}^2}{\sqrt{2(\tilde{\psi}(\tilde{r})-\tilde{E})}}(3\tilde{I}_{1/2} - \tilde{I}_{3/2} + 2\tilde{I}_0)\, d\tilde{r} = \frac{3}{8\pi^2}\tilde{\mathcal{G}}(\tilde{E})\,, \qquad (4.138)$$

where we introduce another dimensionless function

$$\tilde{\mathcal{G}}(\tilde{E}) \equiv \int_0^{\tilde{r}_{\psi=E}}\int_0^1 \frac{\tilde{r}^2}{\sqrt{\tilde{\psi}(\tilde{r})-\tilde{E}}}\left(\frac{1}{\sqrt{\theta}} - \sqrt{\theta}\right)\, g\Big(\tilde{\psi}(\tilde{r})(1-\theta)+\tilde{E}\theta\Big)\, d\theta\, d\tilde{r}\,. \qquad (4.139)$$

Note that for $\tilde{E} \gg \tilde{M}_{\rm BH}/(r_{\rm h}/r_b)$, $\tilde{\mathcal{G}}(\tilde{E}) \propto \tilde{E}^{\Gamma-3}$, and for $\tilde{E} \ll 1$, $\tilde{\mathcal{G}}(\tilde{E}) \propto \tilde{E}^{\beta-3}$ $(\beta \geq 2)$ or $\tilde{\mathcal{G}}(\tilde{E}) \propto \tilde{E}^{\frac{\beta-2}{\beta-1}-1}$ $(1 < \beta < 2)$.

Finally, using these results in equation (4.96) and returning to dimensional units, we obtain

$$\begin{aligned}
q(E) = \frac{P(E)\bar{\mu}(E){J_{\rm c}}^2(E)}{2GM_{\rm BH}r_{\rm T}} &= \frac{32\pi^2G^2m^2}{3GM_{\rm BH}r_{\rm T}}\ln\Lambda\frac{r_b^2}{\sqrt{G\rho_0}}\frac{\sqrt{\rho_0}}{mr_b\sqrt{G}}\frac{3}{8\pi^3}\tilde{\mathcal{G}}(\tilde{E}) \\
&= \frac{4}{\pi}\ln\Lambda\left(\frac{r_b}{r_{\rm T}}\right)\left(\frac{m}{M_{\rm BH}}\right)\tilde{\mathcal{G}}(\tilde{E})\,. \qquad (4.140)
\end{aligned}$$

We follow Spitzer & Hart (1971) and take $\Lambda = 0.4M_{\rm BH}/m$. In terms of our dimensionless distribution function $\tilde{\tilde{f}}(\tilde{E})$, the tidal disruption rate as a function of pericenter distance is therefore

$$\begin{aligned}
\frac{d\gamma}{d\ln r_{\rm p}} &= 8\pi^2\left(\frac{M_{\rm BH}}{m}\right)\left(\frac{r_{\rm T}}{r_b}\right)\sqrt{G\rho_0} \qquad (4.141) \\
&\quad \times \int_{\tilde{E}_{\rm min}}^{\tilde{M}_{\rm BH}r_b/r_{\rm T}} \frac{\tilde{\tilde{f}}(\tilde{E})}{1+q(\tilde{E})^{-1}\xi(q(\tilde{E}))\ln R_{\rm lc}(\tilde{E})^{-1}}\left[1 - 2\sum_{m=1}^{\infty}\frac{e^{-\alpha_m^2 q(\tilde{E})/4}}{\alpha_m}\frac{J_0(\alpha_m u)}{J_1(\alpha_m)}\right]\, d\tilde{E}\,.
\end{aligned}$$

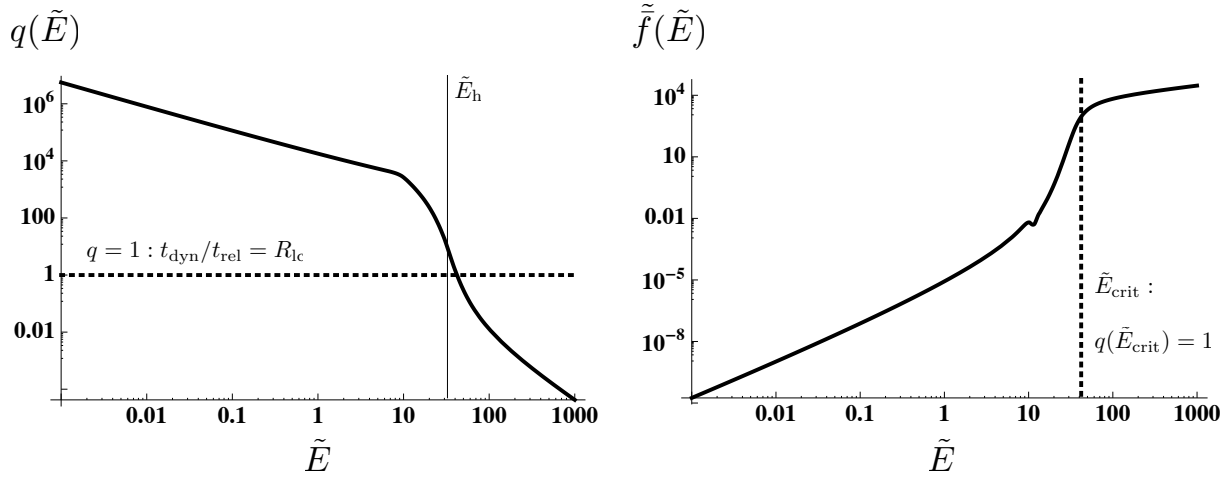

Figure 4.3: Ratio $q(E) \equiv P(E)\bar{\mu}(E)/R_{\rm lc}(E)$ and distribution function $f(E)$ for the galaxy NGC 4467. We plot dimensionless energies $\tilde{E} = E/G\rho_0 r_b^2$, and dimensionless distribution function $\tilde{\tilde{f}} = \sqrt{G^3\rho_0} m r_b^3 f$. Left panel: Lines shows where $q = 1$ (heavy dashed) and the normalized energy $\tilde{E}_{\rm h}$ of a circular orbit at $r_{\rm h} = 0.98\,{\rm pc}$ (thin solid). The energy $\tilde{E}_{\rm crit}$, defined to be where $q = 1$, is close to (and just inside) $\tilde{E}_{\rm h}$, as expected and found by Wang & Merritt (2004). This energy dominates the overall disruption rate. Right panel: Vertical dashed line shows $\tilde{E}_{\rm crit}$. The function $\tilde{f}$ exhibits a "kink" because $\tilde{f}$ is proportional to $d^3\tilde{\mathcal{I}}/d\mathcal{R}^3$: the kink occurs at the energy corresponding to r_b where the surface brightness profile $\tilde{\mathcal{I}}$ transitions (fairly sharply) between power-laws.

4.5 Results: NGC 4467

In this section, we demonstrate application of this methodology to NGC 4467, an elliptical galaxy in the Virgo Cluster that hosts a BH of mass $M_{\rm BH} = 1.1 \times 10^6 M_\odot$ (Wang & Merritt 2004, using the $M_{\rm BH} - \sigma$ relation from Merritt & Ferrarese 2001). The relevant surface brightness parameters presented in Faber et al. (1997) are $\alpha = 7.52$, $\beta = 2.13$, $\Gamma = 0.98$, $\mu_b = 19.98$, and $r_b = 240\,{\rm pc}$, and the mass-to-light ratio is $\Upsilon_V = 6.27$. The density scale is thus $\rho_0 = 9.7 M_\odot\,{\rm pc}^{-3}$ (eq. 4.111), and the normalized BH mass is $\tilde{M}_{\rm BH} = 8.2 \times 10^{-3}$. (Our calculated densities agree with those presented in Table 3 of Faber et al. 1997.) We perform calculations for solar-type stars. Numerical results presented here have been performed with Mathematica 7.01.0.

Figure 4.3 shows $q(\tilde{E})$ (eq. 4.140) and the distribution function $\tilde{\tilde{f}}(\tilde{E})$ (eq. 4.133). We have indicated the energy $\tilde{E}_{\rm crit}$ at which $q = 1$ (see §4.2), which dominates the tidal disruption rate as expected. This energy corresponds to a radius close to (and just inside) the BH's radius of influence, as expected (see first section, also Wang & Merritt 2004).

Figure 4.4 shows our result for the disruption rate as a function of pericenter distance. This rate integrated over all $r_{\rm p}$ (see eq. 4.89) is $\gamma = 8.2 \times 10^{-4}\,{\rm yr}^{-1}$, in reasonable agreement with the result $\gamma = 5.0 \times 10^{-4}\,{\rm yr}^{-1}$ reported in Wang & Merritt (2004). The dotted vertical

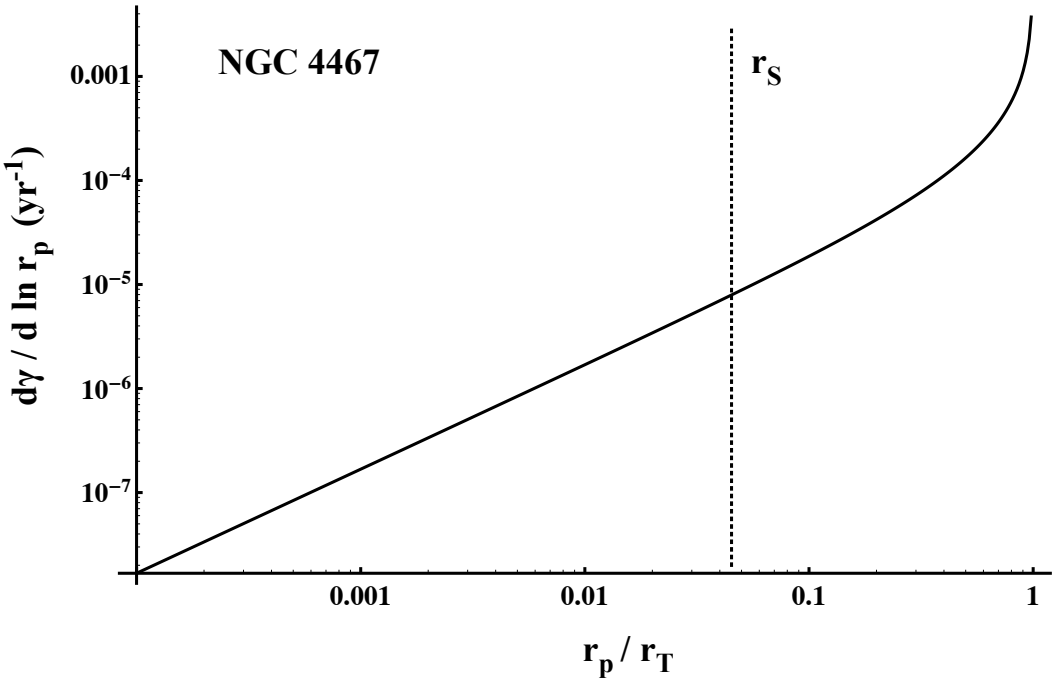

Figure 4.4: Calculated tidal disruption rate $d\gamma/d\ln r_{\rm p}$ as a function of $r_{\rm p}/r_{\rm T}$. The Schwarzschild radius $r_{\rm S} = 0.045 r_{\rm T}$ is indicated; stars on deeper trajectories are directly consumed by the BH. At $r_{\rm p} \ll r_{\rm T}$, only stars in the full loss cone regime ($E \ll E_{\rm crit}$) contribute, giving the scaling $d\gamma/d\ln r_{\rm p} \propto r_{\rm p}$. Close to $r_{\rm T}$, stars at higher energies in the diffusive regime are able to contribute, raising the overall rate. The rate peaks at $r_{\rm p} = r_{\rm T}$.

line shows the location of the Schwarzschild radius; stars on deeper trajectories are directly consumed by the BH rather than experiencing disruption. At $r_{\rm p} \ll r_{\rm T}$, only stars in the full loss cone regime ($E \ll E_{\rm crit}$) contribute, giving the scaling $d\gamma/d\ln r_{\rm p} \propto r_{\rm p}$. Close to $r_{\rm T}$, stars at higher energies in the diffusive regime are able to contribute, raising the overall rate. The disruption of stars very close to $r_{\rm T}$ offers a probe of smaller initial radii from the BH.

4.5.1 Implications for optical transient surveys

Our calculation of $d\gamma/d\ln r_{\rm p}$ has implications for predicted detection rates of tidal disruption events in optical transient surveys. Figure 2.13 (left panel) in Chapter 2 shows our prediction for the observable tidal disruption rate as a function of $M_{\rm BH}$, for a super-Eddington outflow (with our canonical values of $f_{\rm out} = 0.1$ and $f_v = 1$), restricted to redshifts $z < 1$. These calculations assumed that the intrinsic tidal disruption rate for every galaxy is $\gamma = 10^{-5}\,{\rm yr}^{-1}$ (integrated from $r_{\rm S}$ to $r_{\rm T}$) and that this rate is distributed as $d\gamma/d\ln r_{\rm p} \propto r_{\rm p}^0$. As we have seen, the true intrinsic rate distribution rises with $r_{\rm p}$ and is peaked at $r_{\rm p} \sim r_{\rm T}$. To see how this affects optical detection rates, we recalculate our detection predictions for the same super-Eddington outflow parameters but with different assumptions about the in-

trinsic rate. In future work, we will incorporate $d\gamma/d\ln r_{\rm p}$ results for many galaxies hosting BHs of a variety of masses. Here as a preliminary calculation, for each galaxy we assume that $d\gamma/d\ln r_{\rm p}$ has the same shape as for NGC 4467, and that $\gamma = 10^{-5}\,{\rm yr}^{-1}$ (integrated from $r_{\rm p} = 0$ to $r_{\rm T}$).

The resulting predicted detection rates are plotted in Figure 4.5. Compared to Figure 2.13 (left panel), the predicted detection rates are suppressed at $M_{\rm BH} \gtrsim 10^7 M_\odot$, and enhanced at $\sim 10^5 - 10^6 M_\odot$. The reason is that the peak fallback rate is highest at small $r_{\rm p}$ (see eqs. 2.1 & 2.2). At high $M_{\rm BH}$, the fallback rate is only marginally super-Eddington: the less common events at $r_{\rm p} < r_{\rm T}$ are optically brighter than those at $r_{\rm p} \sim r_{\rm T}$. At low $M_{\rm BH}$ and small $r_{\rm p}$, the fallback rate is so super-Eddington that the outflow is edge-limited at early times (see §2.2.1), and so only similarly bright at peak to events at $r_{\rm p} = r_{\rm T}$; the events at low $r_{\rm p}$ fade on timescales short compared to typical survey cadences, however, and so are more difficult to detect. Thus, enhancing the intrinsic rate of the more detectable events at $r_{\rm p} \sim r_{\rm T}$ increases the overall predicted detection rate. The detection rate $d\Gamma/d\ln r_{\rm p}$ rises steeply with $r_{\rm p}$ (approximately proportional to $r_{\rm p}^3$—see Figure 2.12 for the detection rate assuming $d\gamma/d\ln r_{\rm p} \propto r_{\rm p}^0$). The predicted detection rates integrated over $M_{\rm BH}$ and $r_{\rm p}$ differ slightly from those in Table 2.1: here, we predict $300\,{\rm yr}^{-1}$ for Pan-STARRS 3π, $30\,{\rm yr}^{-1}$ for Pan-STARRS MDS, $300\,{\rm yr}^{-1}$ for PTF, and $7000\,{\rm yr}^{-1}$ for LSST (all with the same assumed survey parameters as in Table 2.1).

4.6 Discussion & directions for future work

We have derived an expression for the tidal disruption rate as a function of pericenter distance $d\gamma/d\ln r_{\rm p}$ subject to a set of simple assumptions, and calculated $d\gamma/d\ln r_{\rm p}$ for the galaxy NGC 4467 using observational data for the photometric surface brightness profile, mass-to-light ratio, and BH mass. As expected by the approximate considerations in §4.2, the shape of $d\gamma/d\ln r_{\rm p}$ is proportional to pericenter distance $r_{\rm p}$ for $r_{\rm p} \ll r_{\rm T}$, and rises significantly at $r_{\rm p} \sim r_{\rm T}$. We have used the shape of $d\gamma/d\ln r_{\rm p}$ for NGC 4467 to revise our predictions for the optical detection rates of tidal disruption events: relative to our previous predictions (§2.5.3), detection rates are expected to be somewhat higher at lower $M_{\rm BH}$ and somewhat lower at higher $M_{\rm BH}$.

The first optically-selected TDE candidates, TDE1 and TDE2 from Stripe 82 of the Sloan Digital Sky Survey (van Velzen et al. 2010) and PTF10iya from the Palomar Transient Factory (§6.1, Cenko et al. 2011), appear consistent with our results for $d\gamma/d\ln r_{\rm p}$. We have reasonably modeled TDE1 as an event having $M_{\rm BH} = 9 \times 10^6 M_\odot$ and $r_{\rm p} = r_{\rm T}$, and also modeled[13] TDE2 as an event having $3 \times 10^7 M_\odot$ and $r_{\rm p} = r_{\rm T}$. (These BH masses are suggested by van Velzen et al. 2010, based on the $M_{\rm BH} - L_{\rm bulge}$ relation.) As shown in §6.1, we have also reasonably modeled PTF10iya by $r_{\rm p} = 12 r_{\rm S} = 0.5 r_{\rm T}$ and $M_{\rm BH} = 10^6 M_\odot$. Since

[13]Although the model for TDE2 does not agree well with the color and temporal slope, the conclusion that $r_{\rm p} \sim r_{\rm T}$ should be fairly robust if the value of $M_{\rm BH}$ is correct, since $r_{\rm T} = 2.2 r_{\rm S}$, and $r_{\rm p} < r_{\rm S}$ will not lead to disruption (or $r_{\rm p} < r_{\rm S}/2$ for a maximally spinning BH).

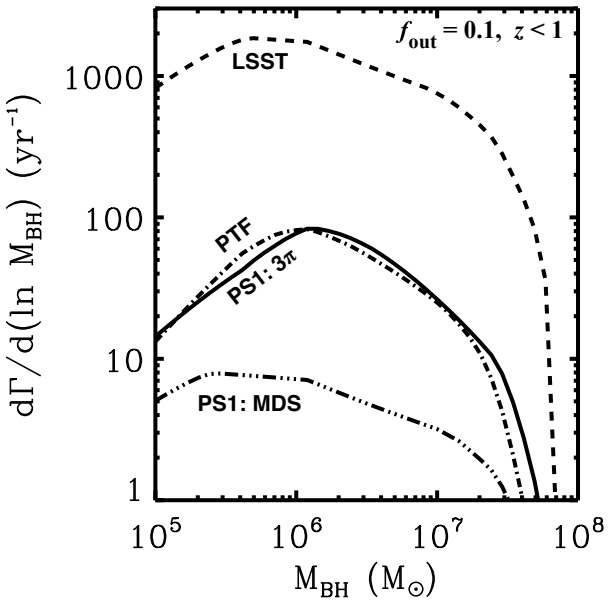

Figure 4.5: Predictions for tidal disruption event detection rates by optical transient surveys: Pan-STARRS 3π Survey (solid), Medium Deep Survey (triple-dot-dashed), Large Synoptic Survey Telescope (dashed), and Palomar Transient Factory (dot-dashed). See Table 2.1 for assumed survey parameters. Compare with left panel of Figure 2.13: there we assume that $d\gamma/d\ln r_{\rm p}$ is independent of $r_{\rm p}$, and here we assume the form of $d\gamma/d\ln r_{\rm p}$ for NGC 4467. The detection rates predicted here are relatively enhanced at low $M_{\rm BH}$ and suppressed at high $M_{\rm BH}$.

the intrinsic tidal disruption rate and detection rate are peaked at $r_{\rm p} \sim r_{\rm T}$, events at $r_{\rm p} \sim r_{\rm T}$ should likely be found in the highest numbers. If the event PTF10iya is at $r_{\rm p} \sim r_{\rm T}/2$, we may expect ~ 8 times as many events at $r_{\rm p} \sim r_{\rm T}$ to be present in the PTF data: at a redshift limit of $z \lesssim 0.2$, we predict a PTF detection rate of $\sim 3\,{\rm yr}^{-1}$. Detailed characterization of the PTF selection function should improve predictions of the detection rate.

We now review the major assumptions and uncertainties in our derivation of $d\gamma/d\ln r_{\rm p}$, and use these to motivate planned future work on this topic. Foremost, we assume that 2-body relaxation is the process that delivers stars to the tidal disruption region: we assume that the galactic nucleus (inside $r_{\rm crit}$ at least) is older than a relaxation time so any stars initially on orbits inside the disruption region were disrupted long ago, and we ignore the possibility of chaotic orbits (which can lead to disruption without 2-body relaxation). The relaxation time at the radius of influence of a $10^6 M_\odot$ BH is $t_{\rm rel}(r_{\rm h}) \sim 10^8\,{\rm yr} \ll$ the age of the universe, so this assumption is reasonable; however, this assumption may no longer be good for $M_{\rm BH} \gtrsim 10^7 M_\odot$ (since $t_{\rm rel} \propto M_{\rm BH}^{1.79}$ assuming $M_{\rm BH} \propto \sigma^{4.24}$: Gültekin et al. 2009). Our derivation assumes that the galactic nucleus has a spherically symmetric density distribution.

We also make two assumptions about the distribution of stellar velocities: (1) the velocities of test stars have only two independent components (radial and azimuthal), and (2) the velocity distribution of stars that induces perturbations is isotropic (f used in calculating the diffusion coefficients depends only on E).

We have additionally assumed that all stars have a single mass m, and that stars are solar type when we perform quantitative calculations. Of course, in reality, more and less[14] massive main sequence stars can disrupt as well, as can giant stars. Which stars dominate the event rate depends primarily on the mass function of stars in the galactic nucleus, and more weakly on the stars' mass-radius relation (which determines the size of $r_{\rm T}$ as a function of stellar mass, and therefore the size of the loss cone ${\theta_{\rm lc}}^2$)[15]: see equations (4.7) and (4.8). For a normal mass function, the disruption rate is dominated by main sequence stars at the peak of the mass function ($m \sim 0.5 M_\odot$). Although the tidal disruption radius $r_{\rm T}$ for giant stars can be ~ 100 times larger than for solar-type stars, the size of the loss cone affects the rate only weakly, and so the relative rarity of giants ($\sim 0.1 - 1\%$ of stars) implies that their disruption rate is substantially below that of main sequence stars.[16] Magorrian & Tremaine (1999) account approximately for the mass function of stars and find only small refinement to their single-population results. However, the process of star formation close to a massive BH may produce a different stellar mass function than elsewhere in galaxies (for example, the disk(s) of young stars in our Galactic Center appears to have a top-heavy initial mass function), and the star formation history in galactic nuclei is complicated and not spatially uniform (Genzel et al. 2010). These effects could perhaps lead the disruption rate to be dominated by massive stars at some pericenter distances in some galactic nuclei.

Another assumption is that the BH and stars make the only contributions to the gravitational potential; gas and dark matter are considered negligible. In our Galactic Center, it is possible that the circumnuclear disk, a collection of molecular and atomic gas and dust about a parsec from the BH, weighing $\sim$ few $\sim 10^4 - 10^6 M_\odot$, could have a dynamical effect on the stars if the true mass is at the upper end of this range (e.g., Šubr et al. 2009). Similarly, giant molecular clouds could affect the tidal disruption rate in other galaxies if they extend deep enough into the gravitational potential of the BH (since the disruption rate is dominated by stars close to the BH's radius of influence) (e.g., Zhao et al. 2002; Perets et al. 2007), perhaps particularly relevant for the gas-rich nuclei of pseudobulges. Dark matter in galactic nuclei likely contributes orders of magnitude too little mass to affect the system dynamically (e.g., Vasiliev & Zelnikov 2008). Interestingly, though, the same dynamical

[14]Less massive stars, which are more compact than solar-type stars, are swallowed hole for sufficiently massive BHs, since $r_{\rm T}$ may lie inside the BH's event horizon.

[15]Considering a full distribution of stellar masses, the relaxation time is roughly constant for different stellar masses, because it depends only on the background distribution of stars. The size of the loss cone affects the event rate only weakly because the rate is dominated by the boundary between the diffusive and full loss cone regimes, and the size of the loss cone enters only logarithmically into the rate in the diffusive regime.

[16]Giant stars are of particular interest nevertheless because they can be disrupted by BHs more massive than $10^8 M_\odot$.

processes that cause stars to be consumed by the BH can also lead to the accretion of dark matter onto the BH (e.g., Read & Gilmore 2003).

Other important assumptions in our derivations are that velocity deflections caused by gravitational scatterings are small compared with the stellar velocity, and that the gravitational scatterings are randomly distributed in direction rather than coherent. Large-amplitude scattering events may significantly raise the rate of stars reaching $r_{\rm p} \ll r_{\rm T}$ in the diffusive regime. At radii $r \ll r_{\rm h}$, the assumption of incoherent scattering events is invalid because stars remain on almost-Keplerian orbits for many [$\sim (M_{\rm BH}/m)(nr^3)^{-1/2}$] orbital periods before precessing significantly; therefore, stars have much longer opportunities to torque each other. This process is called resonant relaxation (Rauch & Tremaine 1996). Both large-amplitude scattering events and resonant relaxation have the potential to affect our results in the diffusive regime, perhaps leading to a less sharp peak at $r_{\rm p} \sim r_{\rm T}$ since stars can diffuse further into the disruption region than we have assumed. We will investigate these effects in future work.

We plan to calculate tidal disruption rates as a function of pericenter distance for a wide variety of observed and model galaxies, with two connected aims: (1) To refine predictions of tidal disruption detection rates, which should help interpret individual candidate detections and help guide observational survey and follow-up strategies, and (2) To identify robust differences between tidal disruption rate profiles for different nuclear profiles, which should help us use future observed detection rates to draw statistical conclusions about the dynamics of different galactic nuclei; for example, if only highly asymmetrical galactic nuclei can give rise to large $d\gamma/d\ln r_{\rm p}$ at $r_{\rm p} \sim 0.1 r_{\rm T}$, and most observed TDE candidates are found to have $r_{\rm p} \sim 0.1 r_{\rm T}$, then we may infer that many galaxies likely have highly asymmetrical nuclei. Future work will thus include: (1) fully exploring results for spherically symmetric galaxy models, (2) extending our model to axisymmetric and then triaxial and asymmetrical galaxy models, and (3) exploring other dynamical effects, as described in the previous paragraph. We plan to calculate $d\gamma/d\ln r_{\rm p}$ for all of the galaxies presented in Faber et al. (1997) and compare the overall disruption rates γ with those calculated by Wang & Merritt (2004). We will then calculate $d\gamma/d\ln r_{\rm p}$ for a selection of the other $\sim$ dozen galaxies that have dynamically measured BH masses and photometry that resolves within $\sim r_{\rm h}$ of the BH (for which γ has not yet been calculated); Gültekin et al. (2009) summarize results for many of these galaxies. We will then extend our $d\gamma/d\ln r_{\rm p}$ calculation to axisymmetric galaxies, drawing on the formalism presented in Magorrian & Tremaine (1999) for calculating γ in axisymmetric galaxies—applicable to the pure-disk galaxies with measured BH masses presented in Kormendy et al. (2010) whose formation mechanism is unclear—and triaxial galaxies, drawing on Merritt & Poon (2004). Triaxial and asymmetrical potentials can set stars on chaotic orbits, which may enter the disruption region without requiring gravitational scattering at all, and therefore may give rise to a significantly different shape for $d\gamma/d\ln r_{\rm p}$. Of particular interest are pseudobulges, which have more flattened shapes and ordered velocities than classical bulges and often host a BH of mass $M_{\rm BH} \sim 10^5 - 10^7 M_\odot$—and which often exhibit asymmetrical structure close to the BH, such as a nuclear bar or spiral. The Galactic Center (a pseudobulge) contains richly complicated structure, including one or two disks of young

massive stars on eccentric orbits, and a population of late-type giant stars distributed fairly isotropically (e.g., Genzel et al. 2010). Furthermore, the galaxies M31 and NGC 4486B (not pseudobulges) also each contain an eccentric disk of stars in the nucleus that may be a ubiquitous signature of past merging BHs (Hopkins & Quataert 2010). Finally, we will predict $d\gamma/d\ln r_{\rm p}$ for other types of disruptions: binary star systems and giant stars, both of which disrupt much further outside $r_{\rm S}$ than solar-type stars, and therefore offer a richer probe of galactic structure thanks to a wider range of possible pericenter distances. Along similar lines, it will be significant to calculate the rate of *partial* stellar disruptions at $r_{\rm p} \sim \text{few} \times r_{\rm T}$ alongside current research to predict the observational appearance of such events.

In this way, our derivations and results presented here for $d\gamma/d\ln r_{\rm p}$ form important groundwork for future stellar dynamical calculations for a variety of types of galactic nuclei. In the not-too-distant future, we can look forward to the time when observational studies of TDEs in transient surveys and theoretical dynamics calculations can converge to improve our understanding of the formation and co-evolution of BHs and their surrounding stellar nuclei.

Acknowledgments

We are very grateful to Milos Milosavljević for sharing his derivation of the distribution function inside the disruption zone. We also thank Josh Burkart, Todd Gingrich, Paul Hand, Nicholas McConnell, Ryan O'Leary, Nathan Roth, and David Strubbe for helpful conversations.

Chapter 5

Dust Dynamics, Surface Brightness Profiles, and Thermal Spectra of Debris Disks: The Case of AU Mic

Abstract

AU Microscopii is a 12 Myr old M dwarf that harbors an optically thin, edge-on disk of dust. The scattered light surface brightness falls with projected distance b from the star as $b^{-\alpha}$; within $b = 43$ AU, $\alpha \approx 1$–2, while outside 43 AU, $\alpha \approx 4$–5. We devise a theory to explain this profile. At a stellocentric distance $r = r_{\rm BR} = 43$ AU, we posit a ring of parent bodies on circular orbits: the "birth ring," wherein micron-sized grains are born from the collisional attrition of parent bodies. The "inner disk" at $r < r_{\rm BR}$ contains grains that migrate inward by corpuscular and Poynting-Robertson (CPR) drag. The "outer disk" at $r > r_{\rm BR}$ comprises grains just large enough to remain bound to the star, on orbits rendered highly eccentric by stellar wind and radiation pressure. How the vertical optical depth $\tau_\perp$ scales with r depends on the fraction of grains that migrate inward by CPR drag without suffering a collision. If this fraction is large, the inner disk and birth ring share the same optical depth, and $\tau_\perp \propto r^{-5/2}$ in the outer disk. By contrast, under collision-dominated conditions, the inner disk is empty, and $\tau_\perp \propto r^{-3/2}$ outside. These scaling relations, which we derive analytically and confirm numerically, are robust against uncertainties in the grain size distribution. By simultaneously modeling the surface brightness and thermal spectrum, we break model degeneracies to establish that the AU Mic system is collision-dominated, and that its narrow birth ring contains a lunar mass of decimeter-sized bodies. The inner disk is devoid of micron-sized grains; the surface brightness at $b \lesssim 43$ AU arises from light forward scattered by the birth ring. Inside $b = 43$ AU, the disk's $V - H$ color should not vary with b; outside, the disk must become bluer as ever smaller grains are probed.

5.1 Introduction

"Debris disks" surrounding young stars are composed of optically thin dust (see the reviews by Artymowicz 2000; Lagrange, Backman, & Artymowicz 2000; Zuckerman 2001). Most debris disks are inferred to exist from measurements of infrared excesses (e.g., Aumann et al. 1984; Habing et al. 2001; Zuckerman & Song 2004). A few disks are close enough to resolve in images, either in scattered starlight (e.g., Smith & Terrile 1984; Schneider et al. 1999; Kalas, Graham, & Clampin 2005) or in thermal emission (e.g., Telesco et al. 2000; Greaves et al. 2004).

Is the observed dust primordial—the remains of an optically thick, gas-rich disk from a previous Herbig Ae or T Tauri phase? Or is it maintained in equilibrium—continuously removed by processes such as Poynting-Robertson drag and replenished by the comminution of larger, colliding parent bodies? A third possibility is that the observed dust represents the transient aftermath of recent cataclysmic events. Dust might be freshly generated, unequilibrated debris from the catastrophic destruction of large planetesimals (Su et al. 2005; Song et al. 2005).

The debris disk encircling the young M dwarf AU Microscopii is a promising place to investigate these questions. It is well resolved in scattered light from optical to near-infrared wavelengths (Kalas, Liu, & Matthews 2004; Krist et al. 2005, hereafter K05; Liu 2004; Metchev et al. 2005). Of central relevance to our study is the disk's surface brightness profile. Within a projected distance b from the star of 43 AU, the surface brightness SB falls approximately as $b^{-1.8}$ (K05). We refer to this region as the "inner disk." Outside 43 AU, in the "outer disk," the slope of the profile changes dramatically: SB $\propto b^{-4.7}$ (K05). This break is observed independently by other researchers (Liu 2004; Metchev et al. 2005). The shape of the profile is all the more significant because it resembles that of the debris disk surrounding β Pictoris (Kalas & Jewitt 1995; Liu 2004), and of the recently discovered disk encompassing HD 139664 (Kalas et al. 2006). AU Mic's disk is also detected in unresolved thermal emission (Liu et al. 2004; Chen et al. 2005). The disk's infrared spectrum peaks at a wavelength of $\sim$100 μm and exhibits no excess at 12 μm; this behavior suggests that the disk contains an inner hole (Liu et al. 2004).

Here we offer a theory that explains these observations quantitatively. The reason why the surface brightness profile breaks at 43 AU is that a narrow ring of parent bodies, analogous to the solar system's Kuiper Belt, orbits the star at a stellocentric radius $r = r_{\rm BR} = 43$ AU. The subscript "BR" refers to our term for the belt of parent bodies, the "birth ring," wherein micron-sized dust grains are born through collisions of larger planetesimals. Grain creation is balanced in steady state by destructive grain-grain collisions and removal by corpuscular and Poynting-Robertson (CPR) drag.[1] Corpuscular drag exerted by the young M dwarf's wind is probably at least a few times more effective at removing dust than Poynting-Robertson drag in the AU Mic system, a possibility first pointed out by Plavchan, Jura, &

[1]Our analysis ignores any gas that might still be orbiting the star. Only upper limits are observed for the column of gas towards the star: $N_{\rm H_2} < 1.7 \times 10^{19}\,{\rm cm}^{-2}$ (Roberge et al. 2005).

Lipscy (2005, hereafter PJL05). The outer disk comprises grains that are only tenuously bound, moving on orbits rendered highly eccentric by stellar wind and radiation forces (e.g., Lecavelier des Etangs et al. 1996; Augereau et al. 2001). These barely bound grains dominate scattering of starlight in the outer disk. By contrast, unbound grains escape the system too quickly for their steady-state population to contribute appreciably to the surface brightness. The inner disk is populated by grains that migrate inward by CPR drag quickly enough to evade collisional destruction. In CPR-dominated (what we refer to as "type A") disks, a large fraction of grains meets this condition, unlike in collision-dominated ("type B") disks. Similar classifications were put forward by Wyatt (2005) and Meyer et al. (2007) in their considerations of disks composed of single-sized grains. We calculate simultaneously the steady-state spatial and size distributions of dust particles, and derive how the outer disk's optical depth scales with radius for type A and type B disks. Our analysis accounts for destructive grain-grain collisions and the detailed dynamics of CPR drag, which reduces not only the orbital semi-major axes of grains but also their orbital eccentricities (Wyatt & Whipple 1950). The reduction of orbital eccentricity is not often considered but is a key component of our theory. Whether type A or type B conditions apply to AU Mic's disk is determined in part by the strength of the stellar wind, which according to previous works is uncertain by orders of magnitude. In this work, we place a novel constraint on the stellar mass loss rate and decide the appropriate disk type by comparing our theoretical models to the observations.

In §5.2, we lay down basic parameters of the AU Mic system: stellar properties, disk optical depths, timescales for grain-grain collisions, and how the star's wind and radiation alter orbits of dust grains. In §5.3, we employ order-of-magnitude physics and analytic scalings to understand how the interplay between collisions, blow-out, and drag shapes the observed surface brightness profiles of the inner and outer disks. There we derive the steady-state grain size distribution as a function of position, including the maximum sizes and total mass of parent bodies. In §5.4, we verify and extend our analytic results with a Monte Carlo simulation of the disk's surface brightness, color, and spectral energy distribution (SED). Models are compared directly with observations. Finally, in §5.5, we summarize our theory, place it in context with our understanding of how planets form, and point out directions for future research.

5.2 Preliminaries

We establish orders of magnitude characterizing the AU Mic system. Stellar properties—including the stellar mass-loss rate that figures prominently throughout our analysis—are reviewed in §5.2.1. Collision times between grains and relative collision velocities are estimated in §5.2.2. Grain dynamics relevant to our theory include blow-out by stellar wind and radiation pressure, as discussed in §5.2.3, and orbital decay by corpuscular and Poynting-Robertson drag, as treated in §5.2.4.

5.2.1 Stellar Properties

AU Microscopii is a spectral type dM1e star located a distance $d = 9.9$ pc from Earth. It has mass $M_* = 0.5 M_\odot$, radius $R_* = 0.93 R_\odot$, effective temperature $T_* = 3500$ K, luminosity $L_* = 0.1 L_\odot$, V magnitude 8.8, and H magnitude 4.8 (Kalas et al. 2004; Metchev et al. 2005; and references therein). The star's age is estimated to be $t_{\rm age} = 12^{+8}_{-4}$ Myr. AU Mic's X-ray luminosity is a prodigious $L_{\rm X} = 5.5 \times 10^{29}\,{\rm erg/s} = 3 \times 10^{-3} L_*$ (Hünsch et al. 1999). The star flares at both X-ray and ultraviolet wavelengths (Magee et al. 2003). The stellar rotation period is 4.87 days (Torres & Ferraz Mello 1973).

How strong is AU Mic's stellar wind? The wind velocity $v_{\rm wind}$ is likely of order the stellar escape velocity $v_{\rm esc} = \sqrt{2GM_*/R_*} \approx 450\,{\rm km/s}$. Plavchan et al. (2005) discuss what is known about mass loss rates $\dot{M}_*$ from M dwarfs, citing values ranging from 10 to as high as 10^4 times the solar mass-loss rate of $\dot{M}_\odot = 2 \times 10^{-14} M_\odot\,{\rm yr}^{-1}$. While the star's youth, flaring activity, and fast rotation suggest that a powerful wind emanates from AU Mic, the star's X-ray emission indicates otherwise. Wood et al. (2002) and Wood et al. (2005) study the relationship between X-ray luminosity and stellar mass loss rate by measuring $\dot{M}_*$ from a handful of M, K, and G dwarfs having ages $\gtrsim 500$ Myr. They establish that the mass flux at the stellar surface $F_M \equiv \dot{M}_*/(4\pi R_*^2)$ increases with X-ray surface flux $F_{\rm X} \equiv L_{\rm X}/(4\pi R_*^2)$ for $F_{\rm X} < 8 \times 10^5\,{\rm erg\,cm^{-2}\,s^{-1}} \equiv F_{\rm X,crit}$. The mass flux $F_{\rm M}$ saturates at a maximum of $10^2 F_{M,\odot}$. For $F_{\rm X} > F_{\rm X,crit}$, F_M drops to $\lesssim 10 F_{M,\odot}$, perhaps because the strong magnetic fields of such extraordinarily X-ray-active stars inhibit stellar winds (see also Schrijver & Title 2001; Strassmeier 2002). AU Mic's X-ray flux $F_{\rm X} \sim 1 \times 10^7\,{\rm erg\,cm^{-2}\,s^{-1}}$ exceeds $F_{\rm X,crit}$, implying at face value a relatively low mass-loss rate. Nevertheless, it is unclear whether the measurements of Wood et al. (2005) apply to this highly variable, pre-main-sequence star. To accommodate the uncertainty in AU Mic's mass-loss rate, we consider in our analysis a wide range of values, $\dot{M}_* \in (1, 10, 10^2, 10^3)\dot{M}_\odot$. We ultimately find in §5.4 that detailed comparison between theoretical models of the disk and observations can, in fact, constrain $\dot{M}_*$.

5.2.2 Collision Times

Consider for the moment a disk of single-sized particles on low-eccentricity orbits. Where the vertical, geometric optical depth equals $\tau_\perp$, the mean free time between collisions is

$$t_{\rm c} \sim \frac{1}{\Omega \tau_\perp}\,, \tag{5.1}$$

where Ω is the local orbital angular frequency. This expression may be derived by recognizing that every $\sim 1/\Omega$ orbital period, a typical particle traverses an optical depth of $\sim\tau_\perp$ over the course of its vertical epicycle. For $\tau_\perp < 1$, the particle collides with probability $\tau_\perp$; for $\tau_\perp > 1$, it undergoes $\tau_\perp$ collisions per orbit.

Detailed fits to observations in §5.4 reveal that the total vertical, geometric optical depth in the birth ring at $r = r_{\rm BR} = 43\,{\rm AU}$ equals $\tau_{\perp,{\rm BR}} \equiv \tau_\perp(r_{\rm BR}) = 4 \times 10^{-3}$. We define a

fiducial collision time

$$t_{\rm c,BR} \equiv \frac{1}{\Omega \tau_{\perp,\rm BR}} \sim 2 \times 10^4 \left(\frac{4 \times 10^{-3}}{\tau_{\perp,\rm BR}} \right) \, {\rm yr} \, . \tag{5.2}$$

The collision lifetime $t_{\rm col}(s)$ is the time a grain of radius s survives before it is destroyed by colliding with another grain. Unlike the case for $t_{\rm c}$, in calculating $t_{\rm col}$ we do not assume that particles have a single size. For a given collisional specific energy Q^* (ergs g^{-1} Greenberg et al. 1978; Fujiwara et al. 1989), targets of size s suffer catastrophic dispersal by smaller projectiles of minimum size

$$\begin{aligned} s_{\rm proj} &\sim \left(\frac{2Q^*}{v_{\rm rel}^2} \right)^{1/3} s \\ &\sim 0.6 \left(\frac{Q^*}{10^7 \, {\rm erg \, g^{-1}}} \right)^{1/3} \left(\frac{100 \, {\rm m \, s^{-1}}}{v_{\rm rel}} \right)^{2/3} s \, , \end{aligned} \tag{5.3}$$

which is comparable to s. By catastrophic dispersal we mean that the mass of the largest postcollision fragment is no greater than half the mass of the original target and that collision fragments disperse without gravitational reassembly. We have normalized the relative speed $v_{\rm rel}$ to the vertical velocity dispersion of visible grains at $r = r_{\rm BR} = 43 \, {\rm AU}$,

$$\Omega \frac{h_{\rm BR}}{2} \sim 100 \, {\rm m \, s^{-1}} \, , \tag{5.4}$$

where the full vertical disk height $h_{\rm BR} \approx 2.75 \, {\rm AU}$ (K05). We have normalized Q^* to a value appropriate for centimeter-sized silicate targets (Greenberg et al. 1978; Fujiwara et al. 1989). Ice targets of similar size have specific energies that are 2 orders of magnitude smaller (Greenberg et al. 1978). On the other hand, it is possible that Q^* increases with decreasing size (Fujiwara et al. 1989; Housen & Holsapple 1990), perhaps as fast as $Q^* \propto s^{-0.5}$. If so, grains having sizes $s \sim 1 \, \mu$m would be $\sim$100 times stronger than their centimeter-sized counterparts, thereby possibly cancelling the reduction in strength due to an icy composition. To keep the telling of our story as simple as possible, we adhere to a nominal, size-independent value of $Q^* = 10^7 \, {\rm erg \, g^{-1}}$. The essential point is that collisions between comparably sized grains in the AU Mic disk are destructive.[2]

5.2.3 Blow-out by Stellar Wind and Radiation Pressure

Grains of certain sizes cannot occupy orbits bound to the star because of stellar wind and radiation (SWR) forces. The ratio of repulsive to gravitational forces felt by a grain equals

[2]Commercial sandblasting machines accelerate abrasive particles up to speeds of 100 m s^{-1}.

$$\beta = \frac{F_{\rm rad} + F_{\rm wind}}{F_{\rm grav}} \tag{5.5}$$

$$= \frac{3}{16\pi} \frac{L_* P_{\rm SWR}}{GM_* c\rho s}\,, \tag{5.6}$$

where the dimensionless factor

$$P_{\rm SWR} \equiv Q_{\rm rad} + Q_{\rm wind} \frac{\dot{M}_* v_{\rm wind} c}{L_*} \tag{5.7}$$

measures the extent to which the ram pressure exerted by the (assumed radial) wind dominates radiation pressure.[3] Here s and $\rho \sim 2\,{\rm g\,cm^{-3}}$ are, respectively, the radius and internal density of a particle, G is the gravitational constant, c is the speed of light, $Q_{\rm rad} \lesssim 2$ is the cross section that the grain presents to radiation pressure in units of the geometric cross section (Burns et al. 1979), and $Q_{\rm wind} \sim 1$ is the analogous dimensionless cross section the grain presents to wind pressure.[4] For $Q_{\rm rad} \sim 2$ (appropriate for the $s > \lambda_*/2\pi$ geometric optics limit where $\lambda_* \approx 1\,\mu$m is the wavelength at which the bulk of the stellar luminosity is emitted), wind pressure is negligible compared to radiation pressure except for the largest value of $\dot{M}_*$ considered. Table 5.1 lists possible values for $P_{\rm SWR}$.

Grains are continually created from colliding parent bodies. Throughout this paper, we assume that parent bodies move on nearly circular ($\beta \ll 1$) orbits, and that the velocities with which grains are ejected from parent bodies are small compared to parent body orbital velocities. These assumptions imply that grains having $\beta \geq 1/2$ are "blown out" by SWR pressure. For constant $P_{\rm SWR}$ with s, the condition $\beta \geq 1/2$ is equivalent to

$$s \leq s_{\rm blow} = \frac{3}{8\pi} \frac{L_* P_{\rm SWR}}{GM_* c\rho} \sim 0.2 \left(\frac{P_{\rm SWR}}{2}\right) \mu{\rm m}\,. \tag{5.8}$$

Grains for which $s < s_{\rm blow}$ are unbound and move on hyperbolic escape trajectories. Grains for which $s = s_{\rm blow}$ move on parabolic escape trajectories. A grain for which $s - s_{\rm blow} \ll s_{\rm blow}$ moves initially on a highly elliptical orbit whose periastron distance $r_{\rm peri,0}$ equals the orbital radius of the parent body. It is these "barely bound" grains that contribute significantly to the scattered light observed in the outer disk. The initial eccentricity e_0 and semi-major axis a_0 of a barely bound grain upon its birth are uniquely related to grain size s via the force ratio β:

$$e_0 = \frac{\beta}{1-\beta}\,, \tag{5.9a}$$

[3]The assumption of a purely radial wind is valid insofar as the azimuthal velocity of the wind $v_{{\rm wind},\phi}$ is less than Ωr. By modelling the stellar magnetic field as that of a rotating (split) monopole (Weber & Davis 1967; Parker 1964), we estimate that $v_{{\rm wind},\phi}/\Omega r \lesssim 1/30$.

[4]Our $Q_{\rm rad}$ equals $Q_{\rm pr}$ from Burns et al. (1979). It should not be confused with $Q_{\rm scat}$, the usual scattering efficiency.

$$a_0 = \frac{r_{\rm peri,0}}{1-e_0}\,, \tag{5.9b}$$

$$\beta = \frac{1}{2}\left(\frac{s_{\rm blow}}{s}\right)\,, \tag{5.9c}$$

where the last relation assumes that $P_{\rm SWR}$ is independent of s.

A consequence of equations (5.1) and (5.9) is that grains on highly eccentric orbits have prolonged collision times. Provided that the optical depth traversed by a grain is concentrated near periastron at $r = r_{\rm peri}$, the optical depth $\tau_\perp$ in (5.1) should be evaluated at $r = r_{\rm peri}$. However, Ω should not necessarily be evaluated for a semi-major axis equal to $r_{\rm peri}$. Instead, from (5.9b),

$$\Omega(e) = \left(\frac{GM_*}{r_{\rm peri}^3}\right)^{1/2}(1-e)^{3/2}\,. \tag{5.10}$$

A related useful quantity is the fraction of time a grain on a fixed orbit spends at radii between $r_{\rm peri}$ and $r_{\rm peri} + \Delta r$:

$$f(e) \sim \left(\frac{\Delta r}{r_{\rm peri}}\right)^{1/2}\frac{(1-e)^{3/2}}{(1+e)^{1/2}}\,, \tag{5.11}$$

valid in the limit of $\Delta r \ll r_{\rm peri}$ and large e.

5.2.4 Corpuscular and Poynting-Robertson Drag

Under the drag due to corpuscular and Poynting-Robertson (CPR) forces (see, e.g., Burns et al. 1979), dust grain orbits having periastron distances $r_{\rm peri}$ and arbitrary eccentricities e collapse to a point in a time

$$t_{\rm CPR} = \frac{4\pi c^2\rho}{3L_*P_{\rm CPR}}E(e)r_{\rm peri}^2 s\,, \tag{5.12}$$

where the dimensionless factor

$$P_{\rm CPR} \equiv Q_{\rm rad} + Q_{\rm wind}\frac{\dot{M}_* c^2}{L_*} \tag{5.13}$$

quantifies the relative importance of wind-driven versus radiation-driven drag. For the values of $\dot{M}_*$ we consider, the stellar wind is at least as important as the stellar radiation: $P_{\rm CPR} > 2$; see Table 5.1. The dimensionless factor

$$E(e) = \frac{8}{5}\frac{(1+e)^2}{e^{8/5}}\int_0^e \frac{x^{3/5}\,dx}{(1-x^2)^{3/2}} \tag{5.14}$$

governs the decay of orbital eccentricity (Wyatt & Whipple 1950). A related useful result from Wyatt & Whipple (1950) is that

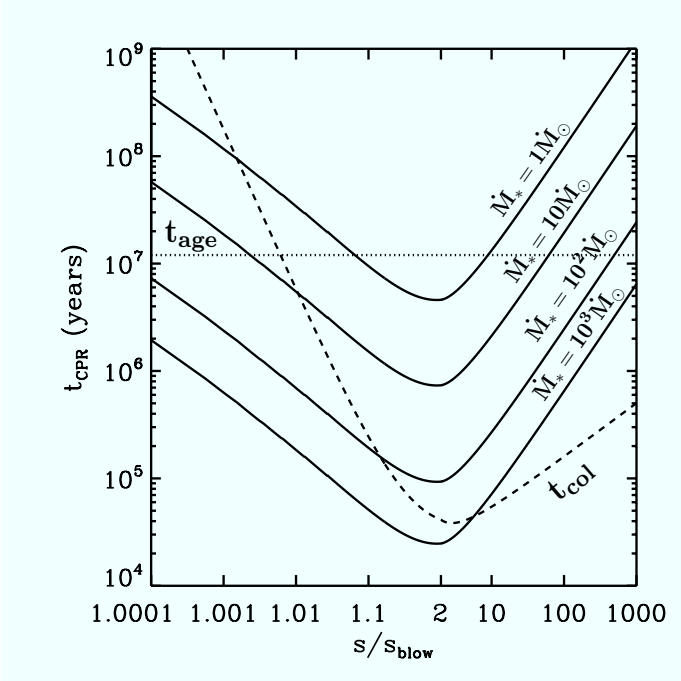

Figure 5.1: CPR drag time as a function of grain size $s/s_{\rm blow}$, for $\dot{M}_*/\dot{M}_\odot = \{1, 10, 10^2, 10^3\}$. To highlight the behavior as $s \to s_{\rm blow}$, the horizontal axis is scaled as $\log(s/s_{\rm blow} - 1)$. The fiducial collision time $t_{\rm col} = t_{\rm c,BR}(s/s_{\rm blow})^{1/2}(1-e_0)^{-3/2}$ is also indicated as a dashed line (see §5.3.1). The size $s_{\rm break}$ corresponds approximately to where this collision time and the CPR drag time are equal. Timescales for removal by CPR drag and collisions can be much shorter than the age of the system, $t_{\rm age}$.

$$\frac{de}{dt} = \left(\frac{15 L_* P_{\rm CPR}}{32\pi c^2 \rho r_{\rm peri,0}^2}\right) \frac{1}{s} \frac{e_0^{8/5}}{(1+e_0)^2} \frac{(1-e^2)^{3/2}}{e^{3/5}} \,. \tag{5.15}$$

The initial effect of CPR drag on a highly eccentric orbit is to reduce the apastron distance while keeping the periastron distance and eccentricity nearly fixed (see Figure 1 of Wyatt & Whipple 1950). For highly eccentric orbits, the time spent during this apastron reduction phase is much longer than the usual CPR-timescales that are cited for $e \ll 1$. As e approaches 1, E diverges as

$$E(e \approx 1) \propto (1-e)^{-1/2} \,. \tag{5.16}$$

Once CPR drag reduces the eccentricity to values less than a few percent, the entire orbit collapses to a point in a time given by $t_{\rm CPR}$ with $E \approx 1$.

Table 5.1 provides sample values of $t_{\rm CPR}(e = e_0)$ for three choices of $s/s_{\rm blow} = \{1.1, 1.5, 15\}$, while Figure 5.1 depicts how $t_{\rm CPR}(e = e_0)$ varies with s, all for $r_{\rm peri} = r_{\rm BR} = 43\,{\rm AU}$.

5.3 Theory

We assemble the ingredients laid out in §5.2 into a theory for the distribution of grain sizes (§5.3.1) and the profile of optical depth (§5.3.2) in the AU Mic disk. Included in our analysis are estimates of the sizes and total mass of the largest parent bodies undergoing a collisional cascade. According to our theory, all of the current optical to near-IR observations probe grains whose population is maintained in steady state and that are still bound—most only barely—to the central star. Contributions to scattered light from unbound and unequilibrated populations of grains are assessed in §5.3.3 and §5.3.4, respectively.

5.3.1 Equilibrium Size Distribution

We posit an annulus of parent bodies extending from $r = r_{\rm BR} - \Delta r/2$ to $r = r_{\rm BR} + \Delta r/2$—the "birth ring"—where grains are born from the collisional attrition of larger parent bodies. These grains travel on orbits whose eccentricities and semi-major axes are continuously modified by CPR drag. Grains are removed from the birth ring either by CPR drag or by collisions with other grains. The goal of this section is to determine the equilibrium size distribution dN/ds as a function of r, where dN is the vertical column density of grains having sizes between s and $s + ds$.

The size distribution of dust in debris disks is commonly assumed to be proportional to $s^{-q_{\rm ce}} = s^{-7/2}$. This scaling is appropriate for grains on low-eccentricity orbits whose collisional strengths are independent of size, whose spatial distribution is homogeneous, and whose numbers are maintained in a purely collisional equilibrium, as first derived by Dohnanyi (1969; see also O'Brien & Greenberg 2003; Pan & Sari 2005). In such equilibrium cascades, as much mass is ground into every size bin as is ground out. One presumption behind the cascade is that collision times are short enough that the system has relaxed into collisional equilibrium. However, Figure 5.1 shows that $t_{\rm CPR}$ and $t_{\rm col}$ are of the same order for some grain sizes. Visible dust may be removed too quickly by CPR drag to participate in a purely collisional, equilibrium cascade.

Instead of making the usual assumption that the size distribution is proportional to $s^{-7/2}$ for all s, we construct the following model. We define $s_{\rm break}$ as the radius of the grain for which

$$t_{\rm col}(s_{\rm break}) = t_{\rm CPR}(s_{\rm break}) \tag{5.17}$$

at $r = r_{\rm BR}$. We expect that grains of a given size can participate in a standard collisional cascade if they have had enough time to collide destructively about once (for numerical estimates of the time required for a cascade to equilibrate see, e.g., Campo Bagatin et al. 1994 and references therein). For $s > s_{\rm break}$, we expect $t_{\rm CPR} > t_{\rm col}$ and a Dohnanyi-like size distribution (modified appropriately for grains on highly eccentric orbits, i.e., for spatial inhomogeneity). For $s < s_{\rm break}$, we will see that $t_{\rm CPR} < t_{\rm col}$. The two regimes are treated in §5.3.1 and §5.3.1, respectively. We discuss which grain sizes carry the bulk of the optical

depth and how collision times vary with grain size in §5.3.1. These considerations are applied to computing $s_{\rm break}$ in §5.3.1. The sizes of the largest parent bodies are estimated in §5.3.1.

Readers interested only in our results for the grain size distribution can examine equations (5.18), (5.21), (5.23), (5.25), (5.26), (5.27), (5.37), and (5.39), and can skip ahead to §5.3.2 where grain dynamics are analyzed.

Equilibrium Size Distribution for $s < s_{\rm break}$

First we define

$$\frac{d\mathcal{N}}{ds} \equiv \int_0^\infty \frac{dN}{ds}\, 2\pi r\, dr \tag{5.18}$$

as the size distribution of grains integrated over the entire disk.

Fresh debris having $s < s_{\rm break}$ continually sprays from colliding bodies having $s > s_{\rm break}$. We assume that the initial or "injection" spectrum of fresh debris follows a power law; the rate at which grains having sizes between s and $s + ds$ are injected into the entire disk obeys

$$\left.\frac{d\dot{\mathcal{N}}}{ds}\right|_{\rm I} = Cs^{-q_{\rm inject}}\,, \tag{5.19}$$

where C is a constant and the subscript "I" denotes "injection." Theoretical considerations of mass conservation suggest $q_{\rm inject} = 3$–4 (Greenberg et al. 1978), while impact experiments using centimeter-sized targets suggest values of $q_{\rm inject} \approx 3.5$–$4$ (Fujiwara et al. 1989, see their Figure 3).

To solve for the steady-state size distribution, we equate the injection rate $d\dot{\mathcal{N}}/ds|_{\rm I}$ to the removal rate $d\dot{\mathcal{N}}/ds|_{\rm R}$. We show in §5.3.1 that removal is dominated by CPR drag onto the central star: $t_{\rm CPR}/t_{\rm col} < 1$ for $s < s_{\rm break}$. Then grains having $s < s_{\rm break}$ drag inward from the birth ring largely unimpeded by collisions, and

$$\left.\frac{d\dot{\mathcal{N}}}{ds}\right|_{\rm R} = \frac{1}{t_{\rm CPR}(s)}\frac{d\mathcal{N}}{ds}\,. \tag{5.20}$$

Equating the injection and removal rates yields

$$\frac{d\mathcal{N}}{ds} \sim Cs^{-q_{\rm inject}} t_{\rm CPR}(s, r_{\rm peri} = r_{\rm BR}) \quad \text{for} \quad s < s_{\rm break}\,. \tag{5.21}$$

The column density dN/ds local to the birth ring is proportional to $d\mathcal{N}/ds$ times the fraction of time spent inside the birth ring:

$$\left.\frac{dN}{ds}\right|_{\rm BR} \propto \frac{d\mathcal{N}}{ds}\frac{\Delta t_{\rm reside}|_{\rm CPR}}{t_{\rm CPR}} \tag{5.22}$$

$$\propto s^{-q_{\rm inject}}\, \Delta t_{\rm reside}|_{\rm CPR} \quad \text{for} \quad s < s_{\rm break}\,, \tag{5.23}$$

where $\Delta t_{\rm reside}|_{\rm CPR}$ is the total time a grain spends inside the birth ring over its CPR-limited lifetime. Figure 5.2 plots $\Delta t_{\rm reside}|_{\rm CPR}$ as a function of s for the parameters $\dot{M}_*/\dot{M}_\odot = 1$, $\Delta r/r_{\rm BR} = 0.1$, and $r_{\rm peri,0} = r_{\rm BR}$. We compute this quantity by explicitly tracking the position of a grain on a decaying orbit. Evidently, $\Delta t_{\rm reside}|_{\rm CPR}$ scales approximately linearly with s for all s. We can understand this linear scaling by examining two extremes. For $s \gg s_{\rm blow}$, orbits are nearly circular always, and $\Delta t_{\rm reside}|_{\rm CPR}$ is merely the time for the grain's orbital radius to decay by $\Delta r/2$. This time is proportional to s since $E \approx 1$ (see equation [5.12]). For $s - s_{\rm blow} \ll s_{\rm blow}$, eccentricities e_0 are large. Over most of a grain's lifetime, the grain's periastron lies inside the birth ring while its apastron lies well outside. Evaluated over intervals shorter than $t_{\rm CPR}$, the fraction of time the grain spends inside the birth ring is given by $f(e)$ with $r_{\rm peri}$ set equal to $r_{\rm BR}$. Applying (5.11) and (5.15), we have

$$\begin{aligned} \Delta t_{\rm reside}|_{\rm CPR} &\sim \int_{e_0}^{0} f(e)\frac{dt}{de}\,de \\ &\propto s\left(\frac{\Delta r}{r_{\rm BR}}\right)^{1/2}\int_0^{e_0}\left(\frac{1+e_0}{1+e}\right)^2\left(\frac{e}{e_0}\right)^{3/5}\frac{de}{e_0} \\ &\propto s\,, \end{aligned} \tag{5.24}$$

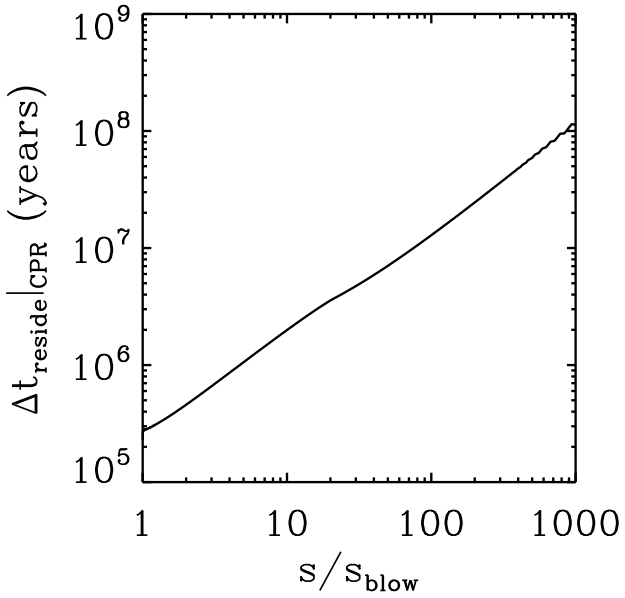

Figure 5.2: The length of time $\Delta t_{\rm reside}|_{\rm CPR}$ a grain spends within the birth ring (at radii between $r_{\rm BR} - \Delta r/2$ and $r_{\rm BR} + \Delta r/2$) as a function of grain size, for grains whose lifetimes are limited by CPR drag. We take $r_{\rm peri,0} = r_{\rm BR} = 43\,{\rm AU}$, $\Delta r/r_{\rm BR} = 0.1$, and $\dot{M}_* = 1\dot{M}_\odot$.

where the integral in the second row is nearly constant with s.

Equilibrium Size Distribution for $s > s_{\rm break}$

For $s > s_{\rm break}$, a collisional cascade is established before CPR drag has time to remove grains. Collisions occur primarily in the birth ring since the vertical optical depth is greatest there. In the birth ring, the usual collisional equilibrium implies

$$\left.\frac{dN}{ds}\right|_{\rm BR} \propto s^{-q_{\rm ce}} = s^{-7/2} \quad \text{for} \quad s > s_{\rm break}\,. \tag{5.25}$$

By the same logic that led to (5.23),

$$\frac{d\mathcal{N}}{ds} \propto \left.\frac{dN}{ds}\right|_{\rm BR} \frac{t_{\rm col}}{\Delta t_{\rm reside}|_{\rm col}} \quad \text{for} \quad s > s_{\rm break}\,, \tag{5.26}$$

where we have assumed (and show in §5.3.1) that $t_{\rm col} < t_{\rm CPR}$ is the appropriate lifetime for grains having $s > s_{\rm break}$. By analogy to $\Delta t_{\rm reside}|_{\rm CPR}$, $\Delta t_{\rm reside}|_{\rm col}$ is the total time a grain spends within the birth ring over a collision-limited lifetime.

In the special case of large initial eccentricity e_0,

$$\begin{aligned}\frac{d\mathcal{N}}{ds} &\propto \left.\frac{dN}{ds}\right|_{\rm BR} \frac{1}{f(e_0)} \\ &\propto \left.\frac{dN}{ds}\right|_{\rm BR} (1-e_0)^{-3/2}\,,\ s > s_{\rm break},\ e_0 \approx 1\,,\end{aligned} \tag{5.27}$$

where we have used the fact that grains having large e_0 and whose lifetimes are limited by $t_{\rm col} < t_{\rm CPR}$ have their periastra within the birth ring and their eccentricities close to their birth values for nearly all their lives.

Optical Depth and Collision Times in the Birth Ring

We estimate the sizes of grains that carry the lion's share of the optical depth in the birth ring. For $s > s_{\rm break}$, the column density in the birth ring obeys $dN/ds \propto s^{-7/2}$. The vertical optical depth contributed by such grains equals

$$\tau_\perp(s > s_{\rm break}) \sim s^3 \frac{dN}{ds} \propto s^{-1/2}\,; \tag{5.28}$$

therefore among grains of size $s > s_{\rm break}$, the optical depth is dominated by grains of size $s_{\rm break}$. What about the regime $s < s_{\rm break}$? From (5.23),

$$\tau_\perp(s < s_{\rm break}) \sim s^3 \frac{dN}{ds} \propto s^{3-q_{\rm inject}}\ \Delta t_{\rm reside}|_{\rm CPR}\,. \tag{5.29}$$

For $q_{\rm inject} \approx 3.5$–4, this quantity either grows or is approximately constant with s. We conclude that grains of size $s \sim s_{\rm break}$ dominate the total geometric optical depth in the birth ring:

$$\tau_\perp(s_{\rm break}) \sim \tau_{\perp,\rm BR}\,, \tag{5.30}$$

which in combination with (5.2), (5.3) and (5.10) implies that

$$t_{\rm col}(s_{\rm break}) \sim t_{\rm c,BR}(1-e_{0,\rm break})^{-3/2}\,, \tag{5.31}$$

where $e_{0,\rm break} \equiv e_0(s_{\rm break})$.

We exploit (5.2), (5.10), and (5.28)–(5.31) to estimate $t_{\rm col}$ for arbitrary s. For $s > s_{\rm break}$,

$$t_{\rm col}(s > s_{\rm break}) \sim t_{\rm c,BR}\left(\frac{s}{s_{\rm break}}\right)^{1/2}(1-e_0)^{-3/2}\,, \tag{5.32}$$

where we have set $e = e_0$ since most of the grain's lifetime is spent with that eccentricity (see §5.2.4). Since in the large-s limit $t_{\rm col} \propto s^{1/2}$ while $t_{\rm CPR} \propto s$, the assumption made in §5.3.1 that grains are removed principally by collisions for $s > s_{\rm break}$ is asymptotically valid. In Figure 5.1, we plot (5.32) as a fiducial size-dependent collision time, replacing $s_{\rm break}$ by $s_{\rm blow}$ to render the curve independent of stellar mass-loss rate. This replacement, performed solely for Figure 5.1, accrues only a slight error since we find in §5.3.1 that $s_{\rm break}$ and $s_{\rm blow}$ are nearly the same.

Next we estimate $t_{\rm col}(s < s_{\rm break})$ and show that $t_{\rm CPR}/t_{\rm col} < 1$ for $s < s_{\rm break}$, as was assumed in §5.3.1. Equation (5.30) implies that grains having $s < s_{\rm break}$ are predominantly destroyed by $s_{\rm break}$-sized grains. Then[5]

$$\begin{aligned} t_{\rm col}(s < s_{\rm break}) &\sim \frac{1}{\Omega(s)\tau_\perp(s_{\rm break})} \\ &\sim t_{\rm col}(s_{\rm break})\left(\frac{1-e_{0,\rm break}}{1-e_0}\right)^{3/2}\,. \end{aligned} \tag{5.33}$$

For convenience, we construct the approximate fitting formula for $t_{\rm CPR}$ from (5.12), (5.16), and (5.17):

$$t_{\rm CPR}(s < s_{\rm break}) \sim t_{\rm col}(s_{\rm break})\left(\frac{s}{s_{\rm break}}\right)\left(\frac{1-e_{0,\rm break}}{1-e_0}\right)^{1/2}\,. \tag{5.34}$$

Combining (5.33) and (5.34), we find that the ratio between CPR and collision lifetimes is

[5]Equation (5.33) overestimates $t_{\rm col}$ because it neglects the fact that grains on highly eccentric orbits intercept an optical depth parallel to the disk in addition to $\tau_{\perp,\rm BR}$. This neglect does not change our derived scaling relations, but it will change certain normalizations, e.g., the threshold $\dot{M}_*$ dividing CPR-dominated from collision-dominated behavior. We are indebted to Y. Wu for pointing out this omission, which will need to be corrected in future work.

$$\left.\frac{t_{\rm CPR}}{t_{\rm col}}\right|_{s<s_{\rm break}} \sim \left(\frac{s}{s_{\rm break}}\right)\left(\frac{1-e_0}{1-e_{0,\rm break}}\right) < 1\,; \tag{5.35}$$

indeed this ratio vanishes as s approaches $s_{\rm blow}$. We have established that inequality (5.35) holds at $r = r_{\rm BR}$, but in fact it holds for all $r = r_{\rm peri} < r_{\rm BR}$, since $t_{\rm CPR} \propto r^2$ while $t_{\rm col} \propto r^{3/2}$. Therefore our assumption that bound grains having $s < s_{\rm break}$ are removed principally by CPR drag is valid.

Calculating $s_{\rm break}$

Equate the collision time (5.32) to the CPR drag time (5.12),

$$(1-e_{0,\rm break})^{-3/2} t_{\rm c,BR} \sim \frac{4\pi c^2 \rho r_{\rm BR}^2}{3 L_* P_{\rm CPR}} s_{\rm break} E(e_{0,\rm break})\,, \tag{5.36}$$

to find

$$s_{\rm break} \sim \begin{cases} 1.002 s_{\rm blow} & = 0.2\,\mu{\rm m} \quad \text{for } \dot{M}_*/\dot{M}_\odot = 1 \\ 1.01 s_{\rm blow} & = 0.2\,\mu{\rm m} \quad \text{for } \dot{M}_*/\dot{M}_\odot = 10 \\ 1.1 s_{\rm blow} & = 0.3\,\mu{\rm m} \quad \text{for } \dot{M}_*/\dot{M}_\odot = 10^2 \\ 2.3 s_{\rm blow} & = 2\,\mu{\rm m} \quad \text{for } \dot{M}_*/\dot{M}_\odot = 10^3\,. \end{cases} \tag{5.37}$$

Larger Parent Bodies

Bodies having $s > s_{\rm break}$ participate in a collisional cascade in which the Dohnanyi-like spectrum extends from $s_{\rm break}$ up to a maximum size $s_{\rm max}$. By definition, $s_{\rm max}$ characterizes those grains whose collisional lifetimes equal the age of the AU Mic disk; by (5.32), this size satisfies

$$t_{\rm col}(s_{\rm max}) \sim t_{\rm c,BR}\left(\frac{s_{\rm max}}{s_{\rm break}}\right)^{1/2} = t_{\rm age}\,, \tag{5.38}$$

where we have dropped the eccentricity-dependent factor since grains having $s = s_{\rm max} \gg s_{\rm blow}$ travel on essentially circular orbits. Then

$$s_{\rm max} \sim \left(\frac{t_{\rm age}}{t_{\rm c,BR}}\right)^2 s_{\rm break} \sim \begin{cases} 10\,{\rm cm} & \text{for } \dot{M}_*/\dot{M}_\odot = 1 \\ 10\,{\rm cm} & \text{for } \dot{M}_*/\dot{M}_\odot = 10 \\ 20\,{\rm cm} & \text{for } \dot{M}_*/\dot{M}_\odot = 10^2 \\ 100\,{\rm cm} & \text{for } \dot{M}_*/\dot{M}_\odot = 10^3\,. \end{cases} \tag{5.39}$$

Our model has no information on parent bodies having $s > s_{\rm max}$. While such bodies likely exist, we do not know whether they are currently in a constructive (planet building) or destructive (debris generating) phase of their evolution. It is not justified to extend the size distribution to $s > s_{\rm max}$ (e.g., to the kilometer size range) as is sometimes done.

5.3.2 Physical Implications of Optical Depth Profiles

The birth ring divides the inner disk from the outer disk. In §5.3.2, we discuss the vertical optical depth in the inner disk. In §5.3.2, we estimate the total disk mass. In §5.3.2, we derive analytically how the vertical optical depth scales with radius in the outer disk.

Inner Disk ($r < r_{\rm BR}$): Competition Between Collisions and CPR-Driven Accretion

We showed in §5.3.1 that grains of size $s \sim s_{\rm break}$ make the largest contribution to the total optical depth at $r \approx r_{\rm BR}$. Bound grains having $s < s_{\rm break}$ tend to be transported inwards by CPR drag, unimpeded by interparticle collisions. Larger grains tend to be collisionally destroyed before reaching the star. How does the vertical optical depth in the inner disk compare with the optical depth in the birth ring?

We define CPR-dominated type A disks to be systems for which $s_{\rm break} - s_{\rm blow} \gg s_{\rm blow}$. In such disks, grains for which $s_{\rm blow} < s < s_{\rm break}$ are numerous, contain a significant fraction of the total optical depth in the birth ring, and tend to accrete onto the central star before undergoing a collision. From continuity, the optical depth $\tau_\perp(r < r_{\rm BR})$ scales approximately as r^0: the inner disk is "filled in."

By contrast, in collision-dominated type B disks, $s_{\rm break} - s_{\rm blow} \ll s_{\rm blow}$. The region inside the birth ring is virtually empty. The reasons for this are twofold. First, the range of sizes of grains that drag in without being collisionally destroyed ($s_{\rm blow} < s < s_{\rm break}$) is narrow; there are not many such grains. Second, because $s_{\rm break}$ is so close to $s_{\rm blow}$, $s_{\rm break}$-sized grains have large initial eccentricity. They spend most of their lifetimes having $r_{\rm peri} \approx r_{\rm peri,0}$ and only a small portion at $r < r_{\rm BR}$ (see §5.2.4).

As judged from (5.37), if $\dot{M}_*/\dot{M}_\odot \gg 10^2$, type A conditions would hold for the AU Mic disk and the inner disk would be filled in. If $\dot{M}_*/\dot{M}_\odot \ll 10^2$, then type B conditions would hold and the inner disk would be empty. In §5.4, we not only check these assertions by detailed Monte Carlo simulations of the AU Mic disk, but also decide which case is favored by the observations.

Total Mass of the Disk

By (5.25), most of the mass of the disk is contributed by the largest grains ($s = s_{\rm max}$), since $s^4 dN/ds \propto s^{1/2}$. We scale from the column density of $s_{\rm break}$-sized grains in the birth ring,

$$\tau_{\perp,\rm BR} \sim \pi s_{\rm break}^3 \left.\frac{dN}{ds}\right|_{s_{\rm break}} \tag{5.40}$$

to estimate the column density of $s_{\rm max}$-sized grains in the birth ring,

$$s_{\rm max} \left.\frac{dN}{ds}\right|_{s_{\rm max}} \sim \frac{\tau_{\perp,\rm BR}}{\pi s_{\rm break}^3} \left(\frac{s_{\rm max}}{s_{\rm break}}\right)^{-7/2} s_{\rm max}\,. \tag{5.41}$$

The total number of such grains is their column density multiplied by the area of the birth ring $2\pi r_{\rm BR}\Delta r$, since $s_{\rm max}$-sized grains undergo a collision long before dragging inwards. Multiplying this total number by the mass of a single grain yields the mass of the disk,

$$\begin{aligned} M_{\rm max} &\sim \frac{8\pi}{3}\rho r_{\rm BR}\tau_{\perp,\rm BR}s_{\rm break}\left(\frac{s_{\rm max}}{s_{\rm break}}\right)^{1/2}\Delta r \\ &\sim 0.01M_\oplus\left(\frac{\Delta r/r_{\rm BR}}{0.1}\right)\left(\frac{\tau_{\perp,\rm BR}}{4\times10^{-3}}\right)^2\left(\frac{s_{\rm break}}{0.2\,\mu{\rm m}}\right), \end{aligned} \tag{5.42}$$

where we have used (5.2) and (5.39), and have normalized $\Delta r/r_{\rm BR}$ and $\tau_{\perp,\rm BR}$ to values that yield good fits to observations, as described in §5.4. The steady comminution of $\sim0.01M_\oplus \sim$ 1 lunar mass's worth of decimeter-sized bodies into micron-sized particles does not seem an unduly heavy burden for the AU Mic system to bear. The solar system is thought to have somehow shed $\sim10M_\oplus$ of rock and ice near $\sim$30 AU over an uncertain timescale of 10–1000 Myr during its "clean-up" phase (Goldreich et al. 2004).

Outer Disk ($r > r_{\rm BR}$): Barely Bound Grains

Grains created at $r = r_{\rm BR} = 43\,{\rm AU}$ and having $s - s_{\rm blow} \lesssim s_{\rm blow}$ occupy initially highly eccentric orbits having periastron distances $r_{\rm peri} = r_{\rm BR}$ (see §5.2.3). Here we show that such barely bound grains establish an outer disk at $r \gg r_{\rm BR}$ whose vertical optical depth scales approximately as $r^{-5/2}$ for CPR-dominated type A disks, and as $r^{-3/2}$ for collision-dominated type B disks. The contribution of unbound grains having $s \le s_{\rm blow}$ relative to that of barely bound grains is assessed in §5.3.3.

The outer disk comprises grains having sizes slightly greater than $s_{\rm blow}$ since only those grains have substantial eccentricities (see equations [5.9]). We refer to such barely bound grains as having sizes $s = s_{\rm blow,+}$. The optical depth in the outer disk should scale approximately as their column density $N_{\rm blow,+}$:

$$\tau_\perp \propto N_{\rm blow,+} \propto \frac{1}{r}\frac{d\mathcal{N}_{\rm blow,+}}{dr}, \tag{5.43}$$

where $\mathcal{N}_{\rm blow,+}$ is the total number of such grains in the entire disk (see [5.18]). By the chain rule,

$$\frac{d\mathcal{N}_{\rm blow,+}}{dr} = \frac{d\mathcal{N}_{\rm blow,+}}{de}\frac{de}{dr}. \tag{5.44}$$

We determine de/dr by making the approximation that at any instant, all grains are located at their apastra:

$$e = \frac{r_{\rm apo} - r_{\rm peri}}{r_{\rm apo} + r_{\rm peri}} \tag{5.45}$$

$$\approx \frac{r - r_{\rm BR}}{r + r_{\rm BR}}\,. \tag{5.46}$$

This approximation should be good for the highly eccentric orbits of the outer disk. Differentiating (5.46), we find for $r \gg r_{\rm BR}$ that

$$\frac{de}{dr} \approx \frac{2r_{\rm BR}}{(r + r_{\rm BR})^2} \propto \frac{1}{r^2}\,. \tag{5.47}$$

The remaining factor in (5.44), $d\mathcal{N}_{\rm blow,+}/de$, is determined by the size distribution of barely bound grains. This differs between type A and type B disks, as seen below. The size distribution determines the initial shape of the eccentricity distribution. The eccentricity distribution is altered over time by CPR drag. Consider grains having identical initial eccentricities e_0 created at a constant rate $\dot{\widetilde{\mathcal{N}}}$. In steady state, CPR drag transports a constant number of particles per time through eccentricity space, $(d\widetilde{\mathcal{N}}/de)(de/dt) \sim \dot{\widetilde{\mathcal{N}}}$. Hence,

$$\frac{d\widetilde{\mathcal{N}}}{de} \propto \left(\frac{de}{dt}\right)^{-1} \propto \frac{e^{3/5}}{(1-e^2)^{3/2}} \quad \text{for} \quad e \le e_0\,, \tag{5.48}$$

where we have used (5.15). Equation (5.48) implies that nearly all barely bound grains have $e \approx e_0$. Therefore the CPR-evolved eccentricity distribution closely resembles the initial eccentricity distribution:

$$\frac{d\mathcal{N}}{de} \sim \frac{d\mathcal{N}}{de_0}\,. \tag{5.49}$$

Now we address the size distribution that determines $d\mathcal{N}/de_0$. For type A disks, for which $s_{\rm break} - s_{\rm blow} \gg s_{\rm blow}$, the size distribution for barely bound grains obeys $d\mathcal{N}/ds \propto s^{-q_{\rm inject}} t_{\rm CPR}(s)$ (see [5.21]). For type B disks, $s_{\rm break} - s_{\rm blow} \ll s_{\rm blow}$; outer-disk grains for which $s_{\rm blow} < s < s_{\rm break}$ are outnumbered by grains having $s > s_{\rm break}$. The relevant size distribution in the outer regions of type B disks is therefore the one appropriate for $s > s_{\rm break}$: $d\mathcal{N}/ds \propto s^{-7/2}(1-e_0)^{-3/2}$ (see [5.27]).[6] We evaluate these distributions for $s = s_{\rm blow,+}$:

$$\frac{d\mathcal{N}_{\rm blow,+}}{ds} \propto E(e_0) \propto (1-e_0)^{-1/2} \quad \text{for Type A disks}\,, \tag{5.50a}$$

[6]This statement for type B disks is only valid not too far from the birth ring. As $r \to \infty$, the only bound grains that are present have sizes between $s_{\rm blow}$ and $s_{\rm break}$. These obey $\tau_\perp \propto r^{-5/2}$, just as they do for type A disks. Therefore for type B disks, the $\tau_\perp \propto r^{-3/2}$ scaling derived in the main text eventually gives way to $\tau_\perp \propto r^{-5/2}$.

$$\frac{d\mathcal{N}_{\rm blow,+}}{ds} \propto (1-e_0)^{-3/2} \quad \text{for Type B disks}\,, \tag{5.50b}$$

using equations (5.12) and (5.16). Now $d\mathcal{N}/de \sim d\mathcal{N}/de_0 = (d\mathcal{N}/ds)(ds/de_0)$. Since equations (5.9) imply that ds/de_0 is approximately constant for $e_0 \approx 1$ (i.e., for $s = s_{\rm blow,+}$), and since $r \approx r_{\rm apo} \approx 2r_{\rm BR}/(1-e_0)$,

$$\frac{d\mathcal{N}_{\rm blow,+}}{de} \propto (1-e_0)^{-1/2} \propto r^{1/2} \quad \text{for Type A disks}\,, \tag{5.51a}$$

$$\frac{d\mathcal{N}_{\rm blow,+}}{de} \propto (1-e_0)^{-3/2} \propto r^{3/2} \quad \text{for Type B disks}\,. \tag{5.51b}$$

Combine (5.43), (5.44), (5.47), and (5.51) to obtain

$$\tau_\perp \propto r^{-5/2} \quad \text{for Type A disks}\,, \tag{5.52a}$$

$$\tau_\perp \propto r^{-3/2} \quad \text{for Type B disks}\,. \tag{5.52b}$$

Note that these scaling relations cannot be obtained by merely assuming that the disk-integrated size distribution obeys the usual Dohnanyi relation $d\mathcal{N}/ds \propto s^{-7/2}$. For type B disks, for example, the key modification arises from the prolonging of the collisional lifetime due to SWR pressure (i.e., the factor of $(1-e_0)^{-3/2}$ in equation [5.51b]). Moreover, the scalings are robust against uncertainties in the size distribution; they do not depend explicitly on either $q_{\rm ce}$ or $q_{\rm inject}$. We verify these scalings by numerical experiments in §5.4.

5.3.3 Unbound Grains ($\beta \geq 1/2$)

The rapid expulsion of unbound ($\beta \geq 1/2$) grains compared to the longer, CPR-driven orbital decay of barely bound ($1/2 - \beta \ll 1$) grains suggests that in steady state, unbound grains contribute little to the surface brightness of the outer disk. On the other hand, unbound grain velocities are nearly constant with radius—for $\beta \approx 1$, velocities are approximately equal to their (circular, Keplerian) birth velocities. As a result, the optical depth of unbound grains should roughly obey $\tau_{\perp,\rm ub} \propto r^{-1}$ and should eventually exceed, at some "cross-over radius," the optical depth of barely bound grains, which scales as $\tau_{\perp,\rm bb} \propto r^{-5/2}$ in type A disks and as $\tau_{\perp,\rm bb} \propto r^{-3/2}$ in type B disks (§5.3.2). In this section, we estimate the value of the cross-over radius, $r_{\rm cross}$, and show in the case of AU Mic that it lies outside the scope of current observations.

Consider a type A disk. In the birth ring, the optical depth of barely bound grains exceeds that of unbound grains by

$$\tau_{\perp,\rm bb}/\tau_{\perp,\rm ub} \sim \int_{s_{\rm blow}}^{2s_{\rm blow}} \frac{dN}{ds}\, s^2\, ds \Bigg/ \int_{\min(s_V)}^{s_{\rm blow}} \frac{dN}{ds}\, s^2\, ds\,. \tag{5.53}$$

The smallest unbound grain of interest is the smallest grain for which $Q_{\rm scat} \sim 1$: $\min(s_V) \approx 0.1\,\mu$m. Since $\tau_{\perp,\rm bb} \propto r^{-5/2}$ while $\tau_{\perp,\rm ub} \propto r^{-1}$, the cross-over radius is

$$r_{\rm cross} \sim \left(\frac{\tau_{\perp,\rm bb}}{\tau_{\perp,\rm ub}}\right)^{2/3} r_{\rm BR}\,. \tag{5.54}$$

By (5.23),

$$\left.\frac{dN}{ds}\right|_{s_{\rm blow}<s<2s_{\rm blow}} \sim D s^{-q_{\rm inject}}\ \Delta t_{\rm reside}|_{\rm CPR} \tag{5.55}$$

in the birth ring, where D is a constant. By the same logic that led to (5.23),

$$\left.\frac{dN}{ds}\right|_{s<s_{\rm blow}} \sim D s^{-q_{\rm inject}} t_{\rm blow}(s) \tag{5.56}$$

in the birth ring, where

$$t_{\rm blow}(s) \sim \frac{\sqrt{r_{\rm BR}\Delta r}}{\Omega_{\rm BR} r_{\rm BR}\sqrt{\beta}} \sim 90\left(\frac{s}{s_{\rm blow}}\right)^{1/2}\sqrt{\frac{\Delta r}{r_{\rm BR}}}\,{\rm yr} \tag{5.57}$$

is the time for an unbound grain to leave the birth ring, and $\Omega_{\rm BR} = \sqrt{GM_*/r_{\rm BR}^3}$. Numerical evaluation of the integrals in (5.53) reveals that

$$r_{\rm cross} \sim \begin{cases} 900\,{\rm AU} & \text{for } \dot{M}_*/\dot{M}_\odot = 10^2 \\ 200\,{\rm AU} & \text{for } \dot{M}_*/\dot{M}_\odot = 10^3\,. \end{cases} \tag{5.58}$$

If instead type B conditions apply for the AU Mic disk, then by considerations analogous to those above, $r_{\rm cross} \gg 10^3\,{\rm AU}$. We compare $r_{\rm cross}$ with the maximum radius probed by current observations—approximately 200 AU—to conclude that under type A conditions, unbound grains contribute at most marginally to the currently observed surface brightness. Under type B conditions, they contribute negligibly.

5.3.4 Unequilibrated Grains ($s_{\rm blow} < s < s_{\rm age}$)

Grains on extremely eccentric orbits may have collisional and CPR lifetimes that exceed the age of the system. Can such grains, whose numbers cannot be assessed within our steady-state model, contribute significantly to the observed surface brightness of the AU Mic disk? Such "unequilibrated grains" have sizes between $s_{\rm blow}$ and $s_{\rm age}$, where

$$t_{\rm age} = \min[t_{\rm CPR}(s_{\rm age}), t_{\rm col}(s_{\rm age})] \tag{5.59}$$

defines $s_{\rm age}$. We apply (5.12) and (5.33) to find that

$$\frac{s_{\rm age}}{s_{\rm blow}} \sim \begin{cases} 1.006 & \text{for } \dot{M}_*/\dot{M}_\odot = 1 \\ 1.002 & \text{for } \dot{M}_*/\dot{M}_\odot = 10 \\ 1.00003 & \text{for } \dot{M}_*/\dot{M}_\odot = 10^2 \\ 1.000002 & \text{for } \dot{M}_*/\dot{M}_\odot = 10^3\,. \end{cases} \tag{5.60}$$

Unequilibrated grains occupy such a narrow range of sizes that they seem unlikely to contribute much to the total optical depth. We ignore the unequilibrated population for the remainder of this paper.

5.4 Monte Carlo Modelling

5.4.1 Procedure

To test several of the analytic results derived in §5.3, we model the AU Mic disk by means of a Monte Carlo simulation. We calculate the geometric optical depth $\tau_\perp(r)$, edge-on surface brightness profile SB(b), and spectral flux density F_ν and then we compare to observations. The input parameters are the stellar mass-loss rate $\dot{M}_*$, optical depth in the center of the birth ring $\tau_{\perp,\mathrm{BR}} \equiv \tau_\perp(r_{\mathrm{BR}})$, and width of the birth ring Δr.

We lay down a number J of dust particles around the central star in a two-dimensional

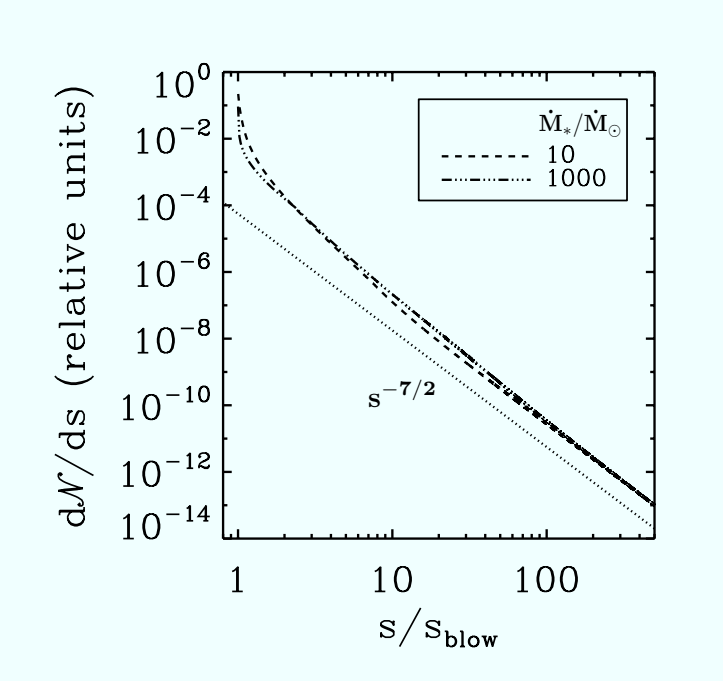

Figure 5.3: Disk-integrated grain size distributions $d\mathcal{N}/ds$. Dashed and triple-dot–dashed curves correspond respectively to $\dot{M}_*/\dot{M}_\odot = \{10, 10^3\}$. A dotted line proportional to the Dohnanyi scaling $s^{-q_{\mathrm{ce}}} = s^{-7/2}$ is overplotted for reference. As s approaches s_{blow}, the population of grains rises significantly above what one would expect from a pure Dohnanyi size spectrum. The deviations from a Dohnanyi spectrum, which differ under type A (e.g., $\dot{M}_* = 10^3\dot{M}_\odot$) and type B (e.g., $\dot{M}_* = 10\dot{M}_\odot$) conditions, are critical for understanding how $\tau_\perp$ scales with r in the outer disk; see §5.3.2.

plane. Each particle's radial coordinate r and azimuth ψ are determined by the particle's semi-major axis a, eccentricity e, true anomaly $\phi_{\rm t}$, and longitude of periastron $\widetilde{\omega}$. Since our model disk is axisymmetric, $\widetilde{\omega}$ is drawn as a uniform deviate from 0 to 2π.

The birth distributions of the remaining orbital elements depend on the distribution of grain sizes s. Orbital elements subsequently evolve from their birth values by CPR drag. The degree of evolution depends on the age of the grain (t) relative to the CPR lifetime ($t_{\rm CPR}$; equation [5.12]) and collision lifetime ($t_{\rm col}$; equations [5.32] and [5.33]). By definition, $s_{\rm break}$ is the grain size for which $t_{\rm CPR} = t_{\rm col}$, and $s_{\rm age}$ is the smallest grain size for which $\min(t_{\rm CPR}, t_{\rm col}) = t_{\rm age}$. Only grains having $s > s_{\rm age}$ can be removed over the age of the system. For $s > s_{\rm break}$, collisions are more important than CPR drag in removing grains ($t_{\rm col} < t_{\rm CPR}$), so we draw the ages t of such particles as a uniform deviate from 0 to $t_{\rm col}(s)$. Grains of size $s < s_{\rm break}$ are removed by CPR drag ($t_{\rm CPR} < t_{\rm col}$), so we draw t for these grains as a uniform deviate from 0 to $t_{\rm CPR}(s)$.

The evolved eccentricity e depends on the initial eccentricity e_0 and the age of the particle, implicitly according to

$$\frac{t}{t_{\rm CPR}} = 1 - \frac{E(e)}{E(e_0)} \left(\frac{1+e_0}{1+e} \right)^2 \left(\frac{e}{e_0} \right)^{8/5} , \tag{5.61}$$

where $E(e)$ is defined by (5.14). The evolved semi-major axis is given by

$$a = a_0 \left(\frac{e}{e_0} \right)^{4/5} \left(\frac{1-e_0^2}{1-e^2} \right) \tag{5.62}$$

(Wyatt & Whipple 1950), where the initial semi-major axis a_0 is derived from the initial periastron $r_{\rm peri,0}$, which we draw in the following way. In our model, all grains are born in the birth ring, an annulus of width Δr centered at $r_{\rm BR}$. At birth, a grain is located at the periastron of its osculating orbit—an orbit rendered eccentric by SWR forces (§5.2.3). We draw $r_{\rm peri,0}$ from a uniform distribution of width Δr centered at $r_{\rm BR}$.

As mentioned, the birth distributions of eccentricities and semi-major axes depend on the distribution of grain sizes s. Although particles in our simulation are born only in the birth ring, their steady-state population may occupy all space, so we must draw s from the global, disk-integrated size distribution $d\mathcal{N}/ds$. We apply results from §5.3.1, made more precise for our Monte Carlo calculation. From (5.21),

$$\frac{d\mathcal{N}}{ds} \propto s^{-q_{\rm inject}} t_{\rm CPR}(s, r_{\rm peri} = r_{\rm BR}) \quad \text{for} \quad s_{\rm age} < s < s_{\rm break} , \tag{5.63}$$

and from (5.26),

$$\frac{d\mathcal{N}}{ds} \propto s^{-7/2} \frac{t_{\rm col}}{\Delta t_{\rm reside}|_{\rm col}} \quad \text{for} \quad s > s_{\rm break} . \tag{5.64}$$

We approximate $t_{\rm col}$ using (5.32), and we evaluate $\Delta t_{\rm reside}|_{\rm col}$ numerically. We take the distribution described by (5.63) and (5.64) to be non-zero only for $s > s_{\rm age}$[7] and to be continuous across $s_{\rm break}$; furthermore, we truncate the distribution at $s_{\rm max} = 500 s_{\rm blow}$ because of computational limitations. We fix $q_{\rm inject} = 4$. The distribution $d\mathcal{N}/ds$ is plotted in Figure 5.3. For each s drawn, e_0 and a_0 are calculated using equations (5.9). For $J = 10^9$, one Monte Carlo simulation takes 8 hr to complete on a 1.33 GHz PowerPC G4 processor.

That the distribution of mean anomalies $\phi_{\rm m}$ is uniform determines the distribution of true anomalies $\phi_{\rm t}$ via Kepler's equation (Murray & Dermott 2000):

$$\phi_{\rm m} = \phi_{\rm e} - e \sin \phi_{\rm e} \,, \tag{5.65}$$

where $\phi_{\rm e}$ is the eccentric anomaly:

$$\tan \frac{\phi_{\rm t}}{2} = \left(\frac{1+e}{1-e} \right)^{1/2} \tan \frac{\phi_{\rm e}}{2} \,. \tag{5.66}$$

Knowing a, e and $\phi_{\rm t}$ for each particle determines its radial distance from the star:

$$r = \frac{a(1-e^2)}{1 + e \cos \phi_{\rm t}} \,. \tag{5.67}$$

5.4.2 Products of the Monte Carlo Calculation

Having laid down J particles of various sizes, we output the following:

1. The geometric vertical optical depth $\tau_\perp(r)$. We first calculate this quantity in relative units by summing the geometric cross sections of particles in a given annulus, and dividing the resultant sum by the area of that annulus. We then normalize this result by matching the input $\tau_{\perp,{\rm BR}}$ to the model's relative optical depth at $r_{\rm BR}$.

2. The surface brightness of the disk observed edge-on at V-band (*Hubble Space Telescope*'s $F606W$) and H-band wavelengths, as a function of projected stellar separation b:

$$\begin{aligned} &{\rm SB}(b, \lambda) \\ &= \iint \frac{\lambda L_{\lambda,*}}{4\pi r^2} Q_{\rm scat}(\lambda, s)\, P(\theta, \lambda, s)\, \pi s^2 \, \frac{dn}{ds}(r, s)\, d\ell \, ds \,, \end{aligned} \tag{5.68}$$

   where $\ell = \pm\sqrt{r^2 - b^2}$ measures distance along our line of sight. The stellar flux incident on a grain in the wave band of interest is $\lambda L_{\lambda,*}/4\pi r^2$, the cross section for scattering is $Q_{\rm scat}\pi s^2$, the scattering angle between the star, grain, and observer is $\theta = \tan^{-1}(\ell/b)$,

[7] For $\dot{M}_*/\dot{M}_\odot = 1$, $s_{\rm age} > s_{\rm break}$ so only (5.64) is relevant.

and the relative power scattered per steradian is P (normalized so that its integral over all solid angle equals unity). We use Mie theory to calculate $Q_{\rm scat}$ and P, adopting the optical constants of pure water ice (Warren 1984). The volumetric number density of grains n is found by dividing the geometric vertical optical depth by the height of the disk:

$$\pi s^2 \frac{dn}{ds}(r,s) = \frac{1}{h(r)} \frac{d\tau_\perp}{ds}(r,s)\,. \tag{5.69}$$

The radial height profile $h(r)$ is derived from the projected disk height $h(b)$, which roughly follows a broken power law that changes slope around $b = r_{\rm BR} = 43\,{\rm AU}$:

$$h(b) = h_{\rm BR} \begin{cases} (b/r_{\rm BR})^{\eta_1} & \text{for } \; b < r_{\rm BR} \\ (b/r_{\rm BR})^{\eta_2} & \text{for } \; b > r_{\rm BR}\,. \end{cases} \tag{5.70}$$

We set $h_{\rm BR} = 2.75\,{\rm AU}$. Krist et al. (2005) fit separate broken power laws to the northwest and southeast extensions of the disk and obtain $\eta_1 \approx 0$ and $\eta_2 \approx 1$–2; see their Figure 7. For simplicity, we take $\eta_1 = 0$ and $\eta_2 = 1$. These values characterize an inner disk that is empty and seen in projection (or that has constant height), and an outer disk in which grains have constant inclination dispersion. We adopt a radial profile $h(r)$ identical to $h(b)$ as given in (5.70) with b replaced by r. We divide the $F606W$ profile by the H profile to obtain a $V - H$ color profile.

3. The spectral flux density F_ν:

$$\begin{aligned} F_\nu &= \frac{1}{d^2} B_\nu(T_*)\,\pi R_*^2 \\ &+ \frac{1}{d^2} \iint B_\nu(T(r,s))\,Q_{\rm emis}(\lambda,s)\,\pi s^2\,\frac{dN}{ds}(r,s)\,2\pi r\,dr\,ds\,, \end{aligned} \tag{5.71}$$

where $B_\nu(T)$ is the Planck function. We model the emissivity of the dust as a broken power law:

$$Q_{\rm emis} = \begin{cases} 1 & \text{for } \; 2\pi s > \lambda \\ 2\pi s/\lambda & \text{otherwise}\,, \end{cases} \tag{5.72}$$

in approximate agreement with the model of Chiang et al. (2007) for ice-mantled silicate grains. Since the peak wavelength of emission from AU Mic is about $1\,\mu$m, all bound grains are large enough to absorb most of the incident stellar flux. We solve

$$\frac{L_*}{4\pi r^2}\pi s^2 = 4\pi \int_0^\infty B_\lambda(T) Q_{\rm emis}(\lambda,s) \pi s^2\,d\lambda \tag{5.73}$$

for the temperature T specific to a given grain size.

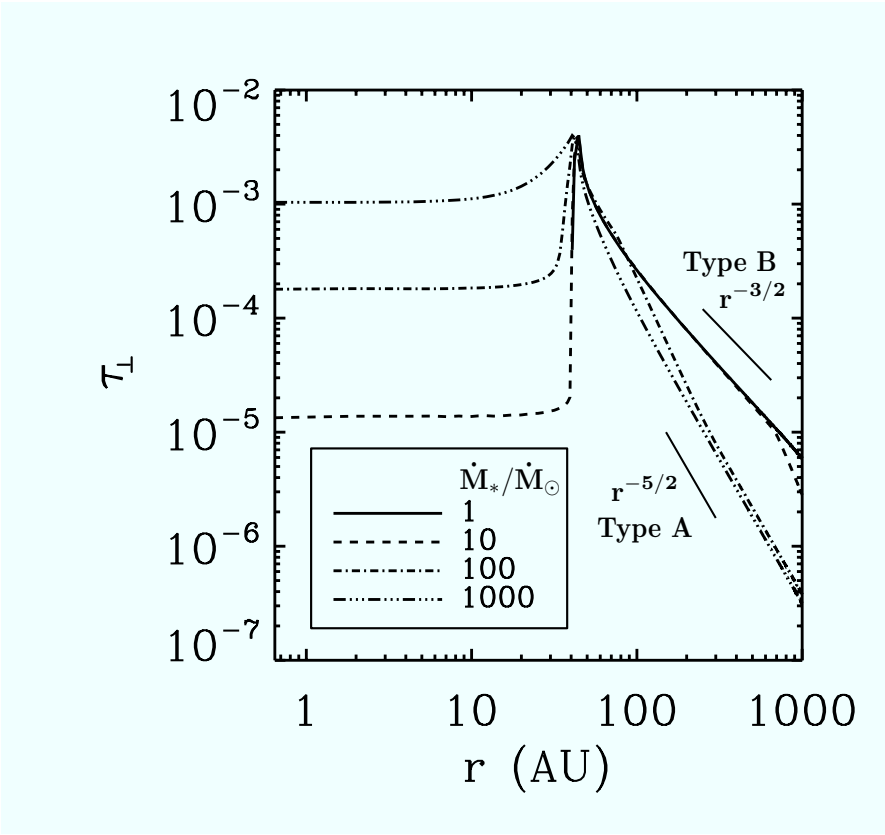

Figure 5.4: Vertical optical depth profiles computed from our Monte Carlo simulations. Solid, dashed, dot-dashed, and triple-dot–dashed curves correspond respectively to $\dot{M}_*/\dot{M}_\odot = \{1, 10, 10^2, 10^3\}$. Values for $\tau_{\perp,\mathrm{BR}} = 0.004$ and $\Delta r/r_{\mathrm{BR}} = 0.1$ are held fixed for all models. The two types of disks, CPR-dominated type A disks and collision-dominated type B disks, may be distinguished. The inner disk for $\dot{M}_* = 1\dot{M}_\odot$ is completely empty because $s_{\mathrm{break}} < s_{\mathrm{age}}$.

5.4.3 Results

By experimenting with various values of $\tau_{\perp,\mathrm{BR}}$, Δr, and $\dot{M}_* \in (1, 10, 10^2, 10^3)\dot{M}_\odot$, we find that $\tau_{\perp,\mathrm{BR}} = 4\times10^{-3}$, $\Delta r/r_{\mathrm{BR}} = 0.1$, and $\dot{M}_* \in (1, 10)\dot{M}_\odot$ yield theoretical surface brightness profiles and spectra that agree encouragingly well with observations. Our preferred values for $\tau_{\perp,\mathrm{BR}}$ and Δr are likely uniquely determined to within factors of a few; $\mathrm{SB}(b = r_{\mathrm{BR}}) \propto \tau_{\perp,\mathrm{BR}}\sqrt{\Delta r}$ while $F_\nu \propto \tau_{\perp,\mathrm{BR}}\Delta r$. The close resemblance of the models for which $\dot{M}_* \lesssim 10\dot{M}_\odot$ means that we cannot do better than place an upper limit on $\dot{M}_*/\dot{M}_\odot$ of $\sim$10. In what follows, we present results for our preferred input parameters, in addition to models for which $\dot{M}_* \in (10^2, 10^3)\dot{M}_\odot$ to study the effect of varying $\dot{M}_*$ alone.

Figure 5.4 displays geometric optical depth profiles $\tau_\perp(r)$. As expected from our analysis in §5.3.2, disks separate into two types, CPR-dominated type A and collision-dominated type

B. As $\dot{M}_*$ increases, disk behavior changes from type B to Type A. One consequence is that the inner disk becomes increasingly filled in. Furthermore, for type A disks, we expect $\tau_\perp \propto r^{-5/2}$ at $r \gg r_{\rm BR}$; this behavior is indeed evident for $\dot{M}_*/\dot{M}_\odot \in (10^2, 10^3)$. For type B disks, we expect $\tau_\perp \propto r^{-3/2}$ at $r \gg r_{\rm BR}$; the models for which $\dot{M}_*/\dot{M}_\odot \in (1, 10)$ exhibit this scaling.

We compare our theoretical surface brightness profiles SB(b) with data from K05 in Figures 5.5 and 5.6, for the cases of high $\dot{M}_*$ and low $\dot{M}_*$, respectively. For all disk models, there is a significant contribution to the surface brightness at $b < r_{\rm BR}$ from starlight that is forward scattered by grains located within the half of the birth ring nearest the observer. As $\dot{M}_*$ increases, the inner disk fills in and the surface brightness at $b < r_{\rm BR}$ increases. In comparison, the surface brightness at $b \gg r_{\rm BR}$ decreases with increasing $\dot{M}_*$, reflecting the transition from the $\tau_\perp \propto r^{-3/2}$ scaling of type B disks to the $\tau_\perp \propto r^{-5/2}$ scaling of type A disks. Examination of either the inner or outer disk profiles reveals that models for which $\dot{M}_*/\dot{M}_\odot \in (1, 10)$ fit the data better than do models for which $\dot{M}_*$ is higher. Discrepancies between these low-$\dot{M}_*$ models and the observations are less than a factor of 2. They might arise in part from our use of a scattering phase function (P) appropriate for idealized spherical grains of pure water ice.

In Figure 5.7, we plot $V - H$ colors. For low values of $\dot{M}_*$, the inner disk is largely evacuated and so there is little variation in color with b for $b < r_{\rm BR}$. The outer disk becomes progressively bluer with b as ever smaller (still bound) grains are probed. All of these trends are in agreement with observations of disk color (S. Metchev 2005, private communication; M. Fitzgerald 2005, private communication).

In Figure 5.8, we plot our theoretical spectra together with flux measurements from Liu et al. (2004) and Chen et al. (2005). The filled inner disks of high-$\dot{M}_*$, type A models produce too much emission at mid-infrared wavelengths to compare well with observations. As was our conclusion from studying the surface brightness profile in reflected starlight, the thermal emission spectra point to stellar mass-loss rates of $\lesssim 10\dot{M}_\odot$.

5.5 Summary and Directions for Future Work

We have constructed a theory to explain the observed optical surface brightness profile and infrared emission spectrum of the debris disk encircling AU Mic. In our theory, the slope of surface brightness versus projected radius b changes abruptly at $b = 43\,{\rm AU}$ because a birth ring of planetesimals exists at stellocentric radius $r = r_{\rm BR} = 43\,{\rm AU}$. This ring has a full radial width $\Delta r \sim 0.1 r_{\rm BR}$ and a vertical, geometric optical depth of $\tau_{\perp,{\rm BR}} \sim 0.004$. The parent bodies in the ring have sizes $s_{\rm max} \sim 10\,{\rm cm}$ and a total mass of $M_{\rm max} \sim 0.01 M_\oplus$. Collisional attrition of parent bodies generates micron-sized grains that scatter starlight at optical wavelengths. The population of visible grains is maintained in steady state: production by colliding parent bodies balances removal by grain-grain collisions and removal by corpuscular and Poynting-Robertson (CPR) drag. The timescales over which removal of visible grains occurs can be orders of magnitude shorter than the age of the

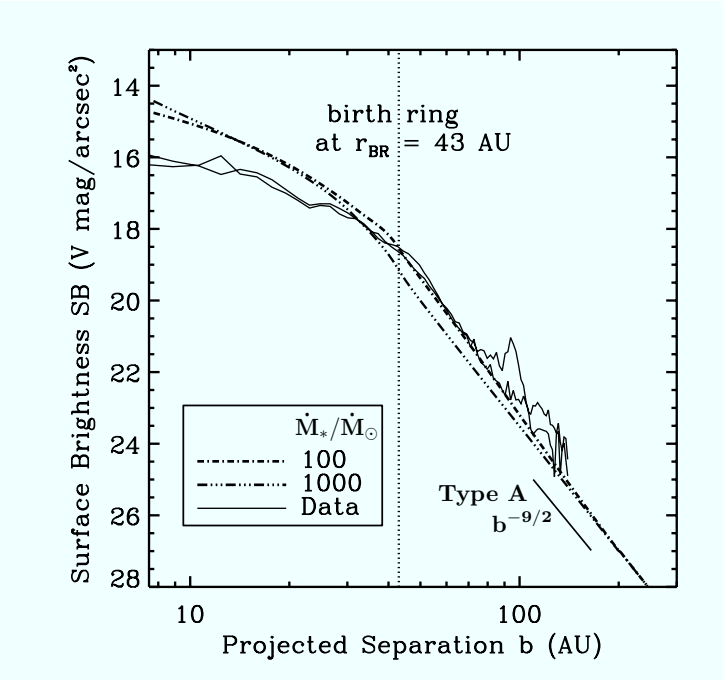

Figure 5.5: Theoretical type A and observed surface brightness profiles. Thin lines are data (for northwest and southeast extensions of the disk) from K05. dot-dashed and triple-dot–dashed curves correspond respectively to $\dot{M}_*/\dot{M}_\odot = \{10^2, 10^3\}$. The vertical dotted line corresponds to $r_{\rm BR} = 43\,{\rm AU}$, the radius of the birth ring containing dust-producing parent bodies. The inset scaling of $b^{-9/2}$ is derived from the rule of thumb that at large b, SB $\propto b^{\gamma-\eta-1}$ for $h \propto r^\eta$ and $\tau_\perp \propto r^\gamma$. According to our theory for type A disks, $\eta = 1$ and $\gamma = -5/2$.

system (∼12 Myr), ensuring steady state.

Collisions between parent bodies initiate a collisional cascade that extends downward in particle size by several orders of magnitude. Grains having sizes $s < s_{\rm blow} \approx 0.2\,\mu$m are expelled from the system by stellar wind and radiation (SWR) pressure and contribute negligibly to the observed optical emission. Instead, barely bound grains, having sizes just larger than $s_{\rm blow}$ and which occupy highly eccentric orbits, make the dominant contribution to the surface brightness in the outer disk at $r > r_{\rm BR}$. The number of such grains rises more steeply than would be expected from a pure Dohnanyi size spectrum as s approaches $s_{\rm blow}$ from above, because grains on high-eccentricity orbits have prolonged lifetimes against CPR drag and collisions. The structure of the outer disk depends on whether these smallest of bound grains are removed principally by CPR drag (type A conditions) or by destructive grain-grain collisions (type B conditions). As the luminosity and/or mass-loss rate of the central star increases, disk behavior grades from type B to type A. As the number of parent

bodies in the birth ring increases, collision rates increase and disk behavior changes from type A to type B. In the outer reaches of type A disks, the vertical optical depth scales approximately as $\tau_\perp \propto r^{-5/2}$. Under type B conditions, $\tau_\perp \propto r^{-3/2}$ (but see footnote 6). We have derived these scaling relations analytically and have verified them by Monte Carlo simulations.

The inner regions at $r < r_{\rm BR}$ are populated by grains that survive long enough before suffering destructive collisions that their periastron distances diminish appreciably by CPR drag. In type A disks, a significant fraction of grains born in the birth ring meet this criterion, so the inner disk is characterized by the same vertical optical depth that characterizes the birth ring. By contrast, under type B conditions, the inner disk is practically empty.

In the case of AU Mic, type B conditions prevail. By fitting simultaneously both the surface brightness profile and the thermal emission spectrum, we not only uniquely determine the vertical optical depth and radial width of the birth ring (see the values cited above), but also constrain the stellar mass-loss rate $\dot{M}_*$ to be $\lesssim 10\dot{M}_\odot$. According to our theory, the inner disk of AU Mic at $r < r_{\rm BR}$ is empty. The observed surface brightness at $b < r_{\rm BR}$ is

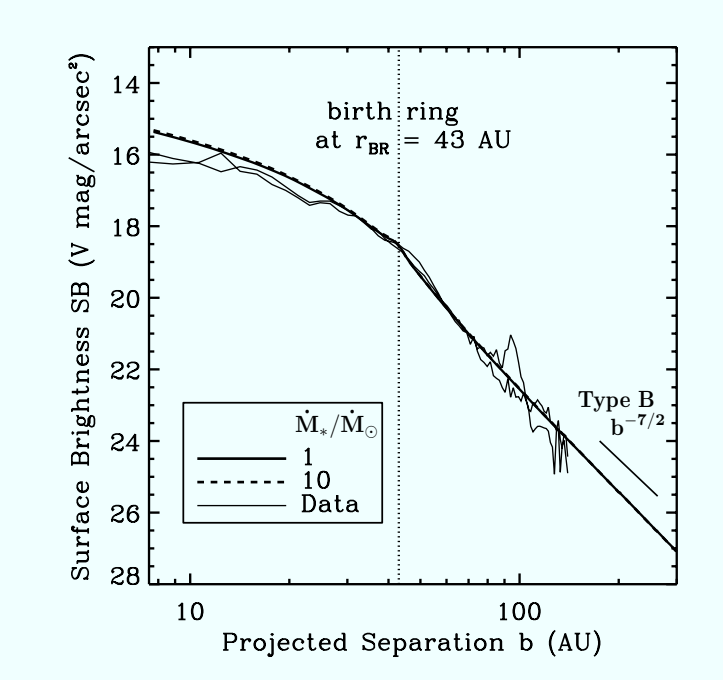

Figure 5.6: Same as Figure 5.5 but for type B disk models. Thick solid and dashed curves correspond respectively to $\dot{M}_*/\dot{M}_\odot = \{1, 10\}$. The vertical dotted line corresponds to $r_{\rm BR} = 43\,{\rm AU}$, the radius of the birth ring containing dust-producing parent bodies. The inset scaling of $b^{-7/2}$ is derived from the rule of thumb that at large b, SB $\propto b^{\gamma-\eta-1}$ for $h \propto r^\eta$ and $\tau_\perp \propto r^\gamma$. According to our theory for type B disks, $\eta = 1$ and $\gamma = -3/2$. Stellar mass-loss rates of 1–$10\dot{M}_\odot$ yield surface brightness profiles that agree better with the data than those derived from rates of 10^2–$10^3\dot{M}_\odot$; contrast with Figure 5.5.

not zero because we are observing the disk edge-on. The primary contribution to the surface brightness at $b < r_{\rm BR}$ arises from starlight that is forward scattered by grains in the birth ring.

Our theory states that the observed structure of the AU Mic disk reflects processes that are balanced in steady state. Equilibrium is likely since the timescales over which collisions and CPR drag operate, even in the rarefied outer disk, are shorter than the age of the system. The outer disk does not comprise "primordial" grains left behind from a now-evaporated gaseous disk, as has been speculated previously. Nor is the manifestation of the debris disk phenomenon in AU Mic the outcome of a recent cataclysm that has not yet equilibrated. That our required parent body mass is modest (equation [5.42]) supports our contention that the AU Mic disk is in steady state.

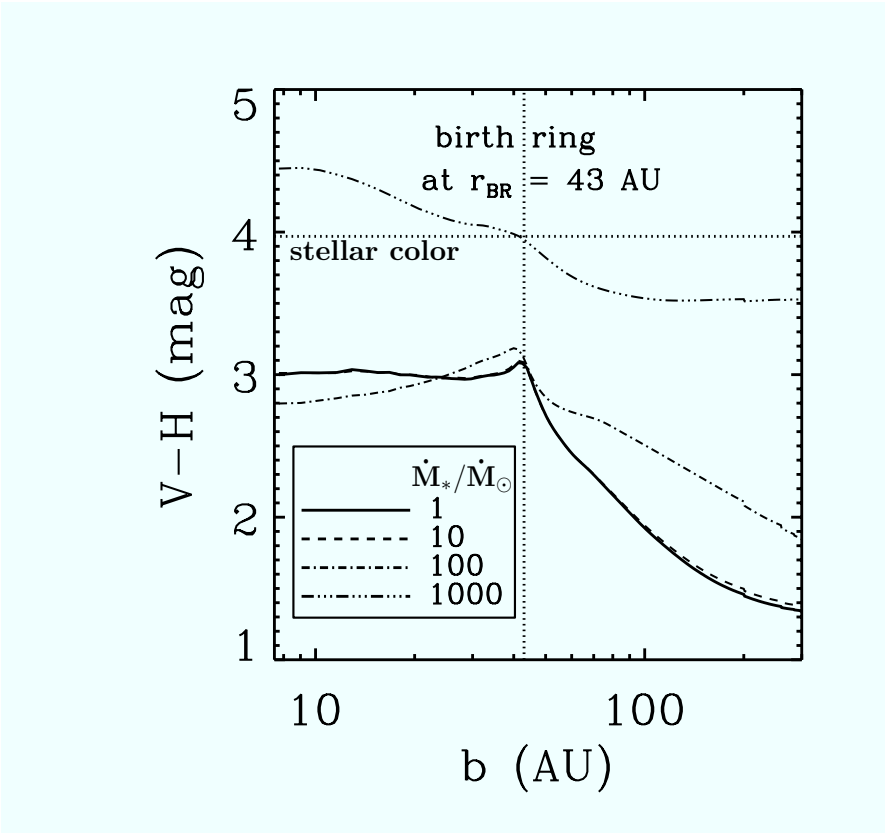

Figure 5.7: Color profile ($F606W - H$) computed using our theoretical Monte Carlo model. Solid, dashed, dot-dashed, and triple-dot–dashed curves correspond respectively to $\dot{M}_*/\dot{M}_\odot = \{1, 10, 10^2, 10^3\}$. The vertical dotted line corresponds to $r_{\rm BR} = 43\,{\rm AU}$, the radius of the birth ring containing dust-producing parent bodies; the horizontal dotted line is the star's color. The outer disk is expected to be bluer in scattered near-infrared light than the inner disk.

As our paper was being completed, we became aware of an independent study of AU Mic by Augereau & Beust (2006). These authors find by inverting the observed surface brightness profile that the underlying vertical optical depth of the AU Mic disk peaks near 35 AU. It is heartening that their conclusion is consonant with one of ours, derived as they are using complementary approaches: detailed data-fitting procedures versus physical reasoning to understand dust dynamics under general circumstances.

The ring of parent bodies at $r_{\rm BR} = 43\,{\rm AU}$ that we envision encircling AU Mic presents a youthful analogue to the Solar System's Kuiper belt (see the Protostars and Planets V review by Chiang et al. 2006). The spatial dimensions of these systems are remarkably similar: The Classical Kuiper belt, containing those planetesimals thought to have formed *in situ*, extends in heliocentric distance from ∼40 AU to ∼47 AU (e.g., Trujillo & Brown

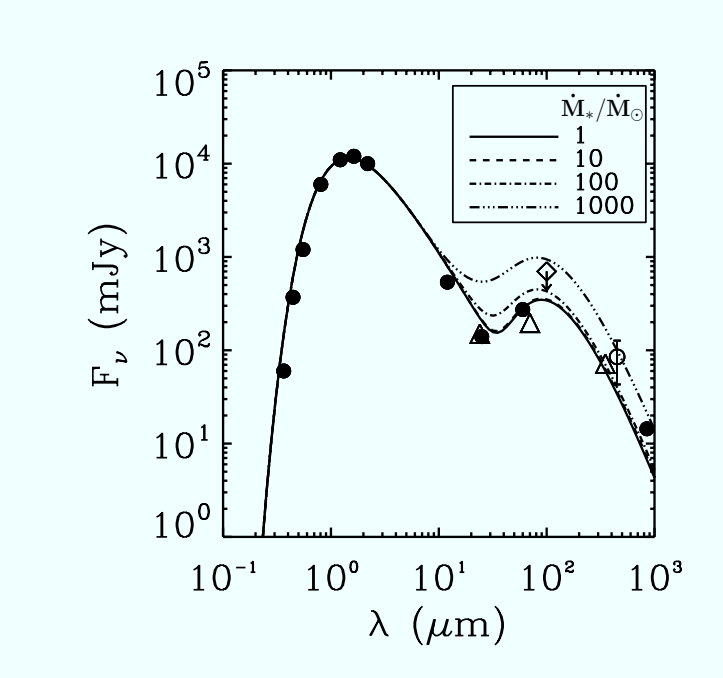

Figure 5.8: Spectra computed using our theoretical Monte Carlo model. Solid, dashed, dot-dashed, and triple-dot–dashed curves correspond respectively to $\dot{M}_*/\dot{M}_\odot = \{1, 10, 10^2, 10^3\}$. Data from Liu et al. (2004) (circles and diamond) and Chen et al. (2005) (triangles) are overlaid; the open circle is a possible detection, and the diamond represents an upper limit. The discrepancy between theory and observation at $\lambda \approx 12\,\mu$m is due to our use of a blackbody spectrum for the central M dwarf; better agreement can be had by employing more realistic stellar atmosphere models (e.g., Allard et al. 2001). The discrepancy between the data and the low-$\dot{M}_*$ models at the longest wavelengths is due at least in part to the fact that the maximum grain size in our simulations is $500 s_{\rm blow} \ll s_{\rm max}$; were we to increase the number of particles J in our simulation, the discrepancy would be reduced.

2001).

We conclude by pointing out directions for future work on AU Mic and other debris disks.

1. *Disk thickness.*—By assuming that we are viewing the AU Mic disk perfectly edge-on, we estimated a full disk height of $h_{\rm BR} \approx 2.75\,{\rm AU}$. The corresponding opening angle is $h_{\rm BR}/r_{\rm BR} \approx 4^\circ$. While our model of a type B disk succeeds in reproducing the observed scaling behavior of disk height ($h \propto b^0$ in the inner disk and $h \propto b^1$ in the outer disk), we have not explained what sets the normalization. Dissipative grain-grain collisions would be expected to damp the inclination dispersion and to reduce $h_{\rm BR}$ to values orders of magnitude smaller than our inferred value.

2. *Application to other systems.*—The debris disk surrounding the A-star β Pictoris closely resembles the AU Mic disk (Liu 2004). The surface brightness profile abruptly changes slope at $b \approx 100\,{\rm AU}$, from SB $\propto b^{-2.4}$ to SB $\propto b^{-4.0}$ (Kalas & Jewitt 1995). Moreover, the vertical scale height h scales with b the same way that it does in the AU Mic disk.[8] Recently, another analogue to the AU Mic disk has been discovered: F-star HD 139664 hosts a debris disk whose surface brightness profile exhibits a sharp break at $\sim$90 AU (Kalas et al. 2006). The theory we have laid out for AU Mic might find ready application to these other systems.

3. *Uniqueness of AU Mic among M dwarfs.*—The pioneering Keck survey conducted by PJL05 at $\lambda = 11.7\,\mu{\rm m}$ reveals that AU Mic is distinguished among their sample of nine M dwarfs having ages of 10–500 Myr in emitting an infrared excess. Why? Do the other M dwarfs not possess disks? As M dwarfs constitute the most numerous stars in the universe, understanding why AU Mic might be exceptional will help to determine the prevalence of planetary systems. Many of the M dwarfs surveyed by PJL05 may simply be much older than AU Mic; their parent body populations may have suffered near complete comminution.

4. *Ubiquity of rings.*—That parent bodies are confined to a ring centered at 43 AU in the AU Mic system calls for explanation. Ring morphologies are so common—witness the examples of HR 4796A (Schneider et al. 1999), ϵ Eridani (Greaves et al. 1998), Fomalhaut (Kalas et al. 2005), and even the Kuiper Belt—that the "debris disk phenomenon" might well be more precisely termed the "debris ring phenomenon." While regions interior to rings might have been purged of material by planets, the physical processes that determine the outer edges of rings remain unclear. Ideas proposed by Takeuchi & Artymowicz (2001) and Klahr & Lin (2005) for how interactions between

[8]That the color of β Pic's outer disk is red rather than blue (by contrast to the case of AU Mic) could be a consequence of the particular grain size required for blow-out in the β Pic system, since for certain grain sizes and compositions, $Q_{\rm scat}(\lambda, s)$ can actually increase with increasing wavelength. See Bohren & Huffman (1983) for a discussion of this phenomenon of "blueing."

solids and gas can concentrate planetesimals into rings might be relevant. That planetary systems have sharp outer edges suggests that planetesimal formation is not a continuous function of disk properties; rather, the formation of planets may require disk properties to meet threshold conditions (e.g., Youdin 2004).

Acknowledgments

This work was made possible by grants from the National Science Foundation and the Alfred P. Sloan Foundation. We are grateful to Peter Plavchan for extensive and helpful discussions, and to John Krist for supplying us with *HST* surface brightness data. We acknowledge encouraging exchanges with Pawel Artymowicz, Doug Baker, Josh Eisner, Mike Fitzgerald, James Graham, Lynne Hillenbrand, Mike Jura, Paul Kalas, Yoram Lithwick, Holly Maness, Stan Metchev, Re'em Sari, and Yanqin Wu. A portion of this work was completed in Awaji Island, Japan, in the cheerful company of the participants of the 2005 Kobe International Planetary School.

Table 5.1: Stellar Wind and Radiation Parameters in the AU Mic System[a]

$\dot{M}_*/\dot{M}_\odot$	$P_{\rm SWR}$	$P_{\rm CPR}$	$s_{\rm blow}(\,\mu{\rm m})^b$	$t_{\rm CPR}(s=1.1s_{\rm blow})(\,{\rm yr})^c$	$t_{\rm CPR}(s=1.5s_{\rm blow})(\,{\rm yr})^c$	$t_{\rm CPR}(s=15s_{\rm blow})(\,{\rm yr})^c$
1	2.0	5.0	0.23	9.5×10^6	4.9×10^6	1.9×10^7
10	2.0	32	0.23	1.5×10^6	7.8×10^5	3.1×10^6
10^2	2.4	3.0×10^2	0.28	1.9×10^5	9.9×10^4	3.9×10^5
10^3	6.4	3.0×10^3	0.74	5.1×10^4	2.6×10^4	1.0×10^5

[a] Assumes $Q_{\rm rad}=2$, $Q_{\rm wind}=1$, $\rho=2\,{\rm g\,cm^{-3}}$, $v_{\rm wind}=450\,{\rm km\,s^{-1}}$, $L_*=0.1L_\odot$, $M_*=0.5M_\odot$, $\dot{M}_\odot=2\times10^{-14}M_\odot\,{\rm yr^{-1}}$, and $r_{\rm peri}=r_{\rm BR}=43\,{\rm AU}$.

[b] The blow-out radius is such that $\beta=1/2$.

[c] Calculated for $e=e_0$. For $s/s_{\rm blow}=\{1.1,1.5,15\}$, $e_0=\{0.83,0.50,0.034\}$ by equations (5.9) and $E(e_0)=\{7.2,2.7,1.1\}$ by equation (5.14).

Chapter 6

Epilogue: Recent observational work

I close by returning to tidal disruptions. During the final year of my thesis, two groundbreaking tidal disruption candidates were discovered by teams led by Berkeley's Dr. S. B. Cenko and Prof. J. S. Bloom. These events are the first optically-selected candidate found in real time, labelled "PTF10iya" (Cenko et al. 2011), and the first TDE candidate found in the γ-rays, labelled "Swift 1644+57" (Bloom et al. 2011). I contributed to the analysis in both of these discoveries, and describe the discoveries and interpretation below.

6.1 PTF10iya

The Palomar Transient Factory uses the Palomar 48" telescope (P48) to robotically image $\approx 8000\,\mathrm{deg}^2$ of sky every five days in the optical R band. On June 6, 2010, a flare of $R = 19.77$ magnitude was found automatically by PTF's "Oarical" software. The event was found to be coincident with a modestly red galaxy at $z = 0.22$ in the Sloan Digital Sky Survey, SDSS J143840.98+373933.4 (hereafter, SDSS J1438). The location of PTF10iya had previously been observed in 2007 – 2008 as part of the Palomar-QUEST survey (compiled as part of the Deep Sky Project). These observations and the SDSS observations are consistent with no previous variability for this object. The object had not previously been detected in the *ROSAT* All-Sky Survey (0.1 – 2.4 keV), *Fermi* Large Area Telescope (100 MeV – 100 GeV) one-year point source catalog, or *VLA* FIRST Survey (1.4 GHz).

The source was followed up at optical wavelengths with the Palomar 60" telescope (P60) in g', r', and i' bands the following day (June 7), and six days later (June 13). Excess optical emission was not seen again after June 13. The blue color and overall brightness of the P60 observations led the team to trigger follow-up by the *Swift* satellite on June 11: PTF10iya was detected in the 0.3 – 10 keV band (with the XRT) and in the far UV (with the UVOT). The UV colors are very blue, and the X-ray spectrum was found to be peaked towards the highest energies. Later *Swift* observations on August 10 detected no X-rays.

High-resolution imaging with adaptive optics on the *Keck* telscope (using the NIRC2 camera in K' band) showed that the event was within 1.2 kpc of the center of SDSS J1438.

Optical spectroscopy with ISIS on the Willian Herschel Telescope and LRIS on Keck, taken right during the event on June 8 and then four days and a month later, showed two important results: the host galaxy exhibits emission lines characteristic of forming stars (but not an AGN), and the flare spectrum is essentially featureless with a strong blue continuum.

The optical light curve of the flare is shown in Figure 6.1: the event is clearly short-lived, lasting only ≈ 10 days. The spectral energy distribution of the flare is shown in Figure 6.2. The SED was fitted to a blackbody of temperature $T \approx 1-2\times10^4\,\mathrm{K}$ accompanied by a hard X-ray component, yielding a bolometric luminosity of $\sim 10^{44}-10^{45}\,\mathrm{erg\,s^{-1}}$ (depending on the galaxy extinction law). The event is unlikely to have been a supernova for several reasons. First, the optical emission is too short-lived (the decay timescale is faster than any known supernova). Second, although there is a class of supernovae that produce X-ray emission, the X-ray emission from PTF10iya is far brighter and shorter-lived than these, and these typically show optical emission lines which PTF10iya does not. Furthermore, PTF10iya

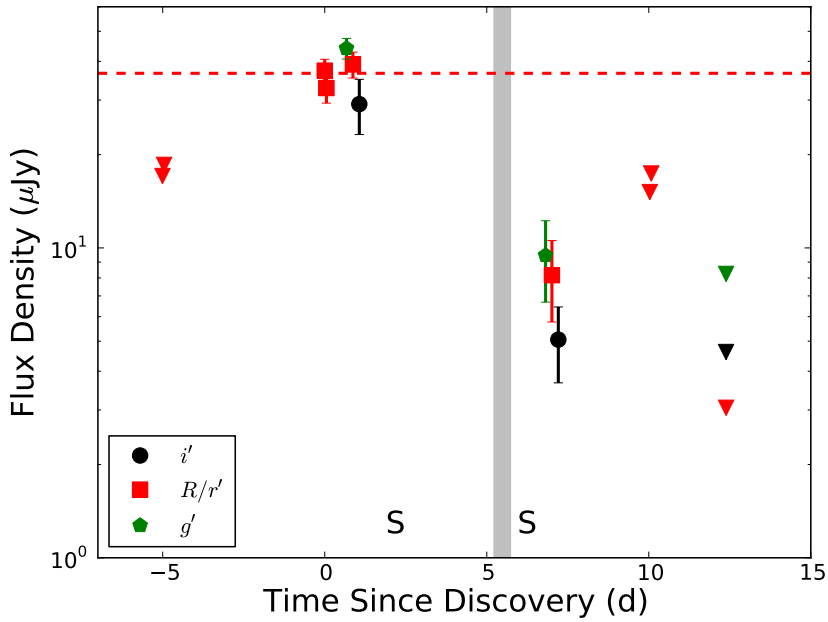

Figure 6.1: Observed optical light curve of PTF10iya, around the time of outburst. The time is referenced to the P48 discovery on Jun 6.302. Inverted triangles represent 3σ upper limits. The shaded grey vertical bar indicates the epoch of our *Swift* X-ray and UV observations. The horizontal dashed line indicates the quiescent (r') magnitude of the host galaxy SDSS J1438. The times of optical spectroscopic observations are marked with an "S". No correction has been applied for extinction within the host galaxy. Note that the i' and g' data have been offset slightly in the horizontal direction for plotting purposes. Figure and caption from Cenko et al. (2011).

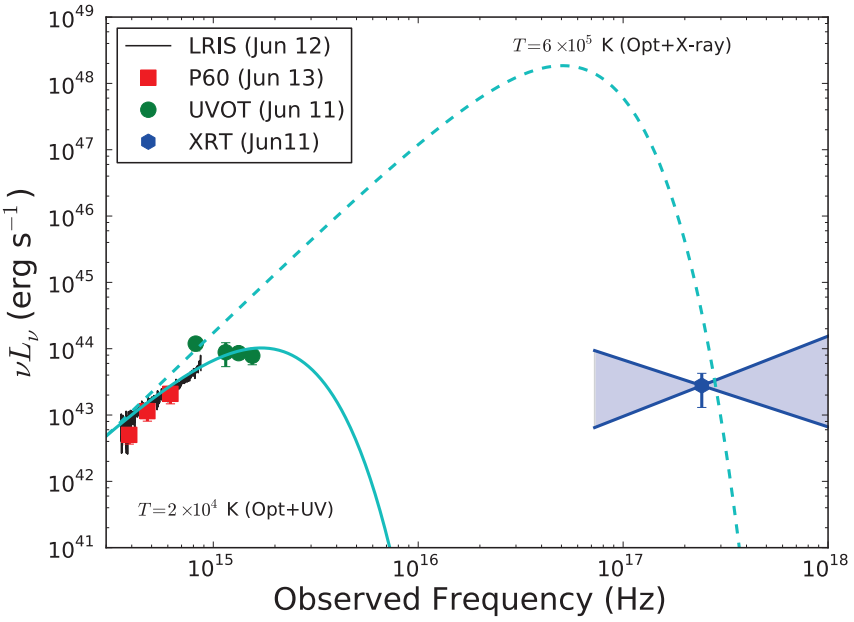

Figure 6.2: Broadband SED of PTF10iya. We have plotted the LRIS spectrum from June 12, P60 photometry from June 13, and UVOT and XRT photometry from June 11. A blackbody fit to incorporate both the optical and X-ray data requires $T \approx 6 \times 10^5\,\mathrm{K}$, but is inconsistent with the observed X-ray spectrum (the range of allowed power-law indices is indicated by the shaded blue region) and severely overpredicts the UV flux. On the other hand, a blackbody fitting both the UV and optical flux ($T = 2 \times 10^4\,\mathrm{K}$) cannot account for the bright X-ray emission. Figure and caption from Cenko et al. (2011).

was unlikely an AGN outburst because (1) it shows no previous variability, (2) the host galaxy's spectrum has emission line ratios inconsistent with the presence of an AGN, and (3) the inconsistency between the SED shape / spectroscopic observations and those of even unusual AGN outbursts.

PTF10iya may therefore have been a flare produced by the tidal disruption of a star. The observed properties of the event are broadly consistent with our predictions for a super-Eddington outflow produced in the aftermath of a disruption—the bright optical emission, fast evolution, blue color, featureless continuum, and hard X-rays. We show in Figure 6.3 a super-Eddington outflow model from Chapter 2 (Strubbe & Quataert 2009) for $M_{\rm BH} = 10^6 M_\odot$, $r_{\rm p} = 12 r_{\rm S} = 0.5 r_{\rm T}$, $f_{\rm out} = 0.4$, and $f_v = 1$, overplotted with UV/optical data from P48, P60, and *Swift* / UVOT. This figure demonstrates the similarity between the observations and our optical/UV predictions. The large photosphere and cool temperature of the gas driven from the BH while the fallback rate is super-Eddington lead to a large optical/UV luminosity that is blue in color. The typical timescale for the evolution of emission from the super-Eddington outflow is $t_{\rm fallback} \sim$ days. In Chapter 3 (Strubbe & Quataert

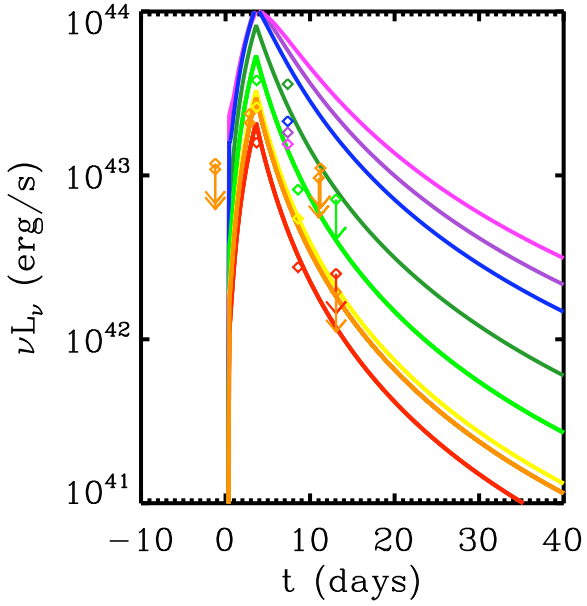

Figure 6.3: Super-Eddington outflow model from Chapter 2 (Strubbe & Quataert 2009) for $M_{\rm BH} = 10^6 M_\odot$, $r_{\rm p} = 12 r_{\rm S} = 0.5 r_{\rm T}$, $f_{\rm out} = 0.4$, and $f_v = 1$, with UV/optical data from Cenko et al. (2011): (red, orange, yellow, light green, dark green, blue, purple, magenta) correspond to (i', R, r', g', U, $UVW1$, $UVM2$, $UVW2$). Time on the horizontal axis is measured from the moment of disruption, which is taken to be 2010 June 2.8 UT. The discrepant UV colors may be due to extinction in the host galaxy.

2011), we show that super-Eddington outflows are typically too hot to produce spectral lines at optical wavelengths, consistent with PTF10iya's featureless continuum. Finally, though this is not yet well-studied, we propose that TDEs may be accompanied by hard X-rays, in particular if the density at the fallback shock at pericenter is too low to give the gas enough time to reach thermal equilibrium before it is driven out; the photons instead can Compton upscatter to produce X-rays. Our super-Eddington outflow model predicts that a few events per year within $z \lesssim 0.2$ should be detectable with PTF (perhaps more if $f_{\rm out}$ is typically large); our predictions seem consistent with this single discovery to date (especially given the complicated uncharacterized follow-up selection biases), though we expect that more should follow soon.

The discovery of PTF10iya is an exciting confirmation of our predictions, and offers a promising sign that PTF and other optical transient surveys will be able to detect, identify, and launch follow up observations of many TDEs in the near future.

6.2 Swift 1644+57

An unusual burst of hard X-rays was detected on March 28, 2011 by the *Swift* satellite's Burst Alert Telescope (which measures in the energy band 15 – 150 keV) (Levan et al. 2011; Burrows et al. 2011). Continuing and follow-up observations revealed that the event, labelled "Swift J164449.3+573451," reached a maximum (isotropic) X-ray luminosity of few $\times\, 10^{48}\,\mathrm{erg\,s^{-1}}$ (and average peak luminosity of $\sim 10^{47}\,\mathrm{erg\,s^{-1}}$), decaying on the long timescale of weeks. The X-ray emission (seen by *Swift*, and also in follow-up observations by *Chandra*) additionally showed strong variability on timescales of seconds to minutes. The source was bright and variable in the near infrared, and bright at millimeter and centimeter wavelengths as well (as observed by a variety of telescopes around the world). The optical emission, however, was dominated by the host galaxy, a compact non-interacting star-forming galaxy at $z = 0.35$ of comparable brightness to the Large Magellanic Cloud. The high-energy emission lasted far longer than a long-duration gamma-ray burst (which decays in minutes), and more luminous than any known AGN (especially considering the modest host galaxy).

We proposed that this extreme panchromatic event was produced by the tidal disruption of a star (Bloom et al. 2011). Specifically, it may be possible that highly super-Eddington accretion onto a BH produces a relativistic magnetically-collimated jet. Observing this jet head-on "down the barrel" would likely reveal relativistically beamed X-rays and γ-rays. These high-energy photons could be Compton upscattered from seed photons originating in the accretion disk or jet, or perhaps due to incomplete thermalization at the fallback shock at pericenter. A typical Lorentz factor for blazars is $\Gamma \sim 10$, which leads to a jet opening angle of $\sim 1/\Gamma \sim 0.1$, indicating that the true luminosity (integrated over all directions) may have been closer to $10^{45}\,\mathrm{erg\,s^{-1}}$, the Eddington luminosity for a $10^7 M_\odot$ BH. Relativistic electrons in the magnetic field would produce radio and near-infrared synchrotron emission (that could be visible even from other similar events witnessed off-axis; Giannios & Metzger 2011). The observed large-amplitude variability could conceivably be produced by the process of circularization of the orbits of gas particles. A super-Eddington outflow and accretion disk may well be present also but not visible above the optical emission of the host galaxy (which appears to be heavily extinguished). If the opening angle postulated above is correct, perhaps 10 such events take place per year (most of which are aimed away from us) in a volume $\sim 10\,\mathrm{Gpc}^3$. Such a volume contains $\sim 10^7 - 10^8$ galaxies, suggesting a rate of $\sim 10^{-7} - 10^{-6}\,\mathrm{yr^{-1}}$, which is lower than other estimates of the tidal disruption rate (e.g., Donley et al. 2002; Magorrian & Tremaine 1999; Wang & Merritt 2004). Perhaps only a fraction of disruptions are super-Eddington enough to produce a jet (e.g., because few have small enough pericenter distances: see Chapter 4); perhaps high BH spin is required to produce a jet, and only a small fraction of BHs have sufficiently high spin; or perhaps more of these events have been detectable but lacked the large-amplitude variability which aided their identification by *Swift* BAT.

Other (non-tidal disruption) explanations for Swift 1644+57 have been proposed (e.g., Quataert & Kasen 2011; Socrates 2011) as well. Nevertheless this extreme event is undoubtedly interesting for the study of tidal disruptions: it may give us new insights into accretion

physics, and demonstrates the ability of *Swift* to find powerful high-energy bursts from TDEs if they are out there.

Bibliography

Abramowicz, M. A., Czerny, B., Lasota, J. P., & Szuszkiewicz, E. 1988, ApJ, 332, 646
Alexander, T. 2005, Phys. Rep., 419, 65
Allard, F., Hauschildt, P. H., Alexander, D. R., Tamanai, A., & Schweitzer, A. 2001, ApJ, 556, 357
Atkinson, J. W., Collett, J. L., Marconi, A., et al. 2005, MNRAS, 359, 504
Augereau, J., & Beust, H. 2006, A&A, 455, 987
Ayal, S., Livio, M., & Piran, T. 2000, ApJ, 545, 772
Bade, N., Komossa, S., & Dahlem, M. 1996, A&A, 309, L35
Bahcall, J. N., & Wolf, R. A. 1976, ApJ, 209, 214
Balbus, S. A., & Hawley, J. F. 2002, ApJ, 573, 749
Balcells, M., Graham, A. W., & Peletier, R. F. 2007, ApJ, 665, 1084
Baldwin, D. E., Cordey, J. G., & Watson, C. J. H. 1972, Nuclear Fusion, 2, 287
Barnes, J. E., & Hernquist, L. E. 1991, ApJ, 370, L65
Bernardi, M., Shankar, F., Hyde, J. B., Mei, S., Marulli, F., & Sheth, R. K. 2010, MNRAS, 404, 2087
Binney, J., & Merrifield, M. 1998, Galactic astronomy, ed. Ostriker, J. P. & Spergel, D. N. (Princeton University Press)
Binney, J., & Tremaine, S. 1987, Galactic dynamics, ed. Ostriker, J. P. & Spergel, D. N. (Princeton University Press)
Blaes, O., Krolik, J. H., Hirose, S., & Shabaltas, N. 2011, ApJ, 733, 110
Blandford, R. D., & Begelman, M. C. 1999, MNRAS, 303, L1
Bloom, J. S., et al. 2009, Whitepaper submitted to the "Optical and IR Astronomy from the Ground" Program Prioritization Panel of the Astro2010 Decadal Survey
Bloom, J. S., et al. 2011, Science, 333, 203
Bogdanović, T., Eracleous, M., Mahadevan, S., Sigurdsson, S., & Laguna, P. 2004, ApJ, 610, 707
Böker, T., Laine, S., van der Marel, R. P., et al. 2002, AJ, 123, 1389
Brassart, M., & Luminet, J.-P. 2008, A&A, 481, 259
Burns, J. A., Lamy, P. L., & Soter, S. 1979, Icarus, 40, 1
Burrows, D. N., et al. 2011, Nature, submitted
Cannizzo, J. K., Lee, H. M., & Goodman, J. 1990, ApJ, 351, 38
Cappellari, M., et al. 2007, MNRAS, 379, 418

Cappelluti, N., et al. 2009, A&A, 495, L9
Carter, B., & Luminet, J. P. 1982, Nature, 296, 211
Castor, J. I. 1970, MNRAS, 149, 111
Cenko, S. B., et al. 2011, MNRAS, submitted
Chen, C. H., et al. 2005, ApJ, 634, 1372
Chen, X., Madau, P., Sesana, A., & Liu, F. K. 2009, ApJ, 697, L149
Chiang, E., Lithwick, Y., Murray-Clay, R., Buie, M., Grundy, W., & Holman, M. 2007, Protostars and Planets V, 895
Clausen, D., & Eracleous, M. 2011, ApJ, 726, 34
Cohn, H., & Kulsrud, R. M. 1978, ApJ, 226, 1087
Di Matteo, T., Springel, V., & Hernquist, L. 2005, Nature, 433, 604
Donley, J. L., Brandt, W. N., Eracleous, M., & Boller, T. 2002, AJ, 124, 1308
Dotan, C., & Shaviv, N. J. 2011, MNRAS, 413, 1623
Drory, N., et al. 2009, ApJ, 707, 1595
Esin, A. A., McClintock, J. E., & Narayan, R. 1997, ApJ, 489, 865
Esquej, P., Saxton, R. D., Freyberg, M. J., et al. 2007, A&A, 462, L49
Esquej, P., Saxton, R. D., Komossa, S., et al. 2008, A&A, 489, 543
Evans, C. R., & Kochanek, C. S. 1989, ApJ, 346, L13
Faber, S. M., et al. 1997, AJ, 114, 1771
Ferland, G. J., Korista, K. T., Verner, D. A., Ferguson, J. W., Kingdon, J. B., & Verner, E. M. 1998, PASP, 110, 761
Ferrarese, L., Côté, P., Dalla Bontà, E., et al. 2006, ApJ, 644, L21
Ferrarese, L., & Merritt, D. 2000, ApJ, 539, L9
Frank, J. 1978, MNRAS, 184, 87
Frank, J., King, A., & Raine, D. 1992, Accretion power in astrophysics. (Cambridge University Press)
Frank, J., & Rees, M. J. 1976, MNRAS, 176, 633
Fujiwara, A., Cerroni, P., Davis, D., Ryan, E., & di Martino, M. 1989, in Asteroids II, ed. R. P. Binzel, T. Gehrels, & M. S. Matthews, 240
Gammie, C. F. 1998, MNRAS, 297, 929
Gebhardt, K., Bender, R., Bower, G., et al. 2000a, ApJ, 539, L13
Gebhardt, K., Lauer, T. R., Kormendy, J., et al. 2001, AJ, 122, 2469
Gebhardt, K., et al. 2000b, AJ, 119, 1157
Genzel, R., Eisenhauer, F., & Gillessen, S. 2010, Reviews of Modern Physics, 82, 3121
Gezari, S., Basa, S., Martin, D. C., et al. 2008, ApJ, 676, 944
Gezari, S., Halpern, J. P., Komossa, S., Grupe, D., & Leighly, K. M. 2003, ApJ, 592, 42
Gezari, S., Heckman, T., Cenko, S. B., et al. 2009, ApJ, 698, 1367
Gezari, S., Martin, D. C., Milliard, B., & others. 2006, ApJ, 653, L25
Ghez, A. M., et al. 2008, ApJ, 689, 1044
Giannios, D., & Metzger, B. D. 2011, ArXiv e-prints
Goldreich, P., Lithwick, Y., & Sari, R. 2004, ARA&A, 42, 549
Greenberg, R., Hartmann, W. K., Chapman, C. R., & Wacker, J. F. 1978, Icarus, 35, 1

Greene, J. E., & Ho, L. C. 2007, ApJ, 670, 92
Greene, J. E., Ho, L. C., & Barth, A. J. 2008, ApJ, 688, 159
Greene, J. E., Peng, C. Y., Kim, M., et al. 2010, ApJ, 721, 26
Greiner, J., Schwarz, R., Zharikov, S., & Orio, M. 2000, A&A, 362, L25
Grindlay, J. E. 2004, in American Institute of Physics Conference Series, Vol. 714, X-ray Timing 2003: Rossi and Beyond, ed. P. Kaaret, F. K. Lamb, & J. H. Swank, 413–422
Grupe, D., Thomas, H.-C., & Leighly, K. M. 1999, A&A, 350, L31
Guillochon, J., Ramirez-Ruiz, E., Rosswog, S., & Kasen, D. 2009, ApJ, 705, 844
Gültekin, K., Richstone, D. O., Gebhardt, K., et al. 2009, ApJ, 698, 198
Halpern, J. P., Gezari, S., & Komossa, S. 2004, ApJ, 604, 572
Häring, N., & Rix, H. 2004, ApJ, 604, L89
Heckman, T. M., Kauffmann, G., Brinchmann, J., Charlot, S., Tremonti, C., & White, S. D. M. 2004, ApJ, 613, 109
Hills, J. G. 1975, Nature, 254, 295
—. 1988, Nature, 331, 687
Hirose, S., Krolik, J. H., & Blaes, O. 2009, ApJ, 691, 16
Ho, L. C. 2008, ARA&A, 46, 475
Holz, D. E., & Hughes, S. A. 2005, ApJ, 629, 15
Hopkins, P. F., & Quataert, E. 2010, MNRAS, 407, 1529
Hopkins, P. F., Richards, G. T., & Hernquist, L. 2007, ApJ, 654, 731
Hopkins, P. F., et al. 2009, MNRAS, 397, 802
Hopman, C., & Alexander, T. 2006, ApJ, 645, 1152
Housen, K. R., & Holsapple, K. A. 1990, Icarus, 84, 226
Hünsch, M., Schmitt, J. H. M. M., Sterzik, M. F., & Voges, W. 1999, A&AS, 135, 319
Ichimaru, S. 1977, ApJ, 214, 840
Kalas, P., Graham, J. R., Clampin, M. C., & Fitzgerald, M. P. 2006, ApJ, 637, L57
Kalas, P., & Jewitt, D. 1995, AJ, 110, 794
Kasen, D., & Ramirez-Ruiz, E. 2010, ApJ, 714, 155
Kaspi, S., Maoz, D., Netzer, H., et al. 2005, ApJ, 629, 61
Katz, B., Budnik, R., & Waxman, E. 2010, ApJ, 716, 781
Khokhlov, A., & Melia, F. 1996, ApJ, 457, L61
King, A. R., & Pounds, K. A. 2003, MNRAS, 345, 657
Kochanek, C. S. 1994, ApJ, 422, 508
Kollmeier, J. A., et al. 2006, ApJ, 648, 128
Komossa, S. 2002, in Rev. Mod. Ast., Vol. 15, JENAM 2001: Astronomy with Large Telescopes from Ground and Space, ed. R. E. Schielicke, 27
Komossa, S., & Bade, N. 1999, A&A, 343, 775
Komossa, S., & Greiner, J. 1999, A&A, 349, L45
Komossa, S., & Merritt, D. 2008, ApJ, 683, L21
Komossa, S., et al. 2008, ApJ, 678, L13
—. 2009, ApJ, 701, 105
Koratkar, A., & Blaes, O. 1999, PASP, 111, 1

Kormendy, J., Drory, N., Bender, R., & Cornell, M. E. 2010, ApJ, 723, 54
Kormendy, J., & Kennicutt, Jr., R. C. 2004, ARA&A, 42, 603
Krist, J. E., et al. 2005, AJ, 129, 1008
Krolik, J. H. 1999, Active galactic nuclei : from the central black hole to the galactic environment (Princeton University Press)
Lacy, J. H., Townes, C. H., & Hollenbach, D. J. 1982, ApJ, 262, 120
Lauer, T. R., et al. 1995, AJ, 110, 2622
—. 2005, AJ, 129, 2138
Levan, A., et al. 2011, Science, 333, 199
Li, L., Narayan, R., & Menou, K. 2002, ApJ, 576, 753
Li, W., et al. 2011, MNRAS, 412, 1441
Lightman, A. P., & Eardley, D. M. 1974, ApJ, 187, L1
Lightman, A. P., & Shapiro, S. L. 1977, ApJ, 211, 244
Liu, M. C. 2004, Science, 305, 1442
Liu, M. C., Matthews, B. C., Williams, J. P., & Kalas, P. G. 2004, ApJ, 608, 526
Lodato, G., King, A. R., & Pringle, J. E. 2009, MNRAS, 392, 332
Lodato, G., & Rossi, E. M. 2011, MNRAS, 410, 359
Loeb, A., & Ulmer, A. 1997, ApJ, 489, 573
Lu, J. R., Ghez, A. M., Hornstein, S. D., Morris, M. R., Becklin, E. E., & Matthews, K. 2009, ApJ, 690, 1463
Luo, B., Brandt, W. N., Steffen, A. T., & Bauer, F. E. 2008, ApJ, 674, 122
Magee, H. R. M., Güdel, M., Audard, M., & Mewe, R. 2003, Advances in Space Research, 32, 1149
Magnier, E. 2007, in ASP Conf. Series, Vol. 364, The Future of Photometric, Spectrophotometric and Polarimetric Standardization, ed. C. Sterken, 153
Magorrian, J., & Tremaine, S. 1999, MNRAS, 309, 447
Magorrian, J., Tremaine, S., Richstone, D., et al. 1998, AJ, 115, 2285
Maksym, W. P., Ulmer, M. P., & Eracleous, M. 2010, ApJ, 722, 1035
McConnell, N. J., Ma, C.-P., Graham, J. R., Gebhardt, K., Lauer, T. R., Wright, S. A., & Richstone, D. O. 2011, ApJ, 728, 100
Merritt, D., & Ferrarese, L. 2001, in Astronomical Society of the Pacific Conference Series, Vol. 249, The Central Kiloparsec of Starbursts and AGN: The La Palma Connection, ed. J. H. Knapen, J. E. Beckman, I. Shlosman, & T. J. Mahoney, 335
Merritt, D., & Poon, M. Y. 2004, ApJ, 606, 788
Meyer, M. R., Backman, D. E., Weinberger, A. J., & Wyatt, M. C. 2007, Protostars and Planets V, 573
Murray, C. D., & Dermott, S. F. 2000, Solar System Dynamics (Cambridge University Press)
Murray, N., Chiang, J., Grossman, S. A., & Voit, G. M. 1995, ApJ, 451, 498
Narayan, R., & Yi, I. 1994, ApJ, 428, L13
National Research Council; Committee for a Decadal Survey of Astronomy and Astrophysics. 2011, New Worlds, New Horizons in Astronomy and Astrophysics (National Academies Press)

Noeske, K. G., et al. 2007, ApJ, 660, L43
Ohsuga, K. 2007, ApJ, 659, 205
Ohsuga, K., & Mineshige, S. 2007, ApJ, 670, 1283
Ohsuga, K., Mori, M., Nakamoto, T., & Mineshige, S. 2005, ApJ, 628, 368
Özişik, M. N. 1993, Heat conduction (New York: Wiley)
Parker, E. N. 1964, ApJ, 139, 93
Peiris, H. V., & Tremaine, S. 2003, ApJ, 599, 237
Perets, H. B., Hopman, C., & Alexander, T. 2007, ApJ, 656, 709
Peterson, B. M., & Ferland, G. J. 1986, Nature, 324, 345
Peterson, B. M., et al. 2004, ApJ, 613, 682
Phinney, E. S. 1989, in IAU Symposium, Vol. 136, The Center of the Galaxy, ed. M. Morris, 543
Pounds, K. A., King, A. R., Page, K. L., & O'Brien, P. T. 2003, MNRAS, 346, 1025
Pringle, J. E. 1981, ARA&A, 19, 137
Quataert, E., & Gruzinov, A. 2000, ApJ, 539, 809
Quataert, E., & Kasen, D. 2011, MNRAS, submitted
Quimby, R. M., et al. 2009, ArXiv e-prints
Ramirez-Ruiz, E., & Rosswog, S. 2009, ApJ, 697, L77
Rau, A., Kulkarni, S. R., Law, N. M., et al. 2009, PASP, 121, 1334
Rauch, K. P., & Tremaine, S. 1996, New Astronomy, 1, 149
Read, J. I., & Gilmore, G. 2003, MNRAS, 339, 949
Rees, M. J. 1977, QJRAS, 18, 429
—. 1988, Nature, 333, 523
Remillard, R. A., & McClintock, J. E. 2006, ARA&A, 44, 49
Renzini, A., Greggio, L., di Serego Alighieri, S., Cappellari, M., Burstein, D., & Bertola, F. 1995, Nature, 378, 39
Richstone, D., Ajhar, E. A., Bender, R., et al. 1998, Nature, 395, A14
Roberge, A., Weinberger, A. J., Redfield, S., & Feldman, P. D. 2005, ApJ, 626, L105
Rosenbluth, M. N., MacDonald, W. M., & Judd, D. L. 1957, Phys. Rev., 107, 1
Rossi, E. M., & Begelman, M. C. 2009, MNRAS, 392, 1451
Rosswog, S., Ramirez-Ruiz, E., & Hix, W. R. 2009, ApJ, 695, 404
Scannapieco, E., & Bildsten, L. 2005, ApJ, 629, L85
Seth, A., Agüeros, M., Lee, D., & Basu-Zych, A. 2008a, ApJ, 678, 116
Seth, A. C., Blum, R. D., Bastian, N., Caldwell, N., & Debattista, V. P. 2008b, ApJ, 687, 997
Shakura, N. I., & Sunyaev, R. A. 1973, A&A, 24, 337
Shapiro, K. L., Cappellari, M., de Zeeuw, T., McDermid, R. M., Gebhardt, K., van den Bosch, R. C. E., & Statler, T. S. 2006, MNRAS, 370, 559
Shapiro, S. L., & Lightman, A. P. 1976, Nature, 262, 743
Shapiro, S. L., & Marchant, A. B. 1978, ApJ, 225, 603
Sharma, P., Quataert, E., & Stone, J. M. 2007, ApJ, 671, 1696
Shen, S., Mo, H. J., White, S. D. M., Blanton, M. R., Kauffmann, G., Voges, W., Brinkmann,

J., & Csabai, I. 2003, MNRAS, 343, 978
Sigurdsson, S., & Rees, M. J. 1997, MNRAS, 284, 318
Silk, J., & Rees, M. J. 1998, A&A, 331, L1
Socrates, A. 2011, ApJ, submitted
Soltan, A. 1982, MNRAS, 200, 115
Spitzer, L. 1987, Dynamical evolution of globular clusters (Princeton University Press)
Spitzer, Jr., L., & Hart, M. H. 1971, ApJ, 164, 399
Stern, D., et al. 2004, ApJ, 612, 690
Stone, J. M., & Pringle, J. E. 2001, MNRAS, 322, 461
Stone, N., & Loeb, A. 2011, MNRAS, 412, 75
Strubbe, L. E., & Chiang, E. I. 2006, ApJ, 648, 652
Strubbe, L. E., & Quataert, E. 2009, MNRAS, 400, 2070
—. 2011, MNRAS, 415, 168
Syer, D., & Ulmer, A. 1999, MNRAS, 306, 35
Takeuchi, S., Mineshige, S., & Ohsuga, K. 2009, PASJ, 61, 783
Torres, C. A. O., & Ferraz Mello, S. 1973, A&A, 27, 231
Ulmer, A. 1999, ApJ, 514, 180
Šubr, L., Schovancová, J., & Kroupa, P. 2009, A&A, 496, 695
van der Marel, R. P. 2004, Coevolution of Black Holes and Galaxies, 37
van Velzen, S., Farrar, G. R., Gezari, S., et al. 2010, ArXiv e-prints
Vasiliev, E., & Zelnikov, M. 2008, Phys. Rev. D, 78, 083506
Verhamme, A., Schaerer, D., & Maselli, A. 2006, A&A, 460, 397
Wang, J., & Merritt, D. 2004, ApJ, 600, 149
Warren, S. G. 1984, Appl. Opt., 23, 1206
Weber, E. J., & Davis, Jr., L. 1967, ApJ, 148, 217
Wehner, E. H., & Harris, W. E. 2006, ApJ, 644, L17
Weymann, R. J., Morris, S. L., Foltz, C. B., & Hewett, P. C. 1991, ApJ, 373, 23
White, S. D. M., & Rees, M. J. 1978, MNRAS, 183, 341
Wyatt, M. C. 2005, A&A, 433, 1007
Wyatt, S. P., & Whipple, F. L. 1950, ApJ, 111, 134
Xu, Y., Xu, H., Zhang, Z., Kundu, A., Wang, Y., & Wu, X.-P. 2005, ApJ, 631, 809
Young, P. J., Shields, G. A., & Wheeler, J. C. 1977, ApJ, 212, 367
Yu, Q., & Tremaine, S. 2002, MNRAS, 335, 965
Yüksel, H., Kistler, M. D., Beacom, J. F., & Hopkins, A. M. 2008, ApJ, 683, L5
Zhao, H., Haehnelt, M. G., & Rees, M. J. 2002, New Astronomy, 7, 385